

Stochastic Simulations and Machine Learning Modeling to Predict Bedload Transport and Bed Topography

Présentée le 27 mai 2024

Faculté de l'environnement naturel, architectural et construit
Laboratoire d'hydraulique environnementale
Programme doctoral en mécanique

pour l'obtention du grade de Docteur ès Sciences

par

Mehrdad KIANI OSHTORJANI

Acceptée sur proposition du jury

Prof. F. Gallaire, président du jury
Prof. C. Ancey, directeur de thèse
Prof. P. Bohórquez Rodríguez de Medina, rapporteur
Dr M. Forghani, rapporteur
Dr G. De Cesare, rapporteur

In the world of probabilities;
don't look for certainty.

To my parents...

Acknowledgements

I am deeply and forever grateful to my mother and father, whose love and advice have served as a light illuminating the correct way throughout my life. The depth of their love surpasses anything. Their unwavering support has been the bedrock of my journey. I am also eternally thankful to my lovely brothers, Mahdi and Mehran, for their relentless encouragement and consistent support, which have been crucial in my pursuits. Now that I am writing my PhD thesis, I remember the days when they would teach me what they learned in school when I was just a little kid. I cherish the memories of our scientific discussions during our walks to school.

I would like to express my profound thanks to my supervisor, Christophe Ancey. PhD students, due to numerous interactions with their supervisor over an extended period, resemble their supervisor in behavior and way of thinking by the end of the PhD. Reflecting on my growth since the start of my PhD, I recognize significant improvements in various areas, much of which I attribute to my interactions with you. Your supervision has provided me with an invaluable opportunity to engage in this research. Over the years, your guidance has been a source of inspiration, continuously driving me forward. Thanks for all the opportunities you provided me and your trust. I am also grateful to Barbara Tinguely and Bob de Graffenried for all the good memories we have made, your help, and for creating a positive environment in the laboratory. My heartfelt appreciation goes to my colleagues for their collaborative spirit, intellectual exchanges, and friendship. Their diverse perspectives and expertise have enriched my research ideas during our fruitful discussions. Also, thanks to my former colleagues, despite never having the opportunity to meet them, could grasp their underlying perspectives through their writings.

Additionally, I extend my sincerest gratitude to Prof. François Gallaire for accepting to be the president of the jury committee and to my examiners, Prof. Patricio Bohórquez, Dr. Giovanni De Cesare, and Dr. Mojtaba Forghani, for their willingness to review my work and constructive comments.

Special thanks are due to my circle of friends. Being in your company has been a source of joy and comfort. One reason for my happiness about the path I have taken is having the opportunity to get to know you along the way. Your friendship has provided a much-needed balance to my life, reminding me of the world beyond academics and changing my point

Acknowledgements

of view in many aspects of life during our fruitful discussions. Your humor, empathy, and understanding have been my sanctuary during the most challenging phases of this journey. The research presented in this thesis was conducted at the School of ENAC and the Environmental Hydraulics Laboratory at École Polytechnique Fédérale de Lausanne (EPFL), Switzerland. This work spans from 2019 to 2024. EPFL provided a healthy work environment to conduct high-quality research. My time here has been both intellectually rewarding and personally enriching. Special thanks go to the Swiss National Science Foundation (SNSF) for granting the funds for this research and making it possible.

In conclusion, I am grateful to everyone who has been a part of this journey. Each of you has left an indelible mark on my life and work. Thank you for being a part of my story.

Lausanne, 1 March 2024

M. K. O.

Abstract

In computational hydraulics models, predicting bed topography and bedload transport with sufficient accuracy remains a significant challenge. An accurate assessment of a river's sediment transport rate necessitates a prior understanding of its bed topography. Therefore, we designed a machine learning model to deduce bathymetry from cost-effective flow surface data, i.e., velocity fields. This model was applied to three case scenarios, especially at the confluence of the Kaskaskia River and Copper Slough in east-central Illinois, United States of America. The results demonstrated the model's effectiveness in gravel-bed river bathymetry estimation.

Although the bed topography can be deduced with good accuracy using indirect approaches, predicting bedload transport still faces a high level of error. One accepted reason among scientists for such high errors is that bedload transport is a noise-driven process. The bedload transport depends on many non-linearly varying parameters with various time and space scales, and these parameters are interrelated. Additionally, the fluctuations in bedload transport significantly influence several aspects of morphodynamic variations, such as bedform and bank erosion. Hence, the spatio-temporal variability of the bedload transport rate is of great importance as an inherent characteristic of gravel-bed rivers. To account for these fluctuations, we developed and validated one- and two-dimensional stochastic bedload models.

In the next step of this thesis, we aim to examine the one-dimensional stochastic bedload model through numerical simulation. To this end, bedform development and bedload transport rate in narrow gravel-bed flumes under supercritical flow regimes have been studied. This examination employs a numerical solver based on the one-dimensional depth-averaged Saint-Venant–Exner equations, integrated with a stochastic bedload model. In this work, we have proposed closure analytical formulas to parameterize the mass exchange rates between the flow and the bed. The numerical solver is implemented by the Finite Volume Method. While the stochastic numerical solver provides a single realization of reality, its key characteristics oscillate around mean values, allowing for meaningful comparisons between numerical outcomes and experimental datasets. The numerical studies concentrate on three key aspects: i. the rate of bedload transport; ii. the amplitude and wavelength of the antidunes; and iii. their migration velocity. These numerical predictions are examined by applying the solver to

Abstract

two laboratory datasets.

Finally, the last aim is to develop a two-dimensional stochastic bedload model that incorporates fluctuations and computes the random time variations in particle activity. To achieve this, the one-dimensional morphodynamic model is generalized to two dimensions. A linear stability analysis was carried out based on the developed governing equations, yielding neutral curves that align with the experimental dataset drawn from the literature. Subsequently, a numerical solver is developed based on the Finite Volume Method. The two-dimensional depth-averaged solver was used to study alternate bar development. It has been applied to gravel-bed experiments conducted in a long and wide gravel-bed flume under steady-state flow conditions. The numerical outcomes successfully captured the bedload transport rate, bar formation, and their growth rates in line with experimental data.

Résumé

Dans les modèles d'hydraulique numérique, prédire la topographie du lit et le transport solide avec une précision suffisante reste un défi majeur. Une évaluation précise du débit solide dans une rivière nécessite une compréhension préalable de la topographie du lit. C'est dans ce contexte que j'ai conçu un modèle d'apprentissage automatique pour déduire la bathymétrie à partir de la mesure de la vitesse à la surface libre de l'écoulement. Ce modèle a été appliqué à trois scénarios, dont un cas de terrain (la confluence de la rivière Kaskaskia et du Copper Slough dans le centre-est de l'Illinois, États-Unis d'Amérique). Les résultats ont montré l'efficacité du modèle dans l'estimation de la bathymétrie des rivières à lit de gravier.

Bien que la topographie du lit puisse être déduite avec une bonne précision en utilisant des approches indirectes, la prédiction du transport de sédiment est associée à des incertitudes significatives. Une raison évoquée parmi les scientifiques pour de telles erreurs est que le transport solide par charriage a une composante fortement aléatoire. Le charriage dépend de nombreux paramètres variant de manière non linéaire sur différentes échelles de temps et d'espace, et ces paramètres sont interdépendants. De plus, les fluctuations du débit solide influent fortement sur les processus morphodynamiques, tels que la formation de dunes et l'érosion des berges. Par conséquent, la variabilité spatio-temporelle du débit solide est d'une grande importance comme caractéristique inhérente des rivières à lit de gravier. Pour tenir compte de ces fluctuations, j'ai généralisé et validé des modèles stochastiques de transport sédimentaire par charriage pour des écoulement unidimensionnels et bidimensionnels.

Dans la seconde partie de ma thèse, j'ai résolu les équations du modèle stochastique de charriage à l'aide d'un modèle numérique dans le cas unidimensionnel. Cela m'a permis d'étudier le développement des formes du lit et le débit solide dans des canaux étroits à lit de gravier pour des régimes d'écoulement supercritiques. Cette étude emploie un solveur numérique basé sur les équations moyennées selon la hauteur appelées équation de Saint-Venant–Exner auxquelles était adjoint un modèle stochastique du charriage. Ces équations doivent être fermées à l'aide d'équations paramétrisant les taux d'échange de masse entre l'écoulement et le lit. Le solveur numérique est fondé sur la méthode des volumes finis. Bien que le solveur numérique stochastique fournisse une seule solution parmi d'autres et ne fournisse pas directement la solution moyennée (moyenne d'ensemble), on observe que les valeurs prédites de débit solide oscillent autour des valeurs moyennes, ce qui permet de

Abstract

comparer les résultats numériques et les données expérimentales. Les études numériques se concentrent sur trois aspects clés : i. le débit solide par charriage; ii. l'amplitude et la longueur d'onde des antidunes; et iii. leur vitesse de migration. Ces prédictions numériques sont examinées en appliquant le solveur à deux groupes distincts de données de laboratoire. Dans la dernière partie de ma thèse, j'ai développé un modèle stochastique de transport sédimentaire bidimensionnel moyenné. Pour ce faire, j'ai généralisé le modèle morphodynamique généralisé aux deux dimensions de l'espace (les équations restant moyennées selon la hauteur). J'ai réalisé une analyse de stabilité linéaire des équations du mouvement. J'ai montré que les courbes neutres que j'ai obtenues sont cohérentes avec l'ensemble de données expérimentales tirées de la littérature. Enfin, j'ai développé un solveur numérique fondé sur la méthode des volumes finis. Le solveur bidimensionnel moyenné selon la hauteur a été utilisé pour étudier le développement des bancs alternés. Il a été appliqué à des expériences de lit de gravier réalisées dans un canal long et large à lit de gravier dans le cas d'écoulements supercritiques permanents. Les résultats numériques prédisent des débits solides qui sont en bon accord avec les données expérimentales.

Contents

Acknowledgements	i
Abstract (English/Français)	iii
List of figures	xi
List of tables	xvii
1 Introduction	1
1.1 Motivation	1
1.2 Bed topography	3
1.3 Sediment transport	4
1.4 Sediment transport rate fluctuations	8
1.5 Realization of fluvial systems	10
1.6 Stochastic bedload transport model	11
1.7 Exner equation	15
1.8 Fluid governing equation	16
1.9 Numerical simulation	16
1.10 Stability analysis	17
1.11 Objectives and research contributions	18
1.12 Dissertation outline	20
2 Bed topography inference from velocity field using deep learning	21
2.1 Introduction	22
2.2 Methodology	25
2.2.1 Data collection	25
2.2.2 Entropy-based velocity profile	27
2.2.3 Neural network	30
2.3 Results and performance	35
2.3.1 Model performance	35
2.3.2 Model predictions	37
2.4 Discussion	42
2.5 Conclusion	45

3	Simulation of antidune migration in straight channel	47
3.1	Introduction	48
3.2	Theoretical model	50
3.2.1	Saint-Venant–Exner equations	50
3.2.2	Stochastic bedload transport model	52
3.2.3	Model calibration	56
3.3	Numerical model	60
3.3.1	Governing equations	60
3.3.2	Initial and boundary conditions	61
3.3.3	Finite volume method	62
3.3.4	Numerical implementation	65
3.4	Simulating antidunes formation and motion	65
3.4.1	Experimental scenarios	65
3.4.2	Bedload transport based on stochastic framework	68
3.4.3	Wavelength and amplitude based on stochastic framework	70
3.4.4	Migration celerity based on stochastic framework	72
3.4.5	Bedload transport based on ensemble-averaged framework	74
3.5	Discussion	77
3.5.1	Antidunes variability	77
3.5.2	Realization of fluvial systems	77
3.6	Conclusion	79
4	Stochastic modeling of bedload transport and bar development	83
4.1	Introduction	84
4.2	Physical problem	86
4.2.1	Saint-Venant–Exner equations	86
4.2.2	Friction model	87
4.2.3	Stochastic bedload transport model	87
4.3	Linear stability analysis	90
4.3.1	Dimensional groups	90
4.3.2	Dispersion relation	92
4.3.3	Neutral curves	93
4.4	Numerical scheme	99
4.4.1	Architecture of the numerical model	99
4.4.2	Finite volume method	100
4.4.3	Numerical implementation	102
4.5	Experimental dataset	103
4.6	Model prediction	104
4.6.1	Bedload transport time series	104
4.6.2	Alternate bar characteristics	106
4.7	Concluding remarks	110

5 Conclusions and outlook	111
5.1 Summary of the thesis	111
5.2 Outcomes	112
5.3 Future perspectives	114
5.3.1 Open challenges	115
A Machine learning model architecture	117
B Sensitivity analysis	119
C Extended Roe solver in one-dimension	123
D Friction source term discretization	129
E Derivation of τ_{bx1} and τ_{by1}	131
F Extended Roe solver in two-dimension	133
Bibliography	156
Curriculum Vitae	157

List of Figures

1.1	(a) Bondo village after the landslide in August 2017, marking Switzerland’s most significant landslide over 130 years, resulting from three million cubic metres of debris from the Piz Cengalo mountain. ©Gian Ehrenzeller. (b) Landslide of 10000 cubic meters fell on the village of Gondo, Valais ©Union of cantonal fire insurances, commission for natural hazard damage prevention. (c) Persistent heavy rains submerged large areas of Switzerland’s northwest and center. The flood impact on the River Aare is shown here, notably affecting parts of Olten, Switzerland. ©Swissinfo.ch. (d) The record-breaking flood of August 2005, primarily impacting the cantons of Luzern, Obwalden, Bern and Uri in Switzerland. A picture from the submerged Ennetburgen, Switzerland. ©Swiss Air Force.	2
1.2	Various bedload deterministic equations are shown in solid lines. Meyer-Peter and Müller, 1948: $\Phi = 8(\tau^* - 0.047)^{1.5}$; Einstein, 1942: $\Phi = 2.1 \exp(-0.391/\tau^*)$; Wong and Parker, 2006a: $\Phi = 4.93(\tau^* - 0.047)^{1.6}$; Ashida and Michiue, 1972: $\Phi = 17(\tau^* - 0.05)(\sqrt{\tau^*} - \sqrt{0.05})$; Parker, 1979: $\Phi = 11.2(\tau^* - 0.03)^{4.5}/\tau^{*3}$; Cheng, 2002: $\Phi = 13\tau^{*1.5} \exp(-0.05/\tau^{*1.5})$. Data points are from Aziz and Scott, 1989; Bogardi and Yen, 1938; H. H. Cao, 1985; Capart and Fraccarollo, 2011; Casey, 1935; P. Gao, 2008; Gilbert and Murphy, 1914; W. H. Graf, 1987; Ho, 1939; Mavis et al., 1935; Meyer-Peter and Müller, 1948; Paintal, 1971a; Recking et al., 2008a; Rickenmann, 1990; Smart, 1984.	6
1.3	Bedload transport rate time series at the gravel-bed flume’s outlet. The top plot corresponds to an experiment conducted under steady-state flow conditions with a flow rate of $Q_l = 15$ L/s, a sediment feed rate of $Q_s = 5$ g/s, and a slope of $S = 1.6\%$, conducted by Dhont, 2017. The bottom plot conducted with an unsteady flow condition involving cyclic hydrographs with a period of 8 hours, minimum and maximum flow discharges of $Q_{l,m} = 10$ L/s and $Q_{l,M} = 20$ L/s, respectively, with sediment feed rate of $Q_s = 2.5$ g/s and a slope of $S = 1.6\%$, carried out by the thesis’s author using the same flume.	9
1.4	Illustration of the processes involved in mass exchanges: λ' , μ , and σ are particle entriantment, collective entrainment, and deposition coefficient, respectively.	13
1.5	Control volume with unit width, length of Δx , and bed height of y_b	15

List of Figures

2.1	A diagram showing the neural network architecture. Convolutional layers are shown in blue, and skip connections are shown in orange. The number in the format of $a \times b \times c$ close to each box indicate the number of channels and image size in the x and z directions, respectively.	23
2.2	Gravel-bed flume illustration, in which all the dataset is gathered based on the experiments performed on this channel. It has 17 m length but the useful length (removing 1.5 m from each side) is 14 m.	24
2.3	An example of experimental topography using the gravel-bed flume. The bed and flow heights are measured from the bottom of the flume. The initial height of the bed is at 31.5 cm.	26
2.4	Velocity plot based on (a) Shannon-entropy and (b) Tsallis-entropy for a cross section in the middle of the channel based on Exp. 3 at $t = 200$ minutes. The border between the white and blue regions indicates the bed topography for one cross section.	30
2.5	(a) Effect of different constant learning rates in terms of validation loss (b) testing models based on validation loss with and without learning rate decay versus training dataset size.	32
2.6	(a) Test error as a function of the dropout rate for a model with 142,689 training parameters, (b) illustrates the influence of the weight decay factor on the training and validation performance.	34
2.7	(a) Validation loss, and (b) relative error for various model complexity and training dataset size.	35
2.8	(a) Training and validation losses for learning rate 0.01, (b) histogram plot of the $L1$ norms of prediction errors (applied to 460 test samples).	37
2.9	Qualitative result of the U-net: the first row is the normalized bed topography fields from the test dataset (ground truth). The second row are the images that are predicted by the U-net. The third row are the error images (ground truth - prediction).	38
2.10	Each column belongs to one experiment. The first row is the profile of the bed topography along the channel length at $z = 5$ cm from the down wall, the second row is the profile at $z = 30$ cm, and the last row is the bed topography at $z = 55$ cm. Ground truth is shown by red and prediction by black color.	39
2.11	Up: Bed topography based on simulation using Iber, down: bathymetry comparison of the Iber and neural network model. The red line is the Iber topography for a cross section at $x = 1.0$ m (down-left), and $x = 5.5$ m (down-right) from flume inlet and the black line represent the neural network model's prediction.	41

2.12 (left) Google Maps (2023). Modified map of the confluence of the Kaskaskia River with the Copper Slough, East-Central Illinois, USA. Retrieved from <https://maps.google.com/>. The arrows show flow direction. The red lines represent the cross-sections where these measurements have been conducted. (right) comparison of the neural network prediction vs the field data measurements. The red and black lines represent the field measurements and neural network model prediction, respectively. 42

2.13 The red dashed line represents the log-law velocity profile in the inner region ($y/h < 0.2$) where \bar{u} is the point velocity averaged for different experiments, u_* is the shear velocity, y is distance from the top of the sediments, $y_0 = 0.2k_s$ is viscous sublayer, k_s is roughness height which is equal to d_{50} , and $Br=8.44$ is integration constant. The blue dot-dashed line is the velocity profile in the outer region ($y/h > 0.2$) where κ is Von Karman's constant, $\Pi = 0.108$ is the wake strength parameter, and δ is the distance between the bed and the point where maximum velocity occurs, here it is equal to h 44

3.1 Illustration of the processes involve in sediment exchanges: λ' , μ and σ are particle entriainment, collective entrainment and deposition exchange rates, respectively. 52

3.2 Partial experimental data available from Ancy et al., 2008 to relate the collective entrainment to deposition rate with $\mu = 0.85\sigma$ 57

3.3 Equation 3.31 fit on experimental dataset from Aziz and Scott, 1989; Bogardi and Yen, 1938; H. H. Cao, 1985; Capart and Fraccarollo, 2011; Casey, 1935; P. Gao, 2008; Gilbert and Murphy, 1914; W. H. Graf, 1987; Ho, 1939; Mavis et al., 1935; Meyer-Peter and Müller, 1948; Paintal, 1971a; Recking et al., 2008a; Rickenmann, 1990; Smart, 1984. 59

3.4 Relationship between characteristic velocities and Froude number, with $\beta = 0.5$. 64

3.5 Numerical bedload time series by applying the stochastic solver to (a) R1, and (b) R7. 68

3.6 Probability density function for number of moving particles based on simulation outputs applied to (a) R1 and (b) R7. 70

3.7 Illustration of antidune migration: numerical bed and flow elevations at $t = 9$ minutes (dashed line) and $t = 10$ minutes (solid line) for R1. The red symbols indicate the locations where local minima have been detected to calculate the mean wavelength. 70

3.8 (a) Temporal evolution of simulation-based bedform amplitude for R1 (blue circle) and R7 (red square) (b) relation between antidune amplitude and wavelength. 71

3.9 Contour plots of the bed elevation perturbation in the $\{x, t\}$ -plane during 2 minutes of simulation time. (a) to (d) correspond to P1 to P4, respectively. . . . 73

3.10 (a) Left: bed elevation using numerical simulation applied to R1 in the $\{x, t\}$ -plane, right: bed elevation at the flume exit. Bedload transport time series using the ensemble-averaged framework correspond to (b) R1 and (c) R7. 75

List of Figures

3.11	Probability density functions of antidunes wavelength over five time periods $[2(\mathcal{T} - 1), 2\mathcal{T}]$ minutes being $\mathcal{T} = 1, \dots, 5$ calculated using simulation run R1.	78
3.12	Illustration of bed (in black) and flow (in blue) elevation at $t = 10$ minutes with four replications with exact same run configuration (R1). The initial bed slope has been removed for a better comparison.	79
3.13	Bedload time series from (a) to (d) with noise seed 300, 444, 500, and 600. The averaged bedload transport rate are: $\bar{q}_s = 8.7, 8.7, 8.7, 8.6$ grain/s with a variance of $\sigma^2 = 10.2, 10.1, 10.5, 10.4$ (grain/s) ² , respectively.	80
4.1	Neutral curve of free alternate bars in (a) $\{k_x, Fr\}$ -plane, (b) $\{k_x, \beta\}$ -plane, (c) $\{k_x, k_y\}$ -plane, (d) $\{k_x, \delta^2\}$ -plane as a function of bed initial slope. The experimental data-points are categorized based on the initial bed slope.	97
4.2	(a) Neutral curve of free alternate bars in the $\{k_x, Fr\}$ -plane as a function of δ_0^2 , and diffusion, (b) neutral curve of free alternate bars in the $\{k_x, \beta\}$ -plane as a function of β_x and β_y . The experimental data-points are shown with black circles.	98
4.3	Relationship between characteristic velocities and Froude number. For a better illustration, $\beta = 0.8$ has been used in this plot.	102
4.4	Bedload transport time series by applying the numerical solver to laboratory experiments (E.1 to E.3, respectively). The averaged bedload transport and its variance respectively are: $\bar{q}_s = 2.5$ g/s, $\sigma^2 = 0.75$ (g/s) ² ; and $\bar{q}_s = 4.9$ g/s, $\sigma^2 = 1.5$ (g/s) ² ; and $\bar{q}_s = 7.4$ g/s and $\sigma^2 = 2.0$ (g/s) ²	105
4.5	(left) Time-averaged bedload transport rate: $\bar{Q}_s(\mathcal{T}) = \int_0^{\mathcal{T}} Q_s(t) dt / \mathcal{T}$, converges to its mean value over the entire simulation time. The dashed lines represent $\bar{Q}_s \pm 5\% \bar{Q}_s$, (right) The probability density function of bedload transport corresponds to three simulation runs.	105
4.6	Illustration of the appearance of alternate bars based on (left) simulation and (right) experiment at $t = 17$ hours.	106
4.7	Top plots of bed topography based on (top) simulation and (bottom) experiment at $t = 17$ hours.	106
4.8	Amplitude of the alternate bars along the longitudinal profiles at $t = 17$ h. Smoothed plots are depicted by the black lines.	107
4.9	Deposition rate contour plot of (top) simulation and (bottom) experiment, calculated over 17 hours for run 1, shows that alternate bars experience intensive aggradation, alternately, on either side of the channel.	108
4.10	Erosion rate contour plot of (top) simulation and (bottom) experiment, calculated over 17 hours for run 1. Pools experience intensive degradation, alternately, on either side of the channel.	109
4.11	Temporal variation of the bed elevation using both simulation and experimental outputs.	109

B.1 (left) Simulation of the continuous model, (right) simulation of the discrete model. Both models are solved numerically using identical parameters: $\lambda' = 10 \text{ s}^{-1}$, $\mu = 4 \text{ s}^{-1}$, $\sigma = 5 \text{ s}^{-1}$, and $\bar{u}_s = 2 \text{ m/s}$. The cell size is $\Delta x = 1 \text{ m}$ with $\tilde{\lambda} = \lambda' / \Delta x$. The approximations $D_u = \nu \Delta x^2 / 2$ and $\nu = \bar{u}_s / \Delta x$ are applied. 120

B.2 A sensitivity analysis was conducted on the mesh size using the continuous bed-load model. Eq. 3.13 was numerically solved for a duration of 500 seconds using $\lambda' = 10 \text{ s}^{-1}$, $\mu = 4 \text{ s}^{-1}$, $\sigma = 5 \text{ s}^{-1}$, $\bar{u}_s = 2 \text{ m/s}$, and $\tilde{\lambda} = \lambda' / \Delta x$. The approximations $D_u = \nu \Delta x^2 / 2$ and $\nu = \bar{u}_s / \Delta x$ are applied. 121

List of Tables

2.1	Input parameters of the experiments.	25
3.1	Experimental conditions in the experiments conducted by Recking et al., 2009 and Pascal et al., 2021. W flume width, d median particle diameter, $i = \tan \theta$ flume slope, Q inflow rate, $\bar{u} = Q/(Wh)$ mean velocity, h flow depth averaged over the flume length, R_h hydraulic radius, $u^* = \sqrt{gh_i}$ the friction velocity, τ^* the Shields stress, $\tau_c^* = 0.15 \tan^{0.275} \theta$ the critical Shields number estimated using the empirical equation proposed by Recking et al., 2008b, $\Phi = q_s / \sqrt{sgd^3}$, L antidune wavelength, A amplitude.	67
3.2	Experimental and simulation outputs regarding bedload transport rate. The laboratory-based and simulation-based averaged bedload transport rates are denoted by \bar{q}_s and \bar{q}'_s , respectively. Furthermore, σ^2 represents the variance of the numerical bedload time series and RE_s denotes its relative errors.	69
3.3	Experimental and numerical results for bedform characteristics. $L_m = 2\pi hFr^2$ is the minimum antidunes wavelength proposed by Kennedy, 1963. The simulated values of wavelength and amplitude are denoted as L' and A' , respectively, and the corresponding relative errors are RE_L and RE_A	72
3.4	Experimental and numerical results concerning antiduens migration celerity. .	74
3.5	Numerical bedload transport characteristics using the ensemble-averaged framework. The experimental and simulation bedload transport are denoted by \bar{q}_s and \bar{q}'_s , respectively. σ^2 represents the variance of the numerical bedload time series, and RE_s denotes its relative error. The bedload prediction using MP-M bedload formula is denoted by $\bar{q}_{s,M}$ and $RE_{s,M}$ is its relative error.	76
4.1	Maximum and minimum of experimental characteristics, namely, width, slope of the channel, water depth and discharges observed in the dataset are mentioned.	95
4.2	Maximum and minimum of the bar wavelength, half-width-to-water-depth ratio β , and wavenumber in the longitudinal k_x and transversal k_y directions, respectively, are presented.	96
4.3	Experiment's input parameters and alternate bar characteristics.	103
4.4	The wavelength and height of alternate bars based on numerical simulation. .	107
A.1	Deep learning model summary.	118

1 Introduction

1.1 Motivation

The study of particle movement within fluids has attracted scientists' attention for a long time. Historically, one of the pioneering observations in this domain was documented by Robert Brown (1773–1858), who studied the kinetic behavior of pollen grains suspended in an aqueous medium (Brown, 1828). The movement of granular materials requires an agent (Costa, 2016). Gravitational forces can initiate movements leading to phenomena such as landslides and debris flows (Takahashi, 1981). In addition, liquid currents can instigate sediment movement, a phenomenon evident in river systems (Abbaspour et al., 2007). Moreover, atmospheric currents, i.e., wind, can cause particle movement, which is commonly observed in desert environments and known as aeolian transport (Kok et al., 2012; Wang et al., 2014).

The study of sediment transport is important in elucidating the mechanisms underlying the morphological evolution of the earth's surface, including domains such as sedimentary geology and geomorphology (Hauer, Leitner, et al., 2018; Tao et al., 2019). Furthermore, this area of study provides insights into the possible effects of infrastructural construction on the riverine environment, a concern central to environmental engineering (W. Graf et al., 2016; Kondolf, 1997). Sediment dynamics also play a crucial role in marine ecosystems and in the design, construction, and protection of critical and fundamental infrastructure in a country (roads, dams, and bridges) by decreasing the risk of river bank erosion, as addressed in hydraulic engineering (Hauer, Wagner, et al., 2018; Rinaldi & Casagli, 1999). Such studies help reduce the risk to human life and crucial infrastructure by facilitating accurate predictions about the size, duration, and location of erosional and depositional events.

Different climate change scenarios are depicted for Switzerland 2050, showing a rise in average precipitation, frequency, and intensity, with precipitation occurring more frequently as rain rather than snow (OcCC, 2007), which may cause torrential floods. Torrential floods are common hazards that affect human life in various regions worldwide, leading to substantial economic implications due to intense erosional and depositional events. For instance, a 2017 landslide in Bondo, Bregaglia, Switzerland, released three million cubic metres of debris, as

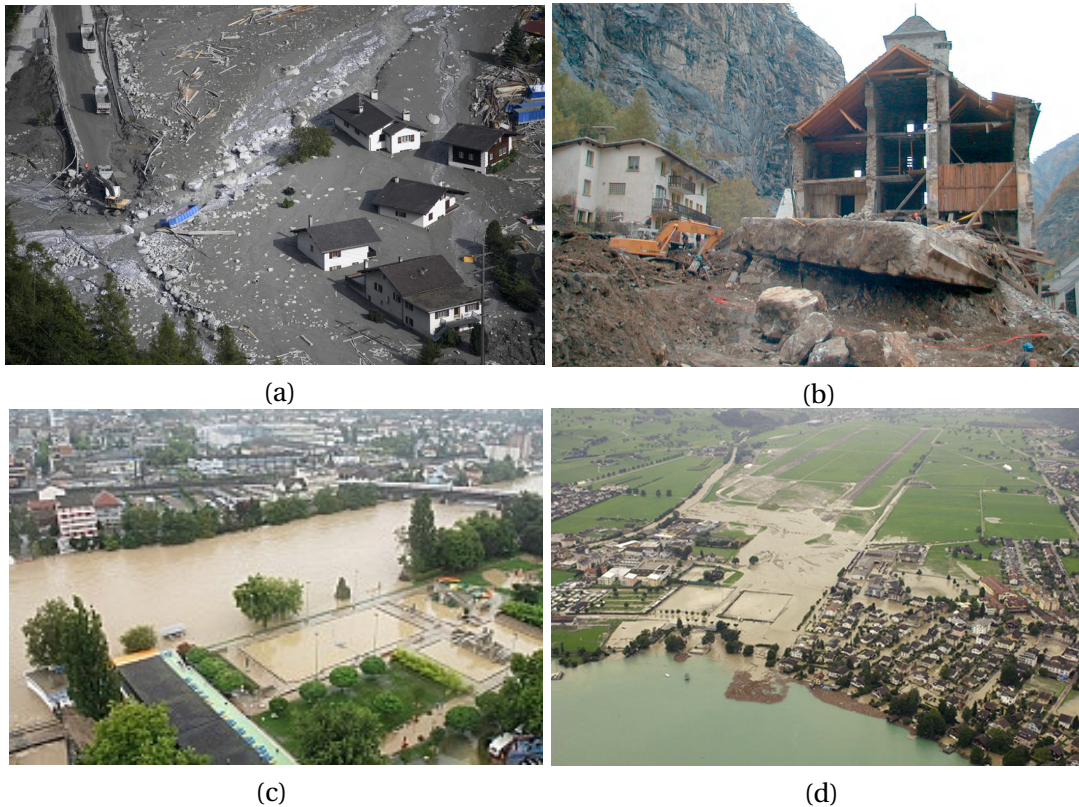


Figure 1.1: (a) Bondo village after the landslide in August 2017, marking Switzerland's most significant landslide over 130 years, resulting from three million cubic metres of debris from the Piz Cengalo mountain. ©Gian Ehrenzeller. (b) Landslide of 10000 cubic meters fell on the village of Gondo, Valais ©Union of cantonal fire insurances, commission for natural hazard damage prevention. (c) Persistent heavy rains submerged large areas of Switzerland's northwest and center. The flood impact on the River Aare is shown here, notably affecting parts of Olten, Switzerland. ©Swissinfo.ch. (d) The record-breaking flood of August 2005, primarily impacting the cantons of Luzern, Obwalden, Bern and Uri in Switzerland. A picture from the submerged Ennetburgen, Switzerland. ©Swiss Air Force.

shown in Fig. 1.1(a). This incident resulted in economic losses of about 41 million CHF. In the fall 2000, another notable mudslide occurred in Gondo, Valais, Switzerland as depicted in Fig. 1.1(b). It destroyed the protective wall constructed to shield the village from such disasters, causing 13 deaths and much damage to the village.

In 2007, northwestern Switzerland experienced extensive flooding after two days of heavy rainfall, leading to damages exceeding 400 million CHF. The aftermath of this deluge on the River Aare is shown in Fig. 1.1(c). Notably, the most expensive flood ever documented, often referred to as 'costliest flood', happened in central Switzerland in August 2005 (Badoux et al., 2014). This event, shown in Fig. 1.1(d), caused widespread destruction to public infrastructure, residential, commercial, as well as agricultural areas, resulting in losses estimated at approximately 3,000 million CHF (Hilker et al., 2009). Overall, from 1972 to 2011, erosional

and depositional events due to torrential floods, has resulted in total financial losses ranging between 4.3–5.1 billion CHF (Badoux et al., 2014).

If we cannot prevent torrential floods, we must learn to adapt to and live with them. Consequently, thorough research into torrential floods becomes imperative. The alterations in riverbed morphology and the dynamics of sediment transport are primary factors that influence flood risk (Nones & Guo, 2023). One of the pioneers in sediment transport research was Paul François du Boys, who undertook significant studies on the Rhone River (du Boys, 1879). He was among the first to introduce a systematic methodology for sediment transport prediction in gravel-bed rivers, suggesting that a requisite shear stress is essential to initiating particle movement (Hager, 2005).

Sediment transport can occur in three modes: bedload, suspended load, and wash load (Komar, 1980). The mode of sediment transport can be determined based on the Rouse number, a non-dimensional number that indicates how sediment will be transported in a current. It is calculated as the ratio of the sediment's settling velocity, denoted by w_s , to the shear velocity, denoted by u_* —the rate of fall compared to the turbulence strength imposing on the particles (Rouse, 1937). The Rouse number is given by $w_s/(\kappa u_*)$, where κ is the von Kármán constant. If it is more than the limit, $w_s/(\kappa u_*) > 2.5$ meaning that the mode of sediment transport is bedload (Rouse, 1938). According to Rouse, 1938, the type of sediment transport is suspension when $0.8 < w_s/(\kappa u_*) < 2.5$ and $w_s/(\kappa u_*) < 0.8$ indicate wash load.

In gravel-bed rivers, the predominant mode of sediment transport is bedload transport (Van Rijn, 1984a). The bedload transport is defined as those of particles that spend the majority of the time at the bottom of the stream, in the bed layer, in contact with the bed (Julien, 2010). These particles experience such things as being entrained into the flow, carried a short distance, and deposited. Their motions can be categorized into three types: rolling, sliding, and saltation (jumping) (W. H. Graf & Altinakar, 2000), all occurring within a thin layer of fluid (Drake et al., 1988). The specific movement of a particle depends on its intrinsic properties, its interaction with other particles, and flow characteristics. As particles in bedload transport consistently interact with the riverbed, the bed topography can significantly influence the bedload transport rate (Church, 2006).

1.2 Bed topography

An accurate assessment of a river's sediment transport rate requires a thorough understanding of its bed topography (Church, 2006). While direct bathymetric measurements, e.g., wading or multi-beam imaging sonar systems, provide this information (Marcus, 2002), they might incur significant costs and be time-consuming. As a result, bathymetry is often deduced via indirect methodologies, e.g., remote sensing techniques (Garambois & Monnier, 2015). These techniques leverage data that is either readily accessible or effortlessly collected and possesses a strong correlation with bed topography.

Chapter 1. Introduction

As per Smith and McLean, 1984, there exists a strong relationship between bed topography and surface flow data, such as the velocity field, especially under one-dimensional flow conditions. Accessing the velocity field data is generally more straightforward compared to bed topography. Various methodologies, including the drifter global positioning system (GPS) (Landon et al., 2014), particle image velocimetry (Lewis & Rhoads, 2015), and synthetic aperture radar (Biondi et al., 2020), can facilitate the velocity field measurements.

Recently, machine learning techniques have been used in geophysics and hydraulics (Yu & Ma, 2021; Zounemat-Kermani et al., 2021) especially for inferring bathymetry from velocity fields (Almeida et al., 2018; Forghani et al., 2021; X. Liu et al., 2022). The interest of these models in water resources modeling is growing due to their ability to estimate complex relationships (Bermúdez et al., 2018; Bhattacharya et al., 2007; X. Liu et al., 2022; Yaseen et al., 2015). Many studies have shown the successful application of data-driven machine learning models across a wide spectrum of hydrological processes, including topics like bathymetry inference (Ghorbanidehno et al., 2021; X. Liu et al., 2022), sediment transport predictions (Afan et al., 2015; Lafdani et al., 2013; Wieprecht et al., 2013), groundwater modeling (Barzegar et al., 2017), rainfall analysis (Jeong & Kim, 2005), water elevation forecasting (Atashi et al., 2022), as well as anticipatory models for floods and droughts (Z. Liu & Merwade, 2018).

For example, regarding sediment transport prediction, artificial neural networks have been used to estimate the daily sediment load in the Johor River in Malaysia by Afan et al., 2015. Moreover, Altunkaynak, 2009 used the genetic algorithm for prediction of the sediment load from discharge measurements and applied it to the Mississippi River in Missouri, St. Louis, USA. In the context of bathymetry inference, Ghorbanidehno et al., 2021 used a fully connected deep neural network to infer bed topography for flow depths in the range of 3–10 m using the depth-averaged flow velocity field. For deep waters, Al Najjar et al., 2021 proposed two novel deep learning techniques and showed that their techniques are able to capture the ocean depth with sufficient accuracy.

The aforementioned examples demonstrate the capability of data-driven models for bed topography prediction. In this technique, the need to solve time-consuming governing equations will be bypassed, and instead, the interested output will be inferred from input data, e.g., flow surface data, quickly and accurately.

1.3 Sediment transport

Following the measurement of bed topography—by either direct or indirect measurements—and knowing the channel geometry, the subsequent step is to estimate the bedload transport rate. Numerous attempts have been made to formulate the bedload transport rate, mostly treating the bedload transport problem as a deterministic one. There are two approaches to predicting bedload transport, namely, equilibrium and non-equilibrium theories (Bohorquez & Ancy, 2016).

The first approach, equilibrium theory, in modeling bedload transport hinges on a critical condition that must be met for bedload movement. This approach introduces a critical tractive force exerted on the boundary, such as the critical Shields number (du Boys, 1879) or critical water discharge (Gilbert & Murphy, 1914) and is independent of flow conditions (steady or unsteady non-uniform flow). It ends up in a deterministic scaled formulation of bedload transport through the fitting of empirical data (Ancey & Recking, 2023). For instance, a particular water discharge is correlated with a specific capacity to transport solid weight, resulting in a one-to-one function of water discharge (Gilbert & Murphy, 1914).

A key implication of this assumption is that sediment transport is viewed as a deterministic process that instantaneously adjusts to changes in flow conditions. For instance, Meyer-Peter and Müller, 1948 and Ashida and Michiue, 1973 proposed two different types of formulae for bedload transport, respectively, as

$$\begin{aligned}\Phi &= 8(\tau^* - \tau_c^*)^{3/2}, & \tau_c^* &= 0.047 \\ \Phi &= 17(\tau^* - \tau_c^*)(\sqrt{\tau^*} - \sqrt{\tau_c^*}), & \tau_c^* &= 0.05\end{aligned}\tag{1.1}$$

where τ^* is the dimensionless shear stress (Shields number), τ_c^* is its threshold value, and Φ is the dimensionless sediment transport rate, defined as

$$\Phi = \frac{\bar{q}_s}{\sqrt{(\rho_s/\rho - 1)gd^3}}\tag{1.2}$$

where \bar{q}_s is the unit bedload transport rate, and ρ_s and ρ represent the sediment and fluid density, respectively. The term g denotes the acceleration due to gravity, while d signifies the mean particle diameter for a uniform grain size. For non-uniform grain size distribution, d_{50} is typically considered, where the index indicates that 50% of the particles have a diameter smaller than d_{50} . The Shields number is defined as

$$\tau^* = \frac{\tau}{(\rho_s - \rho)gd} = \frac{\rho ghS_{red}}{(\rho_s - \rho)gd} = \frac{hS_{red}}{(s - 1)d}\tag{1.3}$$

The variable h represents the flow depth, S_{red} stands for the reduced energy slope, and s is ratio of solid to water density. Regarding deterministic bedload models, it is noteworthy to mention that:

- These models assume the particles are neither eroded nor deposited over time, neglecting the duration spent by the particles in rest and motion, or, in other words, particle jumps assumed to be instantaneous,

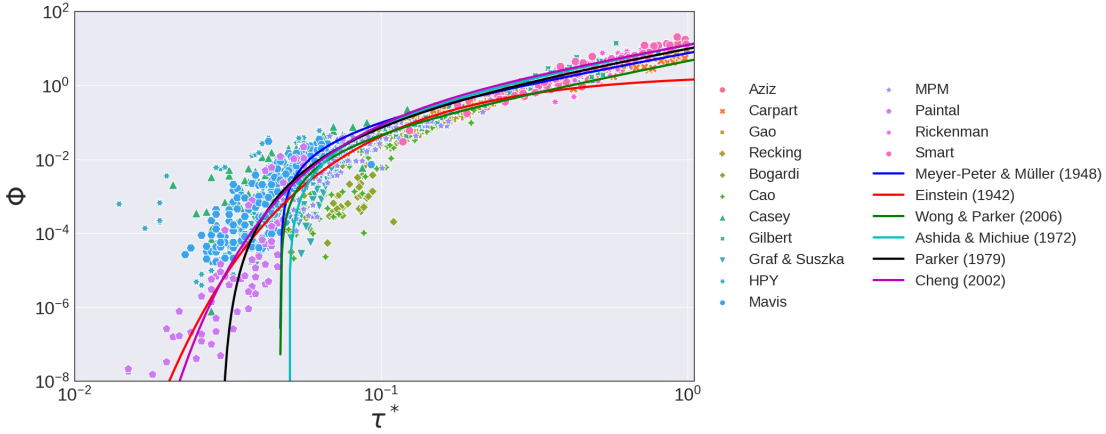


Figure 1.2: Various bedload deterministic equations are shown in solid lines. Meyer-Peter and Müller, 1948: $\Phi = 8(\tau^* - 0.047)^{1.5}$; Einstein, 1942: $\Phi = 2.1 \exp(-0.391/\tau^*)$; Wong and Parker, 2006a: $\Phi = 4.93(\tau^* - 0.047)^{1.6}$; Ashida and Michiue, 1972: $\Phi = 17(\tau^* - 0.05)(\sqrt{\tau^*} - \sqrt{0.05})$; Parker, 1979: $\Phi = 11.2(\tau^* - 0.03)^{4.5}/\tau^{*3}$; Cheng, 2002: $\Phi = 13\tau^{*1.5} \exp(-0.05/\tau^{*1.5})$. Data points are from Aziz and Scott, 1989; Bogardi and Yen, 1938; H. H. Cao, 1985; Capart and Fraccarollo, 2011; Casey, 1935; P. Gao, 2008; Gilbert and Murphy, 1914; W. H. Graf, 1987; Ho, 1939; Mavis et al., 1935; Meyer-Peter and Müller, 1948; Paintal, 1971a; Recking et al., 2008a; Rickenmann, 1990; Smart, 1984.

- It follows that the quantity of sediment introduced into the flume $\Phi_{s,i}$ must be equal to the quantity of sediment that exits the channel $\Phi_{s,o}$ i.e., $\Phi_{s,i} = \Phi_{s,o}$,
- The validity of the deterministic bedload models are vague with the enormous fluctuations in mean bedload transport rate for $\tau^* < 0.1$ as can be seen in Fig. 1.2,
- The models for sediment transport rate Φ usually are a function of Shields number and involve a threshold value, meaning that $\Phi = f(\tau^*)$ for $\tau^* > \tau_c^*$, and $\Phi = 0$ for $\tau^* \leq \tau_c^*$ causing the stubborn paradox (Ancey & Recking, 2023; Bohorquez & Ancey, 2016),
- The relative error in bedload transport predicted, for example by Meyer-Peter and Müller, 1948 formula, by imposing a small error ϵ in τ^* , approximately would be

$$\frac{\Delta\Phi}{\Phi} \approx \frac{d\Phi}{d\tau^*} \frac{\epsilon}{\Phi} \rightarrow \frac{\Delta\Phi}{\Phi} \approx 1.5\epsilon(\tau^* - \tau_c^*)^{-1}$$

meaning that a small error ϵ in τ^* cause the relative error approaches infinity in the threshold of motion,

- The function $\Phi = f(\tau^*)$ implies that for a given Shields number, we can have one specific amount of sediment transport, as it is a one-to-one function of the Shields number (Bohorquez & Ancey, 2016),
- They mostly can be categorized into three groups i. those with a function in the form of $\Phi \propto (\tau^* - \tau_c^*)^\alpha$ being $1 \leq \alpha \leq 16$ (Cohen et al., 2010; Paintal, 1971a) with an accepted value of $\alpha = 3/2$; ii. ones with a function in the form of $\Phi \propto (\tau^* - \tau_c^*)(\sqrt{\tau^*} - \sqrt{\tau_c^*})$; and

- iii. those with exponential function $\Phi \propto \tau^{*\beta} \exp(-cte/\tau^{*\gamma})$ meaning that all formulae have same behavior if τ^* is far from the threshold value τ_c^* : If $\tau^* \rightarrow \infty$ then we can write
 - i. $\Phi \propto (\tau^* - \tau_c^*)^\alpha \approx \tau^{*\alpha}$ being $\alpha = 3/2$ as a common agreement,
 - ii. $\Phi \propto (\tau^* - \tau_c^*)(\sqrt{\tau^*} - \sqrt{\tau_c^*}) \approx \tau^* \sqrt{\tau^*} = \tau^{*3/2}$,
 - iii. $\Phi \propto \tau^{*\beta} \exp(-cte/\tau^{*\gamma}) \approx \tau^{*\beta}$ being $\beta = 3/2$ for example in Cheng, 2002.

And have significant difference if τ^* approaches the threshold as one can see in Fig. 1.2.

It has long been recognized that sediment rates measured from field data differ from deterministic bedload transport relations by one to three orders of magnitude (J. Garcia et al., 2007; Gomez, 1991; Recking, 2010; Rickenmann, 2001, 2018), as illustrated in Fig. 1.2. This magnitude of error is the reason that this seemingly simple question remains unanswered: Given the controlling parameters of a fluvial system, how long does it take to collect a specific amount of sediment at the end of a flume? Applying deterministic bedload transport equations to experimental data that exhibits stochastic tendencies is inappropriate, especially when $\tau^* < 0.1$, as they can at best represent the trend of the experimental data. Referring to Fig. 1.2, it is evident that as the Shields numbers diminish, the variability in sediment transport increases, leading to a greater relative error when using deterministic equations.

The second approach in bedload modeling is Einstein, 1950's in which sediment transport is the result of the unbalancing of entrainment and deposition rates. In this approach, the sediment transport rate is not just a function of Shields number; it is adjusted to the flow conditions (Bohorquez & Ancy, 2016). Although Einstein, 1937 pioneered the probabilistic point of view in his PhD dissertation, his approach ultimately resulted in a deterministic bedload model (Ancy, 2020).

In recent years, several attempts have been made to describe the mechanics of flow over a movable bed from a probabilistic and stochastic point of view. Among them:

- In the work of Parker et al., 2000, they have proposed a probabilistic formulation of the Exner equation. Their derivation has two key assumptions: i. There was no active layer for the sediment bed, meaning that the entire sediment bed was in motion. ii. There were no significant changes in the mean bed level over time, suggesting that these variations had no significant impact on the probability density function (PDF) of bed elevation. Using the aforementioned assumptions, Parker et al., 2000 calculated the PDF of the bed elevation and ended up with the Exner equation in probabilistic form.
- Ancy et al., 2006 made another significant contribution by extending Einstein's framework to account for non-Gaussian fluctuations. This was achieved by incorporating a collective entrainment rate. This sediment transport model is developed using the principles of Markov chain analysis. The model assumed that the probability of observing the particles at each time step was dependent only on the previous time step and that only one event could occur at each time step. This led to a stochastic formulation of bedload transport, which calculated the variation in the number of active particles

within a control volume at each time step. The resulting bedload formulation was of a stochastic advection-diffusion type for Poisson density rate, and a deterministic version for the mean active particle was obtained by taking the ensemble average of the stochastic version.

It is important to highlight three key points here:

- There is a general agreement that bedload transport is a noise-driven process, particularly in cases of low sediment transport,
- The fluctuations in bedload transport have a significant impact on bulk dynamics,
- Current deterministic bedload transport formulas do not account for the fluctuations in particle movement.

Therefore, to enhance the accuracy of bedload transport predictions, we came to the conclusion that incorporating these fluctuations is crucial.

1.4 Sediment transport rate fluctuations

It is difficult to predict bedload transport due to many aspects. These include a limited understanding of the extent to which a riverbed becomes armored, the existence of particle clusters with diverse size distributions, the nature of the processes being noise-driven, the propagation of the noise into the system, a mixture of fast and slow processes, and the interaction of several non-equilibrium or semi-equilibrium processes (Ancy, 2020; Sun et al., 2015). A primary source of prediction inaccuracy stems from the stochastic nature and inherent fluctuations of this phenomenon, which complicate the prediction of bedload transport rate.

Although bedload transport rate fluctuations are observable over a wide range of spatial and temporal scales (Paintal, 1971b), most researchers have focused on their mean value and ignored their fluctuations. For a long time, bedload fluctuations have been ignored in hydraulic studies like in turbulence, as if average quantities were sufficient to describe the flow dynamics, but there is growing evidence that they play a key role (D. Liu et al., 2016; Shih et al., 2017; A. Singh et al., 2010).

These fluctuations cause the mechanics of flow over a movable bed to show stochastic behavior in many respects, meaning that it involves randomness and uncertainty at different levels such as bedload transport rate and bed morphology (Paintal, 1971a; Valyrakis et al., 2013). The particle motion is influenced by various factors such as turbulence, lift, drag, and collision with other particles, making it difficult to predict the exact trajectory of each particle (Cameron et al., 2019; Schmeckle et al., 2007). It results in stochasticity in the rate of bedload transport even in the steady-state flow regime (Benavides et al., 2022).

1.4 Sediment transport rate fluctuations

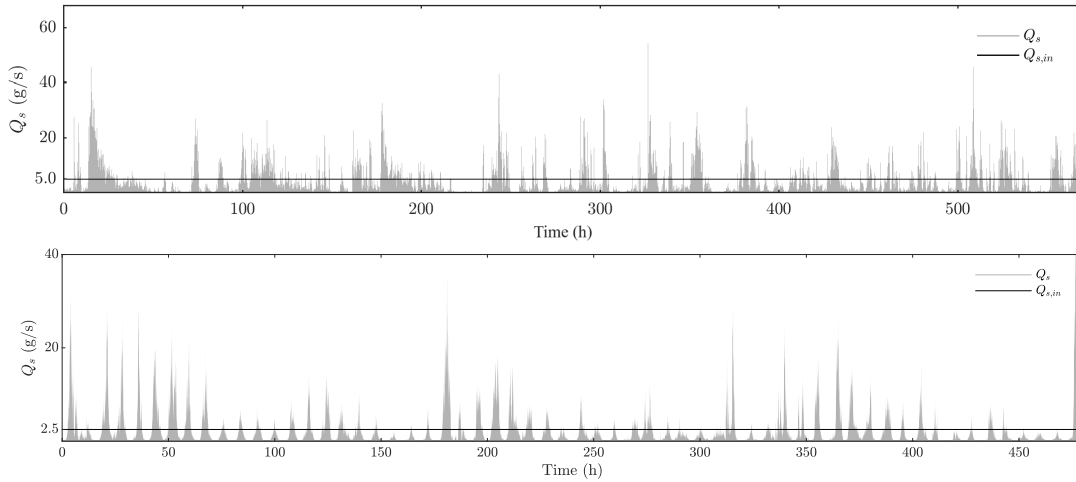


Figure 1.3: Bedload transport rate time series at the gravel-bed flume's outlet. The top plot corresponds to an experiment conducted under steady-state flow conditions with a flow rate of $Q_l = 15$ L/s, a sediment feed rate of $Q_s = 5$ g/s, and a slope of $S = 1.6\%$, conducted by Dhont, 2017. The bottom plot conducted with an unsteady flow condition involving cyclic hydrographs with a period of 8 hours, minimum and maximum flow discharges of $Q_{l,m} = 10$ L/s and $Q_{l,M} = 20$ L/s, respectively, with sediment feed rate of $Q_s = 2.5$ g/s and a slope of $S = 1.6\%$, carried out by the thesis's author using the same flume.

Encountering an inherently stochastic flow is often associated with enormous challenges and difficulties. For instance, the exact moments at which fluctuational lift and drag forces cause the particles to move are difficult to characterize (Cameron et al., 2019; Schmeeckle et al., 2001). It is worth mentioning that these fluctuations are caused by turbulent impulses that are caused by the sudden release of kinetic energy stored within the turbulent flow.

Turbulent impulses are known to play a critical role in both particle entrainment (Cameron et al., 2020; Valyrakis et al., 2010), and deposition (Shih et al., 2017) as they can cause sediment particles to be lifted from the bed and carried away by the flow (Cameron et al., 2019). Shih et al., 2017 uses a quadrant analysis of velocity and pressure sequences to investigate the correlation between turbulent flow structures and particle dislodgement events. The results of their study indicate that turbulent flow structures, particularly those associated with negative velocity and positive pressure fluctuations, play an important role in particle dislodgement.

In a feedback loop, the sediment movements change the turbulence structure (D. Liu et al., 2016; A. Singh et al., 2010). D. Liu et al., 2016 have used numerical simulations to quantify the effects of bedload on various flow parameters, including velocity, turbulence intensity, and Reynolds stress. The results revealed that the higher the bedload concentrations, the higher the turbulence and Reynolds stress.

The turbulent fluctuations and bed topography variations generate randomly varying bedload fluxes, having constant average characterizations of flow and sediment transport. That means

bedload transport modeling needs to be treated as a stochastic problem instead of using the traditional approach in which averaged values are used. Otherwise, the accuracy of the numerical results will be undermined. For example, Recking et al., 2012 applied sixteen most-used traditional bedload transport formulas to four datasets corresponding to different measurements and could estimate the sediment volume transport with more than 200% error, while non-capacity frameworks such as Markov processes in bedload modeling may improve the accuracy because of the local definition of the deposition and entrainment rates (Bohorquez & Ancey, 2015, 2016).

Figure 1.3 presents high-resolution bedload transport time series, illustrating the inherent bedload fluctuations across two long-term experiments: one under a steady-state condition and the other under an unsteady flow condition. Large fluctuations, around 10 times the average bedload transport rate in both experiments, are observable. Here, it is worth mentioning that the time-averaged transport rate for the steady-state experiment shown in Fig. 1.3, defined as $\bar{Q}_s(T) = T^{-1} \int_0^T Q_s(t) dt$ with the sampling time T , converges to the mean sediment transport value over the entire experimental run—which is equal to the input sediment feeding rate—approximately after 225 hours (Dhont & Ancey, 2018). Additionally, a significant finding is that, even under unsteady flow conditions shown in Fig. 1.3, bedload transport eventually converges to the sediment feeding rate, but this occurred after a longer period of time, approximately 265 hours.

These bedload transport fluctuations are random realizations of stochastic processes (Cudden & Hoey, 2003) and can be attributed to micro- and macro-scale factors, such as random particle movements and migration/failures in bed morphology. For example, Dhont, 2017 studied how bedload pulses can be attributed to bed morphology migration/failures that significantly contribute to the amount of bedload transport flushed out of the flume.

The bedload transport fluctuations that correspond to macro-scale factors are frequently reported as intermittent—long duration of minimal transport interrupted by sudden, significant occurrences of sediment transport rate (Benavides et al., 2022; Wang et al., 2014), and periodic—where the sediment transport rate oscillates in a regular manner over time (Ghilaridi et al., 2014; Gomez et al., 1989; Iseya & Ikeda, 1987). To effectively examine the characteristics of bedload transport fluctuations and their contributions, one must employ a stochastic methodology.

1.5 Realization of fluvial systems

The equilibrium theory proposes that a unique bedform characteristic will develop for a specific set of controlling variables. However, experiments show the bedload and morphology are rarely a single-valued response to a specific set of controlling parameters. In other words, repeating exact same experiment several times, even in a steady-state condition, will lead to different realizations (Ashmore, 1988; Warburton & Davies, 1994; Young, 1989), for example:

- Ashmore, 1988 conducted four experiments with different bed slopes and flow discharges using a wide braided flume and the same initial bed configuration, each replicated two times, and sampled the bedload at a rate of 1 sample per 15 minutes during the 60 hours experiment. The bedload transport rate time series have been fully different, with wide fluctuations even for two replications, although they had almost the same mean values. The fluctuations reported to be large, up to four times more than averaged values, even at constant discharges, with the coefficient of variation of the mean transport rate ranging from 27% to 83% with an average of 49% among all experiments.
- Young, 1989 replicated one of his experiments in a wide braided flume, operating at a flow discharge of 0.88 L/s and a slope of 0.74%. One replication lasted 16 hours, while another extended for 20 hours. He also observed different bedload transport time series, where fluctuations reached 4 and 6 times the mean bedload values of 3.13 g/s and 2.75 g/s, respectively. The coefficient of variation for these measurements was 69.7% and 73.3%.
- Warburton and Davies, 1994 conducted eleven replications of one experiment with the same initial condition to study the statistical significance of bedload transport time series and bed topographies. They observed that the bedload time series, sampled every 5 minutes, and channel morphology are different in all eleven replications during the 90 hours run. Although Warburton and Davies, 1994 captured different realizations for bed topography and bedload time series for each replication, they fluctuated around a mean value of 1.21 g/s and a coefficient of variation of 11%. They reported the fluctuations to be up to three to four times higher than the mean value when no external forces existed.

The experiments described above demonstrate that fluctuations in bedload transport are autogenic, show that key variables fluctuate gently around their mean values, and highlight the problem's stochastic nature. Hence, to account for these fluctuations and to be able to capture various realization of the system, our attention has been directed towards the stochastic bedload model suggested by Ancey et al., 2008.

1.6 Stochastic bedload transport model

Ancey et al., 2008 proposed a stochastic advection-diffusion type of equation for bedload transport. This model was developed by treating bedload transport as a probability problem, similar to Einstein's approach in 1937 (Einstein, 1937). Ancey et al., 2006 attempted to extend Einstein's work by generating wide and non-Gaussian fluctuations. As evidenced by the analysis of experimental data, the distribution of the bedload transport rate exhibits a heavy tail (Ancey et al., 2006; Campagnol et al., 2012; Turowski, 2010). They concluded that there was a missing element in the Einsteinian framework. Specifically, they found that bedload transport and particle activity did not exhibit significant fluctuations in the absence of positive feedback effect of mobile particles on the entrainment of additional particles that would amplify these fluctuations (Heyman, 2014).

Chapter 1. Introduction

In other words, the heavy tail of the PDF for bedload transport, indicating wide fluctuations, can be the hallmark of collective motions. This has been supported by laboratory observations (Dinehart, 1999; Drake et al., 1988), and the physical interpretation for the existence of such motion is discussed in Heyman, 2014. Due to the reasons mentioned above, Ancey et al., 2008 generates large and non-Gaussian fluctuations by introducing a collective entrainment mass exchange rate into the bedload formulation. Therefore, the derivation of the model begins by considering three mass exchange rates between the bed and the flow: individual entrainment, collective entrainment, and deposition rates (see Fig. 1.4).

A moving particle can be transformed into a bed particle (at rate σ_0). Alternatively, a bed particle can disturb a moving particle, causing the moving particle to become one of the bed particles (at rate σ_1). However, we can consider both processes as deposition with a rate of $\sigma = \sigma_0 + \sigma_1$. The entrainment process is divided into individual and collective rates. The fluid flow can entrain a bed particle and cause it to move (at rate λ') indicating the individual entrainment. Additionally, a moving particle can interfere with the bed particles and entrain the bed particles (at rate μ) indicating collective entrainment.

An Eulerian approach was taken: considering a control volume and counting the number of mobile particles, represented as \mathbf{n} . The number of mobile particles could be explained by four processes: entrainment, deposition, and particles either exiting or entering the control volume. To quantify the changes in the number of active particles within the control volume, they applied the birth-death—emigration-immigration Markov processes theory. This theory enables the calculation of the probability $P(\mathbf{n}, t)$, which is the likelihood of finding \mathbf{n} moving particles within the control volume at a specific time t (Ancey et al., 2008). These processes are classified as stochastic jump processes. They have made two assumptions:

- Firstly, $P(\mathbf{n}, t)$ is just dependent on the system state at $t - \delta t$ being δt the time step. It means that the waiting time for two particles to pass the control surface follows an exponential distribution (Ancey & Pascal, 2020).
- Secondly, the value of \mathbf{n} changes by 1, 0, or -1 in the time interval $[t, t + \delta t]$, meaning that only one event can happen during the time step δt that prevents coherent particle motion (Ancey, 2020). Therefore, the model is expected to have weak performance at intense bedload transport rates.

By considering \mathcal{M} cells of length Δx and studying the evolution of the system, i.e., calculating $P(\mathbf{n}, t)$ while taking into account the aforementioned phenomena, the model results in a Chapman-Kolmogorov equation (Ancey & Heyman, 2014)

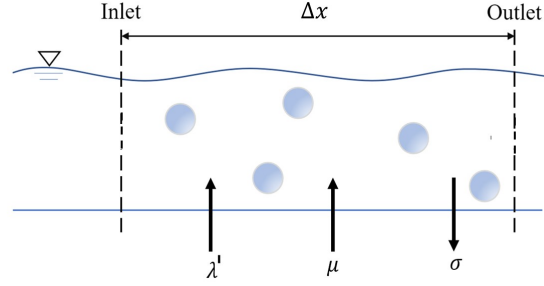


Figure 1.4: Illustration of the processes involved in mass exchanges: λ' , μ , and σ are particle entrainment, collective entrainment, and deposition coefficient, respectively.

$$\begin{aligned} \frac{\partial P}{\partial t}(\mathbf{n}, t) = & \sum_{i=1}^{\mathcal{M}} (n_i + 1) (P(\mathbf{n} + \mathbf{r}_i^{i+1}, t) v_i + P(\mathbf{n} + \mathbf{r}_i^+, t) \sigma_i) \\ & + P(\mathbf{n} + \mathbf{r}_i^-, t) (\lambda'_i + \mu_i (n_i - 1)) \\ & + P(\mathbf{n} + \mathbf{r}_i^{i-1}, t) v_{i-1} n_{i-1} \\ & - P(\mathbf{n}, t) (v_{i-1} n_{i-1} + \lambda'_i + \mu_i n_{i+1} + v_i n_i + \sigma_i n_i) \end{aligned} \quad (1.4)$$

where the migration from the upstream and downstream cells is represented by rate v and

$$\begin{cases} \text{Displacement from cell } j \text{ to cell } i (\mathbf{r}_i^j): & r_i = 1, r_j = -1, r_k = 0 \text{ for } k \neq i, j \\ \text{Entrainment or deposition within cell } i (\mathbf{r}_i^\pm): & r_i = \pm 1, r_k = 0 \text{ for } k \neq i \end{cases}$$

Therefore, \mathbf{r}_i^j is a vector where all entries except two are zero, whereas \mathbf{r}_i^\pm is a vector with all entries except one being zero. To switch from discrete probability space to continuous probability space, Poisson representation could be used to expand any discrete probability space, such as Eq. 1.4 into a series of Poisson distribution with parameter a_i

$$P(\mathbf{n}, t) = \prod_i \int_{\mathbb{R}_+} \frac{e^{-a_i} a_i^n}{n!} f(\mathbf{a}, t) d\mathbf{a} \quad (1.5)$$

After some mathematical derivation and using the Itô convention, we end up with the governing equation for an integrable function, i.e., $f(\mathbf{a}, t)$ as

$$\frac{\partial f(\mathbf{a}, t)}{\partial t} = \sum_i \mu_i \frac{\partial^2 a_i f}{\partial a_i^2} + \frac{\partial}{\partial a_i} \left[\left[\lambda'_i - a_i (\sigma_i - \mu_i + v_i) \right] f \right] + \frac{\partial}{\partial a_{i-1}} (v_{i-1} a_{i-1} f) \quad (1.6)$$

Chapter 1. Introduction

The Langevin representation equivalent (Gardiner et al., 1985) to Eq. 1.6 is

$$da_i(t) = \left(v_{i-1}a_{i-1} + v_i a_i + \lambda'_i - a_i(\sigma_i - \mu_i) \right) dt + \sqrt{2\mu_i a_i} dW_i(t) \quad (1.7)$$

where W_i is a Wiener process that corresponds to cell i . We can let $\Delta x \rightarrow 0$ and by introducing the Poisson density $b_i = \lim_{\Delta x \rightarrow 0} \frac{a_i}{\Delta x}$ (the PDF of the discrete random variable n_i is decomposed into a series of Poisson distributions whose rate is b_i), it results in the following partial differential equation for b

$$\frac{\partial b}{\partial t} + \frac{\partial}{\partial x}(\bar{u}_s b) - \frac{\partial^2}{\partial x^2}(D_u b) = \lambda - \kappa b + \sqrt{2\mu b} \xi_b \quad (1.8)$$

where $\kappa = \sigma - \mu$, $\lambda = \lambda' / \Delta x$, \bar{u}_s and D_u are mean particle velocity and particle diffusivity, respectively, and ξ_b is Gaussian noise term. Taking the ensemble average of Eq. 1.8 result in a governing equation for particle activity

$$\frac{\partial \langle \gamma \rangle}{\partial t} + \frac{\partial}{\partial x}(\bar{u}_s \langle \gamma \rangle) - \frac{\partial^2}{\partial x^2}(D_u \langle \gamma \rangle) = \tilde{\lambda} - \kappa \langle \gamma \rangle \quad (1.9)$$

The particle activity, denoted by γ , is defined as the limit of the ratio of the volume occupied by the particles to the volume of the control space as Δx approaches 0: $\gamma = \lim_{\Delta x \rightarrow 0} \frac{nV_p}{B\Delta x}$, where $V_p = \pi d^3/6$ represents particle volume, B is the control volume width, and d represents the particle diameter. The ensemble average of particle activity is denoted by $\langle \gamma \rangle$ and $\tilde{\lambda} = \lambda V_p / B$.

The derived bedload model is for a one-dimensional case study; however, we could extend the stochastic advection-diffusion equation into two dimensions. One way to extend the model is by generalizing the spatial operators in the system of equations. By expanding the equation into two dimensions, one can obtain

$$\frac{\partial b}{\partial t} + \frac{\partial}{\partial x}(\bar{u}_s b) - \frac{\partial^2}{\partial x^2}(D_u b) + \frac{\partial}{\partial y}(\bar{v}_s b) - \frac{\partial^2}{\partial y^2}(D_v b) = \lambda - \kappa b + \sqrt{2\mu b} \xi_b \quad (1.10)$$

The governing equation for particle activity in two dimensions reads

$$\frac{\partial \langle \gamma \rangle}{\partial t} + \frac{\partial}{\partial x}(\bar{u}_s \langle \gamma \rangle) - \frac{\partial^2}{\partial x^2}(D_u \langle \gamma \rangle) + \frac{\partial}{\partial y}(\bar{v}_s \langle \gamma \rangle) - \frac{\partial^2}{\partial y^2}(D_v \langle \gamma \rangle) = \tilde{\lambda} - \kappa \langle \gamma \rangle \quad (1.11)$$

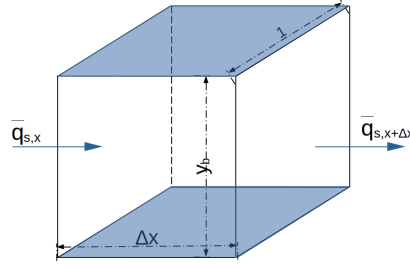


Figure 1.5: Control volume with unit width, length of Δx , and bed height of y_b .

where \bar{v}_s and D_v are mean particle velocity and particle diffusivity in transversal direction, respectively. The described bedload model offers information on the number of active particles, but to accurately simulate bed topography, it is also necessary to employ the Exner equation. The Exner equation is a common approach taken in numerical simulations for continuity of the bed (Murillo & García-Navarro, 2010). It is possible to incorporate the classic Exner equation, which does not consider particle fluctuations, with the aforementioned probabilistic bedload transport model.

1.7 Exner equation

Exner, a meteorologist from Vienna, formulated an equation for sediment mass conservation (Exner, 1925). The mass conservation within a control volume with a length Δx and a unit width (see Fig. 1.5) can be defined as follows:

$\frac{\partial}{\partial t}$ (sediment mass in the control volume) = sediment inflow rate - sediment outflow rate. Thus we have

$$\frac{\partial}{\partial t} \left[\rho_s (1 - \zeta_p) y_b \right] \Delta x \cdot 1 = \rho_s \left[\bar{q}_{s,x} - \bar{q}_{s,x+\Delta x} \right] \cdot 1 \quad (1.12)$$

where ζ_p denotes the bed porosity, which refers to the proportion of the bed's volume occupied by voids rather than sediment, typically considered 0.36 for gravel-beds. After simplification

$$(1 - \zeta_p) \frac{\partial y_b}{\partial t} = - \frac{\partial \bar{q}_{sx}}{\partial x} = \mathcal{D} - \mathcal{E} \quad (1.13)$$

where \mathcal{D} and \mathcal{E} represent the deposition and entrainment rates, respectively. In two-dimension, the Exner equation, will be

$$(1 - \zeta_p) \frac{\partial y_b}{\partial t} = -\frac{\partial \bar{q}_{sx}}{\partial x} - \frac{\partial \bar{q}_{sy}}{\partial y} = \mathcal{D} - \mathcal{E} \quad (1.14)$$

where \bar{q}_{sx} and \bar{q}_{sy} are the average bedload transport rates in the longitudinal and transversal directions, respectively.

1.8 Fluid governing equation

Numerous mathematical theories have been developed to predict the open flow morphodynamics, particularly in straight streams, starting with the work of Callander, 1969. The mathematical theories in computational hydraulics models are mostly based on depth-averaged shallow water equations known as Saint-Venant equations. We may derive the Saint-Venant equations from the Navier-Stokes equations using two fundamental assumptions: i. the hydrostatic pressure and ii. the Boussinesq approximation (Cushman-Roisin & Beckers, 2011).

The two-dimensional Saint-Venant equations consist of three equations: namely, the depth-averaged conservation of mass and two momentum equations for the fluid phase. In a straight channel, the governing equations — ignoring wind effects and Coriolis terms, in addition to diffusion of momentum due to viscosity — are (Mignot et al., 2006; Zhou, 2004)

$$\frac{\partial h}{\partial t} + \frac{\partial}{\partial x}(h\bar{u}) + \frac{\partial}{\partial y}(h\bar{v}) = 0 \quad (1.15)$$

$$\frac{\partial(h\bar{u})}{\partial t} + \frac{\partial}{\partial x}(h\bar{u}^2) + \frac{\partial}{\partial y}(h\bar{u}\bar{v}) + gh\frac{\partial h}{\partial x} = -gh\frac{\partial y_b}{\partial x} - \frac{\tau_{bx}}{\rho} \quad (1.16)$$

$$\frac{\partial(h\bar{v})}{\partial t} + \frac{\partial}{\partial x}(h\bar{u}\bar{v}) + \frac{\partial}{\partial y}(h\bar{v}^2) + gh\frac{\partial h}{\partial y} = -gh\frac{\partial y_b}{\partial y} - \frac{\tau_{by}}{\rho} \quad (1.17)$$

where x and y are the longitudinal and normal coordinates, respectively, and t represents time. The flow depth-average velocities in the x and y directions are $\bar{u} = \bar{u}(x, y, t)$ and $\bar{v} = \bar{v}(x, y, t)$, respectively. The flow depth, from the surface level to the bottom, is indicated by $h = h(x, y, t) = y_s - y_b$, where $y_b(x, y, t)$ and $y_s(x, y, t)$ represent the bed and free surface positions. The bottom shear stresses are τ_{bx} and τ_{by} .

1.9 Numerical simulation

The Saint-Venant equations are depth-averaged Navier-Stokes equations; given that the bottom boundary exchanges mass with the flow, two additional equations—the Exner equation

and advection-diffusion equation for bedload movement—are necessary to capture the morphodynamic variations.

These models simulate the interactions between water flow and sediment transport, leading to bed formation (Tucker & Hancock, 2010). Two distinct strategies can be employed to solve these governing equations: decoupled and fully coupled.

- In the decoupled strategy, the bed topography is assumed to be fixed, and then the shallow water equations are solved. The hydrodynamic variables are then used to update the bed topography via the Exner equation (Siviglia et al., 2022). This method exhibits weak performance in scenarios characterized by rapid changes in bed topography, typically associated with high sediment transport rates. Under such conditions, the decoupled approach is unsuitable due to the intense interactions between water and sediment variables (Hudson & Sweby, 2005; Postacchini et al., 2012). This strategy may face numerical stability problems, as discussed by Cordier et al., 2019. However, it remains appropriate when the flow and bed have weak integration (Soares-Frazão & Zech, 2011).
- In the coupled strategy, the shallow water and sediment transport equations are solved at the same time (Hudson & Sweby, 2005). It will be capable of capturing dynamic interactions between water flow and bed topography. This approach proves effective in conditions characterized by high sediment transport rates and rapid changes in bed morphology (Kassem and Chaudhry, 1998; X. Liu et al., 2008).

The application of these equations is not without challenges. Recent studies have developed advanced numerical schemes to tackle the complexities of the coupled Saint-Venant–Exner model. For example, a splitting method has been proposed by Toro, 2013, which divides the Saint-Venant–Exner equations into hyperbolic and parabolic subsystems (LeVeque et al., 2002).

In addition, the accurate prediction of sediment transport rates and patterns requires careful calibration and validation against empirical data. Furthermore, the assumptions inherent in shallow water and the Exner equations, such as the uniformity of sediment and the treatment of turbulence, can limit their applicability in certain scenarios. A notable contribution in this regard includes the work of Bohorquez and Ancy, 2015, who developed a coupled model for bedload and bed form prediction.

1.10 Stability analysis

The general prediction power of morphodynamic models can be foreseen before solving the governing equations by performing stability analysis. There have been many mathematical theories about stability analysis since the 1960s (Callander, 1969) to predict the morphodynamics of bars, especially the alternate bars in straight flumes. The equations' qualities of

linear stability reveal new information on the validity of the mean equations in the context of pattern formation. The approach starts by adopting several simplifying assumptions that simplify the mathematical problem, e.g., constant water discharge or channel width.

The primary advantage of these analyses lies in their capacity to provide insights that facilitate the straightforward assessment of the governing parameters of physical processes. Moreover, they enable the estimation of the spatial and temporal scales associated with bar morphodynamics. For example, "*why aren't river beds and deserts flat?*" A question has been asked by Kennedy, 1969, and has been addressed by using fluid-stability analysis with the initial disturbance. Moreover, by means of linear theories applied to straight channels, it has been found that forced bars stay stationary while free bars migrate downstream (Schielen et al., 1993; Zolezzi et al., 2005).

1.11 Objectives and research contributions

The aim of this research thesis is to develop a data-driven model for inferring bed topography, specifically for rivers with gravel-beds. Then, the capability of the one-dimensional, depth-averaged stochastic computational hydraulics model in predicting bed topography and bedload transport will be examined by comparing the resulting numerical outputs with experimental data. Lastly, a two-dimensional, depth-averaged stochastic solver will be developed, and its predictions will be examined by applying it to laboratory data.

The specific objectives are to expand the one-dimensional morphodynamic model into a two-dimensional framework and to numerically implement it. To fulfill these objectives, specific targets have been set:

- To evaluate the precision of data-driven modeling in estimating riverine bathymetry,
- To explore the accuracy of the one-dimensional stochastic bedload model when integrated with the Saint-Venant–Exner equations in bed topography and bedload transport rate prediction by applying to narrow gravel-bed flume,
- To extend the one-dimensional stochastic bedload model into two dimensions and integrate it with the two-dimensional Saint-Venant–Exner equations to incorporate particle fluctuations in the computational hydraulic model. Furthermore, the accuracy of the numerical solver in bed topography and bedload transport rate prediction when applied to wide gravel-bed flume has been examined.

To accomplish these aims, I will introduce three main contributions.

Data-driven modeling to infer bed topography

In this work, we have used machine learning techniques to develop a data-driven surrogate model for inferring bed topography from depth-averaged velocity fields. A well-trained neural network model requires numerous data points (either experimental or simulation data). The total experimental dataset comprises 5742 pairs (bed topography and velocity field in image format). Bathymetry is measured during each experiment using the laser-sheet imaging technique, and depth-averaged velocity fields are calculated using statistical methods. The code is written in Python, utilizing the PyTorch library, and has been executed in Colaboratory. The U-Net architecture is employed to train the convolutional neural network (CNN) model. U-net's main strength lies in its ability to deliver good results even with a limited amount of data, thanks to its structured.

The neural network's basic parameters and hyperparameters need to be studied in advance to achieve the best performance. After fine-tuning the model, it was applied to i. a part of the dataset previously unseen by the network; ii. numerical simulation conducted by computational hydraulic software called Iber version 2.5.1; and iii. field data from the confluence of two rivers in Illinois, USA.

One-dimensional depth-averaged numerical simulation

The one-dimensional hydraulic model is integrated with a one-dimensional stochastic advection-diffusion bedload equation, and the numerical solver is implemented using the Finite Volume Method. In this research phase, we implemented the q -wave propagation method using the FORTRAN language.

The accuracy of the proposed set of equations, i.e., the Saint-Venant–Exner equations coupled with the stochastic bedload model, is examined by applying it to laboratory experiments. The model predictions are examined by comparing numerical outcomes to laboratory experiments from Pascal et al., 2021; Recking et al., 2009 conducted in narrow gravel-bed flumes. These experimental datasets allowed us to investigate the bedload time series, antidune amplitude and wavelength characteristics, and their migration celerity.

There are three mass exchange rates in the stochastic bedload model. Before conducting a numerical simulation, we need to parameterize the mass exchange rates. Therefore, we first proposed closure relations to parameterize the particle exchange rates. Then, these closure relations are used to numerically solve the set of governing equations, to reproduce the laboratory experiments.

Two-dimensional depth-averaged numerical simulation

We have extended the work on one-dimensional numerical simulation into two dimensions. Two-dimensional numerical simulations and stability analyses were performed to study the

Chapter 1. Introduction

model's ability to predict the bedload transport rate and the alternate bar characteristics in a wide gravel-bed flume.

The numerical simulation is based on the Finite Volume Method and, more specifically, uses an extended HLL Riemann solver called the f -wave propagation method, implemented using the FORTRAN language. The Riemann problem is solved at every interface (or approximated by different approaches, e.g., the Roe averages) at every time step to gather information about the waves and speeds needed to update the solution for the next time step.

The numerical solver is applied to three steady-state laboratory experiments from Dhont, 2017 conducted in a wide gravel-bed flume to study the model's validity. This experimental dataset allowed us to investigate the bedload time series, alternate bar characteristics, and their growth rates.

1.12 Dissertation outline

This dissertation is composed of three main pillars explained in distinct chapters, in addition to the introduction and conclusion. Every chapter is organized in the style of a research paper and is self-contained regarding the definition of parameters. The dissertation ends with a concluding chapter and includes six appendices that contain the mathematical derivations of the formulations, thus simplifying the main text.

Chapter 2 discusses the details of how the surrogate model for bed topography inference is developed. This methodology, well-known in the medical field, is advantageously applied in the field of hydraulics. This chapter is published as a journal publication (Kiani-Oshtorjani & Ancy, 2023). Appendix A is associated with this chapter.

Chapter 3 presents a comprehensive description of the one-dimensional numerical methodology and its implementation. The details of this implementation are explored and applied to one-dimensional experimental data sourced from existing literature. Appendices B, C, and D are associated with this chapter.

Chapter 4 details the stability analysis of the governing equations and compares the obtained neutral curves with experimental datasets from other research groups. This is done to validate our calculations and assess the predictive capability of the system of governing equations in the context of pattern formation. The development and validation of the two-dimensional numerical solver are explained in detail and examined using experimental data from gravel-bed flume performed in our laboratory. Appendices E and F are related to this chapter.

Chapter 5 provides a summary of the findings and conclusions of the dissertation. It also discusses the limitations of the current work and suggests ideas for future works.

2 Bed topography inference from velocity field using deep learning

Mehrdad Kiani-Oshtorjani ¹ and Christophe Ancey ¹

¹ Environmental Hydraulics Laboratory, École Polytechnique Fédérale de Lausanne, 1015 Lausanne, Switzerland

Accepted in MDPI-water (Kiani-Oshtorjani & Ancey, 2023).

Doctoral candidate's contribution

The candidate performed the entire implementation, analysis, and figures for this chapter. The idea of inferring velocity fields using the entropy-based method was suggested by Prof. Ancey. This chapter is entirely written by the candidate, with editorial comments by Prof. Ancey.

Abstract

Measuring bathymetry has always been a major scientific and technological challenge. In this work, we used a deep learning technique for inferring bathymetry from the depth-averaged velocity field. The training of the neural network is based on 5742 laboratory data using a gravel-bed flume and reconstructed velocity fields (namely, the topographies were obtained from real-world experiments and the velocity fields were estimated using a statistical model). To examine the predictive power of the proposed neural network model for bathymetry inference, we applied the model to flume experiments, numerical simulation, and field data. Results showed the model properly estimates topography, leading to a model for riverine bathymetry estimation with a 31.3% maximum relative error for the case study (confluence of the Kaskaskia River with the Copper Slough in east-central Illinois state, USA).

2.1 Introduction

Imaging riverine bathymetry is fraught with difficulty. Among the available techniques in riverine bathymetry, a typical example is provided by the use of light detection and ranging (LiDAR) systems (Hilldale & Raff, 2008; Marcus, 2002; Wozencraft & Millar, 2005). This technique is based on the estimation of distance by recording the time lapse between sending and receiving a signal and having prior knowledge of the signal's speed. While these techniques do provide direct access to bathymetry, it is time-consuming and costly. Other examples include the use of indirect bathymetry techniques (Zaron, 2017), which usually involve solving an inverse problem relating bed topography to surface elevation (Durand et al., 2008; Simeonov et al., 2019), and surface velocity data (Almeida et al., 2018; Emery et al., 2010).

Inferring variation in riverine bathymetry from surface flow data is predicated on a potent causal relationship between them (Smith & McLean, 1984). This assumption is true, especially in shallow and one-dimensional flow conditions when the magnitude of velocity in the vertical direction is low compared to the streamwise velocity component (Wilson & Özkan-Haller, 2012). Employing surface velocity data is an alternative to estimate bathymetry, thanks to its affordability and sensitivity to river depth (Ghorbanidehno et al., 2021; Landon et al., 2014; Lee et al., 2018; Wilson & Özkan-Haller, 2012). There are several techniques for estimating surface velocity, including the use of drifter global positioning system (GPS) recordings (Honnorat et al., 2010; Landon et al., 2014; MacMahan et al., 2009). For example, Landon et al., 2014 investigated whether drifters' trajectories are sensitive enough to bottom topography to allow for depth determination. They successfully extracted river bathymetry using velocity field measurements collected from drifter GPS records in an ensemble-based data assimilation approach. The estimated bathymetry based on this technique on a shallow braided and deep meandering reach of the Kootenai River in Idaho, in the United States of America (USA) was more accurate than the previous estimations. Wilson and Özkan-Haller, 2012 applied this technique to a one-dimensional (1D) channel and to two real-world reaches, namely the Snohomish River, Washington, and the Kootenai River, Idaho, in the USA. The main difference with Landon et al., 2014 was this: they used depth-averaged velocities (based on numerical solutions to the shallow water equations) and a least-square method to minimize a cost function that combines known information and measured data. By using a state augmentation technique, the measured variable is connected to the unknown parameter, providing a model for deep water bathymetry estimation (depth in the 3–10 m range).

In recent years, deep learning has become one of the most powerful tools for overcoming some deterministic approach limitations (Forghani et al., 2021; Ghorbanidehno et al., 2021; X. Liu et al., 2022; Najjar et al., 2022). It can be used to image bed topography from surface flow data. Due to their ability to identify patterns or trends in data, neural networks are becoming increasingly popular in geophysics and hydraulics (Yu & Ma, 2021). For instance, Ghorbanidehno et al., 2021 used the neural network technique to obtain bed topography based on the depth-averaged flow velocity field, using limited labeled data. In order to reduce network size, the authors combined a fully connected deep neural network with principal

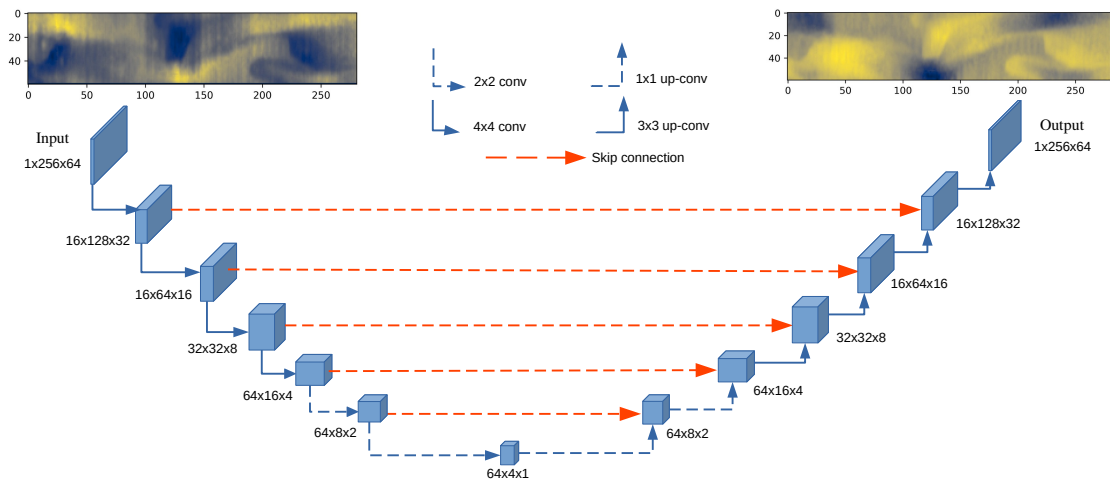


Figure 2.1: A diagram showing the neural network architecture. Convolutional layers are shown in blue, and skip connections are shown in orange. The number in the format of $a \times b \times c$ close to each box indicate the number of channels and image size in the x and z directions, respectively.

component analysis (PCA). PCA is a widely recognized method for reducing the dimensionality of data, where it transforms the data onto a new basis with fewer dimensions (Jackson, 2005). For instance, this could be achieved by calculating the covariance matrix of the training data and extracting its eigenvalue decomposition.

Usually, training the network needs a huge amount of data to avoid the curse of dimensionality (Bellman, 1966), which implies that the data occupy less and less of the data space as the data space moves from lower to higher dimensions. The volume of this space grows so fast that the data cannot keep up and thus becomes sparse—the sparsity problem is a major statistical significance issue. To enhance the training dataset size, Ghorbanidehno et al., 2021 divided the river’s entire domain into small subdomains. As a result, each river profile provided several hundred training samples rather than just one.

The training of the neural network for bathymetry estimation could be done by solving the shallow water equations and using the resulting solutions. A typical example is provided by X. Liu et al., 2022, who employed shared-encoders and separate-decoders, where bathymetry’s input image is encoded and then decoded to three outputs, namely, the flow’s longitudinal and transverse depth-averaged velocity components and the water surface elevation. Two-dimensional (2D) simulations using randomly generated input bathymetry data were used to generate the training data.

Recent advancements in measurement techniques have led to the availability of high-resolution and low-cost surface velocity fields (Almeida et al., 2018). These techniques include the use of Lagrangian drifters (Honnorat et al., 2010; Maximenko et al., 2012), large-scale particle image velocimetry (Bradley et al., 2002; Lewis & Rhoads, 2015), and synthetic aperture radar (Biondi

Chapter 2. Bed topography inference from velocity field using deep learning

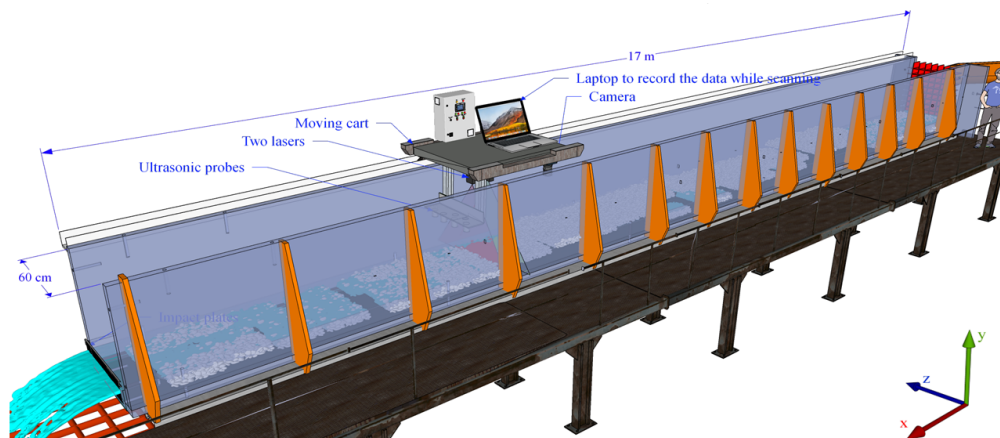


Figure 2.2: Gravel-bed flume illustration, in which all the dataset is gathered based on the experiments performed on this channel. It has 17 m length but the useful length (removing 1.5 m from each side) is 14 m.

et al., 2020; Yoon et al., 2012). This work intends to predict bathymetry by using indirect measurements, i.e., the velocity field, through a convolutional neural network. The neural network training is based on a U-net architecture, used for the first time for segmentation problems (Ronneberger et al., 2015), and to our knowledge, this is the first attempt to use the U-net model for bathymetry inversion. To this end, we used an experimental dataset made of 5742 data points. It was not realistic to measure the velocity field, but we could estimate it using entropy-based models. Figure 2.1 shows the model's architecture. In this network, the encoder and decoder are connected by skip connections, in contrast with regular convolutional networks. By doing so, we ensure we actually lose no information during the feature extraction process (Drozdal et al., 2016; Orhan & Pitkow, 2017). In order to develop a well-trained neural network model, we need to collect a large amount of data. Due to the size of the experimental dataset used in this study, we had no problems with dataset size. As an alternative, if we were dealing with a small dataset, we could divide the experiment domain into smaller regions, thereby, we could increase the amount of data.

In this work, training the convolutional neural network model to infer bathymetry is based on bed topography scans and velocity field estimates. Solving the governing partial differential equations will be bypassed, and the solutions will be found solely by a convolutional neural network that is trained based on a huge experimental dataset. Closely related to our work is Ghorbanidehno et al., 2021's PCA-DNN framework, which combined the traditional fully connected deep learning method and principal component analysis. They trained the deep neural network model based on field data, whereas we focused on a convolutional neural network; besides, our dataset is produced in the laboratory. Our trained model is suitable for gravel-bed rivers, whereas their model is suitable for deep rivers. All of the training networks in this work have been done using Colaboratory on GPU: the Nvidia Tesla P100-PCIE-16GB, manufactured by Nvidia Corporation with headquarters in Santa Clara, California, United

States.

This paper is structured as follows: The methodology for generating the dataset based on experiments and analytical derivation is explained in § 2.2. Moreover, the U-net architecture is described, and the basic parameters, regularization, and hyperparameters—such as dropout, learning rate, weight decay, and training dataset size—are studied in that section. In § 2.3, the model’s performance and accuracy have been studied. In addition, the neural network model’s predictive power has been studied by applying it to flume experiments, the numerical simulation of a gravel-bed flume, and field data performed at the confluence of the Kaskaskia River and Copper Slough in central-east Illinois, USA. § 2.4 and § 2.5 discuss and summarize our achievements and future work, respectively.

2.2 Methodology

2.2.1 Data collection

The dataset is based on the experiments conducted at LHE-EPFL (Dhont, 2017). Table 2.1 represents the input parameters and each experiment’s duration. It consists of three long-term experiments. Experiments were carried out in a tilted flume at an angle of $S = 1.6\%$ and 1.7% , a length of $L = 17$ m and a width of $w = 60$ cm, as depicted in Fig. 2.2. The useful length of the flume is 14 m because of technical limitations (1.5 m from each side is ignored). The flume bed was made of natural gravel with a height of 31.5 cm at the beginning of the experiments. Sediments mean diameter was $d = 5.5$ mm, with a $\sigma = 1.2$ mm standard deviation, and density of $\rho_s = 2660$ kg/m³. The water discharge and sediment feeding rates at the flume inlet were set to 15 L/s and 2.5, 5, and 7 g/s, respectively. Each experiment lasted for hundreds of hours. At the beginning of each experiment, the bed surface was flattened. These long-term experiments are conducted via a sequence of short-term experiments that last 8 hours. To prevent the destruction of the bed topography, these short-term experiments are lunched with very low flow discharge. During the experiment, water discharge and sediment feeding rate were kept constant (Dhont, 2017). Experiment 1 included 1566; experiment 2 consisted of 741; and experiment 3 consisted of 3435 scans, respectively (a total of 5742 scans, each consisting of bed topography and flow depth data). Based on the entropy-based models, we computed the depth-averaged velocity field using the flow depth data and knowing the constant flow discharge as a constraint. In the next following sections, the details of entropy-based models for inferring velocity fields will be explained.

Table 2.1: Input parameters of the experiments.

	Exp. 1	Exp. 2	Exp. 3
Flow rate (L/s)	15	15	15
Flume slope (%)	1.6	1.7	1.6
Sediment feed rate (g/s)	2.5	7.5	5.0
Duration (h)	250	556	118

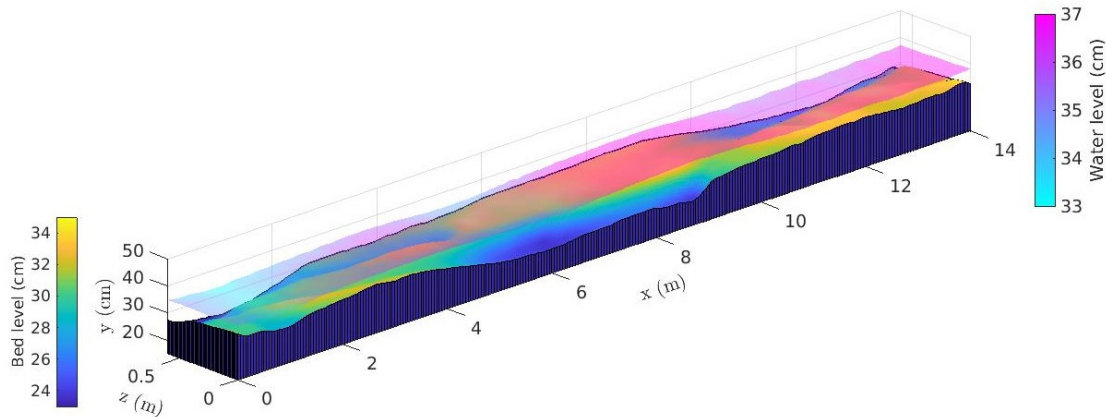


Figure 2.3: An example of experimental topography using the gravel-bed flume. The bed and flow heights are measured from the bottom of the flume. The initial height of the bed is at 31.5 cm.

During an experiment, measurements of the bed topography and flow depth are recorded with a fine resolution. The bed topography is measured by the laser-sheet imaging technique, i.e., using two angled lasers. Those lasers are mounted on an automated moving cart. Water disturbances, caused by a variety of factors (including turbulent flow conditions, varying bed topography, sediment transport, and inflow/outflow perturbations), can interfere with measurements. To overcome this issue, calibration is conducted prior to the experiments. By calibrating the distance between two angled lasers projected on the bed, the bed topography can be induced with a resolution of 60×281 pixels. Every 10 minutes, the cart programmed to scan the bed proceeds using MatLab. Each scan took about 145 seconds and covered $14 \text{ m} \times 60 \text{ cm}$. During each scan, the bed topography by lasers and flow depth by ultrasonic probes are measured. The ultrasonic probes determine flow height, a sound pulse is emitted, and the travel time between the sensor and the object can be used to infer flow depth (see Fig. 2.2).

The sediment feeding system operates as follows: it moves sediments from the hopper to the flume's inlet via a conveyor belt. Subsequently, these sediments are introduced into the channel through a pin board, which spreads the gravel along the width with a Gaussian distribution. The rate at which sediment is fed is regulated by controlling the speed of a rotating cylinder that clogs up the hopper's outlet. The most frequent mode happening in the flume using the aforementioned flow, channel geometry, and sediment characteristics is alternate bars. In Fig. 2.3, the bed topography and alternate bar appearance are illustrated.

Due to erosion, deposition, and transport processes, the bed topography changes over time during the experiments. In turn, the hydraulic conditions in the system are affected by the bed morphology as a result of a feedback loop driven by the movement of particles (Dhont, 2017; Griffiths, 1993). Based on the Froude number, $Fr = v/\sqrt{gh}$ (where g is the gravitational

acceleration, v is flow velocity and obtained by particle image velocimetry using tracking light polystyrene balls, and h is flow depth measured by ultrasonic probes), the flow regime was turbulent and super-critical with a Froude number greater than 1 (Dhont, 2017). Since the flow depth is uniform at the beginning of each experiment, when there is no bed form, the streamwise bed shear stress can be measured by $\tau = \rho g R_h S$ where $R_h = hw/(2h + w)$ is the hydraulic radius and ρ is fluid density. The shear stress is estimated by computing its average value along longitude bed profiles (Dhont, 2017; Venditti et al., 2012). The value of shear stress in our experiments varies between 4.89 to 10.75 kg/m/s². The Shields number and the shear velocity can be obtained by $\tau^* = R_h S / R / d$, and $u^* = \sqrt{\tau / \rho} = \sqrt{g R_h S}$, respectively, where $R = (\rho_s - \rho) / \rho$. The shear velocity varies in a range of $0.07 \leq u^* \text{ (m/s)} \leq 0.10$ and the Shields number changes between $0.05 \leq \tau^* \leq 0.11$ among all experimental data.

In order to have a suitable input/output image size for training the neural network, we applied a bicubic interpolation over a 4×4 pixel neighborhood to the flow depth and bathymetry data to change the size of the data, i.e., bed topography and velocity fields, from 60×281 pixels into 64×256 pixels. Subsequently, the dataset was partitioned into three subsets: the training dataset, the validation dataset, and the test dataset. The distribution of the total number of samples was as follows: 80% for training data and 20% for validation data. Moreover, the training data was again divided into 90% as the training dataset and 10% as the test dataset. Training and validation data will be used to fit the models, and to estimate the prediction error for model selection and hyperparameter tuning, respectively, and finally, a test dataset will be used to assess the generalization error of the selected (best) model. The dataset is composed of 5742 pairwise (bed topography and velocity field) grayscale images, and, therefore, the training, validation, and test datasets consist of 4133, 1149, and 460 data, respectively. The dataset is published attached to this work on <https://rb.gy/84l4hk>. A total of 11484 fields are included in the published dataset, including both bed topography and depth-averaged velocity data.

2.2.2 Entropy-based velocity profile

Entropy is defined as a measure of a system's randomness or disorder and originated from thermodynamics (V. P. Singh, 2016). Shannon was one of the pioneers who developed entropy's mathematical foundation and connected it to information (V. P. Singh, 2016). To obtain the one-dimensional and two-dimensional velocity profiles, it is necessary to maximize the entropy of the velocity distribution in order to obtain the least biased velocity probability density function (Vyas et al., 2020). It is based on Jaynes's principle of maximum entropy, which states that any system in the equilibrium state attempts to maximize its entropy, subject to given constraints (Jaynes, 1957). The entropy of a flume/river must reach its maximum value when it reaches a dynamic (or quasi-dynamic) equilibrium (V. P. Singh et al., 2003). At any location where maximum velocity occurs, the 2D velocity distribution based on entropy theory should be valid (V. P. Singh, 2016).

Chapter 2. Bed topography inference from velocity field using deep learning

As aforementioned, during each experiment, bed topography and flow depth are measured locally with high resolution. Since the flow discharge is fixed to a constant 15 L/s value during all the experiments, the constraint in the entropy-based models is constant flow discharge. Then, the velocity profile can be obtained locally by maximizing entropy. Estimating flow velocity can be achieved using a number of techniques. Two entropic principles are known as Shannon and Tsallis (this entropy is a generalization of the Shannon entropy) that are often applied to river discharge assessment (Bechle & Wu, 2014; V. P. Singh, 2016). Both of these principles connect the maximum flow velocity at a vertical axis of the flow area to the cross-sectional mean flow velocity.

Shannon entropy-based method

The application of Shannon entropy to open-channel flows has been shown by Chiu and colleagues (Chiu, 1987, 1988, 1989). Entropy-based models have been in use in hydraulics for a number of years, and we have some hindsight about their validity (Kumbhakar et al., 2020; Vyas et al., 2020). Building upon Chiu's work, Moramarco et al., 2004 proposed a version of Chiu's entropy-based velocity distribution equation that can calculate the 2D velocity distribution using only the maximum velocity and bathymetry information (Vyas et al., 2020). This model does not require parameter calibration or the isovel equation and only requires knowledge of the maximum velocity and its position. Generally, maximum flow velocity occurs at the water's surface; especially when $w/h > 3.5$, the maximum velocity occurs on the flow surface (Song & Graf, 1996) which is true of our experiments. The velocity equation can be expressed as follows (Moramarco et al., 2004)

$$u = \frac{u_{max}}{M} \log \left[1 + (e^M - 1) \frac{y}{h-D} \exp \left(1 - \frac{y}{h-D} \right) \right] \quad (2.1)$$

The equation for estimating the longitudinal velocity along the vertical axis (u) includes several variables, namely, the maximum flow velocity and its depth from the flow's surface, represented by u_{max} and D , respectively. The Shannon's entropy parameter is symbolized as M , whereas the variable y signifies the vertical position of the velocity with respect to the bed topography. To determine the constant value of the entropy parameter, the following equation can be used

$$\frac{u_m}{u_{max}} = \frac{e^M}{e^M - 1} - \frac{1}{M} \quad (2.2)$$

Tsallis entropy-based method

Tsallis introduced the generalization of Boltzmann–Gibbs–Shannon (known as Shannon) statistics (Tsallis, 1988). According to the Tsallis entropy theory, the 2D velocity equation is expressed as follows (V. P. Singh, 2016)

$$\frac{u}{u_{max}} = \frac{2}{G} \left[G \frac{y}{h+D} \exp\left(1 - \frac{y}{h+D}\right) + \frac{(4-G)^2}{16} \right]^{1/2} - \left(\frac{4-G}{2G} \right) \quad (2.3)$$

where the entropic parameter is denoted as G . Here, $D = 0$ (meaning that the maximum velocity happens on the surface flow) because the flume is considered wide, $w/h > 3.5$, and on the other hand, Song's experiments emphasize this hypothesis (Song & Graf, 1996). The definition of G is

$$\frac{u_m}{u_{max}} = \frac{12+G}{24} \quad (2.4)$$

The mean velocity in a cross section u_m is known based on reckoning the flow discharge and the section area, while u_{max} is determined iteratively by the algorithm expressed in § 2.2.2, by knowing that the maximum velocity is happening on the flow surface, assuming the maximum velocity in the first iteration, and correcting the maximum velocity iteratively by calculating the flow discharge using the estimated velocity profile and comparing with the ground truth.

Depth-averaged velocity fields

The mean velocity over a cross section u_m can be calculated if we know the flow discharge and the section area, while u_{max} is determined iteratively by knowing that the maximum velocity is happening at the water's surface. Water depth and bed topography during the experiments were measured at a high spatial resolution, as detailed in § 2.2.1. Our measurement system provided matrices with dimensions of 60×281 elements (width by length). For each of these 16860 elements, we computed the velocity field using entropy-based models and a depth increment of $dy = 0.1$ mm by employing the algorithm described below and using a trial-and-error approach. As a consequence, the size of the velocity vector at each of these 16860 elements depended on the water depth at that point. The algorithm is as follows:

- Assuming a maximum velocity (e.g., $u_{max} = 1$ m/s) in the initial iteration,
- Calculate the section flow area A using the measured local flow depth data with the assistance of the trapz function in MatLab,
- Determine the mean cross-sectional flow velocity u_m by dividing the flow rate $Q_l = 15$

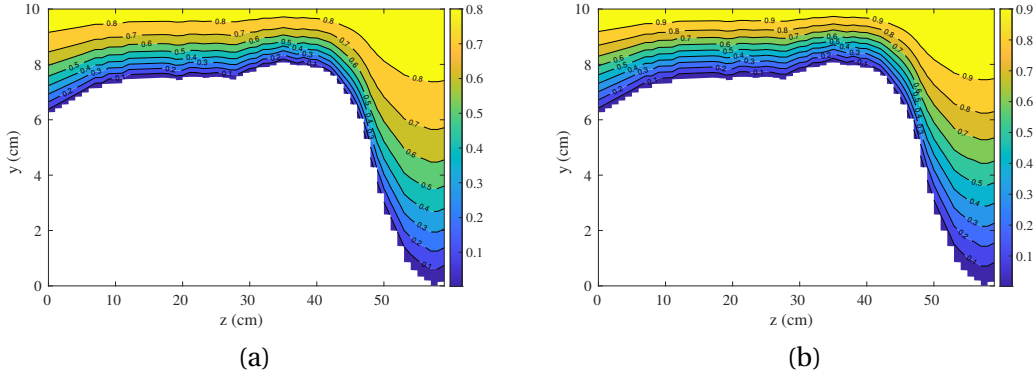


Figure 2.4: Velocity plot based on (a) Shannon-entropy and (b) Tsallis-entropy for a cross section in the middle of the channel based on Exp. 3 at $t = 200$ minutes. The border between the white and blue regions indicates the bed topography for one cross section.

L/s by the section area A ,

- Compute the entropy parameter M based on Eq. 2.2 (or G based on Eq. 2.4 in case using the Tsallis entropy-based method),
- Iterate over each set of 60 data points along the channel width and calculate the velocity profiles for the cross section using Eq. 2.1 (or Eq. 2.3 in case using the Tsallis entropy-based method),
- Estimate the flow discharge $Q_{l,est}$ based on the calculated velocity profiles,
- Adjust the maximum velocity in the initial step and repeat the process until the error $err = Q_l - Q_{l,est}$ is less than 10^{-3} .

The contour plot of the calculated velocity profile is plotted in Fig. 2.4(a). However, for the sake of comparison, the Tsallis entropy-based method has been applied to the same cross section. The velocity profile based on Tsallis entropy is plotted in Fig. 2.4(b). One can see that the velocity gets close to 1 m/s on the surface flow, which coincides with the measured flow surface velocity in the laboratory using particle image velocimetry (PIV) technique by tracking polystyrene balls travelling along the entire flume length (Dhont, 2017). By comparing two velocity fields in Fig. 2.4(a) and Fig. 2.4(b), there is no such difference in using each entropy models. We therefore decided to use Shannon's entropy to calculate the velocity fields in all of our experiments.

2.2.3 Neural network

We use the U-net architecture for our neural network model. In the main journal paper where the U-net has been introduced by Ronneberger et al., 2015, the input and output images were of different sizes and used to solve the segmentation problem. Since our input/output are

of the same size, we reworked the model by changing the convolution function parameters and using the model as a regression problem. The U-net has been used for segmentation (Kohl et al., 2018; Rafique et al., 2022; Siddique et al., 2021), classification (Sudhan et al., 2022; Windheuser et al., 2023; Yan et al., 2022) as well as the regression problem (Jiang et al., 2021; Thuerey et al., 2020; Yao et al., 2018).

It has already been mentioned that the U-net is divided into two parts. Firstly, a standard convolutional neural network architecture is used to perform the contracting process. Leaky ReLU activation units are followed by multiple convolutions with padding in the contracting path. The same structure is repeated several times. One of U-nets' key characteristics lies in the expansive path, i.e., the second path. Using transposed convolution, each stage in the expansive path upsampling the feature map. Afterwards, we concatenate the upsampled feature map with the corresponding layer from the contracting path. Therefore, we obtain a U-shaped network and, perhaps most importantly, contextual information is propagated along the network, enabling a proper reconstruction of context (Ronneberger et al., 2015). In this work, an upsampling followed by a convolution rather than a typical transpose convolution is used instead.

These features allow the model to handle the spatial complexity required for the pixel-wise regression tasks (Huet-Dastarac et al., 2023). Its symmetric structure, combining both down-sampling (reducing the spatial resolution of the feature maps while increasing their depth and detecting the important characteristics in the input image) and upsampling paths (identifying the features while maintaining the spatial resolution of the input), allows for the effective capture of multi-scale spatial information, which is essential for accurate regression predictions (Alom et al., 2018; Ronneberger et al., 2015).

The implementation is based on the Pytorch deep learning framework (Paszke et al., 2019). The table in Appendix A shows the structure of the U-net used in all our tests, with details of the different layers. The schematic of our neural network architecture can be seen in Fig. 2.1, in which a fully convolutional U-net is used. This is a famous architecture that uses a number of convolutions at various spatial resolutions. This network differs mainly from a regular encoder–decoder network in that skip connections are used from encoder to decoder parts. By doing this, the network can use fine-grained details learned in the encoder to reconstruct an image in the decoder. Using it as a whole is the only way to make this network work; if we want to use the decoder as a standalone component, it does not work. No pooling is used, and instead, strides and transposed convolutions are used.

The selection of U-Net's hyperparameters, such as learning rate, number of epochs, batch size, number of layers, activation functions, optimizer, dropout rate, and weight initialization, has a substantial influence on its efficacy. Traditional procedures for hyperparameter optimization, such as grid search or random search (Shekhar et al., 2021) can be used, but they are computationally costly. To solve this issue, some recent research has proposed methods for refining the U-Net hyperparameters (Ghosh et al., 2023). In this study, we used a variety of

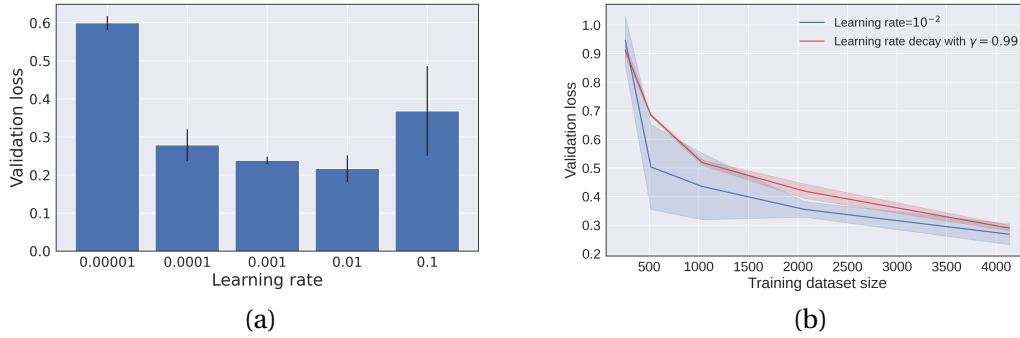


Figure 2.5: (a) Effect of different constant learning rates in terms of validation loss (b) testing models based on validation loss with and without learning rate decay versus training dataset size.

tests to establish the best hyperparameters explained in § 2.2.3 and § 2.2.3. However, for some hyperparameters, such as batch size, the selection method involves trying out several values and selecting the best one by using a random search strategy.

Basic parameters

In order to tune the training hyperparameters, such as learning rate and learning rate decay, we have studied these hyperparameters following Thuerey et al., 2020 using the baseline architecture. The learning rate is a tuning parameter of the optimizer function that determines the step size taken by the optimizer at each iteration while moving toward a loss function minimum. Figure 2.5(a) shows the validation loss using different learning rates varying in a range of $[10^{-5}, 10^{-1}]$. The validation loss is computed by employing the mean absolute error (MAE - $L1$ loss) as the metric, which measures the disparity between the bathymetry field \hat{y} derived from the validation dataset and the bathymetry field predicted by the neural network model, denoted as y . The MAE is calculated by summing the absolute differences between the predicted values (y) and the actual values (\hat{y}), divided by the total number of validation dataset size, denoted as N and expressed as: $MAE = 1/N \sum_{i=1}^N |\hat{y}_i - y_i|$. The error bar, which represents result uncertainty, is calculated by repeating the same configuration four times. As can be seen, it is clear that the lowest and largest learning rates result in the highest validation loss, considering our problem, we have the best learning rate with a learning rate of 10^{-2} .

With gradient-based optimization algorithms, saddle points can be approached, and training takes longer since surface around such points are flatter and gradients are close to zero (Goodfellow et al., 2016). Therefore, rather than using a fixed value for the learning rate, it could be decreased over time. If training no longer improves our loss, the learning rate is changed, with every iteration being based on some cyclic function f . The number of iterations in each cycle is fixed. By using this method, the learning rate is allowed to vary cyclically between reasonable boundaries. We can traverse saddle point plateaus more quickly when

we increase our learning rate, since we are less likely to get trapped in unfavorable states like saddle points. We have performed a test: in it the learning rate decays by a gamma factor in every epoch that is set to be $\gamma = 0.99$ i.e., $lr_{epoch} = \gamma \times lr_{epoch-1}$. Figure 2.5(b) compares validation loss based on this strategy, comparing constant and varying learning rate factors. We found out that the learning rate decay does not help the improvement of the model based on validation loss comparison; for nearly all training dataset sizes, the validation loss when using learning rate decay is greater than that with a constant learning rate, while it helps decrease diversity around the mean value.

Based on Fig. 2.5(a) and Fig. 2.5(b) tests, we used Adam optimizer (Kingma & Ba, 2014) with a fixed learning rate of 0.01 and $\beta_{1,2}=[0.5, 0.999]$ for the rest of the training optimizations. In addition to a nonlinear activation function, each of the network section contains a convolutional layer, batch normalization, and dropout one (refer to Table in Appendix A). In the model, we included the possibility of normalizing batches. During training, it shifts and rescales according to the mean and variance estimated on the batch. The literature has proven that batch normalization makes the training process faster and smoother (Ioffe & Szegedy, 2015; Santurkar et al., 2018). However, it requires a sufficiently large batch size, and our choice of batch size of 100. We did not use any pooling for the training process.

Regularization and hyperparameters

The idea behind regularization is to reduce complexity of the neural network model and inhibits overfitting - that is, the model learns unnecessary details, noises or random fluctuations in the training data as main concepts, insofar as it negatively impacts the model's performance -, and it is essential to study when using deep learning algorithms. For example, dropout, weight decay, data augmentation, and weight initialization are the most often used regularization techniques. Following Thuerey et al., 2020, these techniques have been studied and discussed in the subsequent analysis.

The choice of initialization is highly influential on deep learning algorithms when training deep models. Algorithm converge-ability can be determined by the initial point, with some initial points being so unstable that numerical difficulties arise and the algorithm fails. The weight initialization of a neural network consists of setting its weights at small random values, which determine the starting point of the optimization when training. In order to prevent layer activation outputs from exploding or vanishing gradients during training, an appropriate initialization of the weights is necessary and manages to achieve better performance. Here are the most widely used, among others: the constant initialization, the He normalization (He et al., 2015) and Xavier normalization (Glorot & Bengio, 2010), when dealing with convolutional layers. In deep networks, the performance of the constant initialization scheme usually is subpar (Goodfellow et al., 2016). We chose not to use constant initialization because it sets all computing units to the same state, resulting in symmetric or identical outputs and gradients during backward propagation. This symmetry restricts the flexibility of our network, hence we chose not to use constant initialization. We experimented with two other initialization for

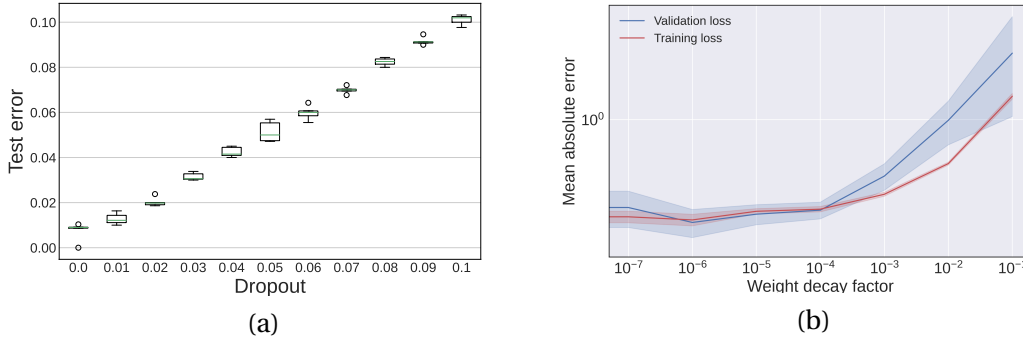


Figure 2.6: (a) Test error as a function of the dropout rate for a model with 142,689 training parameters, (b) illustrates the influence of the weight decay factor on the training and validation performance.

our networks: He and Xavier normalization and the former seems to lead to slightly better performances than the latter. We therefore stuck to that one. Based on the He initialization method, initialization is based on a randomly generated number computed with a Gaussian probability distribution with a mean of zero and a standard deviation of $\sqrt{2/n}$, where n stands for the number of inputs to the node (He et al., 2015).

We can go one step further by adding mechanisms specifically designed to facilitate the training such as dropout (Srivastava et al., 2014). Dropout consists of randomly dropping out neurons in a layer, with a probability that corresponds to the dropout coefficient. We implemented the possibility to include it in the model. Here is this technique's main advantage: it prevents overfitting as the neurons of a layer become less dependent on particular inputs. In Fig. 2.6(a), the influence of the dropout is studied, which has a negative effect on the test error. As the dropout rate decreases, the test error tends to converge to zero. Therefore, the dropout is not recommended for this study and it is considered as zero for the rest of the training. This might be the reason: dropout is usually unnecessary when the network is small compared to the dataset. By adding this regularization, it will worsen performance if the model capacity is already low.

In order to further improve the models' performance, we can also use the weight decay technique, which holds greater significance for fully connected neural networks compared to convolutional neural networks. This approach consists in adding a penalty to the model based on the amplitude of its weights, in order to limit overfitting. The model will all the more be penalized as the values of the network connections increase. This strategy is based on the principle that large weights in a neural network can cause more variance at output and prevent the model from generalizing correctly. The penalty forces weights down, and permits to obtain a less flexible network that is less specialized in the data used for training. This penalty is defined as follows: $L_{weight_decay} = \lambda \sum_i \omega_i^2$ where L_{weight_decay} is the penalty associated with weight decay, ω_i is the i -th weight in the network and λ is a positive coefficient that affects the importance of the penalty. This parameter is yet to be determined, so we carry out training

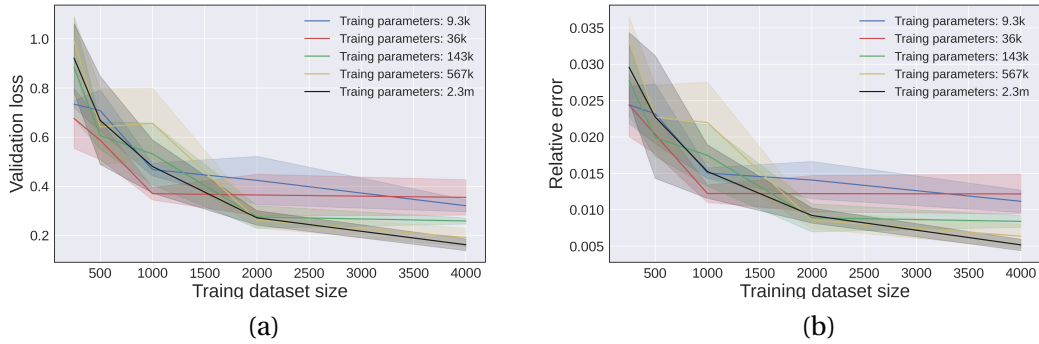


Figure 2.7: (a) Validation loss, and (b) relative error for various model complexity and training dataset size.

with several values of λ as presented in Fig. 2.6(b) in which the validation and training loss are plotted as a function of the weight decay factor. Losses for the weight decay factor larger than 10^{-4} start to increase while the losses for the lower weight decay reach a plateau. The training time using different weight decay factor does not change dramatically, therefore the best weight decay could be chosen by just paying attention to the losses in which 10^{-6} is the best for the rest of the training.

Data augmentation is a technique in deep learning methods that increase the amount of training dataset by leveraging existing data, often via techniques involving alterations in position and color, among others. In physical application, it is also feasible to employ data augmentation, as presented in Ghorbanidehno et al., 2021. Nevertheless, as evidenced by the results detailed in the subsequent subsection, when evaluating the adequacy of data volume relative to the model's complexity through validation error comparison, it becomes apparent that the existing data volume suffices. Consequently, in this study, we refrained from employing any data augmentation techniques.

2.3 Results and performance

2.3.1 Model performance

To investigate the impact of neural network model complexity on the accuracy of its predictions, in the following training runs, the total amount of weights is modified by varying the number of feature maps. For instance, the total weights will quadruple by duplicating the number of input channels (Thurey et al., 2020), hence, by manipulating the number of input/output channels, we can investigate diverse model complexities. Figure 2.7 shows the accuracy results for five distinct network sizes, namely networks with {9.3, 36, 143, 567, 2300}k training parameters, as a function of various dataset sizes including {0.25, 0.5, 1, 2, 4}k data.

A network with 9.3k training parameters, is relatively small for a generative neural network with

Chapter 2. Bed topography inference from velocity field using deep learning

$1 \times 64 \times 256 = 16\text{k}$ outputs, but it allows for faster training time and prevents overfitting in view of the relatively small dataset we are working with. Nevertheless, a network comprising 2.3m training parameters faces challenges concerning time constraints and lacks generalization capabilities - because of relatively small training dataset. Number of training parameters is a crucial number to keep in mind when training neural networks. It is easy to change and increase it, and end up with a network with millions of parameters, then it is highly probable we will be faced with all kinds of convergence and overfitting issues. To avoid the dimensionality curse, the number of parameters must match the amount of training data, as well as scale with the network's depth (Zhang et al., 2021). The exact relationship between these three depends on the problem under consideration.

In Fig. 2.7(a), various models with different complexity - number of training parameters - perform differently when applied to 1149 velocity fields from the test dataset. As depicted in Fig. 2.7(a), both error and error bar tend to be larger when training occurs on a small dataset size. Conversely, as the dataset size increases, the error and error bar decrease. Furthermore, for a large dataset size, increasing the number of training parameters leads to a decrease in validation error. However, for a small dataset size, augmenting the number of training parameters results in an increase in validation error due to overfitting to the data.

In Fig. 2.7(b), the relative error (RE) is computed using the formula: $RE = 1/N \sum_{i=1}^N |y_i - \hat{y}_i| / \hat{y}_i$, where \hat{y} refers to the ground-truth bed elevation, y represents the estimated bed elevation calculated based on the neural network model, and i counts the sample data. Curves in Fig. 2.7(b) show the relative errors for various model sizes and training dataset size. For a given number of training samples, there exists a slight variation among relative errors of different model sizes. However, the decrease in error is comparable when larger amounts of training data are utilized. Once again, the error bar reduces as the dataset size increases. When dealing with the smallest dataset size, an increase in training parameters leads to a corresponding increase in relative error. However, this behavior reverses for larger dataset sizes. Based on the findings in Fig. 2.7, the most optimal model seems to be the one with 2.3m training parameters, achieving a $L1$ loss of 0.16 cm and a relative error of 0.5% when trained on a 4k dataset size. However, this model requires a considerable training time of approximately 2 hours. In comparison, smaller models show faster training times, taking {0.31, 0.39, 0.59, 0.97, 1.8} h - from smallest to largest model for 600 epochs -, when applied to a 4k dataset size.

Considering both the execution time for training and the performance metrics, we have ultimately chosen the model with 143k trainable parameters as the best model. This model exhibits a relative error of 0.85% and a validation loss of 0.26 cm when trained on the 4k dataset size. These results demonstrate that the model has been effectively trained and can generate accurate predictions within a reasonable timeframe.

Figure 2.8(a) shows the best neural network is trained properly without overfitting - given that the training and validation loss plots did not exhibit divergence. After 600 epochs, the

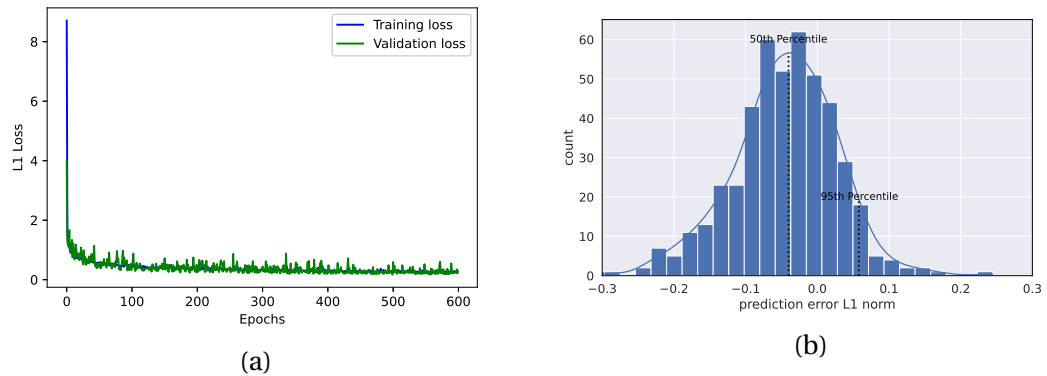


Figure 2.8: (a) Training and validation losses for learning rate 0.01, (b) histogram plot of the $L1$ norms of prediction errors (applied to 460 test samples).

validation and training losses should have decreased from an initial value of around 8.9 cm to 0.02 cm based on the standard settings. It is visually easy to see the loss curves trend down for 100 epochs and, afterwards, the curve flattens out. As we move towards the end by increasing the number of epochs, the validation loss is still decreasing slowly, and most importantly, it is not increasing. Nevertheless, achieving a training loss reduction of more than 0.02 cm will come at the expense of increased training time without significant improvement in loss compared to previous epochs. A divergent validation loss from the training loss would indicate overfitting, something we should avoid. The graph illustrates the models do not exhibit overfitting over time and reach to stable levels of validation and training losses after 600 epochs.

To study the neural network model performances, in which we have tuned the parameters in the previous parts on a larger number of training and validation datasets, we perform an error measurement for all the test dataset. The best model is applied to the test dataset and $L1$ error is calculated. Figure 2.8(b) shows the distribution of $L1$ error varying in a range of $[-0.32, 0.24]$ cm. The 50th - known as the median -, and 95th percentile - meaning that only 5% of the samples exhibit a greater $L1$ error -, are -0.041 cm, and 0.058 cm, respectively with a mean of -0.045 cm. It means, $L1$ error of predicted examples - in the test dataset - by the neural network model lie close to zero. The maximum error is 3.2 cm while the bed topography changes in an interval of 18.19 cm to 37.02 cm, meaning in a 18.83 cm range.

2.3.2 Model predictions

In this section, the best trained network's prediction capability may be investigated further. By selecting the best model, namely, having 143k training parameters and with no dropout, learning rate of 10^{-2} , and choosing 10^{-6} as the weight decay factor, and using the whole dataset, i.e., 4133 data points for the training, the final neural network is established and used for studying accuracy and performance on different case scenarios, namely, on test dataset,

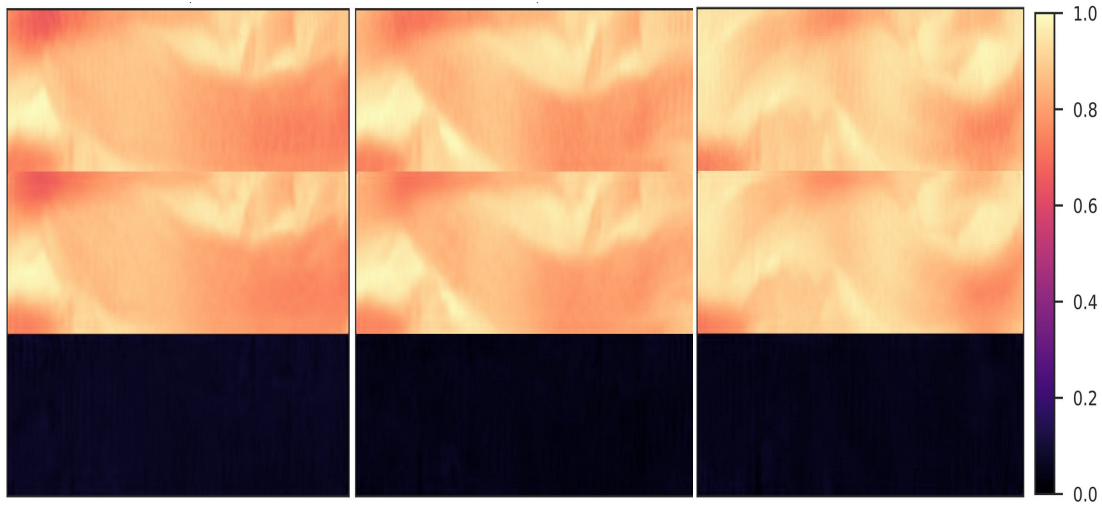


Figure 2.9: Qualitative result of the U-net: the first row is the normalized bed topography fields from the test dataset (ground truth). The second row are the images that are predicted by the U-net. The third row are the error images (ground truth - prediction).

numerical simulation, and real-world case scenarios.

Model's predictions based on experiments

A part of the dataset (460 data points) is kept for testing the neural network model's prediction power. The velocity fields in the test dataset feed into the neural network and the prediction is examined by comparing with the ground truth (experiments). The accuracy of the model is shown in Fig. 2.9 so that each column represents one of the bathymetry in the test dataset. The first row is the ground truth of the bed topography and the second row shows the predicted bathymetry, using the neural network model. The difference between aforementioned topography fields (ground truth - prediction) are presented in the third row. The mean error among all the test dataset is 0.045 cm, while the topography varies in a range of 18.8 cm.

To quantify the model's prediction further, the topography over a longitudinal axis along the flow direction is compared in Fig. 2.10 with the neural network model's predictions. The data presented in the first to third columns of Fig. 2.10 corresponds to the respective data in the first to third columns of Fig. 2.9. The longitudinal axes are located in $z = 5, 30,$ and 55 cm from the down side wall. The black and red solid lines represent the prediction and the ground-truth (experimental data), respectively. As can be seen, the curves variations are finely reproduced and values coincide very well. This allows to conclude that hyperparameters related to the training and the architecture of the neural network model are chosen properly and provide sufficient accuracy. In addition to the validation of the model based on the test dataset, the numerical simulation performed and field data measurements are used to compare with the

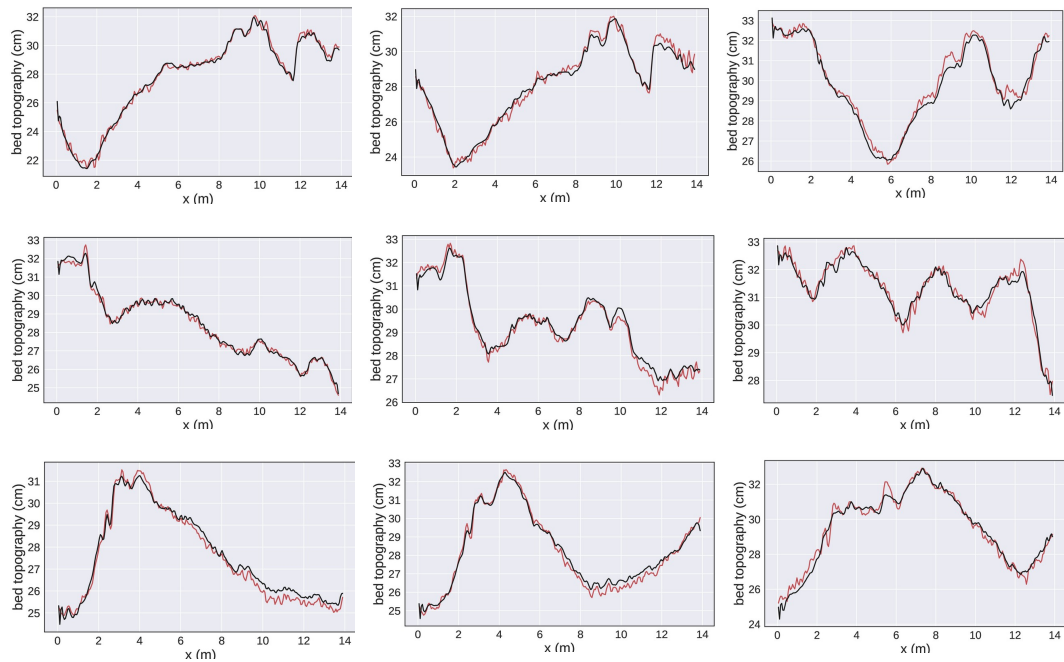


Figure 2.10: Each column belongs to one experiment. The first row is the profile of the bed topography along the channel length at $z = 5$ cm from the down wall, the second row is the profile at $z = 30$ cm, and the last row is the bed topography at $z = 55$ cm. Ground truth is shown by red and prediction by black color.

model's prediction in the next subsections.

Model's predictions based on numerical simulation

In § 2.3.2, the model was applied to the test dataset derived from experiments conducted at LHE-EPFL (Dhont, 2017), and it yielded precise predictions. Since the model is trained on the same experimental dataset - the training part of dataset -, therefore the model prediction using the test dataset in the previous subsection just shows us the model is well trained and that, if someone applied the model to gravel-bed laboratory channel, they can get very accurate results. An important question would be about the model's accuracy on the other applications. In order to further study the model's prediction power, the model will be compared with the simulation performed based on Iber - hydraulic software for the simulation of free surface flows (Bladé et al., 2014).

A gravel-bed flume is simulated based on Iber. A flume with a $Q = 15$ L/s flow discharge, 1% slope, 10 m length and 0.5 m width, using a uniform structured mesh grid with 100 elements in the flow direction and with 10 elements in the transversal direction has been simulated with final time of $t_f = 7200$ minutes. The virtual flume dimensions differ from the dimensions

Chapter 2. Bed topography inference from velocity field using deep learning

of the flume on which the model is trained (0.6 m by 14.0 m). In spite of the difference in size, the trained model can be applied to the simulation flume. Additionally, using the resize function from the OpenCV library with bicubic interpolation, the image size is increased to 256×64 elements, allowing it to be fed into the ML models. The mean particle diameter considers 7 mm in addition of using Manning coefficient of 0.025, and choosing Meyer-Peter and Müller (MP-M) as the bedload model on the software. The simulation input parameters are intentionally selected such that to be close to the input parameters of the experiments upon which the neural network is trained.

The inlet boundary condition is set to constant flow discharge and an open boundary condition for the output has been chosen. Afterwards, the velocity field and the topography at the end of simulation time i.e., $t_f = 7200$ minutes are extracted from Iber. The trained neural network model has been applied to the depth-averaged velocity field extracted from Iber and the topography prediction from the neural network model has been compared with the topography of Iber.

Top plot in Fig. 2.11 is the channel bathymetry based on numerical simulation and down plots are a comparison of the neural network prediction versus the bed profile based on Iber on a cross section at $x = 1.0$ m (left plot), and $x = 5.5$ m (right plot) from flume inlet. Figure 2.11 shows the neural network model's prediction in comparison with the ground-truth (bathymetry from Iber), in which prediction has a 25% maximum relative error. The mean absolute error in cross section $x = 1.0$ m is 0.75 cm, while at the cross section $x = 5.5$ m is 0.14 cm. However, gaining such mean absolute error is small in comparison of the range in which bathymetry changes. This validation shows that, as long as the flow and bed satisfies the mass and momentum conservation laws, the trained model is robust and accurate to predict bathymetry for gravel-bed and shallow flows. Despite finding out about the neural network model performance in laboratory experiments, and simulation, inquiring about model performance on the field data is a natural question and an intriguing subject to examine, which will be answered in the next part.

Model's predictions based on field data

Predicting the trained neural network model on the field data would be interesting to investigate. Thus, we performed model predictions on a river located in east central Illinois state in the USA. Lewis and Rhoads, 2018a, 2018b's work on confluence stream provides the velocity measurements using the acoustic Doppler velocimeter (ADV - Nortek Vectrino+) in addition to bed topography for three cross sections. Experiments were conducted at the confluence of the Kaskaskia River and Copper Slough (KRCS), positioned at $40^{\circ}04'34.1''N$, $88^{\circ}20'53.9''W$, as can be seen in Fig. 2.12. The width is about 20 meters at the confluence center and approximately 10 m downstream. ADVs mounted on a topset wading rod and placed at predetermined cross sections within the flow were used to determine the vertical velocity field. Three cross sections, denoted as A, C, and E (refer to Fig. 2.12), were measured, and these measurements were utilized in our neural network model for the purpose of inferring bathymetry. Sample volumes

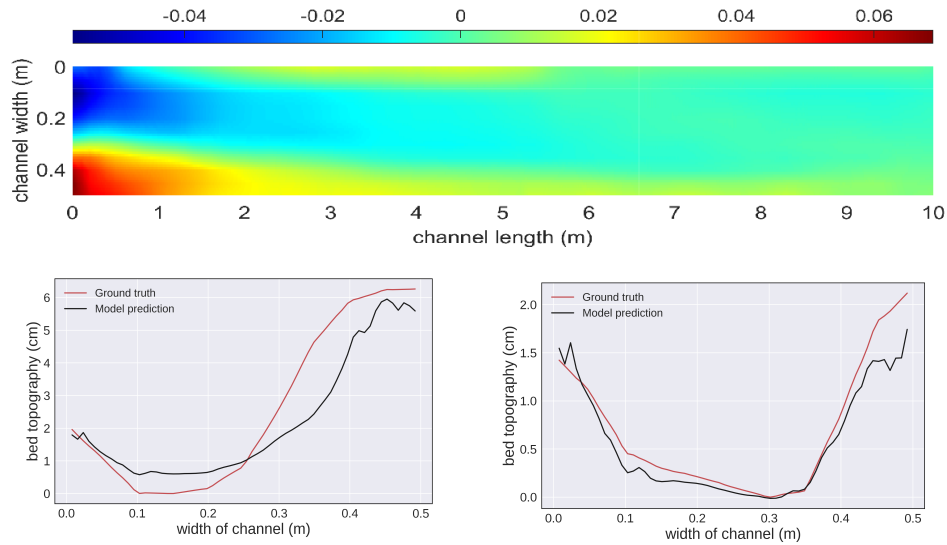


Figure 2.11: Up: Bed topography based on simulation using Iber, down: bathymetry comparison of the Iber and neural network model. The red line is the Iber topography for a cross section at $x = 1.0$ m (down-left), and $x = 5.5$ m (down-right) from flume inlet and the black line represent the neural network model's prediction.

for ADV are 0.125 cm^3 and sampling frequency is 25 Hz, and configured in laboratory mode (Lewis & Rhoads, 2018b). ADV sampling was carried out with a downward-looking probe 6 cm below the surface, to position the sampling volume as close to the surface as possible (Lewis & Rhoads, 2018a). 60 – 80 samples, 60 seconds in length are collected at three cross-sections during one measurement campaign. Cross-sectional ADV measurements were obtained the same day. All field campaigns resulted in only a few centimeters change in water surface elevation between the beginning and the end of the measurements, far less than the average flow depth (Lewis & Rhoads, 2018b). Cross-sectional velocity fields are fed into the neural network model. Given the disparities between real-world and experimental data, our approach involves model calibration (Farahani et al., 2021; Tsai et al., 2021). The neural network model, trained on an experimental dataset, establishes a mapping function denoted as f_m that connects bathymetry and velocity fields: $y = f_m(v_f)$, where v_f represents the velocity field, and y represents the bathymetry field. Due to differences between the real-world data distribution and the laboratory dataset, this mapping function is adjusted to $y = \alpha f_m(v_f)$, with α as a constant calibration parameter (Acuña et al., 2019; H. Gao et al., 2019; Yang et al., 2019). After analyzing one of the cross-sectional data, we determine the optimal value for α to be 14.5, and this value is subsequently applied to the other two cross-sectional data. The bathymetry prediction for the aforementioned cross-sections based on the calibrated neural network model are compared with the field data in Fig. 2.12's right-hand side. The ground truth (field data) is shown in red solid line while the prediction of the trained neural network model has been shown in black color.

Chapter 2. Bed topography inference from velocity field using deep learning

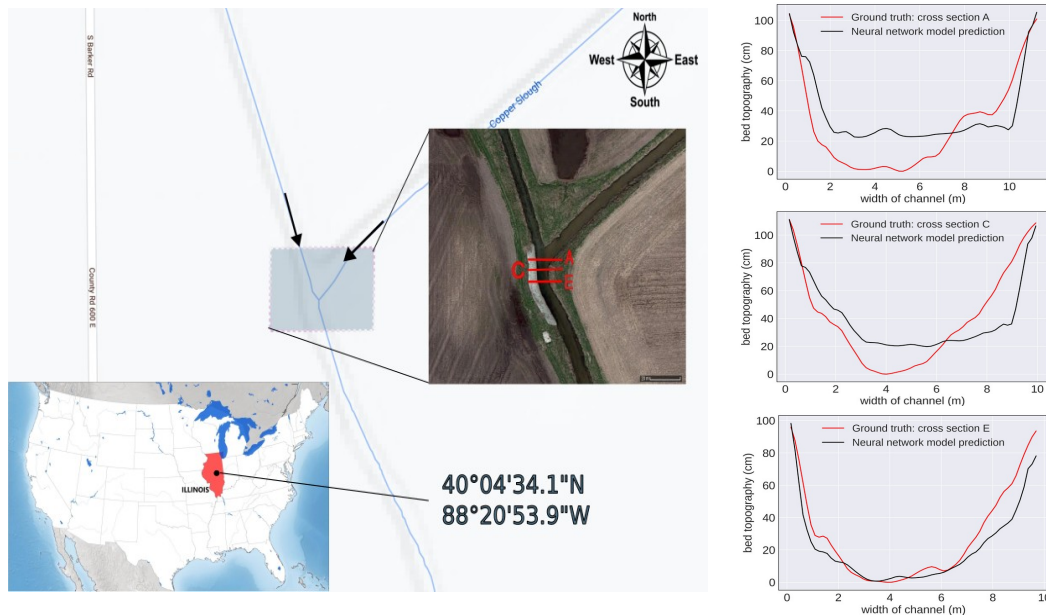


Figure 2.12: (left) Google Maps (2023). Modified map of the confluence of the Kaskaskia River with the Copper Slough, East-Central Illinois, USA. Retrieved from <https://maps.google.com/>. The arrows show flow direction. The red lines represent the cross-sections where these measurements have been conducted. (right) comparison of the neural network prediction vs the field data measurements. The red and black lines represent the field measurements and neural network model prediction, respectively.

The predictions' absolute errors in comparison with the measurements in cross section A, C, and E are 15.0, 15.6, and 6.6 cm, respectively and maximum relative errors are 31.3%, 18.5%, and 8.3%, respectively. However, the maximum relative error and the absolute error is still small compared to the approximately 100 cm depth of the river, while these errors could be decreased by adding a part of the field data to the training dataset, enhancing the number of training data, or using a more complicated model with more layers and training parameters.

2.4 Discussion

This work is concerned with imaging topography from the depth-averaged velocity field, which can be obtained more easily with a lower cost-rate than the bed topography direct measurement. The network connects velocity field and bathymetry. The U-Net is chosen for this purpose. The U-Net architecture is unique. It was first introduced for image segmentation to overcome the problem of limited training samples in the medical field – where image capturing may be expensive (Siddique et al., 2021). Its main strength is its capacity to deliver good results even with a limited number of data, thanks to its structure. Indeed, it is able to keep trace of global and local information by analyzing the image at different scales, and preserve

detailed features through skip connections (Ronneberger et al., 2015). Skip connections from the contracting path help to retain the pieces of spatial information that were lost in the contracting path, allowing the decoder layers to more accurately detect features.

According to our tests, refer to Fig. 2.7, error reduction requires an increase in training dataset, and using a more complicated convolutional neural network model such as increasing the number of feature extractions, and network layers at the cost of increased training time. Also, the relationship between model size and relative errors for a fixed number of training samples can be seen in Fig. 2.7. Notably, even with the same number of training samples, different model sizes exhibit slight variations in relative errors. However, as the volume of training data increases, the overall decrease in error remains comparable across various model sizes. When considering the smallest dataset size in Fig. 2.7, augmenting the number of training parameters results in a corresponding increase in relative error. However, this trend reverses when dealing with larger dataset sizes. Intriguingly, the model containing 2.3m training parameters achieves the best relative error of 0.5% when trained on a 4k dataset. Nevertheless, it demands substantial training time, making it less practical for certain applications. On the other hand, smaller models exhibit faster training times while still delivering reasonably accurate results, which may be sufficient for the given requirements.

In Fig. 2.9, the lower row displays the magnitudes of errors produced by the model when applied to flume experiments. These errors are relatively small in size, and their distribution across the test dataset is depicted in Fig. 2.8(b), revealing that the mean value of the errors is very close to zero. The reason for this favorable performance and relatively small error in Fig. 2.9 can be attributed to the model's application on the test dataset. Notably, the test dataset represents a portion of the same dataset that the model was originally trained on. Consequently, this effective performance on the test data indicates that the model has been well-trained and that the hyperparameters have been appropriately selected, allowing it to generalize well and produce accurate predictions when applied to the flume experiments.

The trained convolutional neural network model used the depth-averaged velocity fields, while field scientists usually measure surface velocities, for instance, by using particle image velocimetry method. Therefore, it was worth asking how much the error propagates when a field scientist feeds the surface velocity fields into the trained model in this work. The experiments (which we have used in this work to train the neural network) have been performed in a straight channel (no cross-stream secondary current), near steady state, with weak sediment transport. In these conditions, the velocity profile has been obtained by Song et al., 1994. Figure 2.13 shows the flow velocity profile for uniform flow at various bed slope $0.25 < S(\%) < 1.5$, and discharge $30 < Q(L/s) < 130$ measured by acoustic Doppler current profilers (ADVP). The log-law for the inner region ($y/h < 0.2$) is presented in red dashed line and the Coles wake law could represent the velocity profile in the outer region ($y/h > 0.2$) in a blue dot-dashed line, and the black solid line is the depth-averaged velocity profile.

As one can see, by increasing the flow depth, the depth-averaged velocity deviates from the

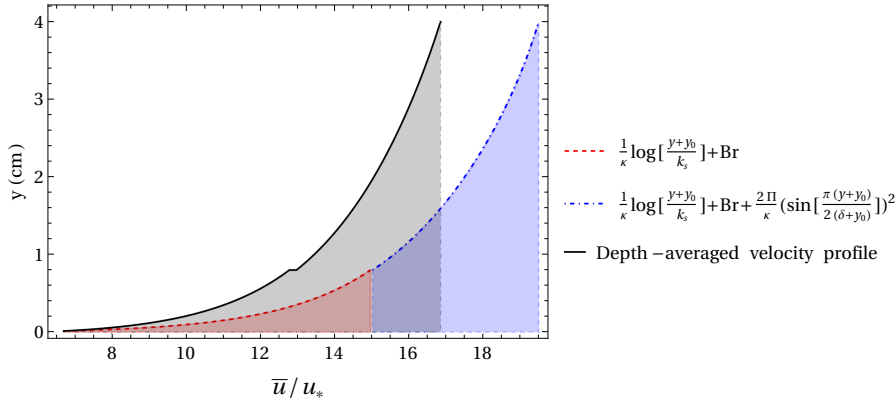


Figure 2.13: The red dashed line represents the log-law velocity profile in the inner region ($y/h < 0.2$) where \bar{u} is the point velocity averaged for different experiments, u_* is the shear velocity, y is distance from the top of the sediments, $y_0 = 0.2k_s$ is viscous sublayer, k_s is roughness height which is equal to d_{50} , and $Br=8.44$ is integration constant. The blue dot-dashed line is the velocity profile in the outer region ($y/h > 0.2$) where κ is Von Karman's constant, $\Pi = 0.108$ is the wake strength parameter, and δ is the distance between the bed and the point where maximum velocity occurs, here it is equal to h .

velocity profile, and the maximum relative error happens on the surface flow, with a 16.8% magnitude. In order to know how this error was propagated in the model prediction, we have applied the trained convolutional neural network model to the surface velocity of field data and gained a 31.3% maximum relative error based on Fig. 2.12. Therefore, however, the training of the neural network model is based on depth-averaged velocity fields but it is possible to use surface velocity to infer bathymetry while accepting several dozen percentage of relative error. A potential source of error originates from the lateral velocity: in the trained model, the lateral velocity is virtually zero compared to what we observed in real-world scenarios. However, we believe that this issue does not prevent us from applying the model to the real-world rivers.

Another concern about this work was about the amount of data needed to suffice for training the neural network. A test on the dataset size in Fig. 2.5(b) shows that 4133 data points was enough for this work's purpose, since the error does not significantly decrease after a 2500 dataset size. However, having 31.3% maximum relative error when the model applied to real rivers is good enough for real-world applications, however further accuracy is possible using a more complicated model (then training time increases and needs more datapoints in order to avoid overfitting) but whether it is necessary or not depends on application of the model. The proposed neural network model trained on 4133 experimental dataset applied to the flume experiments in Fig. 2.10 and Fig. 2.9, on the numerical simulation in Fig. 2.11, and field measurements on a river in Illinois state, USA in Fig. 2.12 and all the comparison, show an acceptable accurate prediction of the model, meaning that the model is trained properly and can be used for academic/industrial applications.

The closer the conditions are to those under which the dataset was collected, the more precise

the predictions become. For instance, when deep learning models are applied to a subset of the experimental data in § 2.3.2, the accuracy of predictions is noticeably higher. Conversely, if the flow conditions diverge from the conditions which the dataset was collected, like when applied to real-world river data in § 2.3.2, the predictions become less accurate. In this section, the model is applied to the following range of hydraulic values (where the model's prediction relative error reached several dozen percentage): the average depth of the upstream tributaries measured 51 cm, while their average speed measured 0.31 m/s. Consequently, the model usage is recommended for the aforementioned flow conditions e.g., shallow flows over gravel-bed conditions. This empirical observation explains why the simulation input parameters presented in § 2.3.2, were chosen to closely match the experimental conditions used to train the neural network.

2.5 Conclusion

We applied the U-net with alternating convolutional layers to encode the velocity field (which was here estimated using a statistical method), followed by alternating convolutional and upsampling layers to decode them and a final convolutional layer with Leaky Relu activation to infer the bed topography. The model contains skip connections, which improves training efficiency. This network has a skipping layer, which allows the decoding part of the network to have additional information about the encoding without losing any information. The final neural network has been established according to the tests performed in order to find out the best parameters, 143k trainable parameters with no dropout, learning rate of 10^{-2} , and choosing 10^{-6} as the weight decay factor, and using the whole dataset i.e., 4133 data points for the training. The network is summarized in Appendix A.

The trained model does not require solving the shallow water equations numerically. It constructs the solution (bathymetry) by just looking at the input data (velocity fields). Overall, after studying the basic and hyperparameters, and training a neural network model, we have found the best model yields a good accuracy (its less than 1% relative error for estimated bathymetry) when working on the test dataset (laboratory experiments), less than 20% maximum relative error when applying the model to the numerical simulations (using Iber), and with a maximum 31.3% relative error by applying the model to field data (confluence of Kaskaskia River with the Copper Slough).

This work shows the possibility of using the U-net architecture for predicting the bathymetry from the velocity field and provides a user-friendly tool for whoever has the velocity field and is interested in deducing the bed topography. The user needs to be aware that this is not a general model for every kind of flume or rivers. This work is based on gravel-bed flume/river and therefore the model provides accurate bathymetry for gravel-bed rivers. The strength of the proposed model is that it is trained on experimental data and the neural network model avoids solving the partial differential equations that governs the flow, and the bed and gives quick access to the bed topography.

3 Simulation of antidune migration in straight channel

Mehrdad Kiani-Oshtorjani ¹ and Christophe Ancey ¹

¹ Environmental Hydraulics Laboratory, École Polytechnique Fédérale de Lausanne, 1015 Lausanne, Switzerland

In preparation for publication.

Doctoral candidate's contribution

The candidate performed the entire implementation, analysis, and figures for this chapter. Part of this chapter comes from additions made by Prof. Ancey to the candidate's initial text.

Abstract

There is growing evidence that bedload transport is driven by noise (i.e., large fluctuations in the number and velocity of moving particles) for a wide range of flow conditions. Capturing the full dynamics of bedload transport requires specific computational hydraulic models. In this paper, we have tested a model based on a set of deterministic equations (the shallow water equations supplemented with the Exner equation) for water and continuity of the bed and a stochastic equation for bedload transport. The set of governing equations was solved numerically using a Riemann solver-based method to study bedload transport and bedform development in a narrow gravel-bed flume with high Froude numbers. To assess the predictive ability of the model, laboratory experiments (super-critical flows over a gravel-bed exhibiting antidunes) were used and have been compared with the numerical results. The resulting bedload time series have been found a maximum relative error as high as -258% for the mean bedload transport. In agreement with experiments, we found that bedforms migrate upstream. The relative errors for the antidune wavelength and amplitude were -41%, and -91.5%, respectively, and observed a good match between measured, and computed antidune celerity.

3.1 Introduction

Like in turbulence, bedload fluctuations have long been ignored in hydraulic studies, as if average quantities were sufficient to describe the flow dynamics, but there is growing evidence that they play a key role (D. Liu et al., 2016; Shih et al., 2017; A. Singh et al., 2010). The motion of individual particles experiences random movements, which could be considered the source of randomness in the system, even in steady-state conditions, resulting in strong fluctuations in bedload flux due to the complex interactions between particles-fluid and particles-particles (Benavides et al., 2022). The bedload fluctuations bring stochastic behaviors at both the grain-scale, such as drag force random fluctuations (Paintal, 1971a; Valyrakis et al., 2013), and macroscopic scale, e.g., bed morphology (Warburton & Davies, 1994).

Although bedload transport rate fluctuations are observable over a wide range of spatial and temporal scales (Paintal, 1971b), most researchers have ignored those fluctuations and focused on the averaged bedload transport rate. By ignoring the stochastic nature of bedload transport, one can easily miss the point that, similar to Reynolds stress in turbulence, bedload transport rate fluctuations create special features on the bulk scale that cannot be simply described without a proper accounting of the role played by fluctuations. For instance, bedload transport rate may be modulated by diffusive effects (Ancey et al., 2015; Charru et al., 2004; Furbish et al., 2017).

The turbulent fluctuations and bed topography variations generate randomly varying bedload fluxes that fluctuate three to four times more than their average value while having constant controlling variables such as constant flow discharge (Warburton & Davies, 1994). That means bedload transport modeling requires being treated as a stochastic problem, despite using averaged characteristics, such as the averaged Shields number, in traditional bedload modeling. Otherwise, the accuracy of the numerical results will be undermined. The latter approach - deterministic equations - estimates the sediment volume transport for a favorable case study - fully mobile and high Shields number - with more than 200% error (Recking et al., 2012), while non-capacity bedload models by considering the temporal and spatial delay of sediment movements (Ancey et al., 2008; Giri & Shimizu, 2006; Nakagawa & Tsujimoto, 1980) derived based on Markov process framework may improve the accuracy because of the local definition of the deposition and entrainment rates (Bohorquez & Ancey, 2015, 2016).

When studying such systems—flow over an erodible bed—we need specific tools for extracting statistical information characterizing them. This makes it possible to compare how distinct systems respond to a given input. The reason lies in the stochastic nature of the system. For instance, several identical experimental configurations, or alternatively, replication of one experiment, could lead to different bedload transport time series and bed morphology after a certain amount of time while having the same statistical characteristics, e.g., average bedload time series, slope, braiding, and sinuosity indexes, and bar area (Ashmore, 1988; Warburton & Davies, 1994; Young, 1989). In Warburton and Davies, 1994 experiments, eleven repetitions of the same experiment with identical initial and boundary conditions led to various bed

topographies and bedload transport time series. Although, in their study, the turbulence fluctuations and irregularity in bed topography strongly influenced sediment dynamics and consequently the bedload transport, and bedform statistical characteristics gently fluctuate around an averaged value under steady-state flow conditions (Dhont & Ancey, 2018).

To incorporate the effects of fluctuations in the bedload formulation, an attempt has been made in recent years by Ancey and Heyman, 2014 to describe the mechanics of flow over a movable bed from a stochastic point of view. They have taken a collective entrainment rate into account to generate non-Gaussian fluctuations. In addition, they introduced white noise in bedload formulation derivation through the jump Markov process framework. This approach ended up with a stochastic formulation of the bedload transport by calculating the variation of the active particle number in a given control volume at each time step. To assess the predictive capacity of the stochastic bedload model, it is essential to couple it with the governing equations for the flow phase, which include the Saint-Venant equations and continuity of the bed, i.e., the Exner equation.

In this work, we study bedform development along with bedload transport rate in narrow gravel-bed flume under a supercritical flow regime by means of numerical simulations. The numerical solver is based on Saint-Venant–Exner equations coupled with the stochastic bedload model. The numerical studies focus on three aspects, namely, i. the rate of bedload transport, ii. the amplitude and wavelength of the antidunes, and iii. their migration velocity. The numerical predictions examined by applying the solver to laboratory experiments from Pascal et al., 2021; Recking et al., 2009. In advance of conducting a numerical simulation, we need to parameterize the mass exchange rates. There are three mass exchange rates in the stochastic bedload model. To this end, we proposed closure relations to parameterize the particle exchange rates. Then, these closure relations are used to solve the governing equations when reproducing the experiments.

The set of governing equations, consisting of four equations, is non-homogeneous. Following the fractional-step method proposed by Toro, 2013, this non-homogeneous system of equations could be split into two sets of equations, namely, a hyperbolic and a parabolic subproblem. Afterwards, each set could be separately solved at each time step. The hyperbolic subproblem is solved by the q -wave propagation algorithm (Ketcheson et al., 2013), and the parabolic subproblem by the Crank-Nicholson algorithm.

This work is structured as follows: the theoretical background, including the governing equations, the stochastic/deterministic bedload model, and the parametrization of the entrainment and deposition terms are explained in § 3.2. The architecture of the numerical model and methodology to solve them are explained in § 3.3. § 3.4 outlines the experimental dataset, which will be utilized for comparison and reproduced by the numerical solver to demonstrate the prediction power of the stochastic and deterministic models with a focus on bedload transport time series, wavelength, amplitude, and migration celerity of the antidunes. Lastly, this work is discussed in § 3.5 and concluded in § 3.6.

3.2 Theoretical model

3.2.1 Saint-Venant–Exner equations

We consider one-dimensional flows over a smooth topography $y = y_b(x, t)$, where x and y denote the coordinates in the horizontal and vertical directions, respectively, and t is time. We use the Saint-Venant–Exner equations to model the bed's morphodynamical evolution and the stream dynamics (N. J. Balmforth & Provenzale, 2001; Cunge & Perdreau, 1973; Cunge et al., 1980)

$$\frac{\partial h}{\partial t} + \frac{\partial h\bar{u}}{\partial x} = 0 \quad (3.1)$$

$$\frac{\partial h\bar{u}}{\partial t} + \frac{\partial h\bar{u}^2}{\partial x} + gh\frac{\partial h}{\partial x} = -gh\frac{\partial y_b}{\partial x} + \frac{\partial}{\partial x} \left(\nu_t h \frac{\partial \bar{u}}{\partial x} \right) - \frac{\tau_b}{\rho} \quad (3.2)$$

$$(1 - \zeta_p) \frac{\partial y_b}{\partial t} = \mathcal{D} - \mathcal{E} = -\frac{\partial \bar{q}_s}{\partial x} \quad (3.3)$$

where $\bar{u}(x, t)$ is the depth-averaged velocity, $h(x, t) = y_s(x, t) - y_b(x, t)$ is the flow depth defined as the distance between the free surface and bed, and $y_s(x, t)$ is the free surface's position. The eddy viscosity is denoted by ν_t , $g = 9.81 \text{ m}^2/\text{s}$ stands for the gravity acceleration, ρ is the water density, τ_b is the bottom shear stress, ζ_p is the bed porosity (as we will study beds made of well sorted gravel, we will set $\zeta_p = 0.36$ in the following), and \bar{q}_s is the bedload transport rate. The deposition and entrainment rates are denoted by \mathcal{D} and \mathcal{E} , respectively.

We followed Kranenburg, 1992 and included diffusion in the momentum equation, which accounts for local changes in the velocity profile in the presence of strong flow-depth gradients. It has been shown that this diffusive term is essential to properly describing the flow dynamics in supercritical flows by limiting the development of short-wavelength instabilities, making the flow-depth profile more consistent with experimental observations, and smoothing discontinuities (N. J. Balmforth & Provenzale, 2001; N. Balmforth et al., 2004; Bohorquez et al., 2019; Kranenburg, 1992; Needham & Merkin, 1984). This diffusive term has been justified by Rastogi and Rodi, 1978, who supplemented the Saint-Venant equations (Eq. 3.1 and Eq. 3.2) with depth-averaged equations for the turbulent kinetic energy and its dissipation rate. For supercritical flows (with Froude numbers exceeding 2), Z. Cao et al., 2015 showed that Rastogi and Rodi's model led to eddy-viscosity values that were too low, and thus, based on empirical grounds, they suggested adding a Boussinesq-like eddy viscosity to Rastogi and Rodi's estimate of the turbulent viscosity

$$\nu_t = c_v h u_* \quad \text{with} \quad u_* = \sqrt{\frac{\tau_b}{\rho}} \quad (3.4)$$

where the dimensionless parameter c_v was found to increase from 0 to 16 when the Froude number was increased from 2 to 6 (Z. Cao et al., 2015), and u_* is the friction velocity. Here, we

used the minimum values suggested by Bohorquez and Ancey, 2015 and set $c_v = 4$.

We used the Darcy–Weisbach equation to model flow resistance

$$\tau_b = \frac{f}{8} \rho \bar{u}^2 \quad (3.5)$$

where the Darcy–Weisbach friction coefficient was computed using Keulegan’s equation

$$\sqrt{\frac{8}{f}} = 6.25 + 5.75 \log \frac{h}{k_s} \quad (3.6)$$

where k_s denotes the bed roughness size. Various values have been proposed for gravel-bed rivers (López & Barragán, 2008). Here, following Pitlick, 1992, we set

$$k_s = 3d_{84} \quad (3.7)$$

where d_{84} is the particle size quantile such that 84% of the grains are finer than d_{84} . Flow resistance is affected by bedload transport and bedforms (Recking et al., 2008b; Van Rijn, 1984b). As we studied supercritical flows over antidunes, we considered that the flow depth profiles were in phase with bed undulations, and therefore bedforms did not increase flow resistance significantly. For the ranges of flow depth and bed slope explored in this paper, bedload transport can increase the Darcy–Weisbach friction coefficient by a factor of 1.5 (Recking et al., 2008b). It is possible to take this increased flow resistance by increasing the bed roughness (Recking et al., 2008b), but as a first approximation, we decided to ignore the influence of bedload transport on f .

Until now, we have used quite consensual elements to close the momentum balance equation Eq. 3.2. The Exner equation gives more scope to explore how effectively some assumptions about bedload transport help to predict the stream’s morphodynamic evolution. Our analysis will have two threads: first, we will investigate the stochastic bedload transport model proposed by Ancey and Heyman, 2014, which allows us to compute the entrainment and deposition rates \mathcal{E} and \mathcal{D} . We will outline this model in the next subsection.

As the model parameters were calibrated only for a finite set of experiments, we will study in §3.2.3 how we can relate these parameters quite generally to flow conditions. Second, we will use an empirical bedload transport equation that is routinely used in the majority of morphodynamical models: using flume data, Meyer-Peter and Müller, 1948 (MP-M) proposed an equation that is today often written (in the absence of sidewall effect) in the dimensionless form (Wong & Parker, 2006b)

$$\Phi = \frac{\bar{q}_s}{\sqrt{sgd_{50}^3}} = 8(\tau^* - \tau_c^*)^{3/2} \quad (3.8)$$

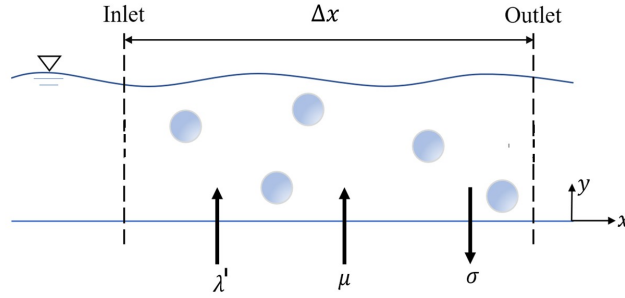


Figure 3.1: Illustration of the processes involve in sediment exchanges: λ' , μ and σ are particle entrainment, collective entrainment and deposition exchange rates, respectively.

where Φ denotes the dimensionless bedload transport rate, $\tau^* = \tau_b / (\Delta\rho g d_{50})$ is the Shields stress (dimensionless bottom shear stress), $\tau_c^* = 0.047$ is the critical threshold of incipient motion, $\Delta\rho = \rho_s - \rho$ is the density difference between sediment and water, $s = \Delta\rho / \rho$ is the scaled density difference, and d_{50} is the median particle diameter. Empirical bedload transport equations such as Eq. 3.8 posit that bedload transport is at equilibrium with the water stream and at full transport capacity (Wainwright et al., 2015; Wu & Wang, 2007), which makes it possible to relate transport rates and water discharges in an univocal way. By contrast, models based on entrainment and deposition rates do not assume a one-to-one relationship between transport rates and water discharge. They are sometimes referred to as non-equilibrium models (this naming may be ambiguous insofar as equilibrium can be understood quite differently depending on the person).

3.2.2 Stochastic bedload transport model

In an attempt to provide a consistent theoretical framework for computing the number of moving particles in a given control volume, Ancy et al., 2008 suggested regarding bedload transport as a Markov counting process. The model principle is simple: one counts the number $N(t)$ of particles that enter or leave the control volume and are deposited or entrained from the bed in this volume over short time steps δt . This counting process is said to be Markovian when what happens at time t depends only on the immediate history $t - \delta t$, and not on past events (there is no memory effect). This assumption (valid at low transport rates) makes it possible to use the arsenal of statistical methods developed for Markov processes. Ancy and Heyman, 2014 then derived the continuum version of this model, where the number N of moving particles in the control volume is replaced with the particle activity γ , which defines the volume of moving particles per streambed area.

The fundamental idea is that entrainment and deposition rates \mathcal{E} and \mathcal{D} are functions of the flow conditions, represented by the Shields stress τ^* , and particle activity. As γ is small, we

can expand these rates into a power series of γ

$$\mathcal{E}(\tau^*, \gamma) = \mathcal{E}_0(\tau^*) + \mathcal{E}_1(\tau^*)\gamma + \dots \quad (3.9)$$

$$\mathcal{D}(\tau^*, \gamma) = \mathcal{D}_0(\tau^*) + \mathcal{D}_1(\tau^*)\gamma + \dots \quad (3.10)$$

where \mathcal{E}_i and \mathcal{D}_i ($i = 1, 2, \dots$) are functions of the Shields stress τ^* alone. As deposition is necessarily dependent on the number of moving particles, the first coefficient is 0: $\mathcal{D}_0 = 0$. A first-order expansion is usually sufficient to capture the statistical behavior of particle entrainment and deposition (Ancey & Pascal, 2020; Ancey et al., 2008). To be consistent with earlier publications, we introduce λ (volumetric entrainment rate), μ (collective entrainment rate), σ (deposition rate), and κ (difference of deposition and collective rate)

$$\mathcal{E}_0 = \lambda, \mathcal{E}_1 = \mu, \mathcal{D}_1 = \sigma, \text{ and } \kappa = \sigma - \mu$$

The results obtained by Ancey et al., 2008 on a single control volume can be generalized to an array of adjacent control volumes of length Δx as shown in Fig. 3.1. The counting process is applied to each control volume separately. Assuming that particles move randomly with mean velocity \bar{u}_s and diffusivity D_u (the exact probability distribution is not essential in a first approximation), Ancey et al., 2015 found that in the continuum limit of $\Delta x \rightarrow 0$, the time and space variations in the ensemble-averaged particle activity $\langle \gamma \rangle$ can be described using an advection diffusion equation

$$\frac{\partial \langle \gamma \rangle}{\partial t} + \frac{\partial}{\partial x}(\bar{u}_s \langle \gamma \rangle) = \lambda - \kappa \langle \gamma \rangle + \frac{\partial^2}{\partial x^2}(D_u \langle \gamma \rangle) \quad (3.11)$$

where particle diffusivity is defined as

$$D = D_u \left(1 + \frac{1}{2} \text{Pe} \right) \text{ where } \text{Pe} = \frac{\bar{u}_s \Delta x}{D_u} \quad (3.12)$$

is the Péclet number.

Two remarks about this equation are in order. First, we note that in the continuum limit of $\Delta x \rightarrow 0$, the Péclet number drops to zero and Eq. 3.11 looks like any advection diffusion equation, but in many practical situations (for instance, when running experiments in a flume and observing bedload in a given area, or discretizing Eq. 3.11 using finite-volume techniques), the Péclet number is nonzero, and thus there is additional diffusion, whose strength is proportional to Δx and which reflects long-range spatial correlation in the particle flux (Ancey et al., 2015). This scale-dependent diffusion is a peculiarity of the model, which is

Chapter 3. Simulation of antidune migration in straight channel

not met in classic diffusion models such as Brownian motion (Ancey et al., 2015).

Second, this equation involves the ensemble-average particle activity $\langle \gamma \rangle$, that is, the statistical average of γ over an infinite set of realizations subject to the same initial and boundary conditions. In this context, the governing equations—the set of equations made of the Saint-Venant–Exner equations (Eq. 3.1–Eq. 3.3) supplemented with the definitions of the entrainment and depositions (Eq. 3.9 and Eq. 3.10) and the advection diffusion equation, Eq. 3.11—are fully deterministic even though Eq. 3.11 was obtained from a stochastic model.

It is possible to work on particular realizations, and not only on the ensemble average of particle activity, when interested in the statistical behavior of particle activity. In that case, one has to solve a generalized Langevin equation for the variable $b(x, t)$ (interpreted below)

$$\frac{\partial b}{\partial t} = \frac{\partial^2 (D_u b)}{\partial x^2} - \frac{\partial (b \bar{u}_s)}{\partial x} + \tilde{\lambda} - \kappa b + \sqrt{2\mu b} \xi_b \quad (3.13)$$

where $\tilde{\lambda} = \lambda/\omega_p$ is the entrainment rate in particules per second and per unit width, ω_p is the particle volume per unit width, and ξ_b denotes the Gaussian noise term $\xi_b(x, t)$ which satisfies

$$\lim_{\Delta x \rightarrow 0} \frac{dW(t)}{\sqrt{\Delta x}} = \xi_b(x, t) dt \quad (3.14)$$

where W denotes the Wiener process. This definition of $\xi_b(x, t)$ is needed to properly encode in numerical simulations. The white noise in Eq. 3.13 is uncorrelated in time and space such that $\langle \xi_b(x, t) \xi_b(x', t') \rangle = \delta_x(x - x') \delta_t(t - t')$, where δ_x and δ_t are Kronecker's deltas (Ancey et al., 2015).

The random variable $b(x, t)$ is called the Poisson rate density (Ancey et al., 2015; Gardiner, 1983). It can be interpreted as follows: Like any random variable, it is characterized by its probability density function $f_b(b, t)$, and we use this density function to compute the number of moving particles. To that end, we can show that the probability $P(n, t)$ of observing n particles at time t in a control volume of length Δx is related to $f_b(b, t)$ by the following expression called the Poisson representation (Gardiner, 1983)

$$P(n, t) = \int_0^\infty \frac{e^{-b\Delta x} (b\Delta x)^n}{n!} f_b(b, t) db \quad (3.15)$$

In short, using the Poisson rate density b makes it possible to work with continuous random variables rather than discrete ones, which is a decisive advantage when deriving a continuum

model in which all variables are supposed to be continuous. We refer the reader to Appendix B, where we performed sensitivity analysis on the mesh length Δx .

The Poisson representation Eq. 3.15 has a particularly interesting property: although the random variable n is expressed as the integral Eq. 3.15 over all possible b values, its moments are a simple linear combination of b moments. For instance, we have the following relationships (which were used to derive Eq. 3.11 from Eq. 3.13)

$$\langle n \rangle = \Delta x \langle b \rangle \text{ and } \text{var } n = \text{var}(b \Delta x) + \Delta x \langle b \rangle$$

Equivalently, if we use particle activity $\gamma = \omega_p n / \Delta x$ instead of the number of particles, we have

$$\langle \gamma \rangle = \omega_p \langle b \rangle \text{ and } \text{var } \gamma = \omega_p^2 \text{var } b + \frac{\omega_p}{\Delta x} \langle b \rangle \quad (3.16)$$

Here we summarize the two possibilities offered by the computational framework proposed by Ancy et al., 2015. In both cases, the governing equations are made of the Saint-Venant–Exner equations (Eq. 3.1–Eq. 3.3), where the entrainment and deposition rates (Eq. 3.9 and Eq. 3.10) are linear functions of particle activity γ . What differs is the nature of γ .

- If we are interested in fully characterizing the stochastic fluctuations of bedload transport, then we have to solve the generalized Langevin equation, Eq. 3.13, for the Poisson density b . The particle activity γ is a random variable, which can be related to b . There is no simple method for relating their probability density functions, but it is easy to simulate realizations of b and γ . Let us assume that we have discretized the governing equations Eq. 3.1–Eq. 3.3 supplemented by the Langevin equation, Eq. 3.13. Let us assume that for a given mesh cell i at time t , we have obtained the value b_i , then the probability of observing particles in this cell is given by the Poisson representation, Eq. 3.15, conditioned by our knowledge of b_i

$$\begin{aligned} P(n, t | b_i, t) &= \int_0^\infty \frac{e^{-b \Delta x} (b \Delta x)^n}{n!} f_b(b, t) \delta(b - b_i) db \\ &= \frac{e^{-b_i \Delta x} (b_i \Delta x)^n}{n!} \end{aligned} \quad (3.17)$$

To determine the particle activity, we just have to draw a random integer n_i from the Poisson distribution, Eq. 3.17, and then set $\gamma_i = \omega_p n_i / \Delta x$. When γ is a random variable, then the source term in the Exner equation, Eq. 3.3, is noised, and thus, in turn, all the variables (h , \bar{u} , y_b) in the governing equations, Eq. 3.1–Eq. 3.3, are random variables even though there is no randomness source in these equations.

- If we are interested in the mean behavior of bedload transport, then we can use the relationships between the moments of b and γ . We have to solve the advection diffu-

sion equation, Eq. 3.11, for the ensemble-average particle activity $\langle\gamma\rangle$. The governing equations are fully deterministic in that case.

3.2.3 Model calibration

The stochastic model involves five parameters: the mean particle velocity \bar{u}_s , particle diffusivity D_u (related to velocity fluctuations), entrainment rates λ and μ , and deposition rate σ . Apart from some specific values obtained for a finite set of experiments (Ancey & Pascal, 2020; Ancey et al., 2008; Heyman et al., 2013, 2016), little is known about the dependence of the model parameters on flow conditions. Here we propose a model calibration based on existing data.

In narrow laboratory flumes (such as the ones used in the model validation in § 3.4), the mean particle velocity \bar{u}_s is often related to the depth-averaged velocity \bar{u} or friction velocity u_* through a dimensionless parameter β

$$\bar{u}_s = \beta \bar{u} \quad (3.18)$$

where β shows weak dependence on the flow conditions. Typically, $\beta \sim 0.5 - 0.6$ is a reasonable approximation (Ancey et al., 2003; Böhm et al., 2004; Chatanantavet et al., 2013; Heyman et al., 2016). Authors such as Auel et al., 2017 and Demiral et al., 2022 preferred to relate the mean particle velocity to friction velocity: $\bar{u}_s = \beta u_*$ with $\beta \sim 20$. In supercritical flows in narrow flumes, particle acceleration is often low, reaching less than 10% of the gravitational acceleration (Heyman et al., 2016), and thus velocity fluctuations are usually low under such flow conditions. For the sake of simplicity, we will use Eq. 3.18 with $\beta = 0.5$ and $D_u = 0$.

Charru et al., 2004 suggested expressing the deposition rate \mathcal{D} as

$$\mathcal{D} = \sigma \gamma = \frac{\langle\gamma\rangle}{t_d} \quad (3.19)$$

where t_d is a characteristic time of deposition for a particle of diameter d

$$t_d = \frac{d}{c_d w_s} \quad (3.20)$$

where w_s is the particle settling velocity and c_d is the deposition factor. Lajeunesse et al., 2010 found that Eq. 3.19 with $c_d = 0.09$ fitted reasonably well their deposition data. When using the data obtained by Ancey et al., 2008 and Ancey and Pascal, 2020, we found that Charru's Eq. 3.19 captured the deposition rates to within 20% when the deposition factor c_d was set at 0.06. Therefore, we will use the value $c_d = 0.06$ in the following. We will use the empirical equation developed by Dietrich, 1982. Dietrich, 1982 proposed an empirical equation for

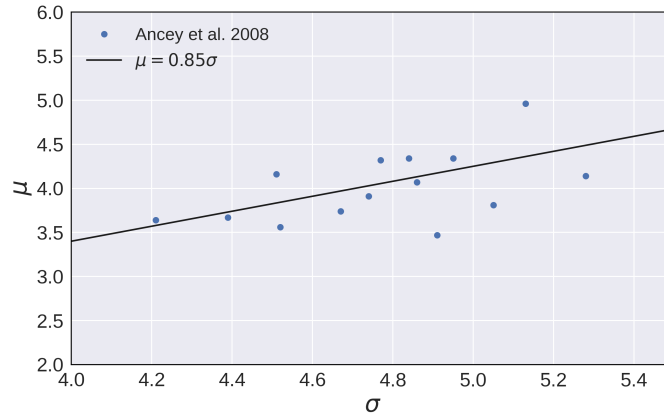


Figure 3.2: Partial experimental data available from Ancey et al., 2008 to relate the collective entrainment to deposition rate with $\mu = 0.85\sigma$.

the settling velocity w_s of spherical particles of diameter d in a Newtonian fluid of kinematic viscosity ν

$$w_s = \left(\frac{\Delta\rho}{\rho} g\nu \right)^{1/3} F^{1/3}(d^*) \text{ with } d^* = \frac{\Delta\rho}{\rho} \frac{gd^3}{\nu^2} = R^2 \quad (3.21)$$

and

$$10^5 \log F = -376715 + 192944 \log d^* - 9815 \log^2 d^* - 575 \log^3 d^* + 56 \log^4 d^* \quad (3.22)$$

where \log gives the logarithm with base 10. The settling velocity as a function of the particle Reynolds number R

$$R = \frac{\sqrt{sgd_{50}^3}}{\nu} \quad (3.23)$$

where ν is the kinematic viscosity of water.

Ancey et al., 2008 found a weak μ dependence on the flow conditions, and on average, μ is closely related the deposition rate σ as can be seen in Fig. 3.2

$$\mu = 0.85\sigma \quad (3.24)$$

Chapter 3. Simulation of antidune migration in straight channel

Substituting Eq. 3.19 into Eq. 3.24, we obtain

$$\mu = 0.85\sigma = 0.85c_d \frac{w_s}{d_{50}} \quad (3.25)$$

This relation implies that the factor κ

$$\kappa = \sigma - \mu = 0.15c_d \frac{w_s}{d_{50}} \quad (3.26)$$

The last parameter, the entrainment rate λ , can be estimated using the mean bedload transport rate \bar{q}_s in the absence of particle diffusion. In that case, Ancy and Heyman, 2014 defined it as

$$\bar{q}_s = \bar{u}_s \langle \gamma \rangle \quad (3.27)$$

Under steady-state conditions, deposition matches entrainment ($\mathcal{D} = \mathcal{E}$), and thus particle activity reaches the steady-state value

$$\langle \gamma \rangle_{ss} = \frac{\lambda}{\sigma - \mu} \quad (3.28)$$

Combining Eq. 3.27 and Eq. 3.28 leads to the desired relation between λ and \bar{q}_s

$$\lambda = \frac{\sigma - \mu}{\bar{u}_s} \bar{q}_s \quad (3.29)$$

Using the dimensionless transport rate $\bar{\Phi}$ ($\bar{q}_s = \sqrt{sgd_{50}^3 \bar{\Phi}}$), the mean particle velocity equation, Eq. 3.18, Darcy–Weisbach friction coefficient $f = 8(u_* / \bar{u})^2$, and Eq. 3.26, we can express the entrainment rate λ as a function of $\bar{\Phi}(\tau^*)$

$$\lambda = \frac{\kappa d_{50}}{\beta} \sqrt{\frac{f}{8}} \frac{\bar{\Phi}(\tau^*)}{\sqrt{\tau^*}} \quad (3.30)$$

This equation shows that the entrainment rate is mainly controlled by the bottom shear stress.

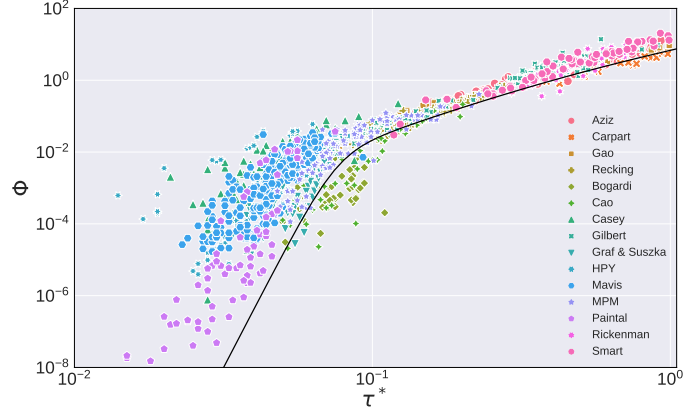


Figure 3.3: Equation 3.31 fit on experimental dataset from Aziz and Scott, 1989; Bogardi and Yen, 1938; H. H. Cao, 1985; Capart and Fraccarollo, 2011; Casey, 1935; P. Gao, 2008; Gilbert and Murphy, 1914; W. H. Graf, 1987; Ho, 1939; Mavis et al., 1935; Meyer-Peter and Müller, 1948; Paintal, 1971a; Recking et al., 2008a; Rickenmann, 1990; Smart, 1984.

If we assume that Φ scales as $\tau^{*3/2}$ at sufficiently high shear stress—like in the Meyer-Peter–Müller equation, Eq. 3.8—, then $\lambda \propto \tau^*$, a linear relation which is roughly confirmed by experiments (Heyman et al., 2016; Lajeunesse et al., 2010).

To close Eq. 3.30, we need a parametrisation of $\Phi(\tau^*)$. Using a large set of laboratory flume data and revisiting Bagnold’s theory, Ancey and Recking, 2023 obtained the following scaling law for dimensionless bedload transport

$$\Phi = (10\tau^*)^{16} \left(1 + \left(\frac{\tau^*}{\tau_1^*} \right)^{3/2} \right)^{-8/9} \left(1 + \left(\frac{\tau^*}{\tau_0^*} \right)^8 \right)^{-13/8} \quad (3.31)$$

where $\tau_0^* = 0.078$ and $\tau_1^* = 0.40$ are the lower and upper limits of the domain named transitional regime by Bagnold, 1966. This equation summarizes three scaling (Ancey & Recking, 2023)

$$\Phi = \begin{cases} \propto \tau^{*16} & \text{No-transport regime (rarefied transport regime)} & \text{if } \tau^* < \tau_0^* \\ \propto \tau^{*3} & \text{Transitional regime (kinetic regime)} & \text{if } \tau_0^* \leq \tau^* < \tau_1^* \\ \propto \tau^{*5/3} & \text{High-transport regime (sheet-flow regime)} & \text{if } \tau^* \geq \tau_1^* \end{cases}$$

The stochastic model developed by Ancey et al., 2015 is valid for low transport rates, thus typically for $\tau^* < \tau_1^*$. The advantage of the parametrisation above is that there is a smooth transition near the threshold of incipient motion: the transport rate, and thus the entrainment

rate λ , become vanishingly small when the bottom shear stress tends to zero, but they remain nonzero.

3.3 Numerical model

3.3.1 Governing equations

We sought numerical solutions to the governing equations involving the Saint-Venant–Exner equations (Eq. 3.1–Eq. 3.3) and the stochastic bedload advection-diffusion equation, Eq. 3.13, using the method of finite volumes (LeVeque, 2002; Toro, 2001). These equations can be recast in the following conservative form

$$\frac{\partial \mathbf{q}}{\partial t} + \frac{\partial \mathbf{f}}{\partial x} + \frac{\partial \mathbf{g}}{\partial x} = \mathbf{s}(x, \mathbf{q}) \quad (3.32)$$

where \mathbf{q} is the vector of the unknowns $\mathbf{q} = [h, h\bar{u}, b, y_b]^T$, $\mathbf{f}(\mathbf{q})$ is the flux function

$$\mathbf{f}(\mathbf{q}) = \left[h\bar{u}, \frac{(h\bar{u})^2}{h} + \frac{gh^2}{2}, \beta\bar{u}b, 0 \right]^T \quad (3.33)$$

the function $\mathbf{g}(\mathbf{q})$ includes the diffusive contributions

$$\mathbf{g}(\mathbf{q}) = \left[0, -\nu h \frac{\partial \bar{u}}{\partial x}, -D_u \frac{\partial b}{\partial x}, 0 \right]^T \quad (3.34)$$

and \mathbf{s} is the source term

$$\mathbf{s} = \left[0, g y_b \frac{\partial y_s}{\partial x} + g \frac{\partial}{\partial x} \left(\frac{y_b^2}{2} - y_s y_b \right) - \frac{f}{8} \bar{u} |\bar{u}|, \lambda - \kappa b + \xi_b \sqrt{2\mu b}, \frac{\kappa\gamma - \lambda}{1 - \zeta_p} \right]^T \quad (3.35)$$

Before solving Eq. 3.32 numerically (see § 3.3.3), we need to slightly reshape it to ensure that its form is consistent with the requirements of well-balanced finite-volume methods. The definition of a well-balanced algorithm is as follows: It should provide us both the time-dependent solution to a boundary initial value problem and the steady-state solution. A nonzero steady-state solution exists whenever the source term is nonzero and entirely balanced by the gradient and diffusive terms

$$\frac{d}{dx} (\mathbf{f}(\mathbf{q}) + \mathbf{g}(\mathbf{q})) = \mathbf{s}(x, \mathbf{q})$$

The main problem with irregular topography is that the bed profile $y_b(x, t)$ may vary substantially over short distances, and thus the bed slope $-\partial_x y_b$ fluctuates considerably. This problem is exacerbated when including noise in the Exner equation, Eq. 3.3.

One strategy to cope with these bed slope fluctuations is to express the driving force $-gh\partial_x y_b$ (per unit density) in the momentum balance equation, Eq. 3.2 in an approximate divergence

form. Following Valiani and Begnudelli, 2006 and making use of the flow depth definition ($h = y_s - y_b$), we can express this force as follows

$$-gh \frac{\partial y_b}{\partial x} = -gh \frac{\partial y_s}{\partial x} + gh \frac{\partial h}{\partial x} \quad (3.36)$$

$$= -g(y_s - y_b) \frac{\partial y_s}{\partial x} + \frac{1}{2}g \frac{\partial h^2}{\partial x} \quad (3.37)$$

$$= gy_b \frac{\partial y_s}{\partial x} + \frac{1}{2}g \frac{\partial}{\partial x} (y_b^2 - 2y_s y_b) \quad (3.38)$$

Admittedly, Eq. 3.38 is not strictly in divergence form since the free-surface slope $\partial_x y_s$ is weighted by the non-constant bed elevation y_b , but as the bed evolves much more slowly than the free surface, y_b is almost constant over short time periods, which justifies that we regard Eq. 3.38 as an approximate divergence form of the driving force.

3.3.2 Initial and boundary conditions

For all simulations, we consider a one-directional flow along a granular bed of length L_x and tilted by an angle θ to the horizon. The water discharge at the flume inlet is q_0 . Actually, the bed is not completely flat: Following Bohorquez and Ancy, 2015, we add a low-amplitude harmonic perturbation to the mean bed elevation

$$y_b(x, 0) = -x \tan \theta + \epsilon \sin \left(\frac{2\pi x}{\Lambda_b} \right) \quad (3.39)$$

where ϵ is the perturbation amplitude and Λ_b is the perturbation's longitudinal wavelength. In our simulations, we set $\epsilon = 10^{-7}$ m and $\Lambda_b = L_x$. Using this initial condition makes it possible to reduce the computational time without changing the late-time solution's characteristics (Defina, 2003).

For the other flow variables h , \bar{u} , and b , the initial values at $t = 0$ correspond to the uniform steady-state

$$h(x, 0) = h_{ss}, \quad \bar{u}(x, 0) = \bar{u}_{ss} \text{ and } b(x, 0) = \langle b \rangle_{ss} \quad (3.40)$$

where h_{ss} and \bar{u}_{ss} are the flow depth and depth-averaged velocity related to the selected water discharge q_0 at the flume inlet and bed slope θ , while the Poisson rate density $\langle b \rangle_{ss}$ is given by Eq. 3.16, where γ_{ss} is given by Eq. 3.28. The flow depth and velocity are determined by solving the nonlinear set of equations, Eq. 3.5 and Eq. 3.6, with $\bar{u}_{ss} = q_0 / h_{ss}$ and $\tau_b = \rho g h_{ss} |y'_b|$. For the sake of simplicity, we neglect sidewall effects on flow dynamics in our simulation—these effects could have been accounted for by using, for instance, Einstein–Johnson's method (Guo, 2017).

We implemented cyclic boundary conditions to mimic the flow conditions in infinitely long flumes.

3.3.3 Finite volume method

We solved the governing equations in the computational domain $0 \leq x \leq L_x$ made of n_x cells with uniform size $\Delta x = L_x/n_x = 1$ cm.

The governing equation written in strong form Eq. 3.32 can be solved numerically using a fractional-step method, which involves splitting the governing equation Eq. 3.32 into

- (i) The non-homogeneous hyperbolic subproblem $\partial_t \mathbf{q} + \partial_x \mathbf{f}(\mathbf{q}) = \mathbf{s}$ and
- (ii) The parabolic subproblem $\partial_t \mathbf{q} = -\partial_x \mathbf{g}$ (LeVeque, 2002).

For solving the hyperbolic subproblem, we used the high-resolution Godunov-type method developed by Ketcheson et al., 2013, while for solving the parabolic subproblem, we utilized the classic Crank-Nicholson method (LeVeque, 2002). We specify these methods below.

We first seek a solution to the homogeneous hyperbolic system in conservative form: $\mathbf{q}_t + \mathbf{f}_x = 0$, or in non-conservative form: $\mathbf{q}_t + \mathbf{A}(\mathbf{q}) \cdot \mathbf{q}_x = 0$, where $\mathbf{A} = \nabla_{\mathbf{q}} \mathbf{f}$ is the Jacobian matrix associated with the flux function \mathbf{f} . We denote the left and right eigenvectors of \mathbf{A} corresponding to the eigenvalues $\hat{\lambda}^p$ by \mathbf{l}^p and \mathbf{r}^p , respectively, with $1 \leq p \leq m$ where $m = 4$ is the dimension of the system, Eq. 3.32. These eigenvalues are:

$$\hat{\lambda}^1 = \bar{u} - \sqrt{gh}, \hat{\lambda}^2 = \bar{u} + \sqrt{gh}, \hat{\lambda}^3 = \beta \bar{u}, \text{ and } \hat{\lambda}^4 = 0$$

As noticed by Bohorquez and Ancey, 2015, the first two eigenvalues $\bar{u} \pm \sqrt{gh}$ are the values classically found for the Saint-Venant equations and fixed beds. They show no dependence on the variables b and y_b , a property that will prove useful in the following when we extend the Roe solver to our problem. We define the matrix of the right eigenvectors \mathbf{R} (each column is an eigenvector \mathbf{r}^p) and left eigenvectors $\mathbf{L} = \mathbf{R}^{-1}$.

Following LeVeque, 2002, we define \mathbf{Q}_i as the average of \mathbf{q} over the integral $[x_{i-1/2}, x_{i+1/2}]$ at time t

$$\mathbf{Q}_i(t) = \frac{1}{\Delta x} \int_{x_{i-1/2}}^{x_{i+1/2}} \mathbf{q}(x, t) dx \quad (3.41)$$

Let us first assume that at time t_n the solution $\mathbf{q}(x, t_n)$ is known and can be approximated by a piecewise-polynomial function $\tilde{\mathbf{q}}(x, t_n)$ (Ketcheson et al., 2013). To update the solution and determine $\mathbf{q}(x, t_{n+1})$, we need to solve a series of Riemann problems at each cell interface $x_{i-1/2}$. As the subproblem is hyperbolic, the right eigenvectors \mathbf{r}^p are real and linearly independent, and they form a basis on which we can decompose any vector. For instance, the jump between two neighboring cells can be decomposed as follows

$$\mathbf{Q}_i - \mathbf{Q}_{i-1} = \sum_{p=1}^m \alpha_{i-1/2}^p \mathbf{r}_{i-1/2}^p = \sum_{p=1}^m \mathcal{W}_{i-1/2}^p \quad (3.42)$$

where $\mathcal{W}_{i-1/2}^p = \alpha_{i-1/2}^p \mathbf{r}_{i-1/2}^p$ is the shock wave that propagates in the direction of the p th eigenvector at speed $\lambda_{i-1/2}^p$, and the factors $\alpha_{i-1/2} = (\alpha_{i-1/2}^p)_{1 \leq p \leq m}$ are defined by

$$\alpha_{i-1/2} = \mathbf{R}_{i-1/2}^{-1} \cdot (\mathbf{Q}_i - \mathbf{Q}_{i-1}) = \mathbf{L}_{i-1/2} \cdot (\mathbf{Q}_i - \mathbf{Q}_{i-1}) \quad (3.43)$$

It can be shown that updating \mathbf{Q}_i from time t_n to $t_{n+1} = t_n + \Delta t$ leads to an estimate of the solution \mathbf{Q}_i^* in the absence of diffusion (Ketcheson et al., 2013)

$$\mathbf{Q}_i^* = \mathbf{Q}_i^n - \frac{\Delta t}{\Delta x} (\mathcal{A}^+ \cdot \Delta \mathbf{q}_{i-1/2} + \mathcal{A}^- \cdot \Delta \mathbf{q}_{i+1/2} + \mathcal{A} \Delta \mathbf{q}_i) + \Delta t \mathbf{S}_i \quad (3.44)$$

where we used the shorthand notation proposed by LeVeque, 2002 for representing the fluctuations. These fluctuations represent the changes in the mean value \mathbf{Q}_i^n caused by the waves \mathcal{W} traveling to the right (associated with the superscript +) or left (associated with the superscript -):

$$\mathcal{A}^\pm \cdot \Delta \mathbf{q}_{i-1/2} = \sum_{p=1}^m \left(\hat{\lambda}^p(\mathbf{q}_{i-1/2}^{\mathcal{L}}, \mathbf{q}_{i-1/2}^{\mathcal{R}}) \right)^\pm \mathcal{W}^p(\mathbf{q}_{i-1/2}^{\mathcal{L}}, \mathbf{q}_{i-1/2}^{\mathcal{R}}) \quad (3.45)$$

$$\mathcal{A} \cdot \Delta \mathbf{q}_i = \sum_{p=1}^m \left(\hat{\lambda}^p(\mathbf{q}_{i-1/2}^{\mathcal{R}}, \mathbf{q}_{i+1/2}^{\mathcal{L}}) \right)^\pm \mathcal{W}^p(\mathbf{q}_{i-1/2}^{\mathcal{R}}, \mathbf{q}_{i+1/2}^{\mathcal{L}}) \quad (3.46)$$

where $\mathcal{A}^- = \min(\mathcal{A}, 0)$ and $\mathcal{A}^+ = \max(\mathcal{A}, 0)$ —The same definition applies for other parameters. The labels \mathcal{L} and \mathcal{R} denote the left and right states of the cell interfaces, respectively.

To compute the fluctuations \mathcal{A}^\pm , we extended the approximate linear Riemann solver proposed by Roe, 1981. As this extension poses no particular problem, we refer the reader to Appendix C.

The mean source term \mathbf{S}_i in Eq. 3.44 is defined as

$$\mathbf{S}_i = \frac{1}{\Delta x} \int_{x-1/2}^{x+1/2} \mathbf{s}(\mathbf{q}, t_n) dx \quad (3.47)$$

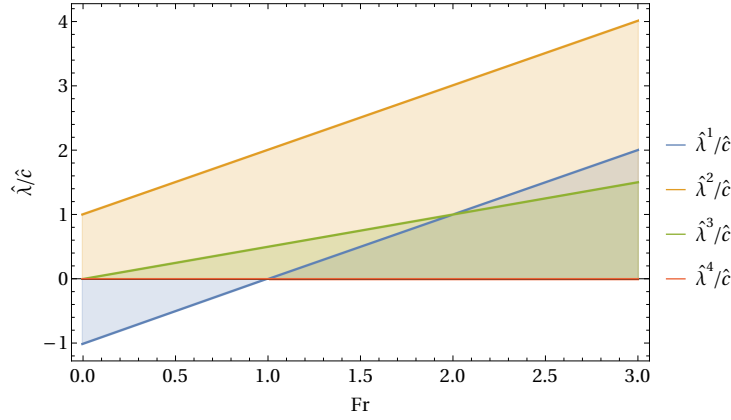


Figure 3.4: Relationship between characteristic velocities and Froude number, with $\beta = 0.5$.

which is evaluated explicitly from the known solution at time t_n . Special attention has been paid to the integration of the friction term in the momentum balance equation, Eq. 3.2. See Appendix D for further information.

The parabolic subproblem is solved using the implicit Crank–Nicholson scheme, which has second-order accuracy in both space and time. The solution to the hyperbolic subproblem \mathbf{Q}_i^* is used as the initial condition for the equations $\partial \mathbf{q}_t = \boldsymbol{\Psi}(\mathbf{q})$ where $\boldsymbol{\Psi} = -\partial_x \mathbf{g}$ includes the diffusive terms in the momentum balance equation, Eq. 3.2, and the advection diffusion equation, Eq. 3.13 for b . The implicit Crank–Nicholson scheme leads us to solve the following linear system for \mathbf{Q}_i^{n+1}

$$\mathbf{Q}_i^{n+1} = \mathbf{Q}_i^* + \frac{\Delta t}{2\Delta x^2} (\boldsymbol{\Psi}(\mathbf{Q}_i^*) + \boldsymbol{\Psi}(\mathbf{Q}_i^{n+1})) \quad (3.48)$$

where

$$\boldsymbol{\Psi}(\mathbf{Q}) = \begin{pmatrix} 0 \\ h_{i-1/2} v_{i-1/2} \bar{u}_{i-1} - (h_{i-1/2} v_{i-1/2} + h_{i+1/2} v_{i+1/2}) \bar{u}_i + h_{i+1/2} v_{i+1/2} \bar{u}_{i+1} \\ D_u b_{i-1} - 2D_u b_i + D_u b_{i+1} \\ 0 \end{pmatrix} \quad (3.49)$$

The interface values in Eq. 3.49 are calculated using averages of the neighboring cells, i.e., $h_{i+1/2} = (h_i + h_{i+1})/2$, and $h_{i-1/2} = (h_{i-1} + h_i)/2$. Equation 3.44 is integrated in time using the ten-stage fourth-order Runge–Kutta method.

3.3.4 Numerical implementation

We implemented the wave decomposition algorithm called the *q-wave* Riemann solver by Ketcheson et al., 2013. The algorithm is based on the discretization presented in §3.3.3. The algorithm used is a fifth-order accurate *weighted essentially nonoscillatory* (WENO) reconstruction of the left and the right cell states, and a fourth-order accurate strong stability preserving Runge–Kutta scheme for marching on time.

The code is implemented in Fortran, compiled with Intel Fortran Compiler 2021.6.0 ran on a Linux operating system using Intel i7-10875H core processors operating at 2.30 GHz. We used the SuiteSparse library to solve the system, Eq. 3.48 (Davis, 2006). The noise term $\xi_b = \text{rand}/\sqrt{\Delta t \Delta x}$ in Eq. 3.35 was generated by specifying a seed number and using the `vdRngGaussian` function `rand` from Intel’s MKL library. As explained in §3.2.2, we used the Poisson representation Eq. 3.17 to link particle activity γ and Poisson rate density b . In practice, this means that after computing b_i in cell i of length Δx , we determined γ_i by drawing a random number n_i of particles from the Poisson distribution with rate $b_i \Delta x$ using the `virngpoisson` provided by Intel’s MKL library function: $\gamma_i = \omega_p n_i / \Delta x$.

3.4 Simulating antidunes formation and motion

The main elements of the stochastic model have been tested against experimental data in earlier publications. Ancey and Heyman, 2014 showed that the model was able to predict the statistical properties of bedload transport rates under steady-state conditions in narrow flumes. In particular, they showed that the collective entrainment coefficient μ played a significant role in the creation of wide (non-Gaussian) fluctuations in the bedload transport rates (setting $\mu = 0$ would produce Gaussian fluctuations). Bohorquez and Ancey, 2015 conducted a stability analysis of the morphodynamic model, Eq. 3.1–Eq. 3.3. They found that under supercritical flow conditions, Eq. 3.1–Eq. 3.3, supplemented by Eq. 3.11 were linearly unstable regardless of the Froude number value, whereas Eq. 3.1–Eq. 3.3 supplemented by the Meyer-Peter–Müller bedload transport equation, Eq. 3.8, became unstable only for Froude numbers in excess of 2.

Here we provide a more quantitative comparison between experimental data and what the morphodynamic model based on Eq. 3.1–Eq. 3.3 and Eq. 3.11 predicts. A particular difficulty is that an experiment can be regarded as one realization of a stochastic process: replicating the same experimental conditions (bed slope, boundary conditions) does not produce the same output: the bedload transport rate’s time series and the position and shape of bedform differ from one realization to another.

3.4.1 Experimental scenarios

We used two data sets issued from two different settings. The only common point of these data sets was the data were related to supercritical flow conditions.

Chapter 3. Simulation of antidune migration in straight channel

The first data set was obtained by Recking et al., 2009 using a 10-cm-wide 6-m-long flume. In all, they carried out 19 experiments with varied water discharges Q , bed slope i , and particle diameter d . We retained only the eleven runs related to the particle size $d = 9$ mm and $\rho_p = 2570$ kg/m³ because Recking et al., 2009 provided the antidune dimensions only for these runs. These runs were named R1 to R11 in Table 3.1. The depth-averaged velocity and flow depth were estimated by solving the Keulegan equation, Eq. 3.6, with a bespoke definition of the roughness size k_s . Although the authors measured the bedload transport rate q_s at the flume outlet, they did not provide further information about the statistical properties of q_s . The antidune wavelength was estimated by dividing the total length over which antidunes were observed by their number.

The second data set was collected by Pascal et al., 2021. These authors used well-sorted, rounded gravel particles with a median diameter $d = 2.9$ mm and a density $\rho_p = 2550$ kg/m³ in a 2.5-m-long 4-cm-wide flume. The authors carried out four experiments in which they kept nearly the same values for the mean bed slope and inflow rate and changed the sediment rate. By filming the flume from the side, they measured the flow-depth and bed profiles, from which they deduced the depth-averaged velocity. Filming the flume outlet allowed them to measure the bedload transport rates at a high temporal resolution (from 60 to 100 Hz). The antidune wavelength and celerity were determined from the bed profile's spatio-temporal variations. Their runs were labelled P1 to P4 in Table 3.1.

Table 3.1: Experimental conditions in the experiments conducted by Recking et al., 2009 and Pascal et al., 2021. W flume width, d median particle diameter, $i = \tan \theta$ flume slope, Q inflow rate, $\bar{u} = Q/(Wh)$ mean velocity, h flow depth averaged over the flume length, R_h hydraulic radius, $u^* = \sqrt{ghi}$ the friction velocity, τ^* the Shields stress, $\tau_c^* = 0.15 \tan^{0.275} \theta$ the critical Shields number estimated using the empirical equation proposed by Recking et al., 2008b, $\Phi = q_s/\sqrt{sgd^3}$, L antidune wavelength, A amplitude.

Run	W cm	d mm	i %	Q L/s	\bar{u} m/s	h mm	R_h/d	\bar{u}/u^*	Fr	τ^*	τ^*/τ_c^*	Φ $\times 10^{-5}$	L m	A m
P1	4	2.9	5.1	0.124	0.37	0.83	2.55	6.08	1.31	0.085	1.28	41	0.06–0.20	0.003–0.008
P2	4	2.9	5.2	0.152	0.41	0.92	2.86	6.30	1.38	0.095	1.43	72	0.08–0.16	0.003–0.009
P3	4	2.9	5.4	0.168	0.44	0.95	2.97	6.52	1.44	0.105	1.55	99	0.09–0.15	0.003–0.01
P4	4	2.9	5.2	0.192	0.46	1.4	3.21	6.68	1.45	0.108	1.62	125	0.08–0.18	0.003–0.01
R1	10	9	5	1.50	0.61	2.41	2.56	5.65	1.26	0.08	1.21	270	0.30	0.02
R2	10	9	5	2.00	0.67	2.91	3.08	5.66	1.26	0.10	1.45	134	0.36	0.01
R3	10	9	5	2.50	0.73	3.38	3.50	5.78	1.26	0.12	1.65	3050	0.40	0.02
R4	10	9	5	3.00	0.77	3.82	3.96	5.74	1.26	0.13	1.86	5240	0.43	0.01
R5	10	9	9	1.00	0.51	1.94	2.11	4.05	1.16	0.11	1.43	1590	0.24	0.01
R6	10	9	9	1.30	0.55	2.31	2.53	3.98	1.16	0.13	1.72	4280	0.32	0.01
R7	10	9	9	1.50	0.58	2.54	2.76	4.02	1.16	0.15	1.87	6590	0.35	0.01
R8	10	9	9	1.70	0.60	2.76	3.02	3.98	1.16	0.16	2.05	9250	0.35	0.01
R9	10	9	13	0.87	0.43	1.98	2.21	2.74	0.98	0.17	1.99	10,100	0.24	0.02
R10	10	9	13	1.00	0.45	2.17	2.42	2.74	0.98	0.18	2.18	14,600	0.24	-
R11	10	9	13	1.10	0.47	2.27	2.55	2.79	1.01	0.19	2.29	17,700	0.27	-

Chapter 3. Simulation of antidune migration in straight channel

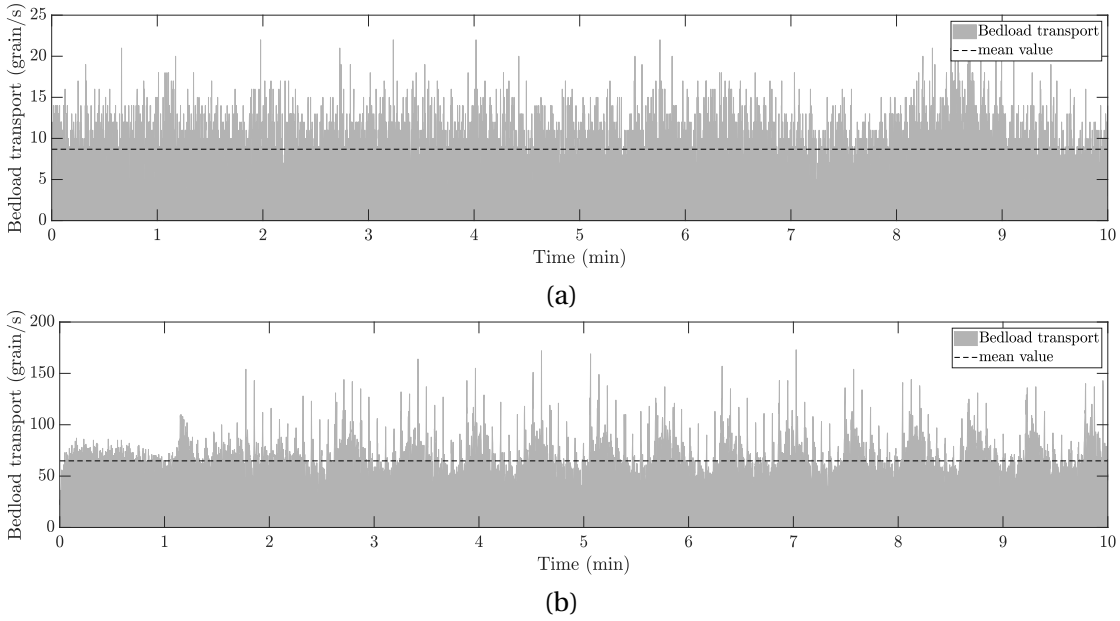


Figure 3.5: Numerical bedload time series by applying the stochastic solver to (a) R1, and (b) R7.

3.4.2 Bedload transport based on stochastic framework

This section's goal is to examine the numerical solver's prediction for bedload transport when it applies to laboratory experiments. Here, the numerical simulation is based on the stochastic bedload model, Eq. 3.13, along with the Saint-Venant–Exner equations, Eq. 3.1–Eq. 3.3. The numerical solver can provide us the number of moving particles in each numerical computational cell. The numerical sediment transport time series at the flume outlet has been computed for each of laboratory dataset. The bedload transport time series for R1 and R7 are presented in Fig. 3.5(a) and Fig. 3.5(b), respectively. The bedload transport is reported in grain/s in this work to provide a physical sense about the magnitude of the numbers.

In Fig. 3.5(a), the mean bedload transport rate is calculated as $\bar{q}_s = 8.6$ grain/s, with a maximum value of $q_{s,\max} = 24$ grain/s. This indicates that the fluctuations in bedload transport are approximately 2.8 times larger than the mean value. In addition, for R7, the mean bedload transport rate is determined $\bar{q}_s = 64.8$ grain/s, with a maximum value of $q_{s,\max} = 173$ grain/s that is 2.7 times more than the mean value.

Throughout the duration of the run, the coefficient of variation – defined as the division of the standard deviation by the mean value – is found to be 37.5% and 27.6% for R1 and R7, respectively. The coefficient of variation indicates that for simulation runs with a higher bedload transport rate, the dispersion of the bedload is less accentuated relative to its mean value. This pattern is analogous to the behavior observed in the experimental data represented in Fig. 3.3.

3.4 Simulating antidunes formation and motion

Run	i	\bar{u} m/s	h cm	\bar{q}_s grain/s	\bar{q}'_s grain/s	σ^2 (grain/s) ²	RE_s %
P1	0.0506	0.37	0.83	62.6	38.2	44.7	39.0
P2	0.0524	0.41	0.92	109.6	65.8	142.4	40.0
P3	0.0541	0.44	0.95	150.4	83.8	268.9	44.3
P4	0.0524	0.46	1.04	191.1	94.8	178.0	50.4
R1	0.0516	0.61	2.41	2.4	8.6	10.5	-258.3
R2	0.0516	0.67	2.91	12.1	22.7	49.9	-87.6
R3	0.0516	0.73	3.38	27.5	35.3	128.3	-28.4
R4	0.0516	0.77	3.82	47.2	47.0	149.4	0.42
R5	0.0853	0.51	1.94	14.3	36.5	48.4	-155.2
R6	0.0853	0.55	2.31	38.5	51.2	144.0	-33.0
R7	0.0853	0.58	2.54	59.3	64.8	313.1	-9.3
R8	0.0853	0.60	2.76	83.2	69.9	213.3	16.0
R9	0.126	0.43	1.98	90.9	82.8	300.3	8.9
R10	0.126	0.45	2.17	131.4	94.4	478.2	28.2
R11	0.126	0.47	2.27	159.3	103.8	920.2	34.8

Table 3.2: Experimental and simulation outputs regarding bedload transport rate. The laboratory-based and simulation-based averaged bedload transport rates are denoted by \bar{q}_s and \bar{q}'_s , respectively. Furthermore, σ^2 represents the variance of the numerical bedload time series and RE_s denotes its relative errors.

The considerable fluctuations observed in the bedload transport, which are several orders of magnitude higher than the mean value, may be attributed to the exit of sediment waves from the flume. Following an initial transient stage, the bedload transport for both runs exhibits significant fluctuations around the mean value. It is important to mention that the bedload transport time series depicted in Fig. 3.5(a) and Fig. 3.5(b) represent only one possible realization of reality. By repeating the stochastic simulation, it would yield different realizations; nevertheless, the key variables would fluctuate modestly around the mean values.

The relative error can be defined as $RE=100 \times (\mathcal{F} - \mathcal{F}')/\mathcal{F}$, where \mathcal{F} is the reference value of the variable of interest, such as mean bedload transport rate, and \mathcal{F}' is the estimated value of \mathcal{F} based on simulation outputs. By applying the numerical solver to the experimental dataset, the mean bedload transport values \bar{q}'_s and their variances σ^2 , which range from 1 to 9 times the mean value, are presented in Table 3.2. The maximum relative error for bedload transport among all simulations is -258.3% . Recking et al., 2012 by testing various bedload transport formulas with huge time-averaged flume experimental dataset found a minimum error of 200%. Therefore, the proposed model in this study is deemed reliable for predicting bedload transport rates in terms of accuracy considering reasonable computational time.

In order to characterize the stationary stochastic processes, we have plotted the probability distribution for numerical bedload transport rates of R1 and R7 in Fig. 3.6(a) and Fig. 3.6(b), respectively. As shown in Fig. 3.6(a) and Fig. 3.6(b), the non-Gaussian wide fluctuations in the bedload transport rate cause the time-averaged values, $\bar{q}'_s = 8.6$ grain/s and $\bar{q}'_s = 64.8$

Chapter 3. Simulation of antidune migration in straight channel

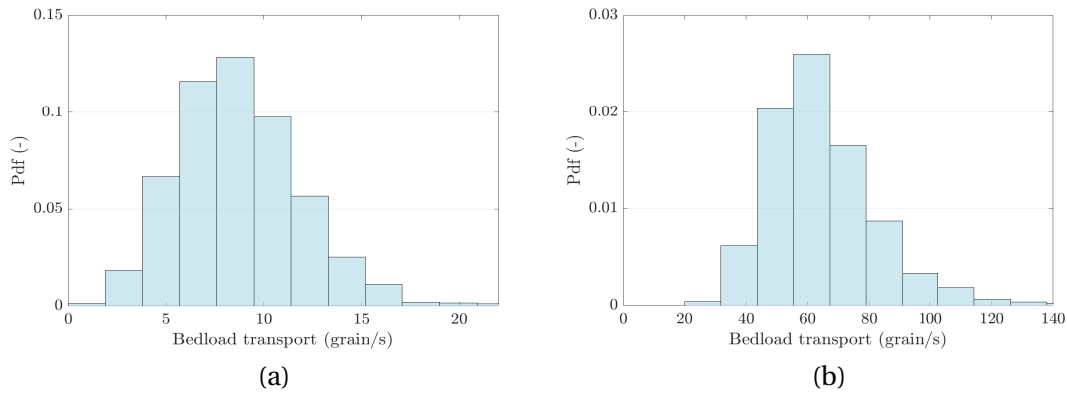


Figure 3.6: Probability density function for number of moving particles based on simulation outputs applied to (a) R1 and (b) R7.

grain/s for R1 and R7, respectively do not be the mode - this does not align with the system's most commonly observed state. In addition, the probability density function exhibits a non-Gaussian shape with a thick tail, indicating the presence of large fluctuations in the bedload time series, which are accounted for in our bedload model as collective entrainment rate.

3.4.3 Wavelength and amplitude based on stochastic framework

It is interesting to study the model's ability in bedform characteristics prediction. Therefore, through numerical solutions of a fully coupled set of stochastic equations, specifically Eq. 3.1–Eq. 3.3 and Eq. 3.13, one can observe a typical bedform shape in Fig. 3.7, which shows the flow and bed elevation based on simulation applied to R1 at $t = 9$ and $t = 10$ minutes. Figure 3.7 shows, firstly, the upstream migration of the antidunes and, secondly, the spatial and temporal variability of the bedform.

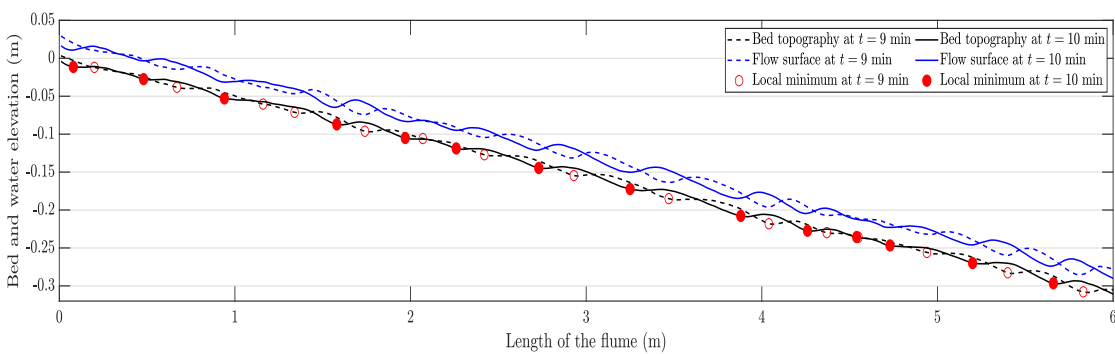


Figure 3.7: Illustration of antidune migration: numerical bed and flow elevations at $t = 9$ minutes (dashed line) and $t = 10$ minutes (solid line) for R1. The red symbols indicate the locations where local minima have been detected to calculate the mean wavelength.

Antidunes geometry is usually characterized by their wavelength and amplitude. The wavelength of an antidune is defined as the distance between successive troughs or crests of the

3.4 Simulating antidunes formation and motion

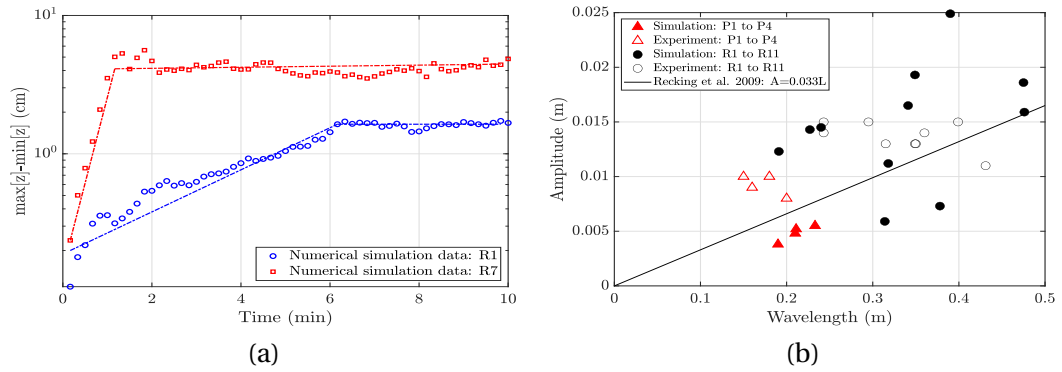


Figure 3.8: (a) Temporal evolution of simulation-based bedform amplitude for R1 (blue circle) and R7 (red square) (b) relation between antidune amplitude and wavelength.

bedform, which can be measured from one minimum point in the bed elevation to the next or from one maximum point to the next. In this study, the wavelength is defined as the length between two adjacent local minimums. To calculate the mean wavelength numerically, we first smoothed the bed topography and then identified the local minimums, as indicated by the red symbols in Fig. 3.7.

The amplitude of an antidune defines as the vertical distance between successive crests and troughs of the bedform. It is quantified as the vertical distance between the lowest point of a trough and the highest point of the crest immediately above it. The wavelength and amplitude of antidunes exhibit spatial and temporal variability along the flume. To enable comparison between numerical and experimental data, the mean numerical wavelength and amplitude have been reported in Table 3.3 with prime notation (L' and A') and compared with the corresponding laboratory dataset by reporting the relative errors. The minimum wavelength of an antidune suggested by Kennedy, 1963 is also provided in Table 3.3 as $L_m = 2\pi hFr^2$.

The amplitude of the bed formation initially increases and eventually reaches a constant value after a certain time period. To quantify the antidunes growth rate, the minimum and maximum elevations of the bed elevation perturbation z were calculated at each time step, and the difference between them is plotted versus time as shown in Fig. 3.8(a), based on numerical simulations applied to R1 and R7. After a transient period of 70 seconds (R7) and 370 seconds (R1), which exhibits exponential growth, the amplitude reaches a plateau, indicating that it no longer increases and has saturated.

The maximum relative error corresponding to the antidune wavelength and amplitude among all numerical simulations in comparison to the experimental dataset is -40.7% and -91.5%, respectively. The large relative error associated with the amplitude may be attributed to the challenges in its laboratory measurement, as mentioned and discussed in Recking et al., 2009.

It is worth mentioning that according to Pascal et al., 2021, the typical amplitude of an antidune ranges from the median grain size to the mean flow depth. Since the amplitude and wavelength show a period of growth and eventual saturation, we decided to compare the maximum range

Chapter 3. Simulation of antidune migration in straight channel

Run	i %	\bar{u} m/s	h cm	L cm	A mm	L_m cm	L' cm	RE_L %	A' mm	RE_A %
P1	5.06	0.37	0.83	6-20	3-8	8.8	19.0	5.0	3.8	52.5
P2	5.24	0.41	0.92	8-16	3-9	10.8	21.0	-31.3	4.8	46.7
P3	5.41	0.44	0.95	9-15	3-10	12.4	21.1	-40.7	5.2	48.0
P4	5.24	0.46	1.04	8-18	3-10	13.2	23.3	-29.4	5.5	45.0
R1	5.16	0.61	2.41	29.5	15	23.8	37.8	-28.1	7.3	51.3
R2	5.16	0.67	2.91	36.0	14	28.8	47.6	-32.2	15.9	-13.6
R3	5.16	0.73	3.38	39.9	15	34.1	47.5	-19.0	18.6	-24.0
R4	5.16	0.77	3.82	43.1	11	38.0	34.9	19.0	19.3	-75.5
R5	8.53	0.51	1.94	24.3	14	16.7	31.4	-29.2	5.9	57.9
R6	8.53	0.55	2.31	31.5	13	19.4	31.8	-1.0	11.2	13.8
R7	8.53	0.58	2.54	34.9	13	21.5	34.1	2.3	16.5	-26.9
R8	8.53	0.60	2.76	35.0	13	23.1	39.0	-11.4	24.9	-91.5
R9	12.6	0.43	1.98	24.3	15	11.8	19.1	21.4	12.3	18.0
R10	12.6	0.45	2.17	23.7	-	13.0	24.0	-1.3	14.5	-
R11	12.6	0.47	2.27	27.4	-	14.1	22.7	8.1	14.3	-

Table 3.3: Experimental and numerical results for bedform characteristics. $L_m = 2\pi hFr^2$ is the minimum antidunes wavelength proposed by Kennedy, 1963. The simulated values of wavelength and amplitude are denoted as L' and A' , respectively, and the corresponding relative errors are RE_L and RE_A .

of them reported by Pascal et al., 2021 with those obtained from our numerical simulations to compute the relative errors.

According to Recking et al., 2009, a linear fit $A = 0.033L$ on the experimental data can represent the relationship between the antidune amplitude and wavelength. However, our numerical simulations mostly overestimate the amplitude for a specific wavelength, suggesting that other parameters may influence the relationship between the two. As shown in Fig. 3.8(b), there is no unique relation between the two, and therefore, further investigation is necessary in this regard.

3.4.4 Migration celerity based on stochastic framework

The migration celerity of antidunes is defined as the speed at which the entire bedform moves upstream over time and is an important parameter for understanding the dynamics of open-channel flows. In this section, we study the migration celerity of antidunes to examine the capability of our stochastic numerical solver.

The simulation results of bed elevation as a function of time are presented in Fig. 3.9 for P1 to P4. In the figure, the troughs and crests of the antidunes can be recognized by the color scheme, where the color yellow represents the crests and the color blue represents the troughs. The simulations demonstrate that after an initial transient stage, during which antidunes

3.4 Simulating antidunes formation and motion

experience exponential growth, trains of antidunes migrate upstream at a constant velocity with some accelerating periods. General speaking, from P1 to P4, the antidunes form sooner, migrate faster upstream, have a larger amplitude and longer wavelength (bigger geometry), and correspond to a higher mean bedload transport rate.

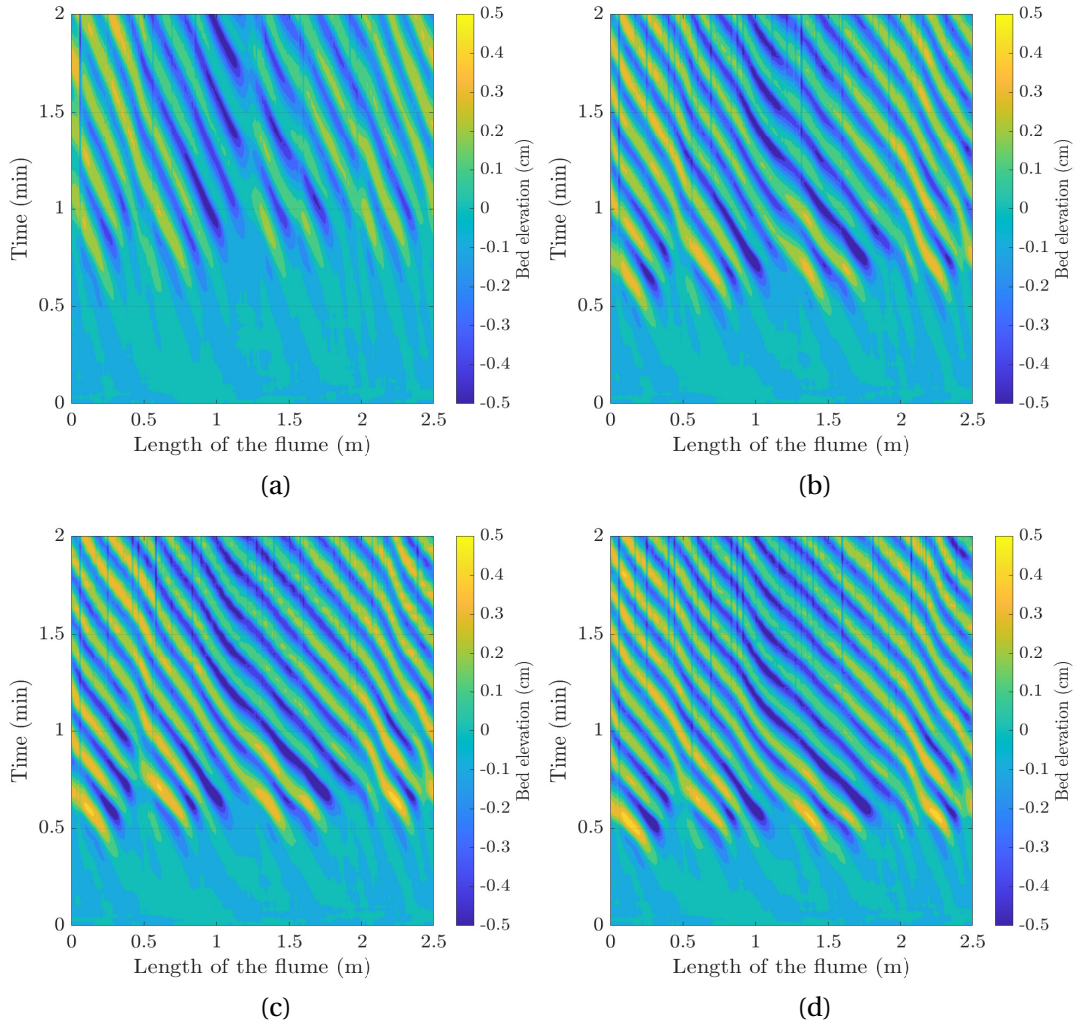


Figure 3.9: Contour plots of the bed elevation perturbation in the $\{x, t\}$ -plane during 2 minutes of simulation time. (a) to (d) correspond to P1 to P4, respectively.

A range of experimental values for the migration celerity of the antidunes for P1 to P4 is reported, which is summarized in Table 3.4. The approach to calculating the migration celerity numerically is to track the movement of the antidune's head over time and calculate the speed of the pattern relative to a stationary observer by $c' = \Delta p / \Delta t$, where Δp is the head position displacement between two time steps Δt , reported in Table 3.4. The simulation migration celerity c' is measured numerically by considering simulation results within $[1.5, 2]$ minutes. The obtained results are within the experimentally reported range.

Chapter 3. Simulation of antidune migration in straight channel

Run	i %	\bar{u} m/s	h cm	c mm/s	c' mm/s
P1	5.06	0.37	6-20	1-16	8.6
P2	5.24	0.41	8-16	1-20	12.6
P3	5.41	0.44	9-15	10-22	15.1
P4	5.24	0.46	8-18	1-30	15.9

Table 3.4: Experimental and numerical results concerning antiduens migration celerity.

3.4.5 Bedload transport based on ensemble-averaged framework

Replication of one specific setup configuration using the stochastic numerical framework - Eq. 3.13 coupled with Eq. 3.1–Eq. 3.3 -, end up with different outcomes that represent only one realization of reality. On the other hand, the ensemble-averaged bedload formulation, Eq. 3.11, is deterministic, meaning that it has one realization by repeating the same numerical run, as it is an ensemble-averaged of all possible realizations of the stochastic framework.

In this section, the interest lies in coupling and solving the deterministic ensemble-averaged bedload formulation, Eq. 3.11, with the shallow water and Exner equations, Eq. 3.1–Eq. 3.3. The simulation-based temporal evolution of the bed topography corresponding to R1 has been plotted on the left-hand side of Fig. 3.10(a), and on the right-hand side, the bed elevation at the flume outlet has been plotted, which varies in a range of 1 cm around the initial bed value.

Figure 3.10(b) and Fig. 3.10(c) depict the bedload transport for R1 and R7, respectively, using the deterministic set of equations—ensemble-averaged framework. By comparing the temporal bed evolution at the flume outlet at $x = 6$ m and the bedload transport time series for R1, one can observe that the bedload peaks correspond to the migration of antidunes indicating that when a sediment wave front passes through a section of a channel, it causes a peak in sediment discharge.

Here, R1 has a mean value of $\bar{q}_s = 9.2$ grain/s with a maximum of $q_{s,\max} = 11.1$ grain/s, indicating that the fluctuations are 1.2 times greater than the average value, while R7 has a mean value of $\bar{q}_s = 61.5$ grain/s and a maximum value of $q_{s,\max} = 143.2$ grain/s, which is 2.3 times greater than the mean value. The bedload transport rate fluctuations are less strong when using the ensemble-averaged framework compared to the stochastic one.

Over the entire run duration, the coefficient of variation is 4.9% and 23.5% for R1 and R7, respectively. The averaged values for the bedload transport were computed using the numerical deterministic solver for P1 to P4 and for R1 to R11, along with their variances, and reported in Table 3.5. The difference between the two presented bedload transport models, i.e., the stochastic and ensemble-averaged models, in terms of mean bedload transport is small and can be neglected. The maximum relative error of the averaged bedload is around -282%, which is close to the maximum relative error when the stochastic framework.

We have calculated the amount of bedload transported for each of the experimental datasets

3.4 Simulating antidunes formation and motion

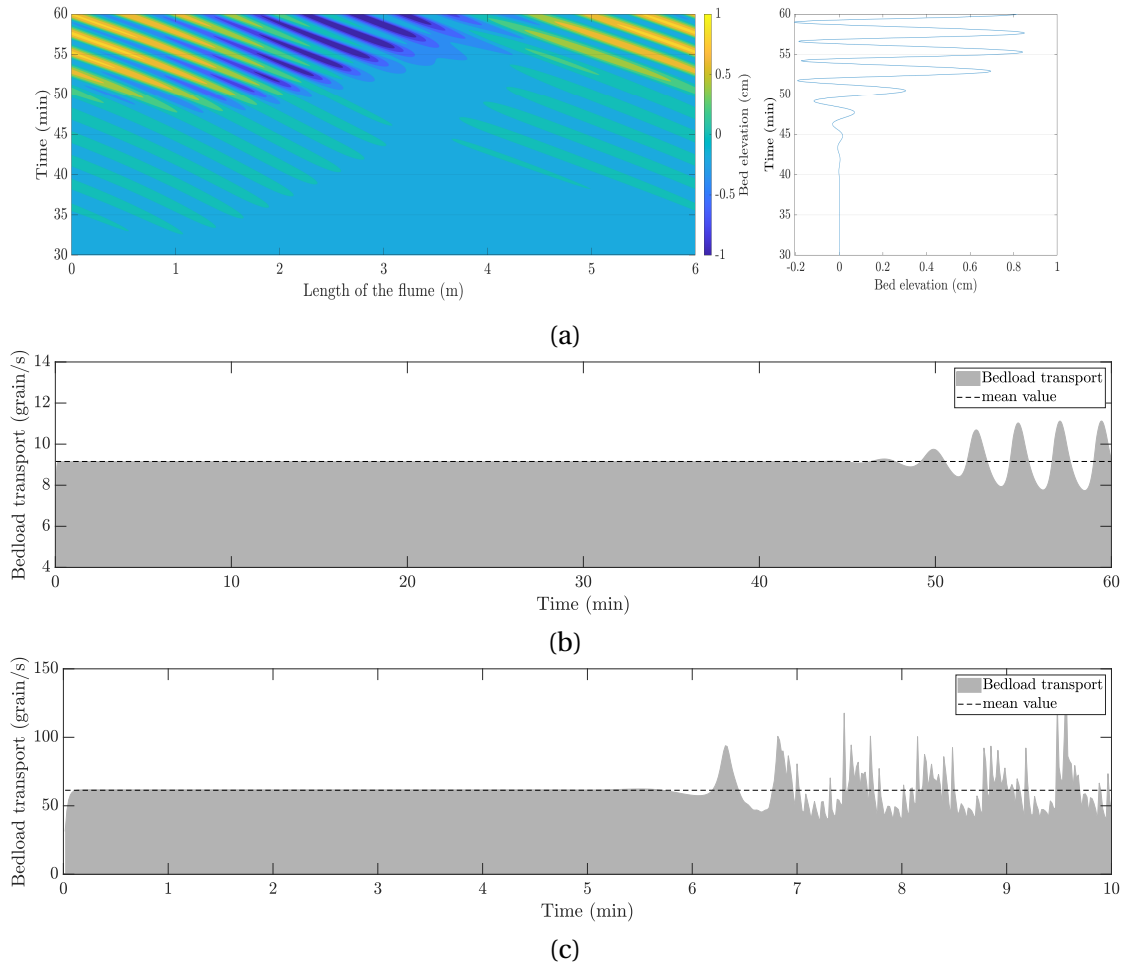


Figure 3.10: (a) Left: bed elevation using numerical simulation applied to R1 in the $\{x, t\}$ -plane, right: bed elevation at the flume exit. Bedload transport time series using the ensemble-averaged framework correspond to (b) R1 and (c) R7.

using MP-M and reported it in Table 3.5 to enable comparison with the model being given. The bedload transport rate using the MP-M formula can be calculated with the averaged-controlling variables. Despite the non-capacity bedload models, this model is a one-to-one function of the averaged Shields number. The minimum and maximum bedload transport relative errors based on the MP-M model ranged from 61% to 1984%, respectively. We have observed higher bedload relative errors by using the MP-M model compared to the presented model. It means the non-capacity bedload models, such as the stochastic model employed in this study in the majority of experiments, are more accurate in bedload transport prediction.

Table 3.5: Numerical bedload transport characteristics using the ensemble-averaged framework. The experimental and simulation bedload transport are denoted by \bar{q}_s and \bar{q}'_s , respectively. σ^2 represents the variance of the numerical bedload time series, and RE_s denotes its relative error. The bedload prediction using MP-M bedload formula is denoted by $\bar{q}_{s,M}$ and $RE_{s,M}$ is its relative error.

Run	i	\bar{u} m/s	h cm	\bar{q}_s grain/s	\bar{q}'_s grain/s	σ^2 (grain/s) ²	RE_s %	$\bar{q}_{s,M}$ grain/s	$RE_{s,M}$ %
P1	0.0506	0.37	0.83	62.6	38.1	24.9	39.1	152.5	143.4
P2	0.0524	0.41	0.92	109.6	65.9	154.2	39.9	225.4	105.6
P3	0.0541	0.44	0.95	150.4	84.0	395.2	44.1	266.3	77.1
P4	0.0524	0.46	1.04	191.1	95.1	335.5	50.2	308.3	61.4
R1	0.0516	0.61	2.41	2.4	9.2	0.2	-281.7	50.6	1983.5
R2	0.0516	0.67	2.91	12.1	22.5	4.9	-86.0	90.5	650.6
R3	0.0516	0.73	3.38	27.5	35.2	75.7	-28.0	134.5	389.9
R4	0.0516	0.77	3.82	47.2	46.6	115.8	1.3	180.6	282.9
R5	0.0853	0.51	1.94	14.3	36.4	18.5	-154.5	117.4	720.4
R6	0.0853	0.55	2.31	38.5	51.1	105.8	-32.8	180.1	367.5
R7	0.0853	0.58	2.54	59.3	61.5	209.3	-3.7	223.3	276.6
R8	0.0853	0.60	2.76	83.2	71.7	102.1	13.8	267.5	221.3
R9	0.126	0.43	1.98	90.9	82.9	434.0	8.8	301.4	231.6
R10	0.126	0.45	2.17	131.4	95.2	816.2	27.5	363.6	176.7
R11	0.126	0.47	2.27	159.3	104.2	1394.6	34.6	397.9	149.8

3.5 Discussion

There are two important points which require further discussions concerning variability of antidunes, and realization of numerical simulations.

3.5.1 Antidunes variability

Spatial and temporal variability of bedform is observed in simulation runs, as has been observed by Pascal et al., 2021. Five probability density functions for antidunes wavelength are calculated over time periods $[2(\mathcal{T} - 1), 2\mathcal{T})$ minutes such that $\mathcal{T} = 1, \dots, 5$ in Fig. 3.11. The obtained findings indicate the absence of antidunes during the initial two-minute period, followed by the emergence of long-wavelength antidunes in the subsequent two-minute interval. Within the time interval $[4, 6)$ minutes, as denoted by the red color, a more frequent occurrence of antidunes with smaller wavelengths was observed. Although temporal variability in the wavelength of antidunes was observed during the development stage (the first 6 minutes), the probability density function remained almost unchanged after the transient stage, while spatial variability along the flume length persisted. It is worth-noting that this behavior during the development stage is visible in the spectra plots presented in Pascal et al., 2021.

Moreover, the initial mean wavelength value at the commencement of the simulation period is considerably higher, yet it progressively converges to a constant and smaller value over time, as visually represented in Fig. 3.11. Antidunes amplitude has a similar behavior shown in Fig. 3.8(a) such that after a transient stage, the amplitude does not grow anymore and remains constant. These constant values are compared with experimental data in Table 3.3. As can be seen in Table 3.3, the mean values of both antidune wavelength and amplitude are more pronounced for simulation runs with higher mean bedload transport rates.

3.5.2 Realization of fluvial systems

The equilibrium theory – sediment transport being in a state of dynamic equilibrium with the flow and the amount of bedload transported is a one-to-one function of a tractive or critical tractive force to be imposed on the boundary such as critical Shields number –, suggests that for a given set of controlling variables, a single bedform characteristic will evolve in fluvial systems. However, experiments show the bedload and morphology are rarely a single-valued response to a specific set of controlling variables. In other words, repeating same experiment several times even in a steady-state condition will end up to different realization (Ashmore, 1988; Warburton & Davies, 1994; Young, 1989).

For example, Ashmore, 1988 conducted four experiments using braided flume and replicated them two times and found out the bedload transport rate time series have been fully different with wide fluctuation even for two replications, although they had almost same mean values. The fluctuations reported to be large up to four times more than averaged values even at

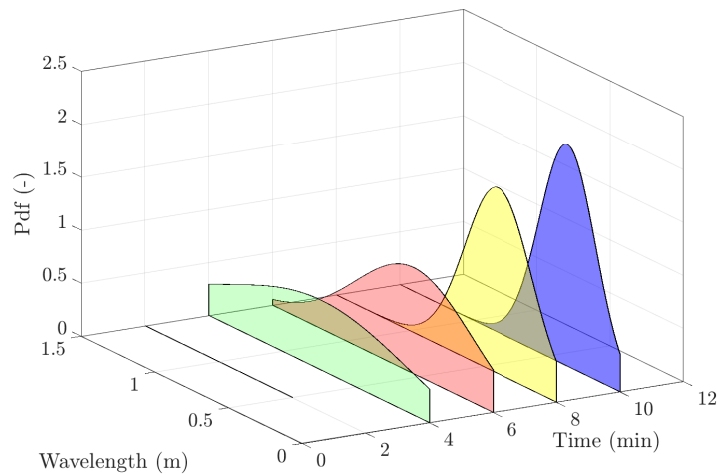


Figure 3.11: Probability density functions of antidunes wavelength over five time periods $[2(\mathcal{T} - 1), 2\mathcal{T}]$ minutes being $\mathcal{T} = 1, \dots, 5$ calculated using simulation run R1.

constant discharges. Another example is the study by Warburton and Davies, 1994 who conducted eleven replication of one experiment. They observed the bedload time series and channel morphology are different in all eleven replications. Although, Warburton and Davies, 1994 captured different realizations for bed topography and bedload time series for each replication, they fluctuated around a mean value. The coefficient of variation for bedload transport was 11% and the bedload fluctuations were up to three to four times higher than the mean value when no external forces existed.

For narrow gravel-bed systems yielding to different realization by replicating one experiment is not unexpected. However, to date, no experimental inquiry has been conducted to explore this phenomenon, to the best of our knowledge. By means of numerical simulation presented in this study and by calculating R1 four times, it yields to different realizations - after a specific amount of time -, as shown in Fig. 3.12.

Although, the bed topographies for different cases are not the same, their statistical behavior remain the same as they fluctuate around a mean value. It is the reason the statistical tools are necessary to describe these sort of stochastic systems. Four different replications of R1 yield four different bedload time series - whereas, the mean and variance of the bedload transport over entire run duration remain almost unchanged (refer to Fig. 3.13).

The above-mentioned experiments and simulation studies provide more evidence to support that i. the fluctuations in bedload transport are autogenic (Gomez et al., 1989; A. Singh et al., 2009), ii. the stochasticity of the problem, and iii. key variables gently fluctuate around mean values. Therefore, comparing an experiment—a single realization—with one simulation—a single realization, too—is not very compelling, as we do not compare the same thing. Therefore, in this paper, we compared the mean values of bedload and form characteristics with the

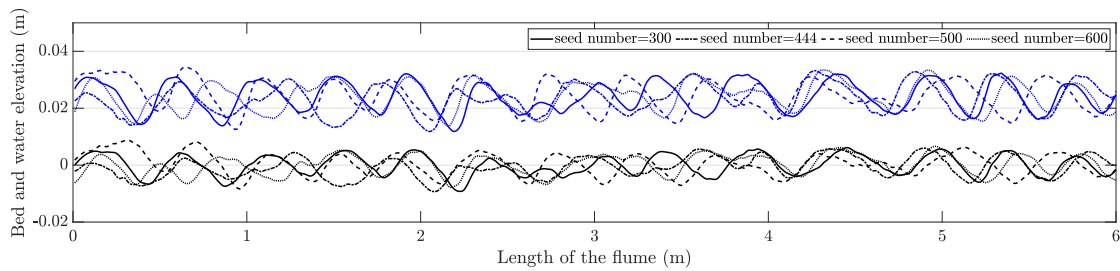


Figure 3.12: Illustration of bed (in black) and flow (in blue) elevation at $t = 10$ minutes with four replications with exact same run configuration (R1). The initial bed slope has been removed for a better comparison.

mean values of experimental data.

It is worth noting that the traditional deterministic bedload models, by fitting a power law curve on the dimensionless experimental data on logarithmic scales, result in high errors in bedload transport (M. H. Garcia, 2008; Recking et al., 2012). For instance, a small variation in the Shields number results in a high variation in bedload transport, as typically modeled by power laws. High variation in bedload prediction can lead to erroneous estimations of bedform and, consequently, erroneous estimations of hydraulic variables. The feedback loop mechanism of the system can exacerbate the error in bedload prediction.

3.6 Conclusion

In this work, the fluctuation of particle movements attracted our attention, which resulted in spatial and temporal variability in bedload transport and bed formation. To capture these fluctuations, we used a stochastic bedload model, which incorporates noise in the bedload formulation, and coupled it with the governing equations for the flow and bed phases. Although using the stochastic bedload model results in only one realization of reality, the key characteristics fluctuate around mean values. These mean values allowed us to compare the numerical results to the experimental dataset. We have used two different laboratory data sets to study the antidune dynamics as well as the bedload transport rate under supercritical flow conditions in gravel-bed channels.

In line with experimental findings, this study revealed that antidunes form in phase with the water surface and migrate upstream with a constant velocity with some accelerating periods. Initially, the growth of antidunes is exponential, but after a transient phase, their growth comes to a halt. Moreover, during the upstream migration of the train antidunes, the sediment transport rate increases as sediment is transported from the downstream-facing slope to the upstream-facing slope. This, consequently, results in the formation of a sediment transport peak at the crest of the antidune. The peak in sediment transport rate can be several times higher than the sediment transport rate over a flat bed. Therefore, the migration of antidunes can have a significant impact on average sediment transport.

Chapter 3. Simulation of antidune migration in straight channel

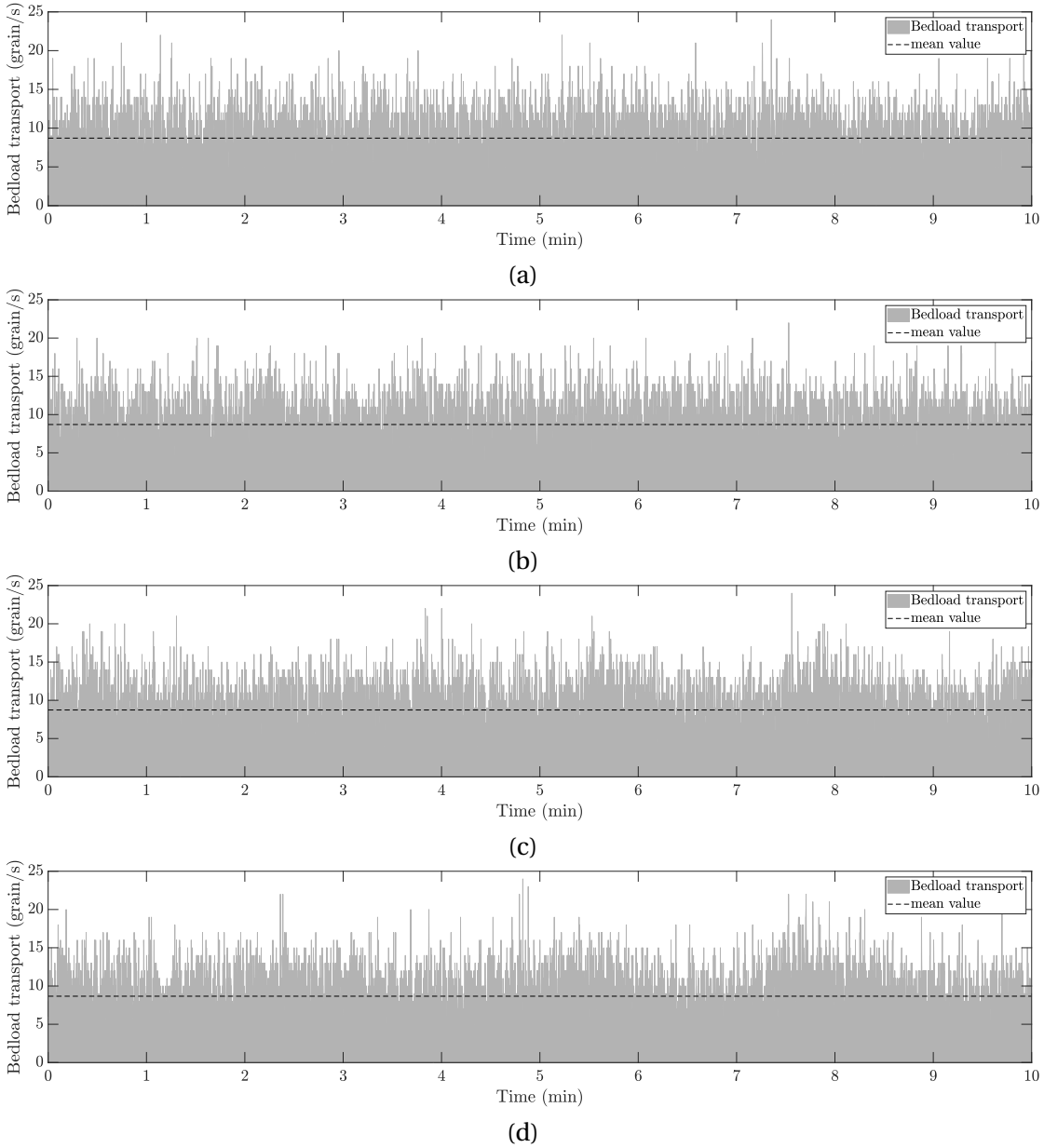


Figure 3.13: Bedload time series from (a) to (d) with noise seed 300, 444, 500, and 600. The averaged bedload transport rate are: $\bar{q}_s = 8.7, 8.7, 8.7, 8.6$ grain/s with a variance of $\sigma^2 = 10.2, 10.1, 10.5, 10.4$ (grain/s)², respectively.

The antidune upstream migration celerity and geometry are more pronounced for runs characterized by a higher mean bedload transport rate; however, we did not observe any relation between the amplitude and wavelength of the antidunes. The proposed numerical model exhibits a relative error of less than 258% in predicting bedload transport. Moreover, the maximum relative error in predicting the wavelength and amplitude of the bedform is found to be -41% and -92%, respectively. The relatively high error in predicting the form amplitude

could be attributed to the challenges in measuring it in a laboratory or model calibration.

Although it is acknowledged that particle-resolved numerical simulations, based on coupling the Lattice Boltzmann Method with the Discrete Element Method, have the potential to provide high accuracy in bedload transport prediction (Schwarzmeier et al., 2023), the computational time required for such methodologies is a major challenge, with more than 80% of the computational time dedicated to discrete element method contact detection (Williams & O'Connor, 1999). This limitation hinders its applicability to large-scale problems. Therefore, the proposed model in this study is deemed reliable for predicting bedload transport rates, considering both its computational efficiency and accuracy.

The advantages of the proposed stochastic bedload transport model are, firstly, the gentle behavior with hydraulic variations, and secondly, taking the particle fluctuations into account, which could affect the bulk scale characteristics. Thirdly, the model demonstrated its ability to predict particle transport and form characteristics with good accuracy. For the future model development we suggest, i. as Warburton and Davies, 1994 mentioned, the current bedload transport state is statistically dependent on two previous time steps, therefore, a second-order Markov process bedload model may lead to a better prediction, ii. the Stratonovich instead of Ito convention is recommended as it has a better physical interpretation, iii. collecting a bank of experimental time-series data to extract their statistical features is a crucial step to calibrate the proposed Markov process based bedload model, and iv. improving bedload prediction requires a comprehensive understanding and modeling of deposition and entrainment processes across a range of hydraulic conditions, both with and without of bed formation.

4 Stochastic modeling of bedload transport and bar development

Mehrdad Kiani-Oshtorjani ¹, Evgeny Karpushov ¹, and Christophe Ancey ¹

¹ Environmental Hydraulics Laboratory, École Polytechnique Fédérale de Lausanne, 1015 Lausanne, Switzerland

In preparation for publication.

Doctoral candidate's contribution

The candidate performed the entire implementation, analysis, and figures. Mr. Karpushov double-checked the mathematical derivation regarding the stability analysis and compared the neutral curves with the experimental dataset. Apart from the section on stability analysis, which was co-authored with Mr. Karpushov, the entire chapter was written by the candidate with editorial comments from Prof. Ancey.

Abstract

In this study, we introduce a two-dimensional stochastic bedload model that provides the number of moving particles. This model departs from traditional capacity-based methodologies, instead adopting a fluid dynamics approach in which the sediment transport rate is dictated by flow conditions rather than exclusively by the Shields number. We have integrated this model with the two-dimensional Saint-Venant–Exner equations to evaluate its predictive efficiency. In the first part of the study, we used linear stability analysis to study the emergence of two-dimensional bedforms under a variety of flow conditions. The resultant data were validated by comparison with an experimental dataset from the literature. The analysis yielded valuable insights, highlighting the essential factors necessary for bedform development. In the second part, we implemented a numerical algorithm based on a Riemann-solver method to study the model's performance. The numerical solver was applied to three controlled, steady-state flume experiments conducted in a gravel-bed flume. In line with experimental data, the numerical simulations predicted the sediment transport rate, alternate bar characteristics, their growth rate, and deposition/erosion rates of the bed.

4.1 Introduction

Bedload transport, characterized by significant non-Gaussian fluctuations, is known to be a stochastic phenomenon (Ancey et al., 2008; Benavides et al., 2022). These individual particle movement fluctuations can spread within the system, leading to a situation where microscopic particle-level fluctuations exert influence on macroscopic scales, such as bedform development and bedform-induced variations in hydraulic conditions. That is why fluvial systems exhibit chaotic behavior. It means that even with identical boundary and initial conditions, such systems lead to various realizations (Ashmore, 1988; Warburton & Davies, 1994).

The difficulties of traditional (deterministic) bedload models in predicting the bedload more accurately than one order of magnitude compared to observed data (Ancey, 2020; Recking et al., 2012) and, consequently, the bed topography (Deigaard, 2006; Van Duin et al., 2017), can be attributed to the overlooking of bedload fluctuations. This oversight occurs when viewing fluvial systems from a capacity perspective (Martínez-Aranda et al., 2019). In this perspective, a given set of controlling variables is assigned a specific maximum load for transporting solid weight (Z. Cao et al., 2012; Wu, 2007).

This capacity is formulated by introducing a tractive force (or critical tractive force) exerted on the boundary (Armanini & Di Silvio, 1988), such as the critical Shields number (du Boys, 1879) or water discharge (Gilbert & Murphy, 1914), to initiate bedload movements: transitioning from clear water (incipient motion) to a mobile bed. It ends up with a deterministic, scaled formulation of bedload transport through the fitting of experimental data. For example, a specific water discharge is correlated with a certain capacity to transport solid weight, resulting in an injective function that relates bedload transport to water discharge (Gilbert & Murphy, 1914).

In other words, in this approach, the fluctuations are smoothed out by averaging the bedload transport. This averaging process potentially erases crucial information related to fluctuations that impact bulk scales (Ancey et al., 2015; Charru et al., 2004; Furbish et al., 2017). For this reason, several modifications have been proposed for deterministic models to better mimic the observed laboratory values, such as introducing different roughness heights in friction formulations (Millar, 1999) or introducing different exponents for power laws in deterministic bedload models (Ancey & Recking, 2023).

In recent years, Benavides et al., 2022; Fan et al., 2014; Li et al., 2023; Pierce et al., 2022 have incorporated the fluctuations into the formulation. These studies have shown promising results in predicting critical incipient motion conditions, the dynamics of individual particles, the dual-mode dynamics of bedload transport, and sediment flux, respectively.

Recently, a stochastic bedload model proposed by Ancey and Heyman, 2014 suggested advection-diffusive type of movement for particles. This stochastic bedload transport model has been effectively coupled in one dimension with shallow water and Exner equations, leading to improved accuracy in predicting bedload transport and bedform evolution, specifically the

formation of antidunes from a flat surface (Bohorquez & Ancey, 2015, 2016; Kiani-Oshtorjani & Ancey, 2024). However, it has yet to be evaluated in a two-dimensional case study.

In this study, we aim to tackle the challenge of incorporating bedload transport fluctuations by supplementing the two-dimensional depth-averaged shallow water equations with a two-dimensional stochastic bedload transport model and using the Exner equation to maintain bed continuity. Our approach differs from conventional bedload transport models that directly link water discharge and particle flux, as it defines particle flux as a stochastic variable. This framework is particularly suitable for simulating the partial mobility regime, which is typically characterized by the emergence of alternate bars.

The inception of alternate bars is indicative of the early stages of the meandering process in rivers. Alternate bars, large-scale bedforms, are characterized by alternating pools and ripples along either side of a channel, with a wavelength many times the channel's width. These features can either experience downward migration (Crosato et al., 2012) or remain stationary (Lisle et al., 1991). The formation of alternate bars is influenced by various factors, including stream obstructions (Struiksmā & Crosato, 1989), suspended bedload (Bertagni & Camporeale, 2018), and channel geometry—for instance, the ratio of half-width-to-flow-depth (Colombini et al., 1987).

Prior to the implementation of the numerical simulation, we studied the linear stability properties of the system of equations. The stability analysis provides us the key parameters influencing our physical problem and indicates which mathematical term in our governing equations is of greater relative importance. To establish the validity of our methodology, we verify the obtained results with experimental data from the literature. Subsequently, we employ a Riemann-based numerical solver, the f -wave method, within a finite volume framework. This numerical solver is applied to laboratory experiments for the analysis of bedload transport and the formation of alternate bars under steady-state conditions.

The structure of this work is organized as follows: In § 4.2, the mathematical theory including the governing equations, and the stochastic bedload model are explained. In § 4.3, we conducted a linear stability analysis and studied the neutral curves correlating the Froude number, half-width-to-depth ratio, lateral wavenumber, and the ratio of grain-size-to-water-depth to the longitudinal wavenumber of the alternate bars. In § 4.4, we detail the wave propagation algorithm employed to numerically solve the governing equations. In § 4.5 and § 4.6, we provide a comprehensive explanation of the obtained results by applying the numerical solver to laboratory experiments and demonstrate the model's capabilities. We present the discussion and conclusion of the study in § 4.7.

4.2 Physical problem

4.2.1 Saint-Venant–Exner equations

We may derive the Saint-Venant equations from the Navier-Stokes equations using the hydrostatic pressure assumption and the Boussinesq approximation (Cushman-Roisin & Beckers, 2011). The two-dimensional Saint-Venant–Exner equations include four equations, namely, the depth-averaged conservation of mass, two momentum equations for the fluid phase, and the Exner equation for continuity of the bed—the bed being erodible. In a straight channel with a slowly varying erodible bottom - ignoring the wind effects and Coriolis terms in addition of diffusion of momentum due to viscosity - the governing equations are (Mignot et al., 2006; Zhou, 2004)

$$\frac{\partial h}{\partial t} + \frac{\partial}{\partial x}(h\bar{u}) + \frac{\partial}{\partial y}(h\bar{v}) = 0 \quad (4.1)$$

$$\frac{\partial(h\bar{u})}{\partial t} + \frac{\partial}{\partial x}(h\bar{u}^2) + \frac{\partial}{\partial y}(h\bar{u}\bar{v}) + gh\frac{\partial h}{\partial x} = -gh\frac{\partial y_b}{\partial x} - \frac{\tau_{bx}}{\rho} \quad (4.2)$$

$$\frac{\partial(h\bar{v})}{\partial t} + \frac{\partial}{\partial x}(h\bar{u}\bar{v}) + \frac{\partial}{\partial y}(h\bar{v}^2) + gh\frac{\partial h}{\partial y} = -gh\frac{\partial y_b}{\partial y} - \frac{\tau_{by}}{\rho} \quad (4.3)$$

$$(1 - \zeta_p)\frac{\partial y_b}{\partial t} = \mathcal{D} - \mathcal{E} = -\frac{\partial \bar{q}_{sx}}{\partial x} - \frac{\partial \bar{q}_{sy}}{\partial y} \quad (4.4)$$

The set of equations represents a flow with varying topography at time t and spatial position (x, y) that are longitudinal and normal coordinates, respectively. The set of equations has infinite solutions, while the boundary and initial conditions will determine the unique solution for our physical problem. The flow depth-average velocities at time t and position (x, y) are denoted by $\bar{u} = \bar{u}(x, y, t)$ and $\bar{v} = \bar{v}(x, y, t)$ in longitudinal and normal directions, respectively. The flow depth from the surface level to the bottom is $h = h(x, y, t) = y_s(x, y, t) - y_b(x, y, t)$, while $y_s(x, y, t)$ and $y_b(x, y, t)$ are the positions of the free surface flow and the bed, respectively.

The bed slopes in the x and y directions given by $\tan\theta_x = -\partial_x y_b$ and $\tan\theta_y = -\partial_y y_b$, respectively. The gravity acceleration is represented by $g = 9.81 \text{ m}^2/\text{s}$ and ρ is the fluid density. The bottom shear stress longitudinal and transversal components are τ_{bx} and τ_{by} , respectively.

The bed porosity is denoted as ζ_p and is assigned a value of 0.36. The averaged bedload transport rates in the streamwise and spanwise directions are represented by \bar{q}_{sx} and \bar{q}_{sy} , as well as the deposition and entrainment rates indicated as \mathcal{D} and \mathcal{E} , respectively. To close the set of equations, suitable closure relations are required to establish the connection between the deposition and entrainment rates, \mathcal{D} and \mathcal{E} , and the shear stresses, τ_{bx} and τ_{by} , to the sediment and flow characteristics.

4.2.2 Friction model

The bed friction stress, indicative of the effect of bed roughness, is related to the flow properties (Shettar & Keshava Murthy, 1996) as follows

$$\begin{aligned}\tau_{bx} &= C_f \rho \bar{u} \sqrt{\bar{u}^2 + \bar{v}^2} \\ \tau_{by} &= C_f \rho \bar{v} \sqrt{\bar{u}^2 + \bar{v}^2}\end{aligned}\quad (4.5)$$

where the friction factor C_f can be determined by $C_f = f/8$. In order to calculate the friction factor, the Keulegan, 1938 equation has been used

$$f = \left(2.03 \log(12.2h/k_s)\right)^{-2}\quad (4.6)$$

where the roughness height k_s is approximated with $5.9d_{50}$ to represent various bedform roughness (Millar, 1999). The initial slope by a well-known formula can be related to Froude number Fr_0 and friction factor C_0 for uniform flow over unperturbed bed (Colombini & Stocchino, 2012)

$$S_0 = Fr_0^2 C_0\quad (4.7)$$

4.2.3 Stochastic bedload transport model

A bedload transport model was recently derived by adopting an Eulerian approach (Ancey & Heyman, 2014). Three rates of mass exchange between the bed and flow were considered: deposition σ , individual entrainment λ' , and collective entrainment μ . The terminology used to describe the collective entrainment has caused some confusion, as it may suggest that multiple particles are simultaneously entrained. However, this is not the case, as the term simply reflects the fact that the likelihood of entrainment is influenced by the number of particles in motion.

The resulting analysis led to a probability problem that could be expressed in terms of joint and conditional probabilities. Although the underlying physical process may have some memory, it may be short-term memory, and not long-term. As a result, the problem was simplified into a Markov process with a single memory step. By leveraging this simplification, a stochastic formulation for bedload transport was proposed. The proposed formulation provides a framework for predicting the number of active particles in a probabilistic manner, taking into account the stochastic nature of the process as

$$\frac{\partial b}{\partial t} + \frac{\partial}{\partial x}(\bar{u}_s b) + \frac{\partial}{\partial y}(\bar{v}_s b) = \frac{\partial^2}{\partial x^2}(D_x b) + \frac{\partial^2}{\partial y^2}(D_y b) + \lambda - \kappa b + \sqrt{2\mu b} \xi_b\quad (4.8)$$

Chapter 4. Stochastic modeling of bedload transport and bar development

where b is the Poisson density rate, the Gaussian noise term is ξ_b and can be generated using the `vdRngGaussian` function (Intel's MKL library). The difference between deposition and collective rates is $\kappa = \sigma - \mu$, and the entrainment rate per unit length is $\lambda = \lambda' / \Delta x$, where Δx is the length of the control volume.

The mean particle velocity is denoted by \bar{u}_s and \bar{v}_s and particle diffusivities by D_x and D_y in streamwise and spanwise directions, respectively. In contrast to the classical advection-diffusion equation, which assumes that diffusivity is independent of spatial scale, our analysis yields a modified diffusivity with $D_x = \bar{u}_s \Delta x / 2$ and $D_y = \bar{v}_s \Delta y / 2$.

The sediment velocities and their directions were then taken into account by estimating them based on relating them to flow velocities by $\bar{u}_s = \beta_x \bar{u}$ and $\bar{v}_s = \beta_y \bar{v}$, where β_x and β_y represent the ratios of sediment velocity to water velocity in the longitudinal and normal directions, respectively. The value of these ratios is set to 1.0, indicating that the sediment velocity and direction are the same as the flow, except when specifically stated otherwise in the context. This is a rough assumption, and for future studies, there is a need to model these parameters with greater precision. By taking the ensemble average of Eq. 4.8 and using Itô convention, an equation for particle activity $\langle \gamma \rangle$ is derived as

$$\frac{\partial \langle \gamma \rangle}{\partial t} + \frac{\partial}{\partial x} (\bar{u}_s \langle \gamma \rangle) + \frac{\partial}{\partial y} (\bar{v}_s \langle \gamma \rangle) = \frac{\partial^2}{\partial x^2} (D_x \langle \gamma \rangle) + \frac{\partial^2}{\partial y^2} (D_y \langle \gamma \rangle) + \tilde{\lambda} - \kappa \langle \gamma \rangle \quad (4.9)$$

The definition of particle activity can be expressed as the volume occupied by the active particles in motion per unit streambed area, in the limit as the area of the control volume approaches zero

$$\gamma = \lim_{\Delta x \rightarrow 0} \frac{n V_p}{B \Delta x} \quad (4.10)$$

where V_p denotes the particle volume, B is the control volume width, and Δx is the control volume length. The volumetric entrainment rate in Eq. 4.9 is $\tilde{\lambda} = \lambda V_p / B$. The Eulerian approach enables the definition of entrainment and deposition rates in the Exner equation as functions of mean particle activity, such as

$$\begin{aligned} \mathcal{E} &= \tilde{\lambda} + \mu \langle \gamma \rangle \\ \mathcal{D} &= \sigma \langle \gamma \rangle \end{aligned} \quad (4.11)$$

The moments of b and γ are linked via

$$\langle \gamma \rangle = \langle b \rangle V_p / B \quad (4.12)$$

The mean bedload transport rate \bar{q}_s in the absence of particle diffusion define as (Ancy &

Heyman, 2014)

$$\bar{q}_s = \bar{u}_s \langle \gamma \rangle \quad (4.13)$$

In the steady-state, the equilibrium value for particle activity satisfy (Bohorquez & Ancy, 2015)

$$\langle \gamma \rangle_{ss} = \frac{\tilde{\lambda}}{\sigma - \mu} \quad (4.14)$$

Consequently, the Exner equation can be rewritten as

$$\frac{\partial y_b}{\partial t} = \frac{\mathcal{D} - \mathcal{E}}{1 - \zeta_p} = \frac{\kappa \langle \gamma \rangle - \tilde{\lambda}}{1 - \zeta_p} = \frac{\kappa V_p B^{-1} \langle b \rangle - \tilde{\lambda}}{1 - \zeta_p} \quad (4.15)$$

In the aforementioned theory for bedload transport, three parameters are crucial: deposition rate, individual and collective entrainment rates. To close the set of equations, it is necessary to relate the entrainment and deposition coefficients to the fluid/solid properties. As an initial approximation, the following equation for κ is suggested by Bohorquez and Ancy, 2015

$$\kappa = c_d \sqrt{\frac{(s-1)g}{d}} \quad (4.16)$$

Based on the analysis of particle flight time by Lajeunesse et al., 2010, we set the deposition coefficient c_d to 0.1, and $s = \rho_s / \rho_w$ is the specific density defined as sediment density over the water density ratio. The following equation is suggested for the erosion rate (Bohorquez & Ancy, 2015)

$$\tilde{\lambda} = \frac{c_e V_p}{\rho d^3} \frac{\tau_b - \tau_{cr}}{\sqrt{(s-1)gd}} \quad (4.17)$$

where the entrainment coefficient c_e was deduced from Durán et al., 2012 equivalent to $c_e = 1.75c_d = 0.175$. Based on experimental investigations by Ancy et al., 2008, it has been shown that the collective entrainment μ exhibits minimal sensitivity to flow conditions (please refer to Chapter 3). Specifically, it was found that μ is, on average, 0.85 times the deposition coefficient, expressed as $\mu = 0.85\sigma$.

4.3 Linear stability analysis

In this section, prior to numerical simulation, the steady and uniform base flow's spatio-temporal stability analysis is examined. The equations' qualities of linear stability reveal new information on the validity of the mean equations in the context of pattern formation. The study of stability analysis was performed using our deterministic set of equations, namely, Eq. 4.1–Eq. 4.4, and Eq. 4.9. The general prediction power of morphodynamic models can be foreseen by performing stability analysis. For instance, according to linear theories applied to straight channels, free alternate bar migrates downstream, while forced bar do not migrate and stay stationary. Additionally, has been found that forced bars are two times bigger than free bars (Schielen et al., 1993; Zolezzi et al., 2005).

The analytical solutions for alternate bars in a straight channel usually make the following assumptions: i. the channel is an infinitely long rectangular channel; ii. the flow is shallow; iii. the flow discharge is constant; iv. the channel width is constant; v. uniformity of the sediment size; and vi. sediment transport is in equilibrium with the flow capacity. The key point in the stability analysis is that we view bars as sediment waves; therefore, we will seek for wavy solutions.

The Saint-Venant–Exner equations, when coupled with the traditional bedload model, have been found to have difficulties in predicting bed formation, as demonstrated in the stability analysis performed by Nelson and Morgan, 2018 and facing this question: *"Why did alternate bars develop in our experiments when theory predicts that the flow was too deep to allow them to form?"*. Despite the discrepancy between the prediction based on the traditional set of equations and observed results in the laboratory, the proposed set of equations, equipped with an advection-diffusion bedload model, Eq. 4.9, was able to accurately predict the bed formation, aligning with the experimental dataset drawn from the literature.

4.3.1 Dimensional groups

Morphodynamic theories can be derived in dimensional or dimensionless form. Here we will follow a dimensionless mathematical treatment of the problem, which is obtained by scaling (or normalizing) each quantity in the equations through appropriate scale quantities. These scale quantities are usually representative of the reach-averaged quantities that describe the hydraulic conditions of the uniform flow that would occur in the channel with a given discharge, slope, width, and grain size.

Working with dimensionless equations is important since this allows us to derive results that are scale-independent, i.e., the same dimensionless result can refer to a large river, e.g., the Navisence river in the Val d'Anniviers, Wallis, Switzerland (Ancy et al., 2014), and to a hydraulic gravel-bed flume in the laboratory, provided they are characterized by the same value of the input dimensionless parameters. Moreover, this allows for the detection of the most important parameters on which the physical problem depends, and it also allows for the

comparison of the relative importance of each mathematical term appearing in the governing equations.

To make the variables dimensionless, we will use the characteristic values $\{H_0, U_0, \langle \gamma \rangle_{ss}, B\}$. Here, $\langle \gamma \rangle_{ss}$ denotes the steady-state particle activity for the variable $\langle \gamma \rangle$, and the channel half-width $B = w/2$ is used for normalizing the streamwise and spanwise coordinates (x, y) . The reach-averaged water depth H_0 serves as the scale for the local water depth (h) , and the reach-averaged uniform flow velocity U_0 is used for scaling the depth-averaged velocity fields (\bar{u}, \bar{v}) . The dimensionless variables are defined as follows

$$\begin{aligned} u' &\leftarrow \frac{\bar{u}}{U_0}, & v' &\leftarrow \frac{\bar{v}}{U_0}, & \eta &\leftarrow \frac{h}{H_0}, & z &\leftarrow \frac{y_b}{H_0}, & \phi &\leftarrow \frac{\langle \gamma \rangle}{\langle \gamma \rangle_{ss}}, \\ x' &\leftarrow \frac{x}{B}, & y' &\leftarrow \frac{y}{B}, & t' &\leftarrow \frac{tU_0}{B}, & \tau'_{bx} &\leftarrow \frac{\tau_{bx}}{\rho U_0^2}, & \tau'_{by} &\leftarrow \frac{\tau_{by}}{\rho U_0^2} \end{aligned} \quad (4.18)$$

By taking into account the non-dimensional parameters Eq. 4.18 and substituting into Eq. 4.1–Eq. 4.4, and Eq. 4.9, the dimensionless equations can be obtained as

$$\begin{aligned} \frac{\partial \eta}{\partial t'} + \frac{\partial \eta u'}{\partial x'} + \frac{\partial \eta v'}{\partial y'} &= 0 \\ Fr_0^2 \left(\frac{\partial \eta u'}{\partial t'} + \frac{\partial \eta u'^2}{\partial x'} + \frac{\partial \eta u' v'}{\partial y'} \right) + \eta \frac{\partial \eta}{\partial x'} &= -\eta \frac{\partial z}{\partial x'} - \beta Fr_0^2 \tau'_{bx} \\ Fr_0^2 \left(\frac{\partial \eta v'}{\partial t'} + \frac{\partial \eta v'^2}{\partial y'} + \frac{\partial \eta u' v'}{\partial x'} \right) + \eta \frac{\partial \eta}{\partial y'} &= -\eta \frac{\partial z}{\partial y'} - \beta Fr_0^2 \tau'_{by} \\ \frac{\partial z}{\partial t} &= \mathcal{K}_e \left(\phi - \frac{(\sqrt{u'^2 + v'^2})^2 - u_*^2}{1 - u_*^2} \right) \\ \frac{\partial \phi}{\partial t} + \beta_x \frac{\partial u' \phi}{\partial x'} + \beta_y \frac{\partial v' \phi}{\partial y'} &= \mathcal{K}_d \left(\frac{(\sqrt{u'^2 + v'^2})^2 - u_*^2}{1 - u_*^2} - \phi \right) + \mathcal{D}_x \frac{\partial^2 \phi}{\partial x'^2} + \mathcal{D}_y \frac{\partial^2 \phi}{\partial y'^2} \end{aligned} \quad (4.19)$$

where the index 0 specifies the value of the variables at steady-state flow condition, and β corresponds to the ratio of half width over water depth. In Eq. 4.19, each variable is dimensionless by reach-averaged uniform flow quantities. The non-dimensional variables in Eq. 4.19 are

$$\begin{aligned} Fr_0 &= \frac{U_0}{\sqrt{gH_0}}, & \delta^2 &= \frac{d}{H_0}, & \mathcal{K}_e &= \frac{\pi c_e \beta (1 - u_*^2) \tan \theta}{6(1 - \zeta_b) Fr_0 \sqrt{s - 1} \delta}, & \mathcal{K}_d &= \frac{c_d \sqrt{s - 1} \beta}{\delta Fr_0} \\ u_* &= \sqrt{\theta_{cr} / \theta_0}, & \mathcal{D}_x &= \frac{D_x}{BU_0}, & \mathcal{D}_y &= \frac{D_y}{BU_0} \end{aligned} \quad (4.20)$$

4.3.2 Dispersion relation

Theories on bar formation in straight channels derive from perturbation analyses imposed on the governing equations (Papa, 2020). Linear theories focus on the stability of uniform flow when subjected to bar perturbation (typically in the form of a bar). For free bars, the focus is to study the system's spontaneous response to such perturbations, and for forced bars, the focus is to examine the system's reaction to external obstructions within the straight channel, such as channel narrowing and bridge piers. For free bars, linear stability analysis studies the resilience of the dimensionless governing differential system (referred to in Eq. 4.19) to imposed small perturbations with amplitude ϵ . The linear expansion of the dependent variables reads

$$(\eta, u', v', z, \phi) = (1, 1, 0, -x, 1) + \epsilon(\eta_1, u_1, v_1, z_1, \phi_1) + O(\epsilon^2) \quad (4.21)$$

$$(\tau'_{bx}, \tau'_{by}) = (\tau_{bx0}, 0) + \epsilon(\tau_{bx1}, \tau_{by1}) + O(\epsilon^2) \quad (4.22)$$

The variables are replaced in Eq. 4.19 while keeping the terms of $O(\epsilon)$ in order to study the effect of the perturbation. Each equation has terms with the same order of magnitude of $O(\epsilon)$ that are collected separately. The equations expressing the balance of $O(1)$ terms retrieve the uniform flow solution, which represents the trivial solution of the governing system. The equations expressing the balance of $O(\epsilon)$ terms are called the linearized equations because they allow to calculate the linear perturbations of our unknowns, i.e., $\{\eta_1, u_1, v_1, z_1, \phi_1\}$ and their dependency on (x, y, t) . In the framework of linear analysis, all terms having $O(\epsilon^2)$ or higher are discarded, and this is not the case of nonlinear theories, of course. The resulting equations reads

$$\begin{aligned} \frac{\partial \eta_1}{\partial t} + \frac{\partial \eta_1}{\partial x} + \frac{\partial u_1}{\partial x} + \frac{\partial v_1}{\partial y} &= 0 \\ Fr_0^2 \left(\frac{\partial u_1}{\partial t} + \frac{\partial u_1}{\partial x} \right) + \frac{\partial \eta_1}{\partial x} - \eta_1 + \frac{\partial z_1}{\partial x} + \beta Fr_0^2 \tau_{bx1} &= 0 \\ Fr_0^2 \left(\frac{\partial v_1}{\partial t} + \frac{\partial v_1}{\partial x} \right) + \frac{\partial \eta_1}{\partial y} + \frac{\partial z_1}{\partial y} + \beta Fr_0^2 \tau_{by1} &= 0 \\ \frac{\partial z_1}{\partial t} - \mathcal{K}_e \left(\phi_1 - \frac{2u_1}{1-u_*^2} \right) &= 0 \\ \frac{\partial \phi_1}{\partial t} + \beta_x \left(\frac{\partial u_1}{\partial x} + \frac{\partial \phi_1}{\partial x} \right) + \beta_y \frac{\partial v_1}{\partial y} - \mathcal{K}_d \left(\frac{2u_1}{1-u_*^2} - \phi_1 \right) - \mathcal{D}_x \frac{\partial^2 \phi_1}{\partial x^2} - \mathcal{D}_y \frac{\partial^2 \phi_1}{\partial y^2} &= 0 \end{aligned} \quad (4.23)$$

The shear stress terms τ_{bx1} and τ_{by1} in Eq. 4.23 in particular have been obtained in Appendix E. After the mathematical derivation, the shear stresses become $\tau_{bx1} = C_0 s_1 u_1 + C_0 s_2 \eta_1$, and $\tau_{by1} = C_0 v_1$. The variable C_0 corresponds to the friction coefficient of the undisturbed uniform flow, and variables s_1 and s_2 are given in Appendix E. The exponential form as a general solution (Colombini & Stocchino, 2012) can be admitted into the linear perturbations equations, i.e.,

Eq. 4.23 in order to obtain the solution such as

$$(\eta_1, u_1, v_1, z_1, \phi_1) = (\eta_2, u_2, v_2, z_2, \phi_2) e^{-i(ct - k_x x - k_y y)} \quad (4.24)$$

where $k_x = 2\pi h/L_x$ is the wavenumber in the longitudinal component being L_x the wavelength in the streamwise direction, whereas $k_y = 2\pi h/L_y = 2\pi/2w/h = \pi/2\beta$ is the wavenumber in the spanwise direction being L_y the wavelength in the spanwise direction. It is worth noting that the bedform is characterized by the transverse wavelength, considering two times the width of the channel.

In Eq. 4.24, the wave complex celerity is represented as $c = c_r + ic_i$, where the real part c_r , denotes the growth rate and the imaginary part c_i , denotes the dimensionless frequency of perturbations. The imaginary part of the wave speed being positive $c_i > 0$, the base flow is said to be unstable, and $c_i < 0$ implies a stable region. If $c_r > 0$, it indicates that the perturbation moves downstream, and if $c_r < 0$, it indicates upstream migration. Additionally, if $c_r > 1$, it means that the bed form perturbation moves faster than the base flow (Bohorquez & Ancey, 2015). After substituting Eq. 4.24 in Eq. 4.23, it leads to the following eigenvalues problem:

$$\left[\begin{array}{c} -ic \begin{pmatrix} 1 & 0 & 0 & 0 & 0 \\ 0 & Fr_0^2 & 0 & 0 & 0 \\ 0 & 0 & Fr_0^2 & 0 & 0 \\ 0 & 0 & 0 & 1 & 0 \\ 0 & 0 & 0 & 0 & 1 \end{pmatrix} + ik_x \begin{pmatrix} 1 & 1 & 0 & 0 & 0 \\ 1 & Fr_0^2 & 0 & 1 & 0 \\ 0 & 0 & Fr_0^2 & 0 & 0 \\ 0 & 0 & 0 & 0 & 0 \\ 0 & \beta_x & 0 & 0 & \beta_x \end{pmatrix} + ik_y \begin{pmatrix} 0 & 0 & 1 & 0 & 0 \\ 0 & 0 & 0 & 0 & 0 \\ 1 & 0 & 0 & 1 & 0 \\ 0 & 0 & 0 & 0 & 0 \\ 0 & 0 & \beta_y & 0 & 0 \end{pmatrix} \\ -k_x^2 \begin{pmatrix} 0 & 0 & 0 & 0 & 0 \\ 0 & 0 & 0 & 0 & 0 \\ 0 & 0 & 0 & 0 & 0 \\ 0 & 0 & 0 & 0 & 0 \\ 0 & 0 & 0 & 0 & -\mathcal{D}_x \end{pmatrix} - k_y^2 \begin{pmatrix} 0 & 0 & 0 & 0 & 0 \\ 0 & 0 & 0 & 0 & 0 \\ 0 & 0 & 0 & 0 & 0 \\ 0 & 0 & 0 & 0 & 0 \\ 0 & 0 & 0 & 0 & -\mathcal{D}_y \end{pmatrix} + \begin{pmatrix} 0 & 0 & 0 & 0 & 0 \\ \mathcal{X}C_0s_2 - 1 & \mathcal{X}C_0s_1 & 0 & 0 & 0 \\ 0 & 0 & \mathcal{X}C_0 & 0 & 0 \\ 0 & \frac{2\mathcal{K}_e}{1-u_*^2} & 0 & 0 & -\mathcal{K}_e \\ 0 & -\frac{2\mathcal{K}_d}{1-u_*^2} & 0 & 0 & \mathcal{K}_d \end{pmatrix} \end{array} \right] \cdot \begin{bmatrix} \eta_2 \\ \bar{u}_2 \\ \bar{v}_2 \\ z_2 \\ \phi_2 \end{bmatrix} = 0 \quad (4.25)$$

where \mathcal{X} stands for $\mathcal{X} = Fr_0^2\beta$. The algebraic system of five equations with five unknowns can be written as $AX = 0$ which admits a non-trivial solution only if the determinant of the matrix of the coefficients A is different from zero. The dispersion equation is obtain by imposing $\det(A) = 0$ which has a general algebraic form, that provides the temporal growth rate of the disturbance for known wavelength or wave number.

In the subsequent section, the neutral curves are plotted by solving $\det(A) = 0$ using Mathematica. To produce these curves, the approach involves seeking the case where the complex part of the wave speed is set to zero (the boundary between $c_i > 0$ and $c_i < 0$), achieved by varying two variables under study while treating the others as constants.

4.3.3 Neutral curves

The wave speed imaginary component c_i was calculated to produce the neutral curves after a number of variables - as was covered in the previous section - were fixed. The neutral curves

Chapter 4. Stochastic modeling of bedload transport and bar development

were obtained by solving the system of $\det(A) = 0$. Such that by varying two variables and solving $\det(A) = 0$ numerically for c , the imaginary part of the solution is obtained and used to produce the corresponding contour plot. This contour plots can be divided into two domains. The domain where $c_i > 0$ is referred as the unstable domain since bed formation appears, when $c_i < 0$, on the other hand, the domain is said to be stable.

Along with these variables, the fixed variables also include the ratio of grain-size-to-water-depth, δ_0^2 , the normal and longitudinal non-dimensional diffusivities, \mathcal{D}_y and \mathcal{D}_x , Froude number Fr_0 , bed slope S_0 , lateral wavenumber k_y , ratio of half width to flow depth β , critical Shields number θ_{cr} and porosity ζ_b . The variables were fixed to the following values: $\delta_0^2 = 0.01$, $\mathcal{D}_x = 0.01$, $\mathcal{D}_y = \mathcal{D}_x/10$, $S_0 = 1\%$, $\beta = 4$, and $\theta_{cr} = 0.047$ when they have not been mentioned.

A dataset is collected based on laboratory experiments for studying the alternate bars conducted by Jaeggi, 1984, Sukegawa, 1971, Kinoshita, 1961, Muramoto and Fujimata, 1978, Ashida and Shiomi, 1966, Ikeda, 1984, Chang et al., 1971, Fujita and Muramoto, 1982, Lanzoni, 2000, M. Garcia and Niño, 1993, Redolfi et al., 2020, Garcia Lugo et al., 2015, Ahmari and Da Silva, 2011, Dhont, 2017, Nelson and Morgan, 2018 to evaluate the validity of the neutral curves. The majority of the dataset is taken from Redolfi, 2021 and has been extended. The minimum and maximum characteristics of the experiments are presented in Table 4.1. The minimum and maximum values of the observed wavenumber in the longitudinal and transversal directions, as well as the half-width-to-water-depth ratio, are determined and reported in Table 4.2.

In Fig. 4.1, the initial bed slope varied among $S_0(\%) = [0.1, 0.2, 0.5, 1.0, 2.0, 5.0]$ while the rest of parameters assumed to be constant to draw the boundaries between the stable and unstable domains (the neutral curves) in the $\{k_x, Fr\}$ -, $\{k_x, \beta\}$ -, $\{k_x, k_y\}$ -, and $\{k_x, \delta^2\}$ -planes. In Fig. 4.1(a), Froude number versus the longitudinal wavenumber have been plotted. By assuming a constant slope, the friction factor can be obtained with Eq. 4.7. As the Froude number is increased, the region of instability for the formation of bed forms with smaller longitudinal wavenumbers becomes increasingly restricted, and this trend is reflected in the behavior of the experimental data points as well.

For small Froude numbers, neutral curves have larger k_x values, i.e., appearing forms with a smaller streamwise dimensionless wavelength that is in line with theoretical and experimental studies by Inoue et al., 2020, and Kennedy, 1963. The boundary between stable and unstable parts can be represented by the function: $1/Fr^2 = \alpha k_x \tanh k_x$, where $\alpha = 8.5$. However, the critical Froude number for the formation of dunes occurs when $\alpha = 1$ (Parker, 1975; Reynolds, 1965).

Table 4.1: Maximum and minimum of experimental characteristics, namely, width, slope of the channel, water depth and discharges observed in the dataset are mentioned.

Researcher	Width cm	Slope -	Water depth cm	Discharges cm ³ /s	Grain size mm
Jaeggi, 1984 (PVC)	30-30	0.0032-0.0124	0.78-4.13	250-3900	3-3
Jaeggi, 1984 (Sand)	30-30	0.0065-0.0128	1.57-3.72	1650-6100	0.52-1.8
Sukegawa, 1971	15-31	0.005-0.02	0.69-5.85	200-13000	0.45-3.55
Kinoshita, 1961	13.2-13.2	0.0125-0.1	0.39-1.61	200-900	0.38-1.7
Muramoto and Fujimata, 1978	13.2-13.2	0.0057-0.0198	0.69-5.91	3000-12000	0.99-0.99
Ashida and Shiomi, 1966	50-50	0.01-0.01429	0.78-2.34	1000-5000	1-1
Ikedo, 1984	32-32	0.0048-0.0186	0.98-3.58	1010-5240	0.13 - 0.13
Chang et al., 1971	45.7-91.4	0.00044-0.0064	1.92-7.59	2832-14160	0.58-3.2
Fujita and Muramoto, 1982	30-200	0.0033-0.01	0.69-3.63	1500-12000	0.88-0.99
Lanzoni, 2000	150-150	0.00162-0.00517	3.3-8.3	20000-47000	0.048- 0.048
M. Garcia and Niño, 1993	40-40	0.0032-0.0056	0.77-2.21	750-2981	0.053-0.053
Redolfi et al., 2020	30.5-30.5	0.01-0.01	1.06-1.99	1000-3000	0.1-0.1
Garcia Lugo et al., 2015	15-60	0.01-0.01	1.17-1.90	1500-2500	0.1-0.1
Ahmari and Da Silva, 2011	-	0.01-0.06	0.65-8.3	240-65300	0.065-0.75
Dhont, 2017	60-60	0.016-0.017	4-4	15000-15000	5.5-5.5
Nelson and Morgan, 2018	88-88	0.0044-0.0055	10-11	49200-67400	3.2-3.3

Chapter 4. Stochastic modeling of bedload transport and bar development

Researcher	Wavelength cm	β -	k_x -	k_y -
Jaeggi, 1984 (PVC)	168-608	3.63-19.23	0.0152-0.154	0.0408-0.216
Jaeggi, 1984 (Sand)	280-780	4.03-9.55	0.0250-0.0617	0.0822-0.195
Sukegawa, 1971	82-396	2.56-20.40	0.0184-0.255	0.0385-0.306
Kinoshita, 1961	60-194	4.1-16.93	0.0163-0.169	0.0464-0.192
Muramoto and Fujimata, 1978	216-720	7.58-39.86	0.00947-0.0471	0.0197-0.104
Ashida and Shiomi, 1966	280-456	10.68-32.65	0.0170-0.0418	0.0245-0.0735
Ikeda, 1984	120-380	4.47-16.33	0.0202-0.161	0.0481-0.176
Chang et al., 1971	411.5-2438.4	5.86-23.81	0.00745-0.0517	0.0330-0.134
Fujita and Muramoto, 1982	280-2010	10.00-24.10	0.0135-0.0343	0.0326-0.0785
Lanzoni, 2000	750-1130	9.04-22.73	0.0188-0.0695	0.0346-0.0869
M. Garcia and Niño, 1993	320-400	9.05-25.98	0.0138-0.0418	0.0302-0.0868
Redolfi et al., 2020	161-344	7.66-14.39	0.0223-0.0778	0.0546-0.103
Garcia Lugo et al., 2015	-	10.95-24.29	-	0.0647-0.287
Ahmari and Da Silva, 2011	-	4.58-42.03	-	0.0374-0.343
Dhont, 2017	400-700	7.5-7.5	0.0071-0.01	0.418-0.418
Nelson and Morgan, 2018	200-250	4-4	0.28-0.28	-

Table 4.2: Maximum and minimum of the bar wavelength, half-width-to-water-depth ratio β , and wavenumber in the longitudinal k_x and transversal k_y directions, respectively, are presented.

To investigate the possible existence of a critical threshold, β_c , influencing the formation of alternate bars, the neutral curve was plotted in the $\{k_x, \beta\}$ -plane, illustrated as a function of the initial bed slope in Fig. 4.1(b). The results indicated that as the initial bed slope increases, the unstable region occupies a smaller area in the $\{k_x, \beta\}$ -plane. This suggests that significant slopes provide less diversity for the formation of alternate bars, in agreement with physical intuition. Interestingly, we observed that smaller values of β corresponded to a wider range of potential k_x for the formation of bars, which is consistent with the experimental data points.

Colombini et al., 1987 conducted a linear stability analysis on the conventional shallow water equation and used the Meyer-Peter-Müller sediment transport model, complemented by the Engelund, 1981 formula for direction of particle movement. Their methodology predicts the existence of critical β_c for the formation of alternate bars. Later, Redolfi, 2021 found inconsistency between the formation of alternate bars in some flume experiments, and critical β value predicted by Colombini et al., 1987. Nevertheless, these experimental data points were captured in the unstable domain in Fig. 4.1(b).

Additionally, Fig. 4.1(b) shows that the critical β_c for bed formation varies with the initial bed slope. Chang et al., 1971 found that bars formed only when $\beta < 24$. Similarly, Kinoshita, 1957 proposed the criterion $\beta < 10$ to 40 for the formation of alternate bars. In 2002, Repetto et al., 2002 studied the stability of channels with varying channel width and in line with our findings

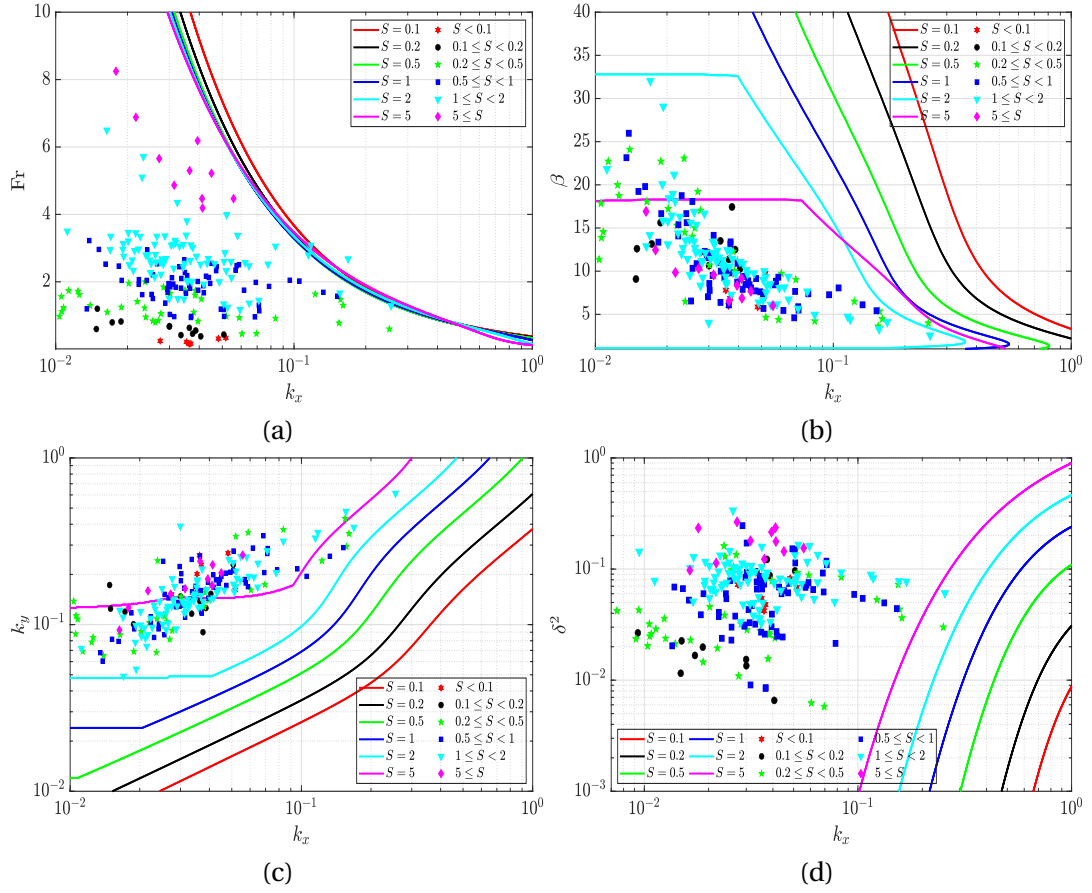


Figure 4.1: Neutral curve of free alternate bars in (a) $\{k_x, Fr\}$ -plane, (b) $\{k_x, \beta\}$ -plane, (c) $\{k_x, k_y\}$ -plane, (d) $\{k_x, \delta_0^2\}$ -plane as a function of bed initial slope. The experimental data-points are categorized based on the initial bed slope.

concluded the region of instability in $\{k_x, \beta\}$ -plane widens with decreasing the Shields number - equivalent by decreasing bed slope as the other parameters are fixed.

In the various experimental runs illustrated in Fig. 4.1(c), it can be observed that a significant longitudinal wavenumber often corresponds to a large normal wavenumber. Additionally, the stability analysis results show a trend similar to the experimental data.

The neutral curves displayed in Fig. 4.1(d) illustrate how δ_0^2 varies as a function of k_x and bed slope. These neutral curves indicate that lower bed slopes are associated with larger domains of instability. The condition $1/(\delta_0^{0.66}(2\beta)^{0.66}) < 0.45$ must be satisfied for the formation of alternate bars according to Muramoto and Fujimata, 1978. This condition aligns with the neutral curves depicted in Fig. 4.1(d), as a smaller value of δ_0^2 indicates less favorable conditions for alternate bar formation. Moreover, the results presented in Fig. 4.1(d) are in agreement with the findings of Eekhout et al., 2013, who showed that a smaller value of δ_0^2 leads to a smaller domain of instability.

Chapter 4. Stochastic modeling of bedload transport and bar development

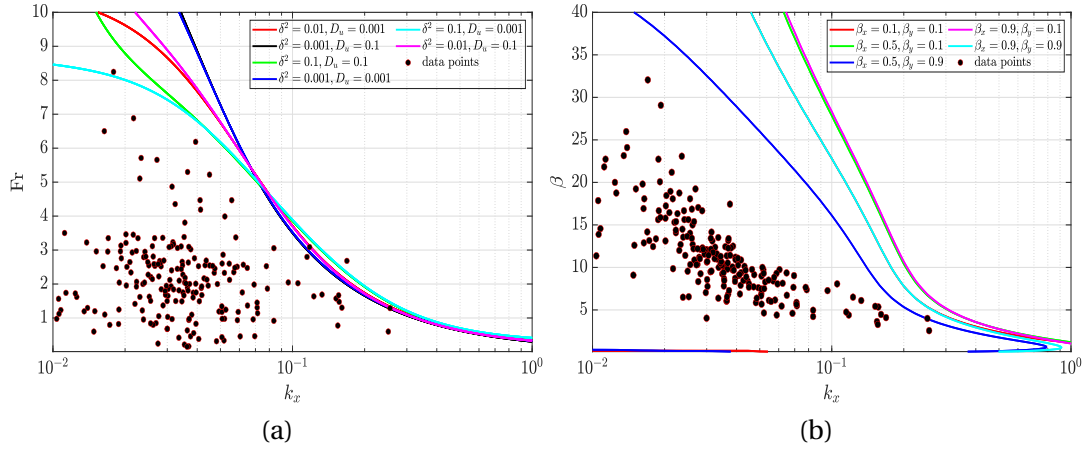


Figure 4.2: (a) Neutral curve of free alternate bars in the $\{k_x, Fr\}$ -plane as a function of δ_0^2 and diffusion, (b) neutral curve of free alternate bars in the $\{k_x, \beta\}$ -plane as a function of β_x and β_y . The experimental data-points are shown with black circles.

In Fig. 4.2(a), we have explored the influence of diffusivity and grain size-to-flow depth ratio on the neutral curves. Unlike the results in Fig. 4.1, the slope is not fixed, and have been obtained using Eq. 4.7.

Figure 4.2(a) shows that for larger values of k_x , the neutral curves remain unchanged regardless of the diffusivity or the grain size-to-flow depth ratio. However, as k_x decreases to 0.1, δ_0^2 becomes a crucial factor, and the results align with those obtained in Fig. 4.1(d), where a larger δ_0^2 creates a more favorable condition for alternate bar formation. Furthermore, diffusivity appears to play a role for $k_x < 0.03$, as an increase in diffusivity results in an increase in the unstable domain. This outcome is consistent with the results of other studies on bed formation, such as Bohorquez and Ancy, 2016, who demonstrated that diffusivity favors the formation of antidunes, particularly those with long wavelengths and small wavenumbers.

Figure 4.2(b) examines the significance of sediment velocity and direction. In this model, the sediment velocity and direction depend on the modeling of β_x and β_y . The findings indicate that the magnitude of $\beta_{x,y}$ does not significantly affect the results, provided that the ratio β_x/β_y remains consistent. This is exemplified in the case of the red neutral curve, where $\beta_{x,y} = 0.1$, and the blue light neutral curve, where $\beta_{x,y} = 0.9$; these two curves overlap. However, the ratio β_x/β_y plays a crucial role in defining the unstable domain. The results suggest that when this ratio exceeds 1, the unstable domain is larger than when it is less than 1.

4.4 Numerical scheme

4.4.1 Architecture of the numerical model

This section provides an overview of the numerical scheme. The non-linear set of governing equations, Eq. 4.1–Eq. 4.4 and Eq. 4.8, reformulated into a vector equation as

$$\frac{\partial \mathbf{q}}{\partial t} + \frac{\partial \mathbf{f}}{\partial x} + \frac{\partial \mathbf{g}}{\partial y} + \frac{\partial \mathbf{k}}{\partial x} + \frac{\partial \mathbf{p}}{\partial y} = \mathbf{s}_b + \mathbf{s}_f \quad (4.26)$$

The conserved variables are denoted by \mathbf{q} vector containing five conserved quantities as

$$\mathbf{q} = [h, h\bar{u}, h\bar{v}, b, y_b]^T \quad (4.27)$$

The Cartesian components of convective fluxes in the streamwise and spanwise directions are expressed by \mathbf{f} and \mathbf{g} , respectively, and have the following components

$$\mathbf{f} = \left[h\bar{u}, \frac{(h\bar{u})^2}{h} + \frac{gh^2}{2}, h\bar{u}\bar{v}, \beta_x \bar{u}b, 0 \right]^T, \quad \mathbf{g} = \left[h\bar{v}, h\bar{u}\bar{v}, \frac{(h\bar{v})^2}{h} + \frac{gh^2}{2}, \beta_y \bar{v}b, 0 \right]^T \quad (4.28)$$

However, the fluxes \mathbf{f} , and \mathbf{g} going to be handled in the hyperbolic subproblem; the fluxes \mathbf{k} , and \mathbf{p} as

$$\mathbf{k} = \left[0, 0, 0, -D_x \frac{\partial b}{\partial x}, 0 \right]^T, \quad \mathbf{p} = \left[0, 0, 0, -D_y \frac{\partial b}{\partial y}, 0 \right]^T \quad (4.29)$$

will be handled in the parabolic subproblem. The source and sink terms are

$$\mathbf{s}_b = \left[0, -gh \frac{\partial y_b}{\partial x}, -gh \frac{\partial y_b}{\partial y}, 0, 0 \right]^T \quad (4.30)$$

$$\mathbf{s}_f = \left[0, -C_f \bar{u} \sqrt{\bar{u}^2 + \bar{v}^2}, -C_f \bar{v} \sqrt{\bar{u}^2 + \bar{v}^2}, \lambda - \kappa b + \xi_b \sqrt{2\mu b}, \frac{\kappa V_p B^{-1} \langle b \rangle - \tilde{\lambda}}{1 - \zeta_p} \right]^T \quad (4.31)$$

These sink terms take the bed slopes and friction losses into consideration within the momentum equations, as well as bedload source terms and the deposition and entrainment rates within the Exner equation. The friction source term, as a function of depth and momentum, can be rewritten as

$$-\frac{\tau_{bx}}{\rho} = -C_f \bar{u} \sqrt{\bar{u}^2 + \bar{v}^2} = -C_f \frac{\sqrt{(h\bar{u})^2 + (h\bar{v})^2}}{h^2} (h\bar{u}) \quad (4.32)$$

In all simulations, the friction coefficient C_f is set to 0.004.

4.4.2 Finite volume method

The equation Eq. 4.26 is solved over a rectangular grid \mathcal{C} with the node coordinates of $\mathcal{C}_{ij} = [x_{i-1/2}, x_{i+1/2}] \times [y_{j-1/2}, y_{j+1/2}]$. The governing equations were decomposed using the fractional-step method, distinguishing between a hyperbolic subproblem that manages the source terms, and a parabolic subproblem that addresses the diffusive component of the governing equations, as detailed in Toro, 2013.

To solve the hyperbolic system, a high-resolution Godunov-type method was employed, i.e., the f -wave (an abbreviation for flux waves) Riemann solver—a technique explained by Bader et al., 2014; Bale et al., 2003; LeVeque, 2011, while for solving the parabolic subproblem, we used the Crank-Nicholson method. The governing equation involves splitting the governing equation into: i. The non-homogeneous hyperbolic subproblem: $\partial_t \mathbf{q} + \partial_x \mathbf{f}(\mathbf{q}) + \partial_y \mathbf{g}(\mathbf{q}) = \mathbf{s}_b + \mathbf{s}_f$, and ii. The parabolic subproblem: $\partial_t \mathbf{q} = -\partial_x \mathbf{k} - \partial_y \mathbf{p}$.

The uniform hyperbolic equation in the longitudinal direction is given by $\mathbf{q}_t + \mathbf{f}_x = 0$. Alternatively, in a non-conservative representation, it can be written as $\mathbf{q}_t + \mathbf{A}(\mathbf{q}) \cdot \mathbf{q}_x = 0$, where $\mathbf{A} = \nabla_{\mathbf{q}} \mathbf{f}$ represents the Jacobian matrix. The linearized matrix $\hat{\mathbf{A}}$'s right eigenvectors are denoted as \mathbf{r}^p where $1 \leq p \leq m = 5$ and its associated eigenvalues are $\hat{\lambda}^p$. The eigenvalues are derived as follows

$$\hat{\lambda}^1 = \bar{u} - \hat{c}, \quad \hat{\lambda}^2 = \bar{u} + \hat{c}, \quad \hat{\lambda}^3 = \hat{u}, \quad \hat{\lambda}^4 = \beta \bar{u}, \quad \text{and} \quad \hat{\lambda}^5 = 0$$

where $\hat{c} = \sqrt{g\bar{h}}$ (please refer to Appendix F). The set of governing equations creates five waves traveling upstream or downstream, depending on their velocity sign. These five wave speeds are plotted in Fig. 4.3 as a function of Froude number.

The algorithm uses approximated averaged flux values as initial data to solve the Riemann problem between the reconstructed values. The solution of the Riemann problem can be obtained through waves resulting from decomposing the jump in fluxes. In this method, the flux difference is split into waves rather than using the cell average values, which is a key aspect of the flux-based wave decomposition methods. This methodology allows for the direct incorporation of bed slope source terms \mathbf{s}_b into formulation (Bale et al., 2003).

By integrating the bed slope source terms directly into the splitting, a well-balanced scheme is attained (Bale et al., 2003). The flux difference in the streamwise direction can thus be split into f -waves, such as

$$\mathbf{f}(\mathbf{Q}_{i,j}) - \mathbf{f}(\mathbf{Q}_{i-1,j}) - \Delta x \mathbf{S}_{i-1/2,j}^b = \sum_{p=1}^m \psi_{i-1/2,j}^p \mathbf{r}_{i-1/2,j}^p \equiv \sum_{p=1}^m \mathcal{Z}_{i-1/2,j}^p \quad (4.33)$$

where the f -waves are $\mathcal{Z}_{i-1/2,j}^p$. Therefore, bed slope source terms \mathbf{s}_b , are handled in the Riemann solver, while \mathbf{s}_f explicitly treated. Here $\mathbf{S}_{i-1/2,j}^b$ is suitable average of \mathbf{s}_b between the neighboring states to obtain them at cell interfaces, and \mathbf{r}^p is the right eigen vector of

the Roe averaged wave decomposition of the Riemann problem. The Roe averaged wave decomposition of the Riemann problem for the presented set of equations is derived in Appendix F and $\psi_{i-1/2,j}$ being

$$\psi_{i-1/2,j} = \mathbf{R}_{i-1/2,j}^{-1} \left(\mathbf{f}(\mathbf{Q}_{i,j}) - \mathbf{f}(\mathbf{Q}_{i-1,j}) - \Delta x \mathbf{S}_{i-1/2,j}^b \right) \quad (4.34)$$

where $\mathbf{R}_{i-1/2,j}^{-1}$ is the matrix of right eigenvectors of the approximated Jacobian $\hat{\mathbf{A}}_{i-1/2}$. The fully discrete scheme is thus

$$\mathbf{Q}_{i,j}^* = \mathbf{Q}_{i,j}^n - \frac{\Delta t}{\Delta x} (\mathcal{A}^+ \Delta \mathbf{Q}_{i-1/2,j} + \mathcal{A}^- \Delta \mathbf{Q}_{i+1/2,j}) \quad (4.35)$$

$$- \frac{\Delta t}{\Delta y} (\mathcal{B}^+ \Delta \mathbf{Q}_{i,j-1/2} + \mathcal{B}^- \Delta \mathbf{Q}_{i,j+1/2}) + \Delta t \mathbf{S}_{i,j}^f \quad (4.36)$$

where \mathcal{A}^\pm determines the direction of the fluctuations and $\mathbf{Q}_{i\mp 1/2,j}$ their origin—same definition applies for the y-direction. The net-updates $\mathcal{A}^\pm \Delta \mathbf{Q}_{i\mp 1/2,j}$ are calculated by solving the one-dimensional Riemann problem on the vertical edges of the cell. It describes the fluctuations in the positive direction that are entering the cell from the left as well as the fluctuations in the negative direction that are entering the cell from the right.

Similar, the net-updates $\mathcal{B}^\pm \Delta \mathbf{Q}_{i,j\mp 1/2}$ are the fluctuations in the positive direction that are entering the cell from the bottom as well as the fluctuations in the negative direction that are entering the cell from the top cell edge, which require Riemann to be computed on the horizontal edges. Adding these fluctuations to the current cell value determines the cell quantity for the next time step. For example, the fluctuations in the streamwise direction can be calculated by

$$\begin{aligned} \mathcal{A}^+ \Delta \mathbf{Q}_{i-1/2,j} &= \sum_{p: s_{i-1/2,j}^p > 0} \mathcal{Z}_{i-1/2,j}^p \\ \mathcal{A}^- \Delta \mathbf{Q}_{i+1/2,j} &= \sum_{p: s_{i-1/2,j}^p < 0} \mathcal{Z}_{i+1/2,j}^p \end{aligned} \quad (4.37)$$

The solution \mathbf{Q}_i^* is then inserted into the parabolic set of equations as the input value. The particle diffusivity terms can be integrated by using Crank–Nicolson. Diffusion terms in the streamwise and transverse directions are given by $D_x = \bar{u}_s \Delta x / 2$ and $D_y = \bar{v}_s \Delta x / 2$, respectively. Since $v \ll 0$, the particle velocity $v_s = \beta_x v \ll 0$ is very small, and consequently, $D_y \ll 0$. Therefore, we have omitted D_y and have implemented only the diffusion term in the streamwise direction using the Crank–Nicolson method.

The solution of the non-homogeneous hyperbolic subproblem is inserted into the Crank–Nicolson algorithm as the input parameter, and the output is the updated solution at t_{n+1}

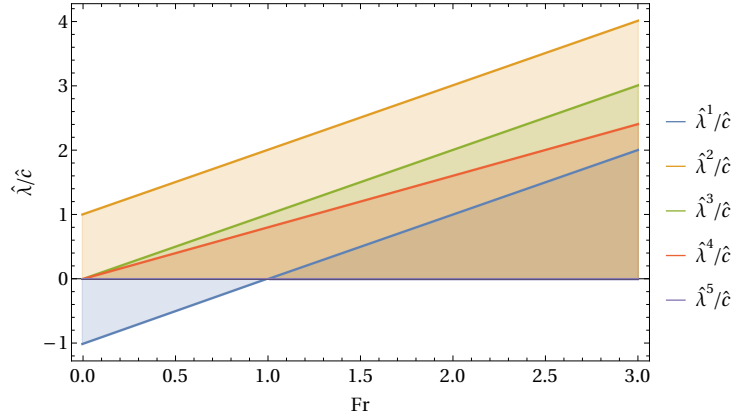


Figure 4.3: Relationship between characteristic velocities and Froude number. For a better illustration, $\beta = 0.8$ has been used in this plot.

$$\mathbf{Q}_{i,j}^{n+1} = \mathbf{Q}_{i,j}^* + \frac{\Delta t}{2\Delta x^2} \left(\Psi(\mathbf{Q}_{i,j}^*) + \Psi(\mathbf{Q}_{i,j}^{n+1}) \right) \quad (4.38)$$

where

$$\Psi(\mathbf{Q}) = \left[0, 0, 0, D_x b_{i-1,j} - 2D_x b_{i,j} + D_x b_{i+1,j}, 0 \right]^T \quad (4.39)$$

This linear system of equations, Eq. 4.38 is solved at each time step using the SuiteSparse library (Davis, 2006).

4.4.3 Numerical implementation

The described set of equation is computed within the rectangular domain \mathcal{C} , bounded by $0 \leq x \leq \Lambda_b = 17$ m and $0 \leq y \leq w = 60$ cm. The mesh consists of $n_x = 255$ and $n_y = 9$ cells along the longitudinal and transversal directions, respectively, each uniformly sized at 0.067 m. Furthermore, the Courant–Friedrichs–Lewy (CFL) condition has been set at a value of 0.5. The initial values for $h(x, y, t)|_{t=0}$, $\bar{u}(x, y, t)|_{t=0}$, $\bar{v}(x, y, t)|_{t=0}$, and $b(x, y, t)|_{t=0}$ are set to steady-state values

$$h(x, y, 0) = h_{ss}, \bar{u}(x, y, 0) = \bar{u}_{ss} \text{ and } b(x, y, 0) = \langle b \rangle_{ss} \quad (4.40)$$

where h_{ss} and \bar{u}_{ss} are the flow depth and depth-averaged velocity being 4.5 cm and 0.56 m/s, respectively, and $\langle b \rangle_{ss}$ is calculated from Eq. 4.12 and Eq. 4.13. The initial condition for the $y_b(x, y, t)|_{t=0}$ is based on Defina's work. Following Defina, 2003, an intentional perturbation was introduced along the bed, characterized as follows:

$$y_b(x, y, 0) = \epsilon \sin(2\pi x / \Lambda_b) \cos(\pi y / w) \quad (4.41)$$

where ϵ denotes the amplitude of perturbation, which is set to 1 cm. It is worth mentioning that Defina, 2003 showed that the initial disturbance amplitude does not impact the equilibrium bar characteristics. However, an increase in ϵ decreases the time required to attain equilibrium.

The solver written in Fortran, was compiled via the Intel® Fortran Compiler (version 2021.2.0) on a Linux 5.15.0-94-generic x86_64 platform and executed on processors of the Intel(R) Core(TM) i7-7700K CPU @ 4.20 GHz. The real-time to simulation-time ratio is approximately 5, indicating that numerical simulations require roughly four days to simulate $T = 17$ hours of real-time for the specified flume geometry and mesh size.

4.5 Experimental dataset

In this section, we describe three steady-state experiments that will be used to evaluate the accuracy of the numerical simulation. These experiments are performed in a wide gravel-bed flume under supercritical flow conditions (Dhont, 2017). The high-resolution data collected during the experiments facilitated the comparison between numerical and experimental outcomes.

The experiments were executed in a gravel-bed flume with dimensions of 17 m in length and 60 cm in width. Due to technical constraints, the effective operational length of the flume was 14 m, with the last 1.5 m at each end being excluded—due to technical issues. The bed was composed of natural gravel, was flattened, and initially had a height of 31.5 cm. The sediment was characterized by $d_{50} = 6$ mm, mean diameter of $d = 5.5$ mm, a standard deviation of 1.2 mm, and a density of $\rho_s = 2660$ kg/m³.

The water discharge and sediment feed rates at the inlet were set to 15 L/s and 2.5, 5, and 7.5 g/s, respectively. Throughout the entire experiment, both the water discharge and sediment feeding rates were kept constant. Every 10 minutes, bed topography and flow depth were scanned using a laser detection technique (image processing) and ultrasonic probes (signal processing), respectively. In Table 4.3, the input parameters of the conducted experiments are reported, along with the measured values of height H_b , and wavelength L_b of the alternate bars.

	E. 1	E. 2	E. 3
Flow rate (L/s)	15	15	15
Flume slope (%)	1.6	1.6	1.7
Sediment feeding rate (g/s)	2.5	5.0	7.5
Bar height (H_b in cm)	1-5	1-5	1-5
Bar wavelength (L_b in m)	2-8	2-8	2-8

Table 4.3: Experiment’s input parameters and alternate bar characteristics.

4.6 Model prediction

Model examination is a crucial step that involves comparing model predictions with observed data to assess the accuracy and reliability of the model. In this section, to validate the numerical simulation, it has been applied to the experimental dataset described in § 4.5. Alongside the study of bedload transport rates, the high resolution experimental data allowed for an analysis of bar characteristics, namely i. height, and wavelength of the alternate bars, ii. erosion and deposition rates of the bed, and iii. alternate bars growth rate.

The model calibration is a primary step when employing hydraulic models. The calibration can be conducted through the analytical derivation, or it can be accomplished by using experimental data. The rates of deposition and entrainment were determined using Eq. 4.16, with the values $\kappa = \sigma - \mu = 5.2$ 1/s, and $\mu = 0.85\sigma = 29.43$ 1/s. For each of the simulation runs, the entrainment rate $\tilde{\lambda}$ was determined by employing both Eq. 4.13 and Eq. 4.14, which facilitated the calculation of $\tilde{\lambda} = \kappa / \bar{u}_s \bar{q}_s$. In this approach, the experimental data is used for calibrating the parameter $\tilde{\lambda}$.

4.6.1 Bedload transport time series

In this section, our main focus will be on evaluating model predictions regarding to bedload transport. We will achieve this by applying numerical simulations to laboratory experiments. Bedload transport estimation with sufficient accuracy is crucial as it significantly impacts the prediction of bed topography and, consequently, the hydraulic conditions. Inaccurate estimation of hydraulic conditions can lead to erroneous predictions of bedload transport, creating a problematic feedback loop.

Figure 4.4 displays the bedload transport time series resulting from applying the numerical solver to the three experiments described in § 4.5. River sediment dynamics can be better understood by using the bedload transport time series alongside with the measured bed topography. It is especially useful for examining how bedload transport affects hydro-morphodynamic processes such as hydraulic conditions, river bank development, and bed erosion and deposition by using joint analysis (Dhont, 2017).

The bedload transport time series fluctuates around a mean value of 2.5 g/s for simulation run 1, with a variance of 0.75 (g/s)². Over the entire simulation run period, the coefficient of variation was 35%. The particle transport fluctuations exceed $q_s / \bar{q}_s = 2.2$, whereas the experiment shows a higher ratio. Dhont and Ancy, 2018 found that around 80% of bedload pulses are caused by sediment waves sent out by pools due to the destruction of bars at the downstream slope face of the bars. Therefore, the absence of such high bedload pulses could be attributed to the omission of the bar failure mechanism in the numerical simulation.

The time-averaged bedload transport is presented in Fig. 4.5 (left), demonstrating that bedload transport converges to the mean sediment transport after a short time, whereas experiments

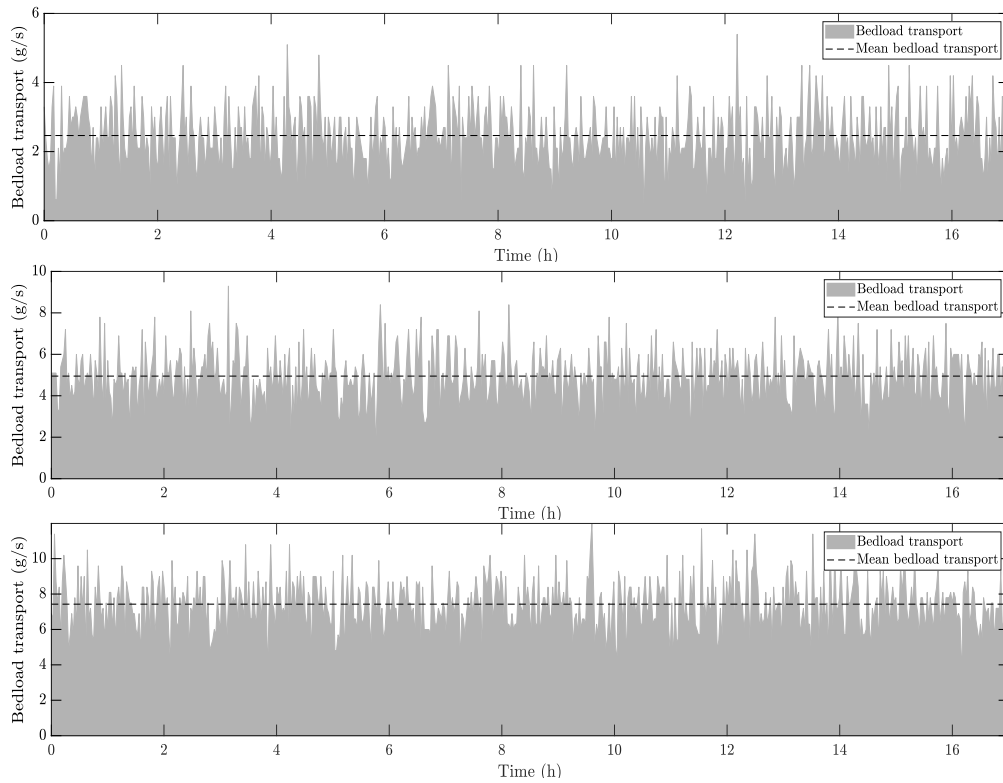


Figure 4.4: Bedload transport time series by applying the numerical solver to laboratory experiments (E.1 to E.3, respectively). The averaged bedload transport and its variance respectively are: $\bar{q}_s = 2.5 \text{ g/s}$, $\sigma^2 = 0.75 \text{ (g/s)}^2$; and $\bar{q}_s = 4.9 \text{ g/s}$, $\sigma^2 = 1.5 \text{ (g/s)}^2$; and $\bar{q}_s = 7.4 \text{ g/s}$ and $\sigma^2 = 2.0 \text{ (g/s)}^2$.

usually take a few hours to converge to the mean bedload values. The reason may lie in setting the initial condition of the numerical solver to steady-state values.

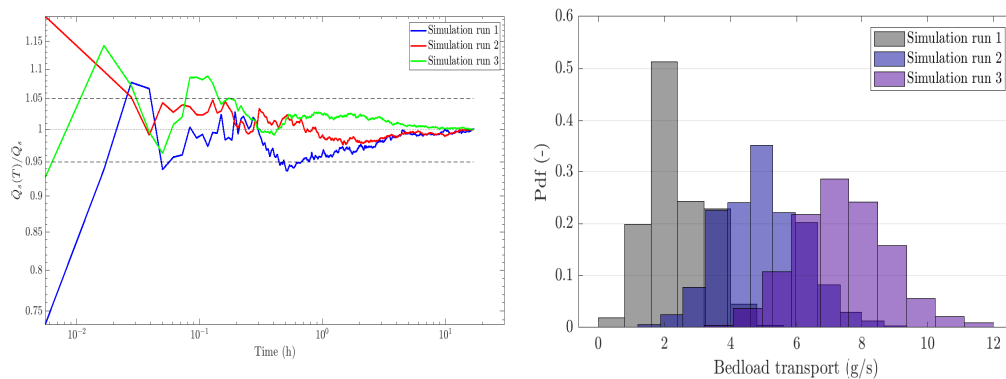


Figure 4.5: (left) Time-averaged bedload transport rate: $\bar{Q}_s(\mathcal{T}) = \int_0^{\mathcal{T}} Q_s(t) dt / \mathcal{T}$, converges to its mean value over the entire simulation time. The dashed lines represent $\bar{Q}_s \pm 5\% \bar{Q}_s$, (right) The probability density function of bedload transport corresponds to three simulation runs.

Chapter 4. Stochastic modeling of bedload transport and bar development

The probability density function of the bedload transport is plotted in Fig. 4.5 (right), showing that simulations associated with higher bedload transport have a larger bedload variation. The reason can be explained as follows: with increased sediment availability and high transport, particle interactions will increase, resulting in larger fluctuations in sediment movement and a wider variation in sediment transport rates.

4.6.2 Alternate bar characteristics

Alternate bar wavelength and height

Due to the stochastic nature of the system under investigation, analyzing the characteristics of alternate bars involves comparing the mean values of bar geometry. Figure 4.6(left) illustrates the three-dimensional bed topography obtained by applying the numerical solver to experiment 1 at $t = 17$ hours, indicating that the stochastic bedload model is capable of capturing bed topography within the same range of variations observed in experiment, as shown in Fig. 4.6(right).

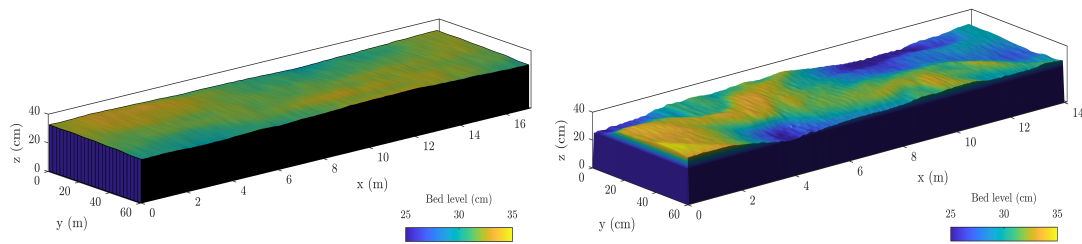


Figure 4.6: Illustration of the appearance of alternate bars based on (left) simulation and (right) experiment at $t = 17$ hours.

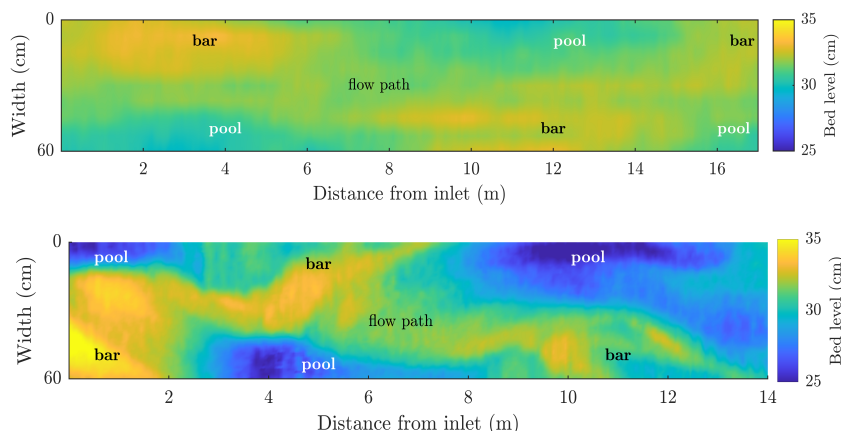


Figure 4.7: Top plots of bed topography based on (top) simulation and (bottom) experiment at $t = 17$ hours.

The top view of Fig. 4.6 is presented in Fig. 4.7. In both figures, the bars, pools, and flow path

	S. 1	S. 2	S. 3
Bar height (H'_b in cm)	1.4	2.3	3.4
Bar wavelength (L'_b in m)	8.6	8.6	8.6

Table 4.4: The wavelength and height of alternate bars based on numerical simulation.

are depicted. The numerical simulations successfully reproduce the alternating three bars in the gravel-bed channel with two pools between them, reflecting experimental observations through our numerical modeling.

Two longitudinal profiles along the channel and on two transversal sides of the flume have been considered in order to study the bar geometry. The profiles are positioned 5 cm away from the upper and lower walls. The sections of the profiles located above the reference line are called bars. The highest points of the bars relative to the reference line are defined as the bar heads. The height of the bar is measured from the reference line to the bar head, while the wavelength of the bar is determined by the distance between two points where the bar profile intersects the reference line, as illustrated in Fig. 4.8.

According to the simulation results applied to experiment 1, the bar's length and height are measured at 8.6 m and 1.4 cm, respectively. The experimental data show that the distribution of bar heights is bimodal, ranging from 1 to 5 cm, and the lengths of the bars fall between 2 m and 8 m. The computed values from simulations, as reported in Table 4.4, are within the reported experimental ranges, indicating the model's ability to predict bar geometry. Interestingly, similar to the behavior of antidunes studied in Chapter 3, larger alternate bar geometry corresponds to a higher mean bedload transport rate.

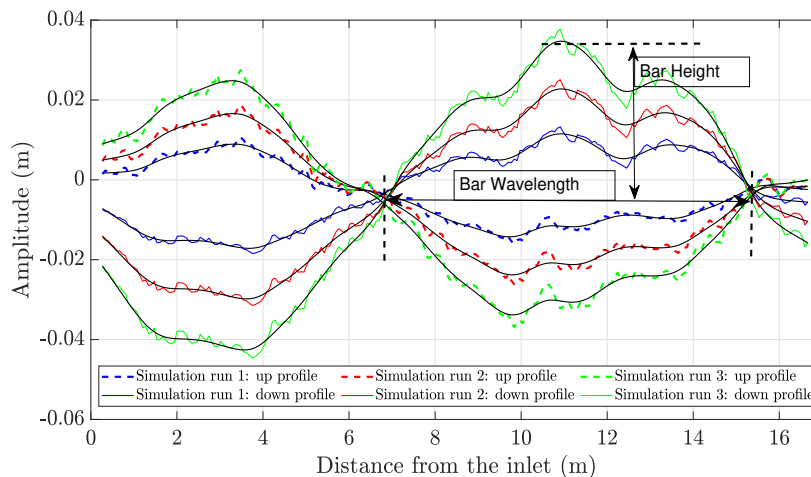


Figure 4.8: Amplitude of the alternate bars along the longitudinal profiles at $t = 17$ h. Smoothed plots are depicted by the black lines.

Bed aggradation and degradation

In this section, the local erosion and deposition of the bed have been studied. These rates are calculated as follows: Let

$$\delta y_b = y_b(x, y, t_{n+1}) - y_b(x, y, t_n) \tag{4.42}$$

The conditional equations to calculate the deposition and erosion rates can be expressed as:

$$\text{Dep} = \begin{cases} \delta y_b & \text{if } \delta y_b > 0 \\ 0 & \text{otherwise} \end{cases} \quad \text{Depo. rate} = \sum \text{Dep} / T$$

$$\text{Ero} = \begin{cases} \delta y_b & \text{if } \delta y_b < 0 \\ 0 & \text{otherwise} \end{cases} \quad \text{Ero. rate} = \sum \text{Ero} / T$$

Figure 4.9 and Fig. 4.10 present the rates of bed deposition and erosion throughout the entire simulation and experimental run 1. This highlights that areas of intense aggradation and degradation extend longitudinally and are alternately positioned on both sides of the channel. The white areas in Fig. 4.9 indicating the absence of deposition, suggesting locations of degradation as one can see in Fig. 4.10. In line with experimental findings, these zones of intense aggradation and degradation are positioned close to the channel walls, either on the right or the left side, spanning 20-30 cm in width and approximately 8 m in length. Comparing these simulation findings with results derived from experimental data shows good agreement in capturing the deposition and erosion rates using numerical simulation.

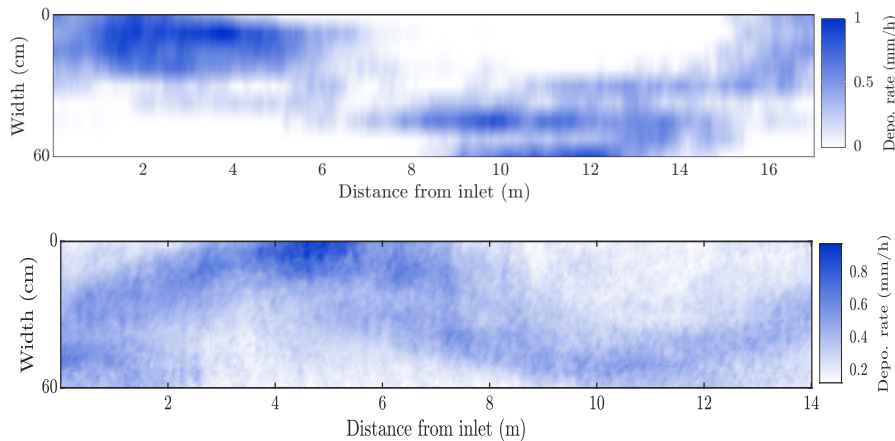


Figure 4.9: Deposition rate contour plot of (top) simulation and (bottom) experiment, calculated over 17 hours for run 1, shows that alternate bars experience intensive aggradation, alternately, on either side of the channel.

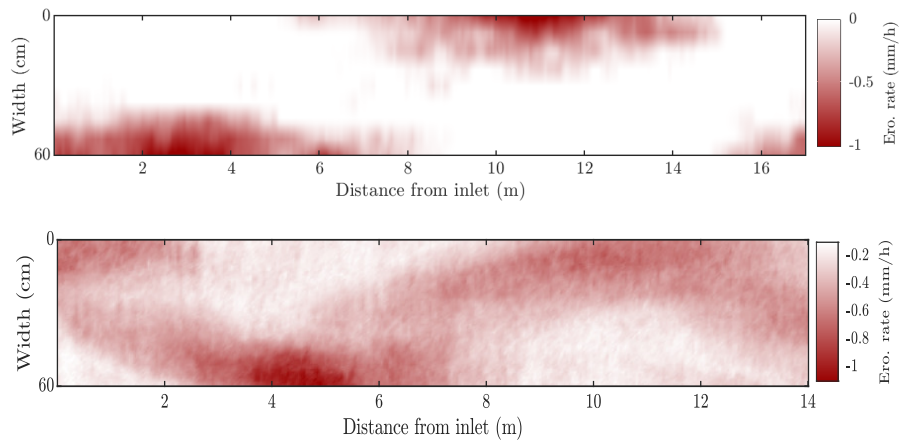


Figure 4.10: Erosion rate contour plot of (top) simulation and (bottom) experiment, calculated over 17 hours for run 1. Pools experience intensive degradation, alternately, on either side of the channel.

Alternate bars growth rate

The simulation and experimental growth rates of alternate bars have been compared in Fig. 4.11. The growth rates for all runs, both simulation and experimental, show a sharp increase initially, followed by a plateau. This suggests that the sediment erosion and deposition processes are very active at the beginning and then reach a state of equilibrium within the first few hours as the curves flatten out.

It also shows that the higher the bedload transport rate, the higher the growth rate. For all three runs, the simulation data follow the experimental trend, indicating that the simulations could capture the growth rate behavior.

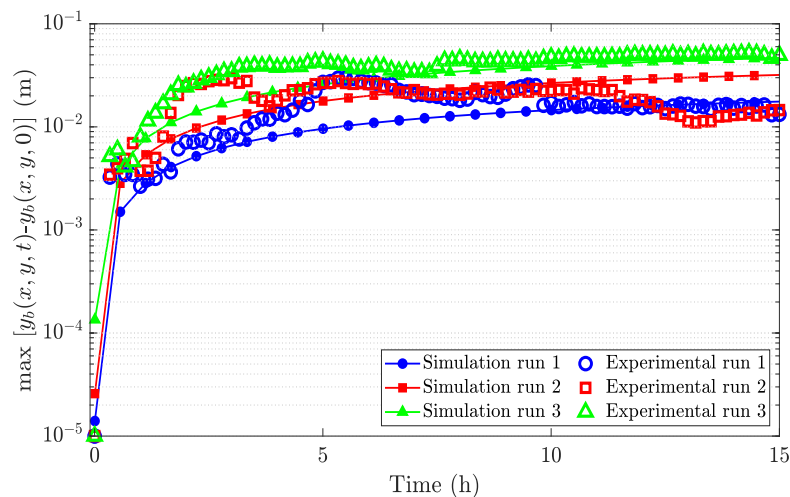


Figure 4.11: Temporal variation of the bed elevation using both simulation and experimental outputs.

4.7 Concluding remarks

In this study, the noise-driven nature of bedload movements has attracted our attention. Therefore, we have developed a two-dimensional stochastic partial differential equation for bedload transport in the form of advection-diffusion. It is developed based on its one-dimensional version. To assess the model's effectiveness in predicting bedload transport and the features of bed topography, we integrated it with shallow water and Exner equations.

The set of governing equations includes five equations: the depth-averaged conservation of mass, two depth-averaged conservation equations of momentum for the fluid phase, the Exner equation for bed continuity, and the bedload stochastic equation providing the number of active particles. A stability analysis was conducted prior to solving the governing equations. The creation of alternate bars was considered in the stability analysis, and the influence of various dimensionless variables on the bars' appearance was studied. The stability analysis demonstrates that the unstable domain of our system of equations accurately captures bed formation, i.e., alternate bars.

Through stability analysis, we have found out that a larger domain of potential wavenumber in the longitudinal direction is associated with a smaller β and Froude number. Additionally, as the slope increases, a critical β_c restricts the development of alternate bars. This critical β_c decreases with an increase in bed slope, meaning that alternate bars are more likely to form on gentler slopes. Moreover, we examined the impacts of diffusivity and sediment velocity on the stability of the bed, and the predictions were in good agreement with experimental data. For example, we found that diffusivity does not significantly affect the creation of alternate bars. Additionally, the magnitude of $\beta_{x,y}$ individually does not significantly impact the unstable domain, but their ratio has a great impact.

The set of governing equations has been solved by splitting the governing equations into a parabolic subproblem without considering the source terms and one hyperbolic subproblem that involves the source terms. The numerical solver was applied to three steady-state experiments conducted in a gravel-bed flume. The main difference among the three experiments is that they have different sediment feeding rates. These experiments provide high-resolution measurements of bed topography, enabling us to compare them with the numerical results.

The numerical studies focus on: i. the bedload transport rate; ii. the geometry of alternate bars (wavelength and height); iii. bed erosion and deposition rates; and iv. the growth rate of the bed. The simulation results capture bedload transport rate and bed topography with good accuracy in comparison with the experimental data. The numerical simulations reveal that the bar formation experiences an exponential growth rate in the initial few hours, followed by a plateau where no further growth occurs (or with a very small growth rate). In addition, the numerical simulations reveals that sediment feeding rate notably affect bar geometry. Consequently, bars tend to be larger and more pronounced under conditions of high sediment transport, while they become smaller and less distinct during minimal sediment transport scenarios.

5 Conclusions and outlook

5.1 Summary of the thesis

As of yet, computational hydraulics models have faced difficulties in predicting the bedload transport rate with accuracy better than one order of magnitude for a given set of controlling variables. Consequently, establishing a protocol to determine the required time with sufficient accuracy for collecting a specific amount of bedload transport has not yet been achieved. In this thesis, we tried to shed a small light to show the roadmap towards answering this longstanding question regarding sediment transport and bed topography prediction.

The natural first step towards the estimation of sediment load for a given water discharge is knowing about bed topography, as it has a strong influence on bedload transport. As in the numerical simulation, the initial step involves importing the bed topography data (usually referred to as Digital Elevation Model–DEM). Therefore, assessing bathymetry is crucial step for predicting bedload transport. This accounts for a significant challenge, both in scientific and technological aspects, in river-based research.

Chapter 1 addressed the challenge of estimating bed topography in shallow gravel-bed streams. The goal was to develop a methodology that allowed for fast inference of bed topography from velocity fields while maintaining high accuracy, achieved through machine learning modeling. However, measuring velocity fields for an extensive spatial areas proved impractical. Therefore, we employed a statistical approach, the Shannon entropy method, to compute velocity fields using available information. Subsequently, with a substantial amount of data collected, we implemented a data-driven model for bathymetry inference. We evaluated the effectiveness of our proposed neural network model for bathymetry estimation by applying it to controlled flume experiments, numerical simulation, and field data.

Importing the DEM file to computational hydraulics solvers and applying traditional bedload models often encounter difficulties in predicting bedload transport. Traditional deterministic bedload models often depend on applying a power law equation to dimensionless experimental data on logarithmic scales. By using these models in numerical simulations, they encounter

huge uncertainties in predicting bedload transport. This issue arises due to neglecting the bedload fluctuations and the fact that minor variation in the Shields number can cause a significant change in the bedload transport predicted by the traditional power law equations. For instance, employing the bedload formula proposed by Meyer-Peter and Müller, 1948: If $\tau^* = 0.06$ but is calculated with just an error of $\epsilon = 5 \times 10^{-3}$, the resulting predicted bedload would be 1.6 times greater than the actual one. Such an error ϵ results in an even higher discrepancy as τ^* decreases. Such high variability in bedload predictions may result in inaccurate estimations of bedform and hydraulic variables. As a result, the feedback loop mechanism within the system may further amplify the inaccuracies in bedload transport predictions.

In Chapters 3 and 4, we have developed the numerical model to account for one of today's major challenges: considering particle fluctuations in the computational hydraulics model. To that end, we used a one- and two-dimensional stochastic bedload model for computing the random time variations in particle activity. This model differs from most current bedload transport models, in which mean bedload transport rates are related to flow rate deterministically. The stochastic model was coupled to the one- and two-dimensional Saint-Venant–Exner equations, respectively, in Chapters 3 and 4.

In Chapters 3 and 4, we studied the bedload transport rate and the development of one- and two-dimensional bedforms. We compared the resulting criteria with experimental evidence. We implemented a numerical algorithm based on the Finite Volume Method. We used it to study antidunes (for the one-dimensional depth-averaged numerical solver) and gravel bar development (for the two-dimensional depth-averaged numerical solver) in long flumes under steady-state conditions and compared the numerical simulations with experimental data. The bed surface was initially flat at the beginning of the simulation, and one small perturbation was imposed. The numerical simulations could capture the bedload transport rate, stages of bedform formation, erosion and deposition zones, and its growth rate in agreement with laboratory experimental data.

5.2 Outcomes

This section provides a summary of the findings from each chapter.

Bed topography inference for shallow flows

In this work, we have inferred the bed topography of gravel bed streams from depth-averaged velocity fields by leveraging advanced machine learning techniques. Overall, after studying the basic and hyperparameters, we have found that, considering our problem, the optimal learning rate is 0.01. Deviating from this value results in a higher validation loss. Additionally, we found that the implementation of learning rate decay does not aid in improving the model performance, as evidenced by the validation loss comparison. For nearly all training dataset sizes, the validation loss with learning rate decay is greater than that with a constant learning

rate. However, learning rate decay does help in reducing variability around the mean value. Moreover, we observed that as the dropout rate decreases, the test error tends to converge towards zero. Therefore, using dropout is not recommended for this study.

The best-trained model achieves accuracy with less than 1% relative error for estimated bathymetry when applied to the test dataset (laboratory experiments). It shows less than 20% maximum relative error when applied to numerical simulation and a maximum of 31.3% relative error when applied to field data collected at the confluence of the Kaskaskia River and Copper Slough. This study shows that the U-net architecture, even with a small dataset, could properly capture the relationship between input (velocity fields) and output data (bathymetry) with sufficient accuracy. This model is designed and specialized for gravel-bed flumes and rivers and is not a one-size-fits-all solution.

One-dimensional computational hydraulics model

In this work, we have implemented a stochastic, one-dimensional, depth-averaged numerical simulation and applied it to narrow, gravel-bed flume experiments. The numerical outcomes align with experimental data, showing that antidunes initially form with a long wavelength and minimal amplitude, then gradually grow in sync with the water surface and consistently migrate upstream. The growth of antidunes is initially exponential, stabilizing after a period of transition. As these antidunes move upstream, there's an increase in sediment transport rate, resulting in a peak at the crest that is significantly higher than the mean bedload transport rate. Thus, the dynamics of antidunes are key in determining average sediment transport rates.

Through the analysis of different realizations of a single numerical simulation, we found that key parameters fluctuate around their mean values—consistent with experimental evidence. However, the probability density function of the antidunes' wavelength remained unchanged after the transient stage, indicating that although temporal variability came to a halt, spatial variability along the length of the flume persisted.

Moreover, the study showed that the velocity and shape of antidunes' upstream migration are more pronounced in conditions of higher bedload transport rates. Additionally, the relationship between the amplitude and wavelength of the antidunes could not be established without considering additional parameters. Additionally, this study indicated a relative error under -258% for bedload transport predictions, with the maximum relative errors for bedform wavelength and amplitude being -41% and -91.5%, respectively. The substantial error in predicting form amplitude may arise from difficulties in laboratory measurements or issues with model calibration.

Two-dimensional computational hydraulics model

After evaluating the predictive capabilities of the one-dimensional depth-averaged computational hydraulics model, we extended the model to two dimensions. For the first time, a

stability analysis was performed using our set of governing equations. The influence of various dimensionless variables on the appearance of bars was thoroughly investigated. The stability analysis shows that our system's unstable domain could capture alternate bar formation, revealing new information about alternate bar formation. For example, a smaller Froude number and β (half-width-to-depth ratio) associated with a larger wavenumber in the longitudinal direction. Additionally, as the bed slope increases, the β_c decreases and further limits the unstable zone.

This solver was applied to high-resolution experimental data gathered under steady-state conditions. The numerical solver is used to study bedload transport and alternate bars formation. The bedform studies involve: i. form geometry; ii. aggradation and degradation in the location where alternate bars and pools appear; and iii. form growth rate. The numerical simulations successfully captured the bedload transport rate, bed topography, areas of aggradation and degradation, and bed form growth rate, consistent with the experimental data.

5.3 Future perspectives

This dissertation focuses on predicting bed topography and bedload transport through various types of modeling, i.e., data-driven surrogate modeling and computational hydraulic modeling, though there is considerable scope for further research.

In the context of data-driven surrogate modeling, we suggest leveraging the large datasets provided by satellite imagery to identify patterns and predict changes in bed topography using deep learning algorithms. Additionally, deep learning techniques can also be applied to predict bedload transport. In scenarios where the focus is not on understanding the physical processes but rather on computational time and prediction accuracy, we can leverage these techniques. For example, using machine learning models to quickly analyze huge amounts of meteorological data can provide accurate weather forecast without solving the complex physical dynamics of weather systems, which may last weeks.

In Chapters 3 and 4, we focused on computational hydraulic modeling in bedload and bed topography prediction in steady-state flow conditions, but exploring unsteady flows could yield intriguing results. Additionally, employing stochastic models in a two-dimensional flume to study various possible realizations opens up possibilities for a deeper understanding of fluvial systems. Furthermore, the two-dimensional numerical solver is applicable to real-world rivers and is interesting to use for river forecasting to find out and highlight its limitations.

We incorporate the noise into the numerical modeling as the particle movement through the fluid is a noise-driven process. The governing equation for such a process is modeled as a stochastic partial differential equation. It needs to be coupled with the Exner equation to numerically capture the bed topography. This integration considers particle fluctuations, which are influential at a bulk scale and show a notable response to hydraulic changes. This approach offers insights beyond traditional bedload models, encompassing aspects like periodicity and

intermittency, which can be related to hydraulic conditions, river bank development, and bed erosion and deposition by using techniques such as joint analysis.

Finally, it would also be interesting to explore the effectiveness of other probabilistic models, such as Charru's and Furbish's, in predicting morphological changes and to compare them with the model presented in this dissertation.

5.3.1 Open challenges

In this dissertation, we have targeted the prediction of bed topography and sediment transport. Nevertheless, numerous interesting challenges remain open for future investigation.

Data-driven surrogate modeling

The use of data-driven surrogate modeling, leveraging advanced machine learning techniques, has shown promising results in geophysics and hydraulics. The surrogate model acts as efficient approximations of complex physical processes, enabling the prediction of sediment transport and changes in riverbed landscapes with a high degree of accuracy. An open challenge in this regard is to incorporate physical governing equations into machine learning models by using techniques like physical-informed neural networks.

Computational hydraulic modeling

According to Warburton and Davies, 1994, the current state of bedload transport shows statistical dependencies on the two preceding time steps. This insight suggests that employing a second-order Markov process in bedload modeling may enhance prediction accuracy. In the derivation of Markov process-based models for bedload transport, adopting the Stratonovich convention is preferable to the Itô convention, because of its better physical interpretation.

The Itô convention is non-anticipative, in contrast to the anticipatory nature of the Stratonovich convention. In the Stratonovich approach, the integrand is assessed at the midpoint of each interval, giving it an anticipatory nature. Conversely, the Itô approach assesses the integrand at the start of each interval, meaning that future increments of the stochastic process do not impact the current value, making it non-anticipative. Beside that, the acquisition and analysis of high-resolution bedload transport time series to extract their statistical characteristics are essential in fine-tuning the proposed bedload model based on Markov processes.

The stochastic bedload model has proven effective in predicting particle transport and bed formation characteristics with good accuracy when calibrated properly. To calibrate the collective entrainment rate, there is not much information in the literature—although collective entrainment occurs less frequently than other processes, it accounts for a significant portion of bedload transport. It is worth noting that one has to be careful about the terminology

used to describe collective entrainment. It has caused some confusion, as it may suggest that multiple particles are simultaneously entrained. However, this is not the case, as the term simply reflects the fact that the likelihood of entrainment is influenced by the number of particles in motion.

Given that fluvial systems consist of slow-term processes, it is essential that the numerical simulation run with greater speed to facilitate long-term simulations. Hence, parallelizing the solver becomes a critical requirement. Additionally, conducting sensitivity analysis on the numerical solver is important to understanding how the system of equations responds to variations in mass exchange rates.

Finally, applying the numerical solvers to real-world riverine environments offers a promising solution, hopefully to overcome the existing challenges faced by professionals in hydraulic engineering in providing a more accurate flood risk map as recent researches have demonstrated the significant impact of sediment dynamics and morphological changes on flood risk.

Experimental study

The need to perform more grain-scale experiments to calibrate the proposed bedload model is greatly felt in this work. The main issue with the proposed parametrization adjusted to the data in Chapter 3 is the enormous fluctuations in the mean bedload transport rate for $\tau^* < 0.1$. Therefore, the determination of the entrainment rate is not accurate enough for this domain. Improving bedload prediction requires a comprehensive understanding and modeling of deposition and entrainment processes by performing grain-scale experiments in a wide range of hydraulic conditions, both in the presence and absence of bed formation.

In Chapter 3, we discussed existing experimental investigations that used braided flumes to study various realizations by repeating one experiment many times. However, as far as we know, there has been no experimental research in this regard using narrow or wide gravel-bed flumes. While it is not unexpected to obtain different realizations by repeating experiments in narrow gravel-bed systems, whether the same holds true for wide gravel-bed flumes is less intuitive. Therefore, experimental study in this regard can help in understanding fluvial systems to a greater degree.

Additionally, addressing the mixed short- and long-term processes involved in the fluvial system necessitates the implementation of long experiment, facilitating a more detailed investigation of the critical processes at play.

A Machine learning model architecture

The neural network consisting a total of 12 layers, with each layer includes activation, upsampling, convolution, batch normalization, and dropout operations. The below table shows the structure of the U-net used in all of our tests. The network weights were initialized following He et al., 2015. After conducting some tests, we found out that dropout does not aid learning by the model, so we do not use it. Instead, we utilize batch normalization. Training was done using Adam (Kingma & Ba, 2014) with $\beta_{1,2} = [0.5, 0.999]$, and $\epsilon = 10^{-8}$ parameter values. Learning rate was kept at a constant value during training. A 0.01 learning rate, and a 100 minibatch size were used in all tests.

Appendix A. Machine learning model architecture

Table A.1: Deep learning model summary.

Layer (type)	Output Shape	Function parameters
InputLayer	[1, 256, 64]	
Conv2-D-1	[16, 128, 32]	$n_{out}/n_{in}=2$, kernel size 4×4 , stride=2, pad=1
BatchNorm2-D-2	[16, 128, 32]	
Dropout2-D-3	[16, 128, 32]	$p = 0$, inplace=True
LeakyReLU-4	[16, 128, 32]	negative slope=0.2, inplace=True
Conv2-D-5	[16, 64, 16]	$n_{out}/n_{in}=2$, kernel size 4×4 , stride=2, pad=1
BatchNorm2-D-6	[16, 64, 16]	
Dropout2-D-7	[16, 64, 16]	$p = 0$, inplace=True
LeakyReLU-8	[16, 64, 16]	negative slope=0.2, inplace=True
Conv2-D-9	[32, 32, 8]	$n_{out}/n_{in}=4$, kernel size 4×4 , stride=2, pad=1
BatchNorm2-D-10	[32, 32, 8]	
Dropout2-D-11	[32, 32, 8]	$p = 0$, inplace=True
LeakyReLU-12	[32, 32, 8]	negative slope=0.2, inplace=True
Conv2-D-13	[64, 16, 4]	$n_{out}/n_{in}=8$, kernel size 4×4 , stride=2, pad=1
BatchNorm2-D-14	[64, 16, 4]	
Dropout2-D-15	[64, 16, 4]	$p = 0$, inplace=True
LeakyReLU-16	[64, 16, 4]	negative slope=0.2, inplace=True
Conv2-D-17	[64, 8, 2]	$n_{out}/n_{in}=8$, kernel size 2×2 , stride=2, pad=0
BatchNorm2-D-18	[64, 8, 2]	
Dropout2-D-19	[64, 8, 2]	$p = 0$, inplace=True
LeakyReLU-20	[64, 8, 2]	negative slope=0.2, inplace=True
Conv2-D-21	[64, 4, 1]	$n_{out}/n_{in}=8$, kernel size 2×2 , stride=2, pad=0
BatchNorm2-D-22	[64, 4, 1]	
Dropout2-D-23	[64, 4, 1]	$p = 0$, inplace=True
LeakyReLU-24	[64, 4, 1]	negative slope=0.2, inplace=True
Upsample-25	[64, 8, 2]	scale factor=2, mode='bilinear'
Conv2-D-26	[64, 8, 2]	$n_{out}/n_{in}=8$, kernel size 1×1 , stride=1, pad=0
BatchNorm2-D-27	[64, 8, 2]	
Dropout2-D-28	[64, 8, 2]	$p = 0$, inplace=True
ReLU-29	[64, 8, 2]	inplace=True
Upsample-30	[128, 16, 4]	scale factor=2, mode='bilinear'
Conv2-D-31	[64, 16, 4]	$n_{out}/n_{in}=8$, kernel size 1×1 , stride=1, pad=0
BatchNorm2-D-32	[64, 16, 4]	
Dropout2-D-33	[64, 16, 4]	$p = 0$, inplace=True
ReLU-34	[64, 16, 4]	inplace=True
Upsample-35	[128, 32, 8]	scale factor=2, mode='bilinear'
Conv2-D-36	[32, 32, 8]	$n_{out}/n_{in}=4$, kernel size 3×3 , stride=1, pad=1
BatchNorm2-D-37	[32, 32, 8]	
Dropout2-D-38	[32, 32, 8]	$p = 0$, inplace=True
ReLU-39	[32, 32, 8]	inplace=True
Upsample-40	[64, 64, 16]	scale factor=2, mode='bilinear'
Conv2-D-41	[16, 64, 16]	$n_{out}/n_{in}=2$, kernel size 3×3 , stride=1, pad=1
BatchNorm2-D-42	[16, 64, 16]	
Dropout2-D-43	[16, 64, 16]	$p = 0$, inplace=True
ReLU-44	[16, 64, 16]	inplace=True
Upsample-45	[32, 128, 32]	scale factor=2, mode='bilinear'
Conv2-D-46	[16, 128, 32]	$n_{out}/n_{in}=2$, kernel size 3×3 , stride=1, pad=1
BatchNorm2-D-47	[16, 128, 32]	
Dropout2-D-48	[16, 128, 32]	$p = 0$, inplace=True
ReLU-49	[16, 128, 32]	inplace=True
Upsample-50	[32, 256, 64]	scale factor=2, mode='bilinear'
Conv2-D-51	[1, 256, 64]	$n_{out}/n_{in}=1$, kernel size 3×3 , stride=1, pad=1
Dropout2-D-52	[1, 256, 64]	$p = 0$, inplace=True

B Sensitivity analysis

In this section, we aim to explore the equivalence between the discrete and continuous bedload models, as well as the sensitivity of the continuous bedload model's solution to the cell size Δx . The discrete bedload model (Ancey et al., 2015)

$$\begin{aligned} \frac{\partial P}{\partial t}(\mathbf{n}, t) = \sum_{i=1} (n_i + 1) & \left(P(\mathbf{n} + \mathbf{r}_i^{i+1}, t) v_i + P(\mathbf{n} + \mathbf{r}_i^+, t) \sigma_i \right) \\ & + P(\mathbf{n} + \mathbf{r}_i^-, t) (\lambda'_i + \mu_i (n_i - 1)) \\ & + P(\mathbf{n} + \mathbf{r}_i^{i-1}, t) v_{i-1} n_{i-1} \\ & - P(\mathbf{n}, t) (v_{i-1} n_{i-1} + \lambda'_i + \mu_i n_{i+1} + v_i n_i + \sigma_i n_i) \end{aligned} \quad (\text{B.1})$$

and its continuous version, Eq. 3.13, are solved independently, without any coupling with the Saint-Venant–Exner equations. Identical parameters are used in both the discrete and continuous formulations: $\lambda' = 10 \text{ s}^{-1}$, $\mu = 4 \text{ s}^{-1}$, $\sigma = 5 \text{ s}^{-1}$, and $\bar{u}_s = 2 \text{ m/s}$. Further, the approximations $D_u = v \Delta x^2 / 2$ and $v = \bar{u}_s / \Delta x$ are applied.

Figure B.1 shows numerical solutions for Eq. B.1 and Eq. 3.13, detailing the bedload transport time series, the autocorrelation of the number of moving particles time series, and the probability density function of bedload transport. Figure B.1(a) and Fig. B.1(b) illustrate the temporal variation in the number of active particles within a central domain cell, compared with the analytical solution (in red solid line)

$$\langle N \rangle_{ss} = \frac{\lambda'}{\sigma - \mu} \quad (\text{B.2})$$

Figure B.1(c) and Fig. B.1(d) depict the autocorrelation of the number of moving particles time series compared with the analytical solution (in black solid line)

Appendix B. Sensitivity analysis

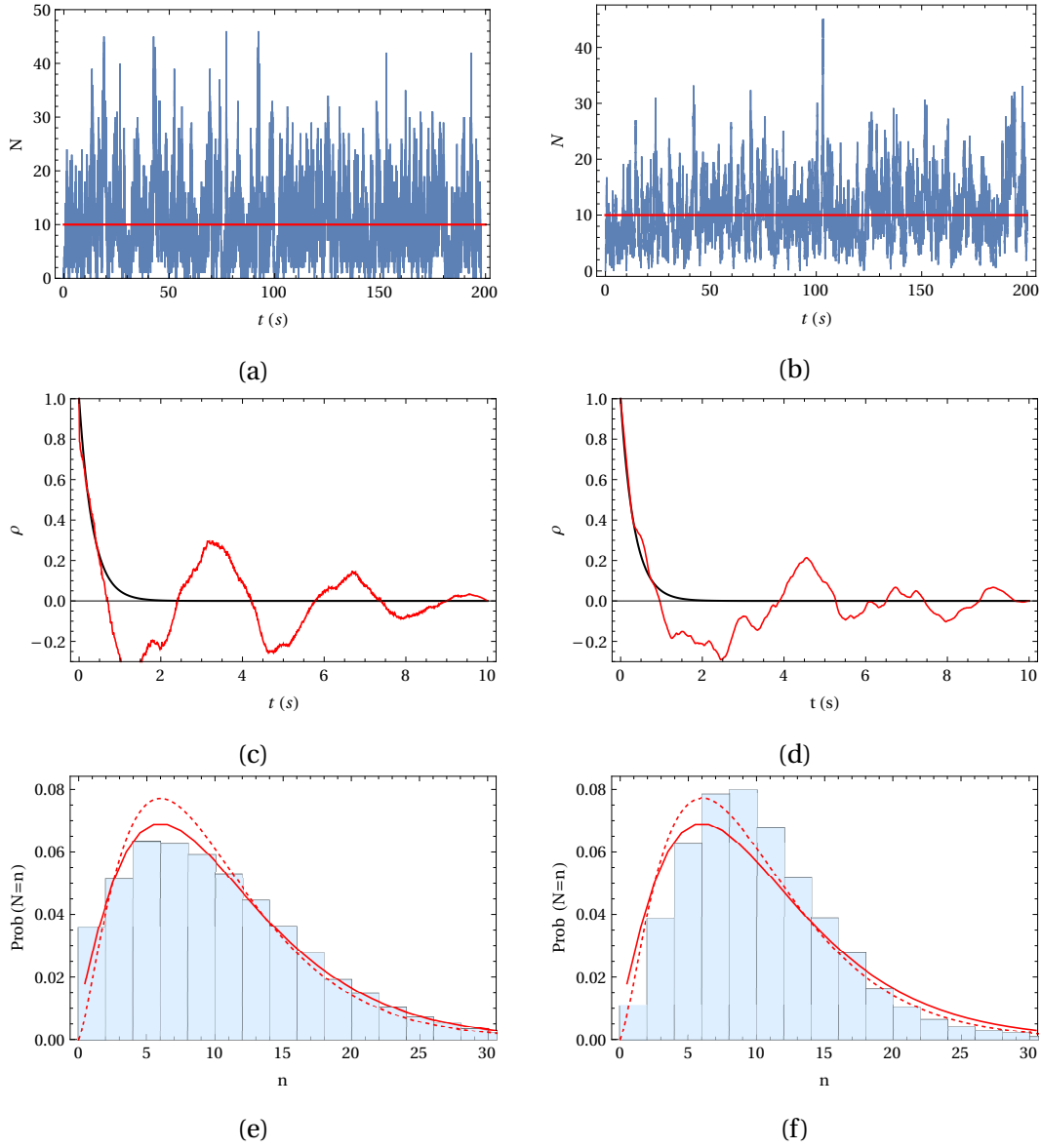


Figure B.1: (left) Simulation of the continuous model, (right) simulation of the discrete model. Both models are solved numerically using identical parameters: $\lambda' = 10 \text{ s}^{-1}$, $\mu = 4 \text{ s}^{-1}$, $\sigma = 5 \text{ s}^{-1}$, and $\bar{u}_s = 2 \text{ m/s}$. The cell size is $\Delta x = 1 \text{ m}$ with $\tilde{\lambda} = \lambda' / \Delta x$. The approximations $D_u = \nu \Delta x^2 / 2$ and $\nu = \bar{u}_s / \Delta x$ are applied.

$$\rho(t) = \exp(-(\nu + \sigma - \mu)t) \quad (\text{B.3})$$

The probability density function of active particles is depicted in Fig. B.1(e) and Fig. B.1(f). In steady-state flow conditions with a non-zero collective entrainment rate μ , the distribution of the number of active particles within the control volume follows a negative binomial

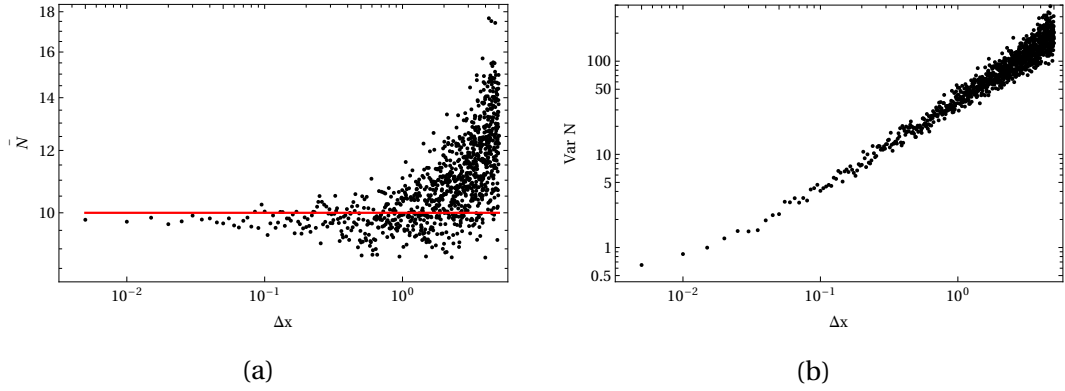


Figure B.2: A sensitivity analysis was conducted on the mesh size using the continuous bedload model. Eq. 3.13 was numerically solved for a duration of 500 seconds using $\lambda' = 10 \text{ s}^{-1}$, $\mu = 4 \text{ s}^{-1}$, $\sigma = 5 \text{ s}^{-1}$, $\bar{u}_s = 2 \text{ m/s}$, and $\tilde{\lambda} = \lambda' / \Delta x$. The approximations $D_u = v \Delta x^2 / 2$ and $v = \bar{u}_s / \Delta x$ are applied.

distribution as

$$\text{prob}(N = n) = \binom{q + n - 1}{q - 1} p^q (1 - p)^n \quad (\text{B.4})$$

where $q = \frac{\lambda'}{\mu}$ and $p = 1 - \frac{\mu}{\sigma}$. The numerical results are compared with the negative binomial distribution (in red solid line) and the gamma distribution, characterized by $\alpha = \frac{\lambda'}{\mu}$ and $\beta = \frac{\mu}{\sigma - \mu}$ (in red dashed line). The findings demonstrate that the probability density function of active particles, as determined through both discrete and continuous models, aligns closely with the analytical solution. Moreover, the specified approximations are validated within the continuous model to accurately reflect the discrete model solution.

Before integrating the bedload model, Eq. 3.13, with the shallow water and Exner equations, it is crucial to examine the impact of mesh size Δx on the solution. To this end, a sensitivity analysis is conducted. This analysis has been done by solving the continuous stochastic bedload model with parameters: $\lambda' = 10 \text{ s}^{-1}$, $\mu = 4 \text{ s}^{-1}$, $\sigma = 5 \text{ s}^{-1}$, and $\bar{u}_s = 2 \text{ m/s}$ across a range of cell lengths Δx .

The averaged number of active particles is calculated in a central domain cell for various control volume sizes. The mean and variance of active particles for varying Δx values are presented in Fig. B.2 (a) and Fig. B.2 (b), respectively, with the analytical solution, as per Eq. B.2 (in red line). The results indicate that selecting $\Delta x < 1$ m leads to convergence to the theoretical value, suggesting the solution for the continuous model becomes independent of Δx .

C Extended Roe solver in one-dimension

Roe, 1981 proposed a method that involves linearizing a nonlinear hyperbolic system of equations

$$\frac{\partial \mathbf{q}}{\partial t} + \mathbf{A} \cdot \frac{\partial \mathbf{q}}{\partial x} = 0,$$

where $\mathbf{A} = \nabla_{\mathbf{q}} \mathbf{f}$ is the Jacobian of the flux function \mathbf{f} , and replacing it with the linear system

$$\frac{\partial \mathbf{q}}{\partial t} + \hat{\mathbf{A}} \cdot \frac{\partial \mathbf{q}}{\partial x} = 0,$$

where the linearized matrix $\hat{\mathbf{A}}$ that must satisfy a number of properties (continuity, hyperbolicity, and Roe linearization). Roe, 1981 showed that this matrix was defined by integrating the Jacobian

$$\hat{\mathbf{A}} = \int_0^1 \frac{d\mathbf{f}(\mathbf{f}(\xi))}{d\mathbf{q}} d\xi$$

using the change of variable $\mathbf{z} = \mathbf{q} / \sqrt{h}$. This method initially applied to the Euler equation was used for solving the Saint-Venant equations and has been routinely used since then (LeVeque, 2002). It can be easily extended to the Eq. 3.32.

We consider the hyperbolic subproblem $\partial_t \mathbf{q} + \partial_x \mathbf{f}(\mathbf{q}) = 0$. We use the same notation as LeVeque, 2002 did

$$\mathbf{q} = \begin{bmatrix} h \\ hu \\ b \\ y_b \end{bmatrix} = \begin{bmatrix} q^1 \\ q^2 \\ q^3 \\ q^4 \end{bmatrix}, \mathbf{f}(\mathbf{q}) = \begin{bmatrix} hu \\ hu^2 + \frac{1}{2}gh^2 \\ \beta ub \\ 0 \end{bmatrix} = \begin{bmatrix} q^2 \\ (q^2)^2 / q^1 + \frac{1}{2}g(q^1)^2 \\ \beta q^2 / q^1 \times q^3 \\ 0 \end{bmatrix} \quad (\text{C.1})$$

and the corresponding Jacobian matrix may be

Appendix C. Extended Roe solver in one-dimension

$$\mathbf{A} = \begin{bmatrix} 0 & 1 & 0 & 0 \\ -(q^2/q^1)^2 + gq^1 & 2q^2/q^1 & 0 & 0 \\ -\beta \frac{q^2}{(q^1)^2} q^3 & \beta q^3/q^1 & \beta q^2/q^1 & 0 \\ 0 & 0 & 0 & 0 \end{bmatrix} = \begin{bmatrix} 0 & 1 & 0 & 0 \\ -u^2 + gh & 2u & 0 & 0 \\ -\beta \frac{ub}{h} & \beta \frac{b}{h} & \beta u & 0 \\ 0 & 0 & 0 & 0 \end{bmatrix} \quad (\text{C.2})$$

We use the same change of variable $\mathbf{z} = \mathbf{q}/\sqrt{h}$ as Roe, 1981 did

$$\mathbf{z} = \begin{bmatrix} z^1 \\ z^2 \\ z^3 \\ z^4 \end{bmatrix} = \begin{bmatrix} \sqrt{h} \\ \sqrt{h}u \\ b/\sqrt{h} \\ yb/\sqrt{h} \end{bmatrix} \Rightarrow \mathbf{q}(\mathbf{z}) = \begin{bmatrix} (z^1)^2 \\ z^1 z^2 \\ z^1 z^3 \\ z^1 z^4 \end{bmatrix} \rightarrow \frac{\partial \mathbf{q}}{\partial \mathbf{z}} = \begin{bmatrix} 2z^1 & 0 & 0 & 0 \\ z^2 & z^1 & 0 & 0 \\ z^3 & 0 & z^1 & 0 \\ z^4 & 0 & 0 & z^1 \end{bmatrix} \quad (\text{C.3})$$

and by rewriting the flux function \mathbf{f} and its Jacobian matrix using this new variable

$$\mathbf{f}(\mathbf{z}) = \begin{bmatrix} z^1 z^2 \\ (z^2)^2 + \frac{1}{2}g(z^1)^4 \\ \beta z^2 z^3 \\ 0 \end{bmatrix} \rightarrow \mathbf{A}(\mathbf{z}) = \begin{bmatrix} z^2 & z^1 & 0 & 0 \\ 2g(z^1)^3 & 2z^2 & 0 & 0 \\ 0 & \beta z^3 & \beta z^2 & 0 \\ 0 & 0 & 0 & 0 \end{bmatrix}. \quad (\text{C.4})$$

We integrate $\partial \mathbf{f}/\partial \mathbf{z}$ and $\partial \mathbf{q}/\partial \mathbf{z}$ along the path

$$z^p = Z_{i-1}^p + (Z_i^p - Z_{i-1}^p)\zeta \quad p = 1, \dots, 4 \quad (\text{C.5})$$

where $\mathbf{Z}_j = \mathbf{z}(\mathbf{Q}_j)$ for $j = i-1, i$. Then $(z^p)'(\zeta) = Z_i^p - Z_{i-1}^p$ is independent of ζ . The integration of each element of these matrices is from $\zeta = 0$ to $\zeta = 1$. As one can see, all elements in $\partial \mathbf{f}/\partial \mathbf{z}$ are linear in ζ except the term in the second row and first column

$$\mathbf{f}(\mathbf{Q}_i) - \mathbf{f}(\mathbf{Q}_{i-1}) = \int_0^1 \frac{d\mathbf{f}(\mathbf{z}(\zeta))}{d\zeta} d\zeta = \int_0^1 \frac{d\mathbf{f}(\mathbf{z}(\zeta))}{d\mathbf{z}} \mathbf{z}'(\zeta) d\zeta = \left[\int_0^1 \frac{d\mathbf{f}(\mathbf{z}(\zeta))}{d\mathbf{z}} d\zeta \right] (\mathbf{Z}_i - \mathbf{Z}_{i-1}) \quad (\text{C.6})$$

$$\mathbf{Q}_i - \mathbf{Q}_{i-1} = \int_0^1 \frac{d\mathbf{q}(\mathbf{z}(\zeta))}{d\zeta} d\zeta = \int_0^1 \frac{d\mathbf{q}(\mathbf{z}(\zeta))}{d\mathbf{z}} \mathbf{z}'(\zeta) d\zeta = \left[\int_0^1 \frac{d\mathbf{q}(\mathbf{z}(\zeta))}{d\mathbf{z}} d\zeta \right] (\mathbf{Z}_i - \mathbf{Z}_{i-1}) \quad (\text{C.7})$$

$\hat{\mathbf{C}}_{i-1/2}$ being $\int_0^1 \frac{d\mathbf{f}(\mathbf{z}(\zeta))}{d\mathbf{z}} d\zeta$ and $\hat{\mathbf{B}}_{i-1/2}$ being $\int_0^1 \frac{d\mathbf{q}(\mathbf{z}(\zeta))}{d\mathbf{z}} d\zeta$, then we have

$$\begin{aligned} \mathbf{f}(\mathbf{Q}_i) - \mathbf{f}(\mathbf{Q}_{i-1}) &= \hat{\mathbf{C}}_{i-1/2} (\mathbf{Z}_i - \mathbf{Z}_{i-1}) \\ \mathbf{Q}_i - \mathbf{Q}_{i-1} &= \hat{\mathbf{B}}_{i-1/2} (\mathbf{Z}_i - \mathbf{Z}_{i-1}) \end{aligned} \quad (\text{C.8})$$

Now we can obtain the desired relation by $\hat{\mathbf{A}}_{i-1/2} = \hat{\mathbf{C}}_{i-1/2} \hat{\mathbf{B}}_{i-1/2}^{-1}$. Integrating the linear terms

$z^p(\zeta)$ yields

$$\begin{aligned} \int_0^1 z^p(\zeta) d\zeta &= \frac{1}{2}(Z_{i-1}^p + Z_i^p) \equiv \bar{Z}^p \\ \int_0^1 (z^1(\zeta))^3 d\zeta &= \frac{1}{4} \left(\frac{(Z_i^1)^4 - (Z_{i-1}^1)^4}{Z_i^1 - Z_{i-1}^1} \right) = \frac{1}{2}(Z_{i-1}^1 + Z_i^1) \times \frac{1}{2} \left[(Z_{i-1}^1)^2 + (Z_i^1)^2 \right] = \bar{Z}^1 \bar{h} \end{aligned} \quad (\text{C.9})$$

where $\bar{h} = \frac{1}{2}(h_{i-1} + h_i)$. Hence we obtain

$$\hat{\mathbf{B}}_{i-1/2} = \begin{bmatrix} 2\bar{Z}^1 & 0 & 0 & 0 \\ \bar{Z}^2 & \bar{Z}^1 & 0 & 0 \\ \bar{Z}^3 & 0 & \bar{Z}^1 & 0 \\ \bar{Z}^4 & 0 & 0 & \bar{Z}^1 \end{bmatrix}, \hat{\mathbf{C}}_{i-1/2} = \begin{bmatrix} \bar{Z}^2 & \bar{Z}^1 & 0 & 0 \\ 2g\bar{Z}^1\bar{h} & 2\bar{Z}^2 & 0 & 0 \\ 0 & \beta\bar{Z}^3 & \beta\bar{Z}^2 & 0 \\ 0 & 0 & 0 & 0 \end{bmatrix} \quad (\text{C.10})$$

By using of Mathematica, we have

$$\hat{\mathbf{B}}_{i-1/2}^{-1} = \begin{bmatrix} \frac{1}{2\bar{Z}^1} & 0 & 0 & 0 \\ -\frac{\bar{Z}^2}{2(\bar{Z}^1)^2} & \frac{1}{\bar{Z}^1} & 0 & 0 \\ -\frac{\bar{Z}^3}{2(\bar{Z}^1)^2} & 0 & \frac{1}{\bar{Z}^1} & 0 \\ -\frac{\bar{Z}^4}{2(\bar{Z}^1)^2} & 0 & 0 & \frac{1}{\bar{Z}^1} \end{bmatrix} \quad (\text{C.11})$$

And so

$$\hat{\mathbf{A}}_{i-1/2} = \hat{\mathbf{C}}_{i-1/2} \hat{\mathbf{B}}_{i-1/2}^{-1} = \begin{bmatrix} 0 & 1 & 0 & 0 \\ g\bar{h} - \left(\frac{\bar{Z}^2}{\bar{Z}^1}\right)^2 & 2\frac{\bar{Z}^2}{\bar{Z}^1} & 0 & 0 \\ -\beta\frac{\bar{Z}^2\bar{Z}^3}{(\bar{Z}^1)^2} & \beta\frac{\bar{Z}^3}{\bar{Z}^1} & \beta\frac{\bar{Z}^2}{\bar{Z}^1} & 0 \\ 0 & 0 & 0 & 0 \end{bmatrix} \quad (\text{C.12})$$

where

$$\frac{\bar{Z}^2}{\bar{Z}^1} = \frac{\frac{1}{2}(Z_{i-1}^2 + Z_i^2)}{\frac{1}{2}(Z_{i-1}^1 + Z_i^1)} = \frac{\sqrt{h_{i-1}}u_{i-1} + \sqrt{h_i}u_i}{\sqrt{h_{i-1}} + \sqrt{h_i}} = \hat{u} \quad (\text{C.13})$$

and

$$\frac{\bar{Z}^3}{\bar{Z}^1} = \frac{\frac{1}{2}(Z_{i-1}^3 + Z_i^3)}{\frac{1}{2}(Z_{i-1}^1 + Z_i^1)} = \frac{\frac{b_{i-1}}{\sqrt{h_{i-1}}} + \frac{b_i}{\sqrt{h_i}}}{\sqrt{h_{i-1}} + \sqrt{h_i}} = \frac{b_{i-1}\sqrt{h_i} + b_i\sqrt{h_{i-1}}}{h_{i-1}\sqrt{h_i} + h_i\sqrt{h_{i-1}}} = \frac{\hat{b}}{\hat{h}} \quad (\text{C.14})$$

We can now simplify the $\hat{\mathbf{A}}_{i-1/2}$ such as

$$\hat{\mathbf{A}}_{i-1/2} = \begin{bmatrix} 0 & 1 & 0 & 0 \\ -\hat{u}^2 + g\hat{h} & 2\hat{u} & 0 & 0 \\ -\beta\frac{\hat{u}\hat{b}}{\hat{h}} & \beta\frac{\hat{b}}{\hat{h}} & \beta\hat{u} & 0 \\ 0 & 0 & 0 & 0 \end{bmatrix} \quad (\text{C.15})$$

Appendix C. Extended Roe solver in one-dimension

The eigenvalues of $\hat{\mathbf{A}}_{i-1/2}$ are

$$\begin{bmatrix} \hat{u} - \hat{c} \\ \hat{u} + \hat{c} \\ \beta \hat{u} \\ 0 \end{bmatrix} \quad (\text{C.16})$$

where

$$\hat{\lambda}^1 = \hat{u} - \hat{c}, \quad \hat{\lambda}^2 = \hat{u} + \hat{c}, \quad \hat{\lambda}^3 = \beta \hat{u}, \quad \hat{\lambda}^4 = 0 \quad (\text{C.17})$$

and four different corresponding eigenvectors

$$\mathbf{R} = \begin{bmatrix} \frac{\sqrt{g}\hat{h} + \sqrt{\hat{h}}\hat{u}(\beta-1)}{\beta\hat{b}\sqrt{g}} & -\frac{\sqrt{\hat{h}}(\sqrt{g}\hat{h}-\hat{u})(\sqrt{g}\hat{h}-\hat{u}+\hat{u}\beta)}{\beta\hat{b}\sqrt{g}} & 1 & 0 \\ \frac{\sqrt{\hat{h}}(\sqrt{g}\hat{h}+\hat{u}-\hat{u}\beta)}{\beta\hat{b}\sqrt{g}} & \frac{\sqrt{\hat{h}}(\sqrt{g}\hat{h}+\hat{u})(\sqrt{g}\hat{h}+\hat{u}-\hat{u}\beta)}{\beta\hat{b}\sqrt{g}} & 1 & 0 \\ 0 & 0 & 1 & 0 \\ 0 & 0 & 0 & 1 \end{bmatrix} \quad (\text{C.18})$$

which each row shows an eigenvector. After simplifying we have

$$\hat{\mathbf{r}}^1 = \begin{bmatrix} 1 \\ \hat{u} - \hat{c} \\ \frac{g\hat{b}\beta}{\hat{c}(\hat{c} + \hat{u}\beta - \hat{u})} \\ 0 \end{bmatrix}, \quad \hat{\mathbf{r}}^2 = \begin{bmatrix} 1 \\ \hat{u} + \hat{c} \\ \frac{g\hat{b}\beta}{\hat{c}(\hat{c} - \hat{u}\beta + \hat{u})} \\ 0 \end{bmatrix}, \quad \hat{\mathbf{r}}^3 = \begin{bmatrix} 0 \\ 0 \\ 1 \\ 0 \end{bmatrix}, \quad \hat{\mathbf{r}}^4 = \begin{bmatrix} 0 \\ 0 \\ 0 \\ 1 \end{bmatrix} \quad (\text{C.19})$$

where $\hat{c} = \sqrt{g\hat{h}}$. If we simplify \mathbf{R}

$$\mathbf{R} = \begin{bmatrix} 1 & 1 & 0 & 0 \\ \hat{u} - \hat{c} & \hat{u} + \hat{c} & 0 & 0 \\ \frac{g\hat{b}\beta}{\hat{c}(\hat{c} + \hat{u}\beta - \hat{u})} & \frac{g\hat{b}\beta}{\hat{c}(\hat{c} - \hat{u}\beta + \hat{u})} & 1 & 0 \\ 0 & 0 & 0 & 1 \end{bmatrix} \quad (\text{C.20})$$

From Eq. 3.42 we can write

$$\begin{aligned} \mathbf{Q}_i - \mathbf{Q}_{i-1} &= \alpha_{i-1/2}^1 \hat{\mathbf{r}}^1 + \alpha_{i-1/2}^2 \hat{\mathbf{r}}^2 + \alpha_{i-1/2}^3 \hat{\mathbf{r}}^3 + \alpha_{i-1/2}^4 \hat{\mathbf{r}}^4 \\ &\equiv \mathcal{W}_{i-1/2}^1 + \mathcal{W}_{i-1/2}^2 + \mathcal{W}_{i-1/2}^3 + \mathcal{W}_{i-1/2}^4 \end{aligned} \quad (\text{C.21})$$

The coefficients $\alpha_{i-1/2}^p$ are computed by solving this linear system, which can be done explicitly

by inverting the right eigenvectors matrix \mathbf{R}

$$\mathbf{R}^{-1} = \begin{bmatrix} \frac{\hat{c} + \hat{u}}{2\hat{c}} & \frac{-1}{2\hat{c}} & 0 & 0 \\ \frac{\hat{c} - \hat{u}}{2\hat{c}} & \frac{1}{2\hat{c}} & 0 & 0 \\ -\frac{\hat{b}g(\hat{c}^2 - \hat{u}^2(\beta - 1))\beta}{\hat{c}^2(\hat{c} + \hat{u}(\beta - 1))(\hat{c} + \hat{u} - \hat{u}\beta)} & -\frac{\hat{b}g\hat{u}(-1 + \beta)\beta}{\hat{c}^2(\hat{c} + \hat{u}(\beta - 1))(\hat{c} + \hat{u} - \hat{u}\beta)} & 1 & 0 \\ 0 & 0 & 0 & 1 \end{bmatrix} \quad (\text{C.22})$$

where, $R_{31}^{-1} = -\frac{1}{2}(R_{31} + R_{32}) + \frac{\hat{u}}{2\hat{c}}(R_{32} - R_{31})$ and $R_{32}^{-1} = -\frac{1}{2\hat{c}}(R_{32} - R_{31})$, therefore, by multiplying this by the vector $\Delta() \equiv \mathbf{Q}_i - \mathbf{Q}_{i-1}$ gives the vector of α -coefficients, and hence

$$\begin{bmatrix} \alpha^1 \\ \alpha^2 \\ \alpha^3 \\ \alpha^4 \end{bmatrix} = \mathbf{R}^{-1} \times \begin{bmatrix} \Delta h \\ \Delta(hu) \\ \Delta b \\ \Delta y_b \end{bmatrix} \quad (\text{C.23})$$

therefore finally we have

$$\begin{aligned} \alpha^1 &= \frac{(\hat{c} + \hat{u})\Delta h - \Delta(hu)}{2\hat{c}} \\ \alpha^2 &= \frac{(\hat{c} - \hat{u})\Delta h + \Delta(hu)}{2\hat{c}} \\ \alpha^3 &= -\frac{1}{2}(R_{31} + R_{32})\Delta h + \frac{\hat{u}}{2\hat{c}}(R_{32} - R_{31})\Delta h - \frac{1}{2\hat{c}}(R_{32} - R_{31})\Delta(hu) + \Delta b \\ \alpha^4 &= \Delta y_b \end{aligned} \quad (\text{C.24})$$

and now the fluctuations using Eq. 3.45 can be computed.

D Friction source term discretization

The friction term is solved by splitting method by solving

$$\frac{dq}{dt} = s_f \quad (\text{D.1})$$

where $s_f = -\tau_b/\rho$. The implicit discretization method yields $\frac{q^{t+1}-q^t}{\Delta t} = s_f^{t+1}$. If we express s_f^{t+1} using Taylor expansion, we have

$$s_f^{t+1} = s_f^t + \left(\frac{\partial s_f}{\partial q}\right)^t \Delta q + O(\Delta q^2) \quad (\text{D.2})$$

where $\Delta q = q^{t+1} - q^t$. By simplifying Eq. D.2, one can obtain

$$q^{t+1} = q^t + \Delta t \frac{s_f^t}{1 - \Delta t \left(\frac{\partial s_f}{\partial q}\right)^t} \quad (\text{D.3})$$

which

$$\frac{s_f}{1 - \Delta t (\partial s_f / \partial q)} = \frac{-\tau_b/\rho}{1 - \Delta t (\partial(-\tau_b/\rho) / \partial q)} = \frac{-\frac{1}{8} f \bar{u} |\bar{u}|}{1 + \Delta t f |\bar{u}| / 4h} = \frac{-f h \bar{u} |\bar{u}|}{8h + 2\Delta t f |\bar{u}|} \quad (\text{D.4})$$

E Derivation of τ_{bx1} and τ_{by1}

In order to obtain the linearize shear stresses in Eq. 4.23, we followed Colombini et al., 1987. One can consider the friction factor as a function of dimensionless water height η and Shields number θ as

$$C_f = C_f(\eta, \theta) = C_0 + \epsilon C_1 \quad (\text{E.1})$$

By expansion of the function and considering the linearized Shields number as $\theta = \theta_0 + \epsilon \theta_1$, we can obtained the expressions for C_0 , and C_1 as follows

$$C_f = C_0 + \epsilon \left[\frac{\partial C}{\partial \eta} \eta_1 + \frac{\partial C}{\partial \theta} \theta_1 \right] \quad (\text{E.2})$$

By defining $C_T = \left(\frac{\partial C}{\partial \theta} \right) \frac{\theta_0}{C_0}$, and $C_D = \left(\frac{\partial C}{\partial \eta} \right) \frac{1}{C_0}$, and $\theta'_1 := \theta_1 / \theta_0$, one can write them as

$$C_f = C_0 + \epsilon C_1 = C_0 + \epsilon \left[C_D \eta_1 C_0 + C_T C_0 \theta'_1 \right] \quad (\text{E.3})$$

Therefore, $C_1 = C_D \eta_1 C_0 + C_T C_0 \theta'_1$. The Shields number as a function of dimensionless numbers can be expressed as

$$\theta = \frac{C_f Fr_0^2 (u'^2 + v'^2)}{(s-1)\delta^2} \quad (\text{E.4})$$

Thus in order to linearized the Shields number

$$\theta = \theta_0 + \epsilon \theta_1 = \frac{C_0 Fr_0^2}{(s-1)\delta^2} + \epsilon \left[\frac{2C_0 Fr_0^2}{(s-1)\delta^2} u_1 + \frac{Fr_0^2}{(s-1)\delta^2} C_1 \right] \quad (\text{E.5})$$

Therefore θ'_1 can be obtained

$$\theta'_1 := \frac{\theta_1}{\theta_0} = 2u_1 + C_1/C_0 = 2u_1 + \eta_1 C_D + C_T \theta'_1 \rightarrow \theta'_1 = \frac{2u_1}{1-C_T} + \frac{C_D}{1-C_T} \eta_1 \quad (\text{E.6})$$

Appendix E. Derivation of τ_{bx1} and τ_{by1}

The aforementioned derivation is going to be used for linearizing the shear stress and calculating τ_{bx1} and τ_{by1} as follows

$$\begin{aligned}\tau'_{bx} &= \tau_{bx0} + \epsilon \tau_{bx1} = C_0 + \epsilon \left[2C_0 u_1 + C_D \eta_1 C_0 + \frac{2C_T C_0}{1 - C_T} u_1 + \frac{C_D C_T C_0}{1 - C_T} \eta_1 \right] \\ &= C_0 + \epsilon \left[\frac{2C_0}{1 - C_T} u_1 + \frac{C_D C_0}{1 - C_T} \eta_1 \right] \\ \tau'_{by} &= \tau_{by0} + \epsilon \tau_{by1} = 0 + \epsilon C_0 v_1\end{aligned}\tag{E.7}$$

Then τ_{bx1} can be simplified as $\tau_{bx1} = C_0 s_1 u_1 + C_0 s_2 \eta_1$ where $s_1 = 2/(1 - C_T)$, and $s_2 = C_D/(1 - C_T)$, and $\tau_{by1} = C_0 v_1$.

F Extended Roe solver in two-dimension

The nonlinear hyperbolic system of equations can be written in the strong form of

$$\mathbf{q}_t + \mathbf{f}_x + \mathbf{g}_y = 0 \quad (\text{E1})$$

where \mathbf{q} , \mathbf{f} , and \mathbf{g} are vectors on \mathbb{R}^m ($m = 5$ is number of equations) and defined using the notation used by LeVeque et al., 2002 as

$$\mathbf{q} = \begin{bmatrix} h \\ hu \\ hv \\ b \\ y_b \end{bmatrix} = \begin{bmatrix} q_1 \\ q_2 \\ q_3 \\ q_4 \\ q_5 \end{bmatrix} \quad (\text{E2})$$

The Roe average, an approximation of the exact solution to the Riemann problem, can be employed to reduce computational time. This section details the derivation of the Roe matrix for the governing equations. Given that the Riemann problem is inherently one-dimensional, it is necessary to determine the Roe average for both the longitudinal and transversal directions. But the derivation for the longitudinal direction is elaborated upon here. By splitting the set of equation, one can consider the normal direction, i.e., $\mathbf{q}_t + \mathbf{f}_x = 0$ where

$$\mathbf{q} = \begin{bmatrix} h \\ hu \\ hv \\ b \\ y_b \end{bmatrix} = \begin{bmatrix} q_1 \\ q_2 \\ q_3 \\ q_4 \\ q_5 \end{bmatrix}, \mathbf{f}(\mathbf{q}) = \begin{bmatrix} hu \\ hu^2 + \frac{1}{2}gh^2 \\ huv \\ \beta ub \\ 0 \end{bmatrix} = \begin{bmatrix} q_2 \\ q_2^2/q_1 + \frac{1}{2}gq_1^2 \\ q_2q_3/q_1 \\ \beta q_2q_4/q_1 \\ 0 \end{bmatrix} \quad (\text{E3})$$

Appendix F. Extended Roe solver in two-dimension

and the corresponding Jacobian matrix is

$$\mathbf{f}'(\mathbf{q}) = \begin{bmatrix} 0 & 1 & 0 & 0 & 0 \\ -(q_2/q_1)^2 + gq_1 & 2q_2/q_1 & 0 & 0 & 0 \\ -\frac{q_2q_3}{q_1^2} & q_3/q_1 & q_2/q_1 & 0 & 0 \\ -\beta\frac{q_2q_4}{q_1^2} & 0 & \beta q_4/q_1 & \beta q_3/q_1 & 0 \\ 0 & 0 & 0 & 0 & 0 \end{bmatrix} = \begin{bmatrix} 0 & 1 & 0 & 0 & 0 \\ gh - u^2 & 2u & 0 & 0 & 0 \\ -uv & v & u & 0 & 0 \\ -\frac{b\beta u}{h} & \frac{b\beta}{h} & 0 & \beta u & 0 \\ 0 & 0 & 0 & 0 & 0 \end{bmatrix} \quad (\text{F4})$$

As a parameter vector we choose $\mathbf{z} = h^{-1/2}\mathbf{q}$ following similar parameter transformation have been used by Roe, 1981 for Euler equation, so that

$$\mathbf{z} = \begin{bmatrix} z_1 \\ z_2 \\ z_3 \\ z_4 \\ z_5 \end{bmatrix} = \begin{bmatrix} \sqrt{h} \\ \sqrt{hu} \\ \sqrt{hv} \\ b/\sqrt{h} \\ y_b/\sqrt{h} \end{bmatrix} \Rightarrow \mathbf{q}(\mathbf{z}) = \begin{bmatrix} (z_1)^2 \\ z_1 z_2 \\ z_1 z_3 \\ z_1 z_4 \\ z_1 z_5 \end{bmatrix} \rightarrow \frac{\partial \mathbf{q}}{\partial \mathbf{z}} = \begin{bmatrix} 2z_1 & 0 & 0 & 0 & 0 \\ z_2 & z_1 & 0 & 0 & 0 \\ z_3 & 0 & z_1 & 0 & 0 \\ z_4 & 0 & 0 & z_1 & 0 \\ z_5 & 0 & 0 & 0 & z_1 \end{bmatrix} \quad (\text{F5})$$

and by rewriting matrix \mathbf{f} using the parameter vector, one can obtain

$$\mathbf{f}(\mathbf{z}) = \begin{bmatrix} z_1 z_2 \\ (z_2)^2 + \frac{1}{2}g(z_1)^4 \\ z_2 z_3 \\ \beta z_2 z_4 \\ 0 \end{bmatrix} \rightarrow \frac{\partial \mathbf{f}}{\partial \mathbf{z}} = \begin{bmatrix} z_2 & z_1 & 0 & 0 & 0 \\ 2gz_1^3 & 2z_2 & 0 & 0 & 0 \\ 0 & z_3 & z_2 & 0 & 0 \\ 0 & \beta z_4 & 0 & \beta z_2 & 0 \\ 0 & 0 & 0 & 0 & 0 \end{bmatrix} \quad (\text{F6})$$

We now integrate along the path

$$z^p = Z_{i-1}^p + (Z_i^p - Z_{i-1}^p)\zeta \quad p = 1, \dots, 5 \quad (\text{F7})$$

where $\mathbf{Z}_j = \mathbf{z}(\mathbf{Q}_j)$ for $j = i-1, i$ and then integrate each element of these matrices from $\zeta = 0$ to $\zeta = 1$. As one can see, all elements are linear in ζ except one term

$$\mathbf{f}(\mathbf{Q}_i) - \mathbf{f}(\mathbf{Q}_{i-1}) = \int_0^1 \frac{d\mathbf{f}(\mathbf{z}(\zeta))}{d\zeta} d\zeta = \int_0^1 \frac{d\mathbf{f}(\mathbf{z}(\zeta))}{d\mathbf{z}} \mathbf{z}'(\zeta) d\zeta = \left[\int_0^1 \frac{d\mathbf{f}(\mathbf{z}(\zeta))}{d\mathbf{z}} d\zeta \right] (\mathbf{Z}_i - \mathbf{Z}_{i-1}) \quad (\text{F8})$$

$$\mathbf{Q}_i - \mathbf{Q}_{i-1} = \int_0^1 \frac{d\mathbf{q}(\mathbf{z}(\zeta))}{d\zeta} d\zeta = \int_0^1 \frac{d\mathbf{q}(\mathbf{z}(\zeta))}{d\mathbf{z}} \mathbf{z}'(\zeta) d\zeta = \left[\int_0^1 \frac{d\mathbf{q}(\mathbf{z}(\zeta))}{d\mathbf{z}} d\zeta \right] (\mathbf{Z}_i - \mathbf{Z}_{i-1}) \quad (\text{F9})$$

If we simplify the obtained equations, then we have

$$\begin{aligned}\mathbf{f}(\mathbf{Q}_i) - \mathbf{f}(\mathbf{Q}_{i-1}) &= \hat{\mathbf{C}}_{i-1/2}(\mathbf{Z}_i - \mathbf{Z}_{i-1}) \\ \mathbf{Q}_i - \mathbf{Q}_{i-1} &= \hat{\mathbf{B}}_{i-1/2}(\mathbf{Z}_i - \mathbf{Z}_{i-1})\end{aligned}\quad (\text{E10})$$

From these we can obtain the desired relation by using $\hat{\mathbf{A}}_{i-1/2} = \hat{\mathbf{C}}_{i-1/2} \hat{\mathbf{B}}_{i-1/2}^{-1}$. Integrating the linear terms $z^p(\zeta)$ yields

$$\begin{aligned}\int_0^1 z^p(\zeta) d\zeta &= \frac{1}{2}(Z_{i-1}^p + Z_i^p) \equiv \bar{Z}^p \\ \int_0^1 (z^1(\zeta))^3 d\zeta &= \frac{1}{4} \left(\frac{(Z_i^1)^4 - (Z_{i-1}^1)^4}{Z_i^1 - Z_{i-1}^1} \right) = \frac{1}{2}(Z_{i-1}^1 + Z_i^1) \cdot \frac{1}{2} \left[(Z_{i-1}^1)^2 + (Z_i^1)^2 \right] = \bar{Z}^1 \bar{h}\end{aligned}\quad (\text{E11})$$

where $\bar{h} = \frac{1}{2}(h_{i-1} + h_i)$. Hence, we obtain

$$\hat{\mathbf{B}}_{i-1/2} = \begin{bmatrix} 2\bar{Z}_1 & 0 & 0 & 0 & 0 \\ \bar{Z}_2 & \bar{Z}_1 & 0 & 0 & 0 \\ \bar{Z}_3 & 0 & \bar{Z}_1 & 0 & 0 \\ \bar{Z}_4 & 0 & 0 & \bar{Z}_1 & 0 \\ \bar{Z}_5 & 0 & 0 & 0 & \bar{Z}_1 \end{bmatrix}, \quad \hat{\mathbf{C}}_{i-1/2} = \begin{bmatrix} \bar{Z}_2 & \bar{Z}_1 & 0 & 0 & 0 \\ 2gh\bar{Z}_1 & 2\bar{Z}_2 & 0 & 0 & 0 \\ 0 & \bar{Z}_3 & \bar{Z}_2 & 0 & 0 \\ 0 & \beta\bar{Z}_4 & 0 & \beta\bar{Z}_2 & 0 \\ 0 & 0 & 0 & 0 & 0 \end{bmatrix}\quad (\text{E12})$$

The inverse $\hat{\mathbf{B}}_{i-1/2}^{-1}$ would be

$$\hat{\mathbf{B}}_{i-1/2}^{-1} = \begin{bmatrix} \frac{1}{2\bar{Z}_1} & 0 & 0 & 0 & 0 \\ -\frac{\bar{Z}_2}{2\bar{Z}_1^2} & \frac{1}{\bar{Z}_1} & 0 & 0 & 0 \\ -\frac{\bar{Z}_3}{2\bar{Z}_1^2} & 0 & \frac{1}{\bar{Z}_1} & 0 & 0 \\ -\frac{\bar{Z}_4}{2\bar{Z}_1^2} & 0 & 0 & \frac{1}{\bar{Z}_1} & 0 \\ -\frac{\bar{Z}_5}{2\bar{Z}_1^2} & 0 & 0 & 0 & \frac{1}{\bar{Z}_1} \end{bmatrix}\quad (\text{E13})$$

And so

$$\hat{\mathbf{A}}_{i-1/2} = \hat{\mathbf{C}}_{i-1/2} \hat{\mathbf{B}}_{i-1/2}^{-1} = \begin{bmatrix} 0 & 1 & 0 & 0 & 0 \\ g\bar{h} - \frac{\bar{Z}_2^2}{\bar{Z}_1^2} & \frac{2\bar{Z}_2}{\bar{Z}_1} & 0 & 0 & 0 \\ -\frac{\bar{Z}_2\bar{Z}_3}{\bar{Z}_1^2} & \frac{\bar{Z}_3}{\bar{Z}_1} & \frac{\bar{Z}_2}{\bar{Z}_1} & 0 & 0 \\ -\frac{\beta\bar{Z}_2\bar{Z}_4}{\bar{Z}_1^2} & \frac{\beta\bar{Z}_4}{\bar{Z}_1} & 0 & \frac{\beta\bar{Z}_2}{\bar{Z}_1} & 0 \\ 0 & 0 & 0 & 0 & 0 \end{bmatrix}\quad (\text{E14})$$

Appendix F. Extended Roe solver in two-dimension

where

$$\begin{aligned}
 \frac{\bar{Z}^2}{\bar{Z}^1} &= \frac{\frac{1}{2}(Z_{i-1}^2 + Z_i^2)}{\frac{1}{2}(Z_{i-1}^1 + Z_i^1)} = \frac{\sqrt{h_{i-1}}u_{i-1} + \sqrt{h_i}u_i}{\sqrt{h_{i-1}} + \sqrt{h_i}} = \hat{u} \\
 \frac{\bar{Z}^3}{\bar{Z}^1} &= \frac{\frac{1}{2}(Z_{i-1}^3 + Z_i^3)}{\frac{1}{2}(Z_{i-1}^1 + Z_i^1)} = \frac{\sqrt{h_{i-1}}v_{i-1} + \sqrt{h_i}v_i}{\sqrt{h_{i-1}} + \sqrt{h_i}} = \hat{v} \\
 \frac{\bar{Z}^4}{\bar{Z}^1} &= \frac{\frac{1}{2}(Z_{i-1}^4 + Z_i^4)}{\frac{1}{2}(Z_{i-1}^1 + Z_i^1)} = \frac{\frac{b_{i-1}}{\sqrt{h_{i-1}}} + \frac{b_i}{\sqrt{h_i}}}{\sqrt{h_{i-1}} + \sqrt{h_i}} = \frac{b_{i-1}\sqrt{h_i} + b_i\sqrt{h_{i-1}}}{h_{i-1}\sqrt{h_i} + h_i\sqrt{h_{i-1}}} = \frac{\hat{b}}{\hat{h}}
 \end{aligned} \tag{F15}$$

We can now simplify the $\hat{\mathbf{A}}_{i-1/2}$ as following

$$\hat{\mathbf{A}}_{i-1/2} = \begin{bmatrix} 0 & 1 & 0 & 0 & 0 \\ g\hat{h} - \hat{u}^2 & 2\hat{u} & 0 & 0 & 0 \\ -\hat{u}\hat{v} & \hat{v} & \hat{u} & 0 & 0 \\ -\frac{\beta\hat{b}\hat{u}}{\hat{h}} & \frac{\beta\hat{b}}{\hat{h}} & 0 & \beta\hat{u} & 0 \\ 0 & 0 & 0 & 0 & 0 \end{bmatrix} \tag{F16}$$

The five different eigenvalues of $\hat{\mathbf{A}}_{i-1/2}$ are

$$\begin{bmatrix} \hat{u} - \hat{c} \\ \hat{u} + \hat{c} \\ \hat{u} \\ \beta\hat{u} \\ 0 \end{bmatrix} \tag{F17}$$

And its five correspondence eigenvectors are

$$\hat{\mathbf{r}}^1 = \begin{bmatrix} 1 \\ \hat{u} - \hat{c} \\ \hat{v} \\ \frac{g\hat{b}\beta}{\hat{c}(\hat{c} + \hat{u}\beta - \hat{u})} \\ 0 \end{bmatrix}, \quad \hat{\mathbf{r}}^2 = \begin{bmatrix} 1 \\ \hat{u} + \hat{c} \\ \hat{v} \\ \frac{g\hat{b}\beta}{\hat{c}(\hat{c} - \hat{u}\beta + \hat{u})} \\ 0 \end{bmatrix}, \quad \hat{\mathbf{r}}^3 = \begin{bmatrix} 0 \\ 0 \\ 1 \\ 0 \\ 0 \end{bmatrix}, \quad \hat{\mathbf{r}}^4 = \begin{bmatrix} 0 \\ 0 \\ 0 \\ 1 \\ 0 \end{bmatrix}, \quad \hat{\mathbf{r}}^5 = \begin{bmatrix} 0 \\ 0 \\ 0 \\ 0 \\ 1 \end{bmatrix} \tag{F18}$$

where $\hat{c} = \sqrt{g\hat{h}}$. We define \mathbf{R} such as

$$\mathbf{R} = \begin{bmatrix} 1 & 1 & 0 & 0 & 0 \\ \hat{u} - \hat{c} & \hat{u} + \hat{c} & 0 & 0 & 0 \\ \hat{v} & \hat{v} & 1 & 0 & 0 \\ \frac{g\hat{b}\beta}{\hat{c}(\hat{c} + \hat{u}\beta - \hat{u})} & \frac{g\hat{b}\beta}{\hat{c}(\hat{c} - \hat{u}\beta + \hat{u})} & 0 & 1 & 0 \\ 0 & 0 & 0 & 0 & 1 \end{bmatrix} \tag{F19}$$

so that each column consist of one eigenvector. According to Eq. 4.34, one can write

$$\mathbf{f}_i - \mathbf{f}_{i-1} = \psi_{i-1/2}^1 \hat{r}^1 + \psi_{i-1/2}^2 \hat{r}^2 + \psi_{i-1/2}^3 \hat{r}^3 + \psi_{i-1/2}^4 \hat{r}^4 + \psi_{i-1/2}^5 \hat{r}^5 \quad (\text{F20})$$

The coefficients $\psi_{i-1/2}^p$ are computed by solving this linear system, which can be done explicitly by inverting the matrix of right eigenvectors, \mathbf{R} . \mathbf{R}^{-1} is equal to

$$\mathbf{R}^{-1} = \begin{bmatrix} \frac{\hat{c} + \hat{u}}{2\hat{c}} & -\frac{1}{2\hat{c}} & 0 & 0 & 0 \\ \frac{\hat{c} - \hat{u}}{2\hat{c}} & \frac{1}{2\hat{c}} & 0 & 0 & 0 \\ -\hat{v} & 0 & 1 & 0 & 0 \\ -\frac{\hat{b}\beta g(\hat{c}^2 - (\beta-1)\hat{u}^2)}{\hat{c}^2(\hat{c} + (\beta-1)\hat{u})(\hat{c} - \beta\hat{u} + \hat{u})} & -\frac{\hat{b}(\beta-1)\beta g \hat{u}}{\hat{c}^2(\hat{c} + (\beta-1)\hat{u})(\hat{c} - \beta\hat{u} + \hat{u})} & 0 & 1 & 0 \\ 0 & 0 & 0 & 0 & 1 \end{bmatrix} \quad (\text{F21})$$

where, $R_{41}^{-1} = -\frac{1}{2}(R_{41} + R_{42}) + \frac{\hat{u}}{2\hat{c}}(R_{42} - R_{41})$ and $R_{42}^{-1} = -\frac{1}{2\hat{c}}(R_{42} - R_{41})$ therefore, by multiplying \mathbf{R}^{-1} by the vectors $\Delta(\mathbf{f}) \equiv \mathbf{f}_i - \mathbf{f}_{i-1}$, the vector of ψ^m -coefficients can be computed as

$$\begin{bmatrix} \psi^1 \\ \psi^2 \\ \psi^3 \\ \psi^4 \\ \psi^5 \end{bmatrix} = \mathbf{R}^{-1} \times \begin{bmatrix} \Delta(hu) \\ \Delta(hu^2 + \frac{1}{2}gh^2) \\ \Delta(huv) \\ \Delta(\beta ub) \\ 0 \end{bmatrix}, \begin{bmatrix} \Lambda_1 \\ \Lambda_2 \\ \Lambda_3 \\ \Lambda_4 \\ \Lambda_5 \end{bmatrix} = \mathbf{P}^{-1} \times \begin{bmatrix} \Delta(hv) \\ \Delta(huv) \\ \Delta(hv^2 + \frac{1}{2}gh^2) \\ \Delta(\beta vb) \\ 0 \end{bmatrix} \quad (\text{F22})$$

Therefore, finally, we have

$$\begin{aligned} \psi^1 &= \frac{(\hat{u} + \hat{c})\Delta(hu) - \Delta(hu^2 + \frac{1}{2}gh^2)}{2\hat{c}} \\ \psi^2 &= \frac{-(\hat{u} - \hat{c})\Delta(hu) + \Delta(hu^2 + \frac{1}{2}gh^2)}{2\hat{c}} \\ \psi^3 &= -\hat{v}\Delta(hu) + \Delta(huv) \\ \psi^4 &= -\frac{(R_{41} + R_{42})}{2}\Delta(hu) + \frac{\hat{u}}{2\hat{c}}(R_{42} - R_{41})\Delta(hu) - \frac{1}{2\hat{c}}(R_{42} - R_{41})\Delta(hu^2 + \frac{1}{2}gh^2) + \Delta(\beta ub) \\ \psi^5 &= 0 \end{aligned} \quad (\text{F23})$$

Thus the fluctuations can be calculated using Eq. 4.34.

Bibliography

- Abbaspour, K. C., Yang, J., Maximov, I., Siber, R., Bogner, K., Mieleitner, J., Zobrist, J., & Srinivasan, R. (2007). Modelling hydrology and water quality in the pre-alpine/alpine thur watershed using swat. *Journal of Hydrology*, 333(2-4), 413–430.
- Acuña, G. J., Ávila, H., & Canales, F. A. (2019). River model calibration based on design of experiments theory. a case study: meta river, colombia. *Water*, 11(7), 1382.
- Afan, H. A., El-Shafie, A., Yaseen, Z. M., Hameed, M. M., Wan Mohtar, W. H. M., & Hussain, A. (2015). Ann based sediment prediction model utilizing different input scenarios. *Water Resources Management*, 29(4), 1231–1245.
- Ahmari, H., & Da Silva, A. M. F. (2011). Regions of bars, meandering and braiding in da silva and yalin's plan. *Journal of Hydraulic Research*, 49(6), 718–727.
- Al Najar, M., Thoumyre, G., Bergsma, E. W., Almar, R., Benschila, R., & Wilson, D. G. (2021). Satellite derived bathymetry using deep learning. *Machine Learning*, 1–24.
- Almeida, T. G., Walker, D. T., & Warnock, A. M. (2018). Estimating river bathymetry from surface velocity observations using variational inverse modeling. *Journal of Atmospheric and Oceanic Technology*, 35(1), 21–34.
- Alom, M. Z., Hasan, M., Yakopcic, C., Taha, T. M., & Asari, V. K. (2018). Recurrent residual convolutional neural network based on u-net (r2u-net) for medical image segmentation. *arXiv preprint arXiv:1802.06955*.
- Altunkaynak, A. (2009). Sediment load prediction by genetic algorithms. *Advances in Engineering Software*, 40(9), 928–934.
- Ancey, C., & Heyman, J. (2014). A microstructural approach to bed load transport: mean behaviour and fluctuations of particle transport rates. *Journal of Fluid Mechanics*, 744, 129–168.
- Ancey, C. (2020). Bedload transport: a walk between randomness and determinism. part 1. the state of the art. *Journal of Hydraulic Research*, 58(1), 1–17.
- Ancey, C., Bigillon, F., Frey, P., & Ducret, R. (2003). Rolling motion of a bead in a rapid water stream. *Physical Review E*, 67(1), 011303.
- Ancey, C., Böhm, T., Jodeau, M., & Frey, P. (2006). Statistical description of sediment transport experiments. *Physical Review E*, 74(1), 011302.
- Ancey, C., Bohorquez, P., & Heyman, J. (2015). Stochastic interpretation of the advection-diffusion equation and its relevance to bed load transport. *Journal of Geophysical Research: Earth Surface*, 120(12), 2529–2551.

Bibliography

- Ancey, C., Bohorquez, P., & Bardou, E. (2014). Sediment transport in mountain rivers. *Ercoftac Bulletin*, 100, 37–52.
- Ancey, C., Davison, A., Böhm, T., Jodeau, M., & Frey, P. (2008). Entrainment and motion of coarse particles in a shallow water stream down a steep slope. *Journal of Fluid Mechanics*, 595, 83–114.
- Ancey, C., & Pascal, I. (2020). Estimating mean bedload transport rates and their uncertainty. *Journal of Geophysical Research: Earth Surface*, 125(7), e2020JF005534.
- Ancey, C., & Recking, A. (2023). Scaling behavior of bedload transport: what if bagnold was right? *Earth-Science Reviews*, 104571.
- Armanini, A., & Di Silvio, G. (1988). A one-dimensional model for the transport of a sediment mixture in non-equilibrium conditions. *Journal of Hydraulic Research*, 26(3), 275–292.
- Ashida, K., & Michiue, M. (1973). Studies on bedload transport rate in open channel flows. *IAHR Int. Symp. River Mech.*, 1(10), 407–417.
- Ashida, K., & Shiomi, Y. (1966). Study on the hydraulics behaviour of meander in channels. *Disaster Prevention Research Institute Annuals*, 457–477.
- Ashida, K., & Michiue, M. (1972). Study on hydraulic resistance and bed-load transport rate in alluvial streams. *Proceedings of the Japan Society of Civil Engineers*, 1972(206), 59–69.
- Ashmore, P. E. (1988). Bed load transport in braided gravel-bed stream models. *Earth Surface Processes and Landforms*, 13(8), 677–695.
- Atashi, V., Gorji, H. T., Shahabi, S. M., Kardan, R., & Lim, Y. H. (2022). Water level forecasting using deep learning time-series analysis: a case study of red river of the north. *Water*, 14(12), 1971.
- Auel, C., Albayrak, I., Sumi, T., & Boes, R. M. (2017). Sediment transport in high-speed flows over a fixed bed: 1. particle dynamics. *Earth Surface Processes and Landforms*, 42(9), 1365–1383.
- Aziz, N. M., & Scott, D. E. (1989). Experiments on sediment transport in shallow flows in high gradient channels. *Hydrological Sciences Journal*, 34(4), 465–478.
- Bader, M., Breuer, A., Hölzl, W., & Rettenberger, S. (2014). Vectorization of an augmented riemann solver for the shallow water equations. *2014 International Conference on High Performance Computing & Simulation (HPCS)*, 193–201.
- Badoux, A., Andres, N., & Turowski, J. (2014). Damage costs due to bedload transport processes in switzerland. *Natural Hazards and Earth System Sciences*, 14(2), 279–294.
- Bagnold, R. A. (1966). *An approach to the sediment transport problem from general physics*. US government printing office.
- Bale, D. S., LeVeque, R. J., Mitran, S., & Rossmanith, J. A. (2003). A wave propagation method for conservation laws and balance laws with spatially varying flux functions. *SIAM Journal on Scientific Computing*, 24(3), 955–978.
- Balmforth, N. J., & Provenzale, A. (2001). *Geomorphological fluid mechanics* (Vol. 582). Springer Science & Business Media.
- Balmforth, N., Craster, R., & Sassi, R. (2004). Dynamics of cooling viscoplastic domes. *Journal of Fluid Mechanics*, 499, 149–182.

- Barzegar, R., Fijani, E., Moghaddam, A. A., & Tziritis, E. (2017). Forecasting of groundwater level fluctuations using ensemble hybrid multi-wavelet neural network-based models. *Science of the Total Environment*, 599, 20–31.
- Bechle, A. J., & Wu, C. H. (2014). An entropy-based surface velocity method for estuarine discharge measurement. *Water Resources Research*, 50(7), 6106–6128.
- Bellman, R. (1966). Dynamic programming. *Science*, 153(3731), 34–37.
- Benavides, S. J., Deal, E., Rushlow, M., Venditti, J. G., Zhang, Q., Kamrin, K., & Perron, J. T. (2022). The impact of intermittency on bed load sediment transport. *Geophysical Research Letters*, 49(5), e2021GL096088.
- Bermúdez, M., Ntegeka, V., Wolfs, V., & Willems, P. (2018). Development and comparison of two fast surrogate models for urban pluvial flood simulations. *Water Resources Management*, 32(8), 2801–2815.
- Bertagni, M. B., & Camporeale, C. (2018). Finite amplitude of free alternate bars with suspended load. *Water Resources Research*, 54(12), 9759–9773.
- Bhattacharya, B., Price, R., & Solomatine, D. (2007). Machine learning approach to modeling sediment transport. *Journal of Hydraulic Engineering*, 133(4), 440–450.
- Biondi, F., Addabbo, P., Clemente, C., & Orlando, D. (2020). Measurements of surface river doppler velocities with along-track insar using a single antenna. *IEEE Journal of Selected Topics in Applied Earth Observations and Remote Sensing*, 13, 987–997.
- Bladé, E., Cea, L., Corestein, G., Escolano, E., Puertas, J., Vázquez-Cendón, E., Dolz, J., & Coll, A. (2014). Iber: herramienta de simulación numérica del flujo en ríos. *Revista internacional de métodos numéricos para cálculo y diseño en ingeniería*, 30(1), 1–10.
- Bogardi, J., & Yen, C. H. (1938). *Traction of pebbles by flowing water*. <https://doi.org/10.17077/etd.005164>
- Böhm, T., Ancey, C., Frey, P., Reboud, J.-L., & Ducottet, C. (2004). Fluctuations of the solid discharge of gravity-driven particle flows in a turbulent stream. *Physical Review E*, 69(6), 061307.
- Bohorquez, P., Cañada-Pereira, P., Jimenez-Ruiz, P., & del Moral-Erencia, J. (2019). The fascination of a shallow-water theory for the formation of megaflood-scale dunes and antidunes. *Earth-Science Reviews*, 193, 91–108.
- Bohorquez, P., & Ancey, C. (2015). Stochastic-deterministic modeling of bed load transport in shallow water flow over erodible slope: linear stability analysis and numerical simulation. *Advances in Water Resources*, 83, 36–54.
- Bohorquez, P., & Ancey, C. (2016). Particle diffusion in non-equilibrium bedload transport simulations. *Applied Mathematical Modelling*, 40(17-18), 7474–7492.
- Bradley, A. A., Kruger, A., Meselhe, E. A., & Muste, M. V. (2002). Flow measurement in streams using video imagery. *Water Resources Research*, 38(12), 51–1.
- Brown, R. (1828). *A brief account of microscopical observations... on the particles contained in the pollen of plants; and on the general existence of active molecules in organic and inorganic bodies*. Richard Taylor.
- Callander, R. (1969). Instability and river channels. *Journal of Fluid Mechanics*, 36(3), 465–480.

Bibliography

- Cameron, S., Nikora, V., & Marusic, I. (2019). Drag forces on a bed particle in open-channel flow: effects of pressure spatial fluctuations and very-large-scale motions. *Journal of Fluid Mechanics*, 863, 494–512.
- Cameron, S., Nikora, V., & Witz, M. (2020). Entrainment of sediment particles by very large-scale motions. *Journal of Fluid Mechanics*, 888, A7.
- Campagnol, J., Radice, A., & Ballio, F. (2012). Scale-based statistical analysis of sediment fluxes. *Acta Geophysica*, 60(6), 1744–1777.
- Cao, H. H. (1985). *Résistance hydraulique d'un lit de gravier mobile à pente raide: étude expérimentale* [Doctoral dissertation, EPFL].
- Cao, Z., Hu, P., Hu, K., Pender, G., & Liu, Q. (2015). Modelling roll waves with shallow water equations and turbulent closure. *Journal of Hydraulic Research*, 53(2), 161–177.
- Cao, Z., Li, Z., Pender, G., & Hu, P. (2012). Non-capacity or capacity model for fluvial sediment transport. *Proceedings of the Institution of Civil Engineers-Water Management*, 165(4), 193–211.
- Capart, H., & Fraccarollo, L. (2011). Transport layer structure in intense bed-load. *Geophysical Research Letters*, 38(20).
- Casey, H. J. (1935). *Über geschiebebewegung* (Vol. 19). Preuß. Versuchsanst. f. Wasserbau u. Schiffbau.
- Chang, H.-Y., Simons, D. B., & Woolhiser, D. A. (1971). Flume experiments on alternate bar formation. *Journal of the Waterways, Harbors and Coastal Engineering Division*, 97(1), 155–165.
- Charru, F., Mouilleron, H., & Eiff, O. (2004). Erosion and deposition of particles on a bed sheared by a viscous flow. *Journal of Fluid Mechanics*, 519, 55–80.
- Chatanantavet, P., Whipple, K. X., Adams, M. A., & Lamb, M. P. (2013). Experimental study on coarse grain saltation dynamics in bedrock channels. *Journal of Geophysical Research: Earth Surface*, 118(2), 1161–1176.
- Cheng, N.-S. (2002). Exponential formula for bedload transport. *Journal of Hydraulic Engineering*, 128(10), 942–946.
- Chiu, C.-L. (1987). Entropy and probability concepts in hydraulics. *Journal of Hydraulic Engineering*, 113(5), 583–599.
- Chiu, C.-L. (1988). Entropy and 2-d velocity distribution in open channels. *Journal of Hydraulic Engineering*, 114(7), 738–756.
- Chiu, C.-L. (1989). Velocity distribution in open channel flow. *Journal of Hydraulic Engineering*, 115(5), 576–594.
- Church, M. (2006). Bed material transport and the morphology of alluvial river channels. *Annu. Rev. Earth Planet. Sci.*, 34, 325–354.
- Cohen, H., Laronne, J. B., & Reid, I. (2010). Simplicity and complexity of bed load response during flash floods in a gravel bed ephemeral river: a 10 year field study. *Water Resources Research*, 46(11).
- Colombini, M., Seminara, G., & Tubino, M. (1987). Finite-amplitude alternate bars. *Journal of Fluid Mechanics*, 181, 213–232.

- Colombini, M., & Stocchino, A. (2012). Three-dimensional river bed forms. *Journal of Fluid Mechanics*, 695, 63–80.
- Cordier, F., Tassi, P., Claude, N., Crosato, A., Rodrigues, S., & Pham Van Bang, D. (2019). Numerical study of alternate bars in alluvial channels with nonuniform sediment. *Water Resources Research*, 55(4), 2976–3003.
- Costa, P. J. M. (2016). Sediment transport. In M. J. Kennish (Ed.), *Encyclopedia of estuaries* (pp. 562–567). Springer Netherlands. https://doi.org/10.1007/978-94-017-8801-4_187
- Crosato, A., Desta, F. B., Cornelisse, J., Schuurman, F., & Uijttewaal, W. S. (2012). Experimental and numerical findings on the long-term evolution of migrating alternate bars in alluvial channels. *Water Resources Research*, 48(6).
- Cudden, J. R., & Hoey, T. B. (2003). The causes of bedload pulses in a gravel channel: the implications of bedload grain-size distributions. *Earth Surface Processes and Landforms: The Journal of the British Geomorphological Research Group*, 28(13), 1411–1428.
- Cunge, J. A., Holly, F. M., & Verwey, A. (1980). *Practical Aspects of Computational River Hydraulics*. Pitman publishing.
- Cunge, J. A., & Perdreau, N. (1973). Mobile bed fluvial mathematical models. 7, 561–580.
- Cushman-Roisin, B., & Beckers, J.-M. (2011). *Introduction to geophysical fluid dynamics: physical and numerical aspects*. Academic press.
- Davis, T. A. (2006). *Direct methods for sparse linear systems*. SIAM.
- Defina, A. (2003). Numerical experiments on bar growth. *Water Resources Research*, 39(4).
- Deigaard, R. (2006). Breaking antidunes: cyclic behavior due to hysteresis. *Journal of Hydraulic Engineering*, 132(6), 620–623.
- Demiral, D., Albayrak, I., Turowski, J. M., & Boes, R. M. (2022). Particle saltation trajectories in supercritical open channel flows: roughness effect. *Earth Surface Processes and Landforms*, 47(15), 3588–3610.
- Dhont, B. (2017). *Sediment pulses in a gravel-bed flume with alternate bars* [Doctoral dissertation, EPFL].
- Dhont, B., & Ancey, C. (2018). Are bedload transport pulses in gravel bed rivers created by bar migration or sediment waves? *Geophysical Research Letters*, 45(11), 5501–5508.
- Dietrich, W. E. (1982). Settling velocity of natural particles. *Water Resources Research*, 18(6), 1615–1626.
- Dinehart, R. L. (1999). Correlative velocity fluctuations over a gravel river bed. *Water Resources Research*, 35(2), 569–582.
- Drake, T. G., Shreve, R. L., Dietrich, W. E., Whiting, P. J., & Leopold, L. B. (1988). Bedload transport of fine gravel observed by motion-picture photography. *Journal of Fluid Mechanics*, 192, 193–217.
- Drozdal, M., Vorontsov, E., Chartrand, G., Kadoury, S., & Pal, C. (2016). The importance of skip connections in biomedical image segmentation. *International Workshop on Deep Learning in Medical Image Analysis, International Workshop on Large-Scale Annotation of Biomedical Data and Expert Label Synthesis*, 179–187.

Bibliography

- du Boys, P. (1879). Le Rhône et les rivières à lit affouillable – étude du régime du Rhône et de l'action exercée par les eaux sur un lit à fond de graviers indéfiniment affouillable. *Annales des Ponts et Chaussées*, 49, 141–195.
- Durán, O., Andreotti, B., & Claudin, P. (2012). Numerical simulation of turbulent sediment transport, from bed load to saltation. *Physics of Fluids*, 24(10), 103306.
- Durand, M., Andreadis, K. M., Alsdorf, D. E., Lettenmaier, D. P., Moller, D., & Wilson, M. (2008). Estimation of bathymetric depth and slope from data assimilation of swath altimetry into a hydrodynamic model. *Geophysical Research Letters*, 35(20).
- Eekhout, J., Hoitink, A., & Mosselman, E. (2013). Field experiment on alternate bar development in a straight sand-bed stream. *Water Resources Research*, 49(12), 8357–8369.
- Einstein, H. A. (1937). Der geschiebetrieb als wahrscheinlichkeitsproblem (bedload transport as a probability problem) [English translation by W. W. Sayre]. In H. W. Shen (Ed.), *Sedimentation (symposium to honor h. a. einstein)* (pp. C1–C105). ETHZ.
- Einstein, H. A. (1942). Formulas for the transportation of bed load. *Transactions of the American Society of Civil Engineers*, 107(1), 561–577.
- Einstein, H. A. (1950). *The bed-load function for sediment transportation in open channel flows*. US Department of Agriculture.
- Emery, L., Smith, R., McNeal, D., Hughes, B., Swick, L. W., & MacMahan, J. (2010). Autonomous collection of river parameters using drifting buoys. *Oceans 2010 MTS/IEEE Seattle*, 1–7.
- Engelund, F. (1981). The motion of sediment particles on an inclined bed. *Progress Rep*, 53.
- Exner, F. (1925). Ueber die wechselwirkung zwischen wasser und geschiebe in flüssen. *Sitzungsberichte der kaiserlichen Akademie der Wissenschaften Wien, Abteilung IIA*, 134, 165–205.
- Fan, N., Zhong, D., Wu, B., Foufoula-Georgiou, E., & Guala, M. (2014). A mechanistic-stochastic formulation of bed load particle motions: from individual particle forces to the Fokker-Planck equation under low transport rates. *Journal of Geophysical Research: Earth Surface*, 119(3), 464–482.
- Farahani, A., Voghoei, S., Rasheed, K., & Arabnia, H. R. (2021). A brief review of domain adaptation. *Advances in Data Science and Information Engineering: Proceedings from ICDATA 2020 and IKE 2020*, 877–894.
- Forghani, M., Qian, Y., Lee, J., Farthing, M. W., Hesser, T., Kitanidis, P. K., & Darve, E. F. (2021). Application of deep learning to large scale riverine flow velocity estimation. *Stochastic Environmental Research and Risk Assessment*, 35(5), 1069–1088.
- Fujita, Y., & Muramoto, Y. (1982). Experimental study on stream channel processes in alluvial rivers. *Bulletin of the Disaster Prevention Research Institute*, 32(1), 49–96.
- Furbish, D. J., Fathel, S. L., & Schmeeckle, M. W. (2017). Particle motions and bedload theory: the entrainment forms of the flux and the Exner equation. *Gravel-Bed Rivers: Processes and Disasters*, 97–120.
- Gao, H., Birkel, C., Hrachowitz, M., Tetzlaff, D., Soulsby, C., & Savenije, H. H. (2019). A simple topography-driven and calibration-free runoff generation module. *Hydrology and Earth System Sciences*, 23(2), 787–809.

- Gao, P. (2008). Transition between two bed-load transport regimes: saltation and sheet flow. *Journal of Hydraulic Engineering*, 134(3), 340–349.
- Garambois, P.-A., & Monnier, J. (2015). Inference of effective river properties from remotely sensed observations of water surface. *Advances in Water Resources*, 79, 103–120.
- Garcia, J., Conchon, E., Pérennou, T., & Brunstrom, A. (2007). Kaunet: improving reproducibility for wireless and mobile research. *Proceedings of the 1st international workshop on System evaluation for mobile platforms*, 21–26.
- Garcia, M., & Niño, Y. (1993). Dynamics of sediment bars in straight and meandering channels: experiments on the resonance phenomenon. *Journal of Hydraulic Research*, 31(6), 739–761.
- Garcia, M. H. (2008). Sediment transport and morphodynamics. *Sedimentation Engineering*, 110, 21–163.
- Garcia Lugo, G., Bertoldi, W., Henshaw, A., & Gurnell, A. (2015). The effect of lateral confinement on gravel bed river morphology. *Water Resources Research*, 51(9), 7145–7158.
- Gardiner, C. W. (1983). *Handbook of Stochastic Methods*. Springer Verlag.
- Gardiner, C. W., et al. (1985). *Handbook of stochastic methods* (Vol. 3). Springer Berlin.
- Ghilardi, T., Franca, M. J., & Schleiss, A. J. (2014). Period and amplitude of bedload pulses in a macro-rough channel. *Geomorphology*, 221, 95–103.
- Ghorbanidehno, H., Lee, J., Farthing, M., Hesser, T., Darve, E. F., & Kitanidis, P. K. (2021). Deep learning technique for fast inference of large-scale riverine bathymetry. *Advances in Water Resources*, 147, 103715.
- Ghosh, S., Singh, A., & Kumar, S. (2023). Bbbc-u-net: optimizing u-net for automated plant phenotyping using big bang big crunch global optimization algorithm. *International Journal of Information Technology*, 1–13.
- Gilbert, G. K., & Murphy, E. C. (1914). *The transportation of debris by running water*. US Government Printing Office.
- Giri, S., & Shimizu, Y. (2006). Numerical computation of sand dune migration with free surface flow. *Water Resources Research*, 42(10).
- Glorot, X., & Bengio, Y. (2010). Understanding the difficulty of training deep feedforward neural networks. *Proceedings of the thirteenth international conference on artificial intelligence and statistics*, 249–256.
- Gomez, B. (1991). Bedload transport. *Earth-Science Reviews*, 31(2), 89–132.
- Gomez, B., Naff, R. L., & Hubbell, D. W. (1989). Temporal variations in bedload transport rates associated with the migration of bedforms. *Earth Surface Processes and Landforms*, 14(2), 135–156.
- Goodfellow, I., Bengio, Y., & Courville, A. (2016). *Deep learning* [<http://www.deeplearningbook.org>]. MIT Press.
- Graf, W., Leitner, P., Hanetseder, I., Ittner, L., Dossi, F., & Hauer, C. (2016). Ecological degradation of a meandering river by local channelization effects: a case study in an austrian lowland river. *Hydrobiologia*, 772, 145–160.
- Graf, W. H. (1987). Sediment transport in steep channel. *Journal of Hydroscience and Hydraulic Engineering, JSCE*, 5(1), 11–26.

Bibliography

- Graf, W. H., & Altinakar, M. S. (2000). *Hydraulique fluviale: écoulement et phénomènes de transport dans les canaux à géométrie simple* (Vol. 16). PPUR presses polytechniques.
- Griffiths, G. A. (1993). Sediment translation waves in braided gravel-bed rivers. *Journal of Hydraulic Engineering*, 119(8), 924–937.
- Guo, J. (2017). Exact procedure for einstein–johnson’s sidewall correction in open channel flow. *Journal of Hydraulic Engineering*, 143(4), 06016027.
- Hager, W. H. (2005). Du Boys and sediment transport. *Journal of Hydraulic Research*, 43(3), 227–233.
- Hauer, C., Wagner, B., Aigner, J., Holzapfel, P., Flödl, P., Liedermann, M., Tritthart, M., Sindelar, C., Pulg, U., Klösch, M., et al. (2018). State of the art, shortcomings and future challenges for a sustainable sediment management in hydropower: a review. *Renewable and Sustainable Energy Reviews*, 98, 40–55.
- Hauer, C., Leitner, P., Unfer, G., Pulg, U., Habersack, H., & Graf, W. (2018). The role of sediment and sediment dynamics in the aquatic environment. In S. Schmutz & J. Sendzimir (Eds.), *Riverine ecosystem management: science for governing towards a sustainable future* (pp. 151–169). Springer International Publishing. https://doi.org/10.1007/978-3-319-73250-3_8
- He, K., Zhang, X., Ren, S., & Sun, J. (2015). Delving deep into rectifiers: surpassing human-level performance on imagenet classification. *Proceedings of the IEEE International Conference on Computer Vision*, 1026–1034.
- Heyman, J. (2014). *A study of the spatio-temporal behaviour of bed load transport rate fluctuations* [Doctoral dissertation, EPFL].
- Heyman, J., Bohorquez, P., & Ancey, C. (2016). Entrainment, motion, and deposition of coarse particles transported by water over a sloping mobile bed. *Journal of Geophysical Research: Earth Surface*, 121(10), 1931–1952.
- Heyman, J., Mettra, F., Ma, H., & Ancey, C. (2013). Statistics of bedload transport over steep slopes: separation of time scales and collective motion. *Geophysical Research Letters*, 40(1), 128–133.
- Hilker, N., Badoux, A., & Hegg, C. (2009). The swiss flood and landslide damage database 1972–2007. *Natural Hazards and Earth System Sciences*, 9(3), 913–925.
- Hilldale, R. C., & Raff, D. (2008). Assessing the ability of airborne lidar to map river bathymetry. *Earth Surface Processes and Landforms*, 33(5), 773–783.
- Ho, P.-Y. (1939). *Abhängigkeit der geschiebebewegung von der kornform und der temperatur* [Doctoral dissertation]. Selbstverl.,
- Honnorat, M., Monnier, J., Rivière, N., Huot, É., & Le Dimet, F.-X. (2010). Identification of equivalent topography in an open channel flow using lagrangian data assimilation. *Computing and Visualization in Science*, 13(3), 111–119.
- Hudson, J., & Sweby, P. K. (2005). A high-resolution scheme for the equations governing 2d bed-load sediment transport. *International Journal for Numerical Methods in Fluids*, 47(10-11), 1085–1091.
- Huet-Dastarac, M., Nguyen, D., Jiang, S., Lee, J., & Montero, A. B. (2023). Can input reconstruction be used to directly estimate uncertainty of a regression u-net model?—application

- to proton therapy dose prediction for head and neck cancer patients. *arXiv preprint arXiv:2310.19686*.
- Ikeda, S. (1984). Prediction of alternate bar wavelength and height. *Journal of Hydraulic Engineering*, 110(4), 371–386.
- Inoue, T., Watanabe, Y., Iwasaki, T., & Otsuka, J. (2020). Three-dimensional antidunes coexisting with alternate bars. *Earth Surface Processes and Landforms*, 45(12), 2897–2911.
- Ioffe, S., & Szegedy, C. (2015). Batch normalization: accelerating deep network training by reducing internal covariate shift. *International Conference on Machine Learning*, 448–456.
- Iseya, F., & Ikeda, H. (1987). Pulsations in bedload transport rates induced by a longitudinal sediment sorting: a flume study using sand and gravel mixtures. *Geografiska Annaler: Series A, Physical Geography*, 69(1), 15–27.
- Jackson, J. E. (2005). *A user's guide to principal components*. John Wiley & Sons.
- Jaeggi, M. N. (1984). Formation and effects of alternate bars. *Journal of Hydraulic Engineering*, 110(2), 142–156.
- Jaynes, E. T. (1957). Information theory and statistical mechanics. *Physical Review*, 106(4), 620.
- Jeong, D.-I., & Kim, Y.-O. (2005). Rainfall-runoff models using artificial neural networks for ensemble streamflow prediction. *Hydrological Processes: An International Journal*, 19(19), 3819–3835.
- Jiang, Z., Tahmasebi, P., & Mao, Z. (2021). Deep residual u-net convolution neural networks with autoregressive strategy for fluid flow predictions in large-scale geosystems. *Advances in Water Resources*, 150, 103878.
- Julien, P. Y. (2010). Bedload. In *Erosion and sedimentation* (pp. 195–215). Cambridge University Press.
- Kassem, A. A., & Chaudhry, M. H. (1998). Comparison of coupled and semicoupled numerical models for alluvial channels. *Journal of Hydraulic Engineering*, 124(8), 794–802.
- Kennedy, J. F. (1963). The mechanics of dunes and antidunes in erodible-bed channels. *Journal of Fluid Mechanics*, 16(4), 521–544.
- Kennedy, J. F. (1969). The formation of sediment ripples, dunes, and antidunes. *Annual Review of Fluid Mechanics*, 1(1), 147–168.
- Ketcheson, D. I., Parsani, M., & LeVeque, R. J. (2013). High-order wave propagation algorithms for hyperbolic systems. *SIAM Journal on Scientific Computing*, 35(1), A351–A377.
- Keulegan, G. H. (1938). *Laws of turbulent flow in open channels* (Vol. 21). National Bureau of Standards Gaithersburg, MD, USA.
- Kiani-Oshtorjani, M., & Ancey, C. (2023). Bed topography inference from velocity field using deep learning. *Water*, 15(23), 4055.
- Kiani-Oshtorjani, M., & Ancey, C. (2024). Simulation of antidune migration in straight channel. *In preparation for Advances in Water Resources*.
- Kingma, D. P., & Ba, J. (2014). Adam: a method for stochastic optimization. *arXiv preprint arXiv:1412.6980*.
- Kinoshita, R. (1957). On the formation of river dunes, an observation of the meandering state. *Translation, JSCE, English translation by G. Parker*, 42, 1–21.

Bibliography

- Kinoshita, R. (1961). Investigation of channel deformation in ishikari river. *Report of Bureau of Resources*, 174.
- Kohl, S., Romera-Paredes, B., Meyer, C., De Fauw, J., Ledsam, J. R., Maier-Hein, K., Eslami, S., Jimenez Rezende, D., & Ronneberger, O. (2018). A probabilistic u-net for segmentation of ambiguous images. *Advances in Neural Information Processing Systems*, 31.
- Kok, J. E., Parteli, E. J., Michaels, T. I., & Karam, D. B. (2012). The physics of wind-blown sand and dust. *Reports on progress in Physics*, 75(10), 106901.
- Komar, P. D. (1980). Modes of sediment transport in channelized water flows with ramifications to the erosion of the martian outflow channels. *Icarus*, 42(3), 317–329.
- Kondolf, G. M. (1997). Profile: hungry water: effects of dams and gravel mining on river channels. *Environmental management*, 21(4), 533–551.
- Kranenburg, C. (1992). On the evolution of roll waves. *Journal of Fluid Mechanics*, 245, 249–261.
- Kumbhakar, M., Ghoshal, K., & Singh, V. P. (2020). Two-dimensional distribution of streamwise velocity in open channel flow using maximum entropy principle: incorporation of additional constraints based on conservation laws. *Computer Methods in Applied Mechanics and Engineering*, 361, 112738.
- Lafdani, E. K., Nia, A. M., & Ahmadi, A. (2013). Daily suspended sediment load prediction using artificial neural networks and support vector machines. *Journal of Hydrology*, 478, 50–62.
- Lajeunesse, E., Malverti, L., & Charru, F. (2010). Bed load transport in turbulent flow at the grain scale: experiments and modeling. *Journal of Geophysical Research: Earth Surface*, 115(F4).
- Landon, K. C., Wilson, G. W., Özkan-Haller, H. T., & MacMahan, J. H. (2014). Bathymetry estimation using drifter-based velocity measurements on the kootenai river, idaho. *Journal of Atmospheric and Oceanic Technology*, 31(2), 503–514.
- Lanzoni, S. (2000). Experiments on bar formation in a straight flume: 1. uniform sediment. *Water Resources Research*, 36(11), 3337–3349.
- Lee, J., Ghorbanidehno, H., Farthing, M. W., Hesser, T. J., Darve, E. F., & Kitanidis, P. K. (2018). Riverine bathymetry imaging with indirect observations. *Water Resources Research*, 54(5), 3704–3727.
- LeVeque, R. J. (2002). *Finite Volume Methods for Hyperbolic Problems*. Cambridge University Press.
- LeVeque, R. J., et al. (2002). *Finite volume methods for hyperbolic problems* (Vol. 31). Cambridge university press.
- LeVeque, R. J. (2011). A well-balanced path-integral f-wave method for hyperbolic problems with source terms. *Journal of Scientific Computing*, 48(1-3), 209–226.
- Lewis, Q. W., & Rhoads, B. L. (2015). Resolving two-dimensional flow structure in rivers using large-scale particle image velocimetry: an example from a stream confluence. *Water Resources Research*, 51(10), 7977–7994.
- Lewis, Q. W., & Rhoads, B. L. (2018a). Lspiv measurements of two-dimensional flow structure in streams using small unmanned aerial systems: 1. accuracy assessment based on

- comparison with stationary camera platforms and in-stream velocity measurements. *Water Resources Research*, 54(10), 8000–8018.
- Lewis, Q. W., & Rhoads, B. L. (2018b). Lspiv measurements of two-dimensional flow structure in streams using small unmanned aerial systems: 2. hydrodynamic mapping at river confluences. *Water Resources Research*, 54(10), 7981–7999.
- Li, Z., Kiani Oshtorjani, M., Chen, D., Zhang, Y., & Sun, H. (2023). Dynamics of dual-mode bedload transport with three-dimensional alternate bars migration in subcritical flow: experiments and model analysis. *Journal of Geophysical Research: Earth Surface*, 128(3), e2022JF006882.
- Lisle, T. E., Ikeda, H., & Iseya, F. (1991). Formation of stationary alternate bars in a steep channel with mixed-size sediment: a flume experiment. *Earth Surface Processes and Landforms*, 16(5), 463–469.
- Liu, D., Liu, X., Fu, X., & Wang, G. (2016). Quantification of the bed load effects on turbulent open-channel flows. *Journal of Geophysical Research: Earth Surface*, 121(4), 767–789.
- Liu, X., Landry, B., & García, M. (2008). Two-dimensional scour simulations based on coupled model of shallow water equations and sediment transport on unstructured meshes. *Coastal Engineering*, 55(10), 800–810.
- Liu, X., Song, Y., & Shen, C. (2022). Bathymetry inversion using a deep-learning-based surrogate for shallow water equations solvers. *arXiv preprint arXiv:2203.02821*.
- Liu, Z., & Merwade, V. (2018). Accounting for model structure, parameter and input forcing uncertainty in flood inundation modeling using bayesian model averaging. *Journal of Hydrology*, 565, 138–149.
- López, R., & Barragán, J. (2008). Equivalent roughness of gravel-bed rivers. *Journal of Hydraulic Engineering*, 134(6), 847–851.
- MacMahan, J., Brown, J., & Thornton, E. (2009). Low-cost handheld global positioning system for measuring surf-zone currents. *Journal of Coastal Research*, 25(3), 744–754.
- Marcus, W. A. (2002). Mapping of stream microhabitats with high spatial resolution hyperspectral imagery. *Journal of Geographical Systems*, 4(1), 113–126.
- Martínez-Aranda, S., Murillo, J., & García-Navarro, P. (2019). A comparative analysis of capacity and non-capacity formulations for the simulation of unsteady flows over finite-depth erodible beds. *Advances in Water Resources*, 130, 91–112.
- Mavis, F. T., Ho, C., Tu, Y.-C., Liu, T.-y., & Soucek, E. (1935). The transportation of detritus by flowing water (I).
- Maximenko, N., Hafner, J., & Nüiler, P. (2012). Pathways of marine debris derived from trajectories of lagrangian drifters. *Marine Pollution Bulletin*, 65(1-3), 51–62.
- Meyer-Peter, E., & Müller, R. (1948). Formulas for bed load transport. In *Proceedings of the 2nd meeting of the international association of hydraulic structures research (IAHSR)* (pp. 39–64).
- Mignot, E., Paquier, A., & Haider, S. (2006). Modeling floods in a dense urban area using 2d shallow water equations. *Journal of Hydrology*, 327(1-2), 186–199.
- Millar, R. G. (1999). Grain and form resistance in gravel-bed rivers résistances de grain et de forme dans les rivières à graviers. *Journal of Hydraulic Research*, 37(3), 303–312.

Bibliography

- Moramarco, T., Saltalippi, C., & Singh, V. P. (2004). Estimation of mean velocity in natural channels based on chiu's velocity distribution equation. *Journal of Hydrologic Engineering*, 9(1), 42–50.
- Muramoto & Fujimata. (1978). The classification of meso-scale river bed configuration and the criterion of its formation. *Proceedings of the Japanese Conference on Hydraulics*, 22, 275–282.
- Murillo, J., & García-Navarro, P. (2010). An exner-based coupled model for two-dimensional transient flow over erodible bed. *Journal of Computational Physics*, 229(23), 8704–8732.
- Najar, M. A., Benshila, R., Bennioui, Y. E., Thoumyre, G., Almar, R., Bergsma, E. W., Delvit, J.-M., & Wilson, D. G. (2022). Coastal bathymetry estimation from sentinel-2 satellite imagery: comparing deep learning and physics-based approaches. *Remote Sensing*, 14(5), 1196.
- Nakagawa, H., & Tsujimoto, T. (1980). Sand bed instability due to bed load motion. *Journal of the Hydraulics Division*, 106(12), 2029–2051.
- Needham, D. J., & Merkin, J. H. (1984). On roll waves down an open inclined channel. *Proceedings of the Royal Society of London. A. Mathematical and Physical Sciences*, 394(1807), 259–278.
- Nelson, P. A., & Morgan, J. A. (2018). Flume experiments on flow and sediment supply controls on gravel bedform dynamics. *Geomorphology*, 323, 98–105.
- Nones, M., & Guo, Y. (2023). Can sediments play a role in river flood risk mapping? learning from selected european examples. *Geoenvironmental Disasters*, 10(1), 20.
- OcCC. (2007). Climate change and switzerland 2050. expected impacts on environment, society and economy.
- Orhan, A. E., & Pitkow, X. (2017). Skip connections eliminate singularities. *arXiv preprint arXiv:1701.09175*.
- Paintal, A. (1971a). Concept of critical shear stress in loose boundary open channels. *Journal of Hydraulic Research*, 9(1), 91–113.
- Paintal, A. (1971b). A stochastic model of bed load transport. *Journal of Hydraulic Research*, 9(4), 527–554.
- Papa, D. V. (2020). *Morphology and morphodynamics of braided rivers: an experimental investigation* [Doctoral dissertation, EPFL].
- Parker, G. (1975). Sediment inertia as cause of river antidunes. *Journal of the Hydraulics Division*, 101(2), 211–221.
- Parker, G. (1979). Hydraulic geometry of active gravel rivers. *Journal of the Hydraulics Division*, 105(9), 1185–1201.
- Parker, G., Paola, C., & Leclair, S. (2000). Probabilistic exner sediment continuity equation for mixtures with no active layer. *Journal of Hydraulic Engineering*, 126(11), 818–826.
- Pascal, I., Ancey, C., & Bohorquez, P. (2021). The variability of antidune morphodynamics on steep slopes. *Earth Surface Processes and Landforms*, 46(9), 1750–1765.

- Paszke, A., Gross, S., Massa, F., Lerer, A., Bradbury, J., Chanan, G., Killeen, T., Lin, Z., Gimelshein, N., Antiga, L., et al. (2019). Pytorch: an imperative style, high-performance deep learning library. *Advances in Neural Information Processing Systems*, 32.
- Pierce, J. K., Hassan, M., & Ferreira, R. (2022). Stochastic description of the bedload sediment flux. *Earth Surface Dynamics Discussions*, 2022, 1–23.
- Pitlick, J. (1992). Flow resistance under conditions of intense gravel transport. *Water Resources Research*, 28(3), 891–903.
- Postacchini, M., Brocchini, M., Mancinelli, A., & Landon, M. (2012). A multi-purpose, intra-wave, shallow water hydro-morphodynamic solver. *Advances in Water Resources*, 38, 13–26.
- Rafique, M. U., Zhu, J., & Jacobs, N. (2022). Automatic segmentation of sinkholes using a convolutional neural network. *Earth and Space Science*, 9(2), e2021EA002195.
- Rastogi, A. K., & Rodi, W. (1978). Predictions of heat and mass transfer in open channels. *Journal of the Hydraulics division*, 104(3), 397–420.
- Recking, A. (2010). A comparison between flume and field bed load transport data and consequences for surface-based bed load transport prediction. *Water Resources Research*, 46(3).
- Recking, A., Bacchi, V., Naaim, M., & Frey, P. (2009). Antidunes on steep slopes. *Journal of Geophysical Research: Earth Surface*, 114(F4).
- Recking, A., Frey, P., Paquier, A., Belleudy, P., & Champagne, J.-Y. (2008a). Bed-load transport flume experiments on steep slopes. *Journal of Hydraulic Engineering*, 134(9), 1302–1310.
- Recking, A., Frey, P., Paquier, A., Belleudy, P., & Champagne, J.-Y. (2008b). Feedback between bed load transport and flow resistance in gravel and cobble bed rivers. *Water Resources Research*, 44(5).
- Recking, A., Liébault, F., Peteuil, C., & Jolimet, T. (2012). Testing bedload transport equations with consideration of time scales. *Earth Surface Processes and Landforms*, 37(7), 774–789.
- Redolfi, M. (2021). Free alternate bars in rivers: key physical mechanisms and simple formation criterion. *Water Resources Research*, 57(12), e2021WR030617.
- Redolfi, M., Welber, M., Carlin, M., Tubino, M., & Bertoldi, W. (2020). Morphometric properties of alternate bars and water discharge: a laboratory investigation. *Earth Surface Dynamics*, 8(3), 789–808.
- Repetto, R., Tubino, M., & Paola, C. (2002). Planimetric instability of channels with variable width. *Journal of Fluid Mechanics*, 457, 79.
- Reynolds, A. J. (1965). Waves on the erodible bed of an open channel. *Journal of Fluid Mechanics*, 22(1), 113–133.
- Rickenmann, D. (1990). *Bedload transport capacity of slurry flows at steep slopes* [Doctoral dissertation, ETH Zurich].
- Rickenmann, D. (2001). Comparison of bed load transport in torrents and gravel bed streams. *Water Resources Research*, 37(12), 3295–3305.

Bibliography

- Rickenmann, D. (2018). Variability of bed load transport during six summers of continuous measurements in two austrian mountain streams (fischbach and ruetz). *Water Resources Research*, 54(1), 107–131.
- Rinaldi, M., & Casagli, N. (1999). Stability of streambanks formed in partially saturated soils and effects of negative pore water pressures: the sieve river (italy). *Geomorphology*, 26(4), 253–277.
- Roe, P. L. (1981). Approximate riemann solvers, parameter vectors, and difference schemes. *Journal of Computational Physics*, 43(2), 357–372.
- Ronneberger, O., Fischer, P., & Brox, T. (2015). U-net: convolutional networks for biomedical image segmentation. *International Conference on Medical image computing and computer-assisted intervention*, 234–241.
- Rouse, H. (1937). Modern conceptions of the mechanics of fluid turbulence. *Transactions of the American Society of Civil Engineers*, 102(1), 463–505.
- Rouse, H. (1938). Experiments on the mechanics of sediment suspension. *Proceedings of the fifth international congress for applied mechanics*, 55, 550–554.
- Santurkar, S., Tsipras, D., Ilyas, A., & Madry, A. (2018). How does batch normalization help optimization? *Advances in Neural Information Processing Systems*, 31.
- Schielen, R., Doelman, A., & De Swart, H. (1993). On the nonlinear dynamics of free bars in straight channels. *Journal of Fluid Mechanics*, 252, 325–356.
- Schmeeckle, M. W., Nelson, J. M., Pitlick, J., & Bennett, J. P. (2001). Interparticle collision of natural sediment grains in water. *Water Resources Research*, 37(9), 2377–2391.
- Schmeeckle, M. W., Nelson, J. M., & Shreve, R. L. (2007). Forces on stationary particles in near-bed turbulent flows. *Journal of Geophysical Research: Earth Surface*, 112(F2).
- Schwarzmeier, C., Rettinger, C., Kemmler, S., Plewinski, J., Núñez-González, F., Köstler, H., Rúde, U., & Vowinkel, B. (2023). Particle-resolved simulation of antidunes in free-surface flows. *Journal of Fluid Mechanics*, 961, R1.
- Shekhar, S., Bansode, A., & Salim, A. (2021). A comparative study of hyper-parameter optimization tools. *2021 IEEE Asia-Pacific Conference on Computer Science and Data Engineering (CSDE)*, 1–6.
- Shettar, A. S., & Keshava Murthy, K. (1996). A numerical study of division of flow in open channels. *Journal of Hydraulic Research*, 34(5), 651–675.
- Shih, W., Diplas, P., Celik, A. O., & Dancy, C. (2017). Accounting for the role of turbulent flow on particle dislodgement via a coupled quadrant analysis of velocity and pressure sequences. *Advances in Water Resources*, 101, 37–48.
- Siddique, N., Paheding, S., Elkin, C. P., & Devabhaktuni, V. (2021). U-net and its variants for medical image segmentation: a review of theory and applications. *IEEE Access*, 9, 82031–82057.
- Simeonov, J. A., Holland, K. T., & Anderson, S. P. (2019). River discharge and bathymetry estimation from inversion of surface currents and water surface elevation observations. *Journal of Atmospheric and Oceanic Technology*, 36(1), 69–86.

- Singh, A., Fienberg, K., Jerolmack, D. J., Marr, J., & Foufoula-Georgiou, E. (2009). Experimental evidence for statistical scaling and intermittency in sediment transport rates. *Journal of Geophysical Research: Earth Surface*, 114(F1).
- Singh, A., Porté-Agel, E., & Foufoula-Georgiou, E. (2010). On the influence of gravel bed dynamics on velocity power spectra. *Water Resources Research*, 46(4).
- Singh, V. P. (2016). *Introduction to tsallis entropy theory in water engineering*. CRC Press.
- Singh, V. P., Yang, C. T., & Deng, Z. (2003). Downstream hydraulic geometry relations: 1. theoretical development. *Water Resources Research*, 39(12).
- Siviglia, A., Vanzo, D., & Toro, E. F. (2022). A splitting scheme for the coupled saint-venant-exner model. *Advances in Water Resources*, 159, 104062.
- Smart, G. M. (1984). Sediment transport formula for steep channels. *Journal of Hydraulic Engineering*, 110(3), 267–276.
- Smith, J. D., & McLean, S. (1984). A model for flow in meandering streams. *Water Resources Research*, 20(9), 1301–1315.
- Soares-Frazão, S., & Zech, Y. (2011). Hllc scheme with novel wave-speed estimators appropriate for two-dimensional shallow-water flow on erodible bed. *International Journal for Numerical Methods in Fluids*, 66(8), 1019–1036.
- Song, T., & Graf, W. H. (1996). Velocity and turbulence distribution in unsteady open-channel flows. *Journal of Hydraulic Engineering*, 122(3), 141–154. [https://doi.org/10.1061\(asce\)0733-9429\(1996\)122:3\(141\)](https://doi.org/10.1061(asce)0733-9429(1996)122:3(141))
- Song, T., Graf, W., & Lemmin, U. (1994). Uniform flow in open channels with movable gravel bed. *Journal of Hydraulic Research*, 32(6), 861–876.
- Srivastava, N., Hinton, G., Krizhevsky, A., Sutskever, I., & Salakhutdinov, R. (2014). Dropout: a simple way to prevent neural networks from overfitting. *The Journal of Machine Learning Research*, 15(1), 1929–1958.
- Struiksmá, N., & Crosato, A. (1989). Analysis of a 2-d bed topography model for rivers. *River Meandering*, 12, 153–180.
- Sudhan, M., Sinthuja, M., Pravinth Raja, S., Amutharaj, J., Charlyn Pushpa Latha, G., Sheeba Rachel, S., Anitha, T., Rajendran, T., Waji, Y. A., et al. (2022). Segmentation and classification of glaucoma using u-net with deep learning model. *Journal of Healthcare Engineering*, 2022.
- Sukegawa, N. (1971). Study on meandering of streams in straight channels. *Report of Bureau of Resources, Department of Science and Technology*.
- Sun, H., Chen, D., Zhang, Y., & Chen, L. (2015). Understanding partial bed-load transport: experiments and stochastic model analysis. *Journal of Hydrology*, 521, 196–204.
- Takahashi, T. (1981). Debris flow. *Annual Review of Fluid Mechanics*, 13(1), 57–77.
- Tao, J., Wang, Z. B., Zhou, Z., Xu, F., Zhang, C., & Stive, M. J. (2019). A morphodynamic modeling study on the formation of the large-scale radial sand ridges in the southern yellow sea. *Journal of Geophysical Research: Earth Surface*, 124(7), 1742–1761.
- Thuerey, N., Weißenow, K., Prantl, L., & Hu, X. (2020). Deep learning methods for reynolds-averaged navier–stokes simulations of airfoil flows. *AIAA Journal*, 58(1), 25–36.
- Toro, E. F. (2001). *Shock-Capturing Methods for Free-Surface Shallow Flows*. Wiley.

Bibliography

- Toro, E. F. (2013). *Riemann solvers and numerical methods for fluid dynamics: a practical introduction*. Springer Science & Business Media.
- Tsai, W.-P., Feng, D., Pan, M., Beck, H., Lawson, K., Yang, Y., Liu, J., & Shen, C. (2021). From calibration to parameter learning: harnessing the scaling effects of big data in geoscientific modeling. *Nature Communications*, *12*(1), 5988.
- Tsallis, C. (1988). Possible generalization of boltzmann-gibbs statistics. *Journal of Statistical Physics*, *52*, 479–487.
- Tucker, G. E., & Hancock, G. R. (2010). Modelling landscape evolution. *Earth Surface Processes and Landforms*, *35*(1), 28–50.
- Turowski, J. M. (2010). Probability distributions of bed load transport rates: a new derivation and comparison with field data. *Water Resources Research*, *46*(8).
- Valiani, A., & Begnudelli, L. (2006). Divergence form for bed slope source term in shallow water equations. *Journal of Hydraulic Engineering*, *132*(7), 652–665.
- Valyrakis, M., Diplas, P., & Dancey, C. L. (2013). Entrainment of coarse particles in turbulent flows: an energy approach. *Journal of Geophysical Research: Earth Surface*, *118*(1), 42–53.
- Valyrakis, M., Diplas, P., Dancey, C. L., Greer, K., & Celik, A. O. (2010). Role of instantaneous force magnitude and duration on particle entrainment. *Journal of Geophysical Research: Earth Surface*, *115*(F2).
- Van Duin, O. J., Hulscher, S. J., Ribberink, J. S., & Dohmen-Janssen, C. M. (2017). Modeling of spatial lag in bed-load transport processes and its effect on dune morphology. *Journal of Hydraulic Engineering*, *143*(2), 04016084.
- Van Rijn, L. C. (1984a). Sediment transport, part I: bed load transport. *Journal of Hydraulic Engineering*, *110*(10), 1431–1456.
- Van Rijn, L. C. (1984b). Sediment transport, part III: bed forms and alluvial roughness. *Journal of Hydraulic Engineering*, *110*(12), 1733–1754.
- Venditti, J., Nelson, P., Minear, J., Wooster, J., & Dietrich, W. (2012). Alternate bar response to sediment supply termination. *Journal of Geophysical Research: Earth Surface*, *117*(F2).
- Vyas, J. K., Perumal, M., & Moramarco, T. (2020). Discharge estimation using tsallis and shannon entropy theory in natural channels. *Water*, *12*(6), 1786.
- Wainwright, J., Parsons, A. J., Cooper, J. R., Gao, P., Gillies, J. A., Mao, L., Orford, J. D., & Knight, P. G. (2015). The concept of transport capacity in geomorphology. *Reviews of Geophysics*, *53*(4), 1155–1202.
- Wang, Z.-T., Zhang, C.-L., & Wang, H.-T. (2014). Intermittency of aeolian saltation. *The European Physical Journal E*, *37*, 1–6.
- Warburton, J., & Davies, T. (1994). Variability of bedload transport and channel morphology in a braided river hydraulic model. *Earth Surface Processes and Landforms*, *19*(5), 403–421.
- Wieprecht, S., Tolossa, H. G., & Yang, C. T. (2013). A neuro-fuzzy-based modelling approach for sediment transport computation. *Hydrological Sciences Journal*, *58*(3), 587–599.
- Williams, J. R., & O'Connor, R. (1999). Discrete element simulation and the contact problem. *Archives of Computational Methods in Engineering*, *6*(4), 279–304.

- Wilson, G., & Özkan-Haller, H. T. (2012). Ensemble-based data assimilation for estimation of river depths. *Journal of Atmospheric and Oceanic Technology*, 29(10), 1558–1568.
- Windheuser, L., Karanjit, R., Pally, R., Samadi, S., & Hubig, N. (2023). An end-to-end flood stage prediction system using deep neural networks. *Earth and Space Science*, 10(1), e2022EA002385.
- Wong, M., & Parker, G. (2006a). One-dimensional modeling of bed evolution in a gravel bed river subject to a cycled flood hydrograph. *Journal of Geophysical Research: Earth Surface*, 111(F3).
- Wong, M., & Parker, G. (2006b). Reanalysis and correction of bed-load relation of meyer-peter and müller using their own database. *Journal of Hydraulic Engineering*, 132(11), 1159–1168.
- Wozencraft, J., & Millar, D. (2005). Airborne lidar and integrated technologies for coastal mapping and nautical charting. *Marine Technology Society Journal*, 39(3).
- Wu, W. (2007). *Computational river dynamics*. CRC Press.
- Wu, W., & Wang, S. S. (2007). One-dimensional modeling of dam-break flow over movable beds. *Journal of Hydraulic Engineering*, 133(1), 48–58.
- Yan, C., Fan, X., Fan, J., & Wang, N. (2022). Improved u-net remote sensing classification algorithm based on multi-feature fusion perception. *Remote Sensing*, 14(5), 1118.
- Yang, Y., Pan, M., Beck, H. E., Fisher, C. K., Beighley, R. E., Kao, S.-C., Hong, Y., & Wood, E. F. (2019). In quest of calibration density and consistency in hydrologic modeling: distributed parameter calibration against streamflow characteristics. *Water Resources Research*, 55(9), 7784–7803.
- Yao, W., Zeng, Z., Lian, C., & Tang, H. (2018). Pixel-wise regression using u-net and its application on pansharpening. *Neurocomputing*, 312, 364–371.
- Yaseen, Z. M., El-Shafie, A., Jaafar, O., Afan, H. A., & Sayl, K. N. (2015). Artificial intelligence based models for stream-flow forecasting: 2000–2015. *Journal of Hydrology*, 530, 829–844.
- Yoon, Y., Durand, M., Merry, C. J., Clark, E. A., Andreadis, K. M., & Alsdorf, D. E. (2012). Estimating river bathymetry from data assimilation of synthetic swot measurements. *Journal of Hydrology*, 464, 363–375.
- Young, W. J. (1989). *Bedload transport in braided gravel-bed rivers: a hydraulic model study* [Doctoral dissertation, Lincoln College, University of Canterbury].
- Yu, S., & Ma, J. (2021). Deep learning for geophysics: current and future trends. *Reviews of Geophysics*, 59(3), e2021RG000742.
- Zaron, E. D. (2017). Recent developments in bottom topography mapping using inverse methods. *Data Assimilation for Atmospheric, Oceanic and Hydrologic Applications (Vol. III)*, 241–258.
- Zhang, C., Bengio, S., Hardt, M., Recht, B., & Vinyals, O. (2021). Understanding deep learning (still) requires rethinking generalization. *Communications of the ACM*, 64(3), 107–115.
- Zhou, J. G. (2004). *Lattice boltzmann methods for shallow water flows* (Vol. 4). Springer.
- Zolezzi, G., Guala, M., Termini, D., & Seminara, G. (2005). Experimental observations of up-stream overdeepening. *Journal of Fluid Mechanics*, 531, 191–219.

Bibliography

Zounemat-Kermani, M., Batelaan, O., Fadaee, M., & Hinkelmann, R. (2021). Ensemble machine learning paradigms in hydrology: a review. *Journal of Hydrology*, 598, 126266.

Mehrdad KIANI OSHTORJANI

PERSONAL DATA

PLACE AND DATE OF BIRTH: Isfahan, Iran | 28 Dec 1993

ADDRESS: Rue de la Borde 33B - 1018 Lausanne

PHONE: +41 (0) 76 750 98 99

EMAIL: mehrdad.kiani@epfl.ch

ORCID: 0000-0002-2882-6133

EDUCATION

2019-2024 Ph.D. in Mechanical Engineering, EPFL, Switzerland

2016-2019 M.Sc. in Computational Science and Engineering, EPFL, Switzerland

2012-2016 B.Sc. in Mechanical Engineering, IUT, Iran

SKILLSET

Programming: Python, C/C++, C#, R, Visual Basic, Fortran
Git, GitHub, Computational Software Development, Version Control
Docker, Cloud Computing, SQL/NoSQL, Pandas

Familiar OS : Linux, Windows

Data science : Machine Learning, Deep Learning, PyTorch & Autograd, Tensorflow
& Keras, PINN, Computer Vision, Statistical Analysis, Image Processing
Parallel Computing (OpenMP, MPI, CUDA), Optimization

Engineering : 2D/3D CAD Design, Mathematical Modeling, Computational Fluid Dynamics
Ansys, COMSOL, EES, LIGGGHTS, Paraview, ImageJ, SolidWorks, CATIA
Abaqus, INVENTOR, AutoCAD, MatLab, Mathematica, Maple, Iber, GeoClaw

Numerical Schemes : LBM, Level set, FDM, FVM, FEM, BEM, DEM

Highlights: Raspberry pi, Sensors (flow meter, pressure, temperature, humidity)
Microprocessor: Proteus, Code Vision (AVR, PLC)

Languages : Persian, French, English

Soft Skills : Works well in team, fast learner, good at problem solving

RESEARCH JOURNAL PUBLICATION

Accurate buoyancy and drag force models to predict particle segregation in vibrofluidized beds, Phys. Rev. E 103, 062903 – Published 14 June 2021, <https://doi.org/10.1103/PhysRevE.103.062903>

Conjugate heat transfer in isolated granular clusters with interstitial fluid using lattice Boltzmann method, International Journal of Heat and Mass Transfer, 187, p.122539, <https://doi.org/10.1016/j.ijheatmasstransfer.2022.122539>

Bed topography inference from velocity field using deep learning, Water 15, no. 23: 4055. <https://doi.org/10.3390/w15234055>

Dynamics of dual-mode bedload transport with three-dimensional alternate bars migration in subcritical flow: Experiments and model analysis, Journal of Geophysical Research: Earth Surface: e2022JF006882, <https://doi.org/10.1029/2022JF006882>

In Preparation for publication: "Stochastic simulation study on bedload transport and bedform development" by M. Kiani-Oshtorjani, and C. Ancey

In Preparation for publication: "Stochastic modeling of bedload transport and bar development: linear stability analysis and numerical simulation" by M. Kiani-Oshtorjani, E. Karpushov, and C. Ancey

WORK EXPERIENCE

NOV, 2019 – APR, 2024	PhD Scholar at Environmental Hydraulics Laboratory (LHE), EPFL, Lausanne, Switzerland <i>Title: "Stochastic Simulations and Machine Learning Modeling to Predict Bedload Transport and Bed Topography."</i>
JUL, 2019 – OCT, 2019	Intern at Environmental Hydraulics Laboratory (LHE), EPFL, Lausanne, Switzerland <i>Title: "Numerical Solutions to a Set of Equations Coupling Stochastic and Deterministic Processes"</i>
OCT, 2018 – APR, 2019	Master Thesis at Laboratory of Energy and Engineering (LEE), ETH, Zürich, Switzerland <i>Title: "Simulation of Segregation and Instabilities in Agitated Granular Systems"</i>
JUL – DEC, 2017	Intern at ABB Corporate Research and Development section, Dättwil, Baden, Switzerland <i>Title: "Magnetic Components for Power Electronics: Numerical Analysis and Optimization of Winding Conductors Using COMSOL Multiphysics."</i>
FEB – JUN, 2017	Semester Project at WIND Engineering and Renewable Energy Laboratory (WIRE), EPFL, Lausanne, Switzerland <i>Title: "Simulation of Turbine Wakes Using Ansys-Fluent."</i>
SEP, 2016 – JAN, 2017	Semester Project at Laboratory for Hydraulic Machines (LMH), EPFL, Lausanne, Switzerland <i>Title: "Formulation and Implementation of a Turbulence Model for the Finite Volume Particle Method."</i>
SEP, 2015 – FEB, 2016	Bachelor Thesis at National High Performance Computing Center (NH-PCC), IUT, Isfahan, Iran <i>Title: "Simulation of Formation and Movement of Gas Bubbles in a Liquid Using the Lattice Boltzmann Method"</i>
JUN – SEP 2015	Intern at National High Performance Computing Center (NHPCC), IUT, Isfahan, Iran <i>Title: "Simulation of Droplet Deformation Impacting a Solid Surface Using the Lattice Boltzmann Method."</i>

TEACHING EXPERIENCES

- Supervision of several Master's thesis, semester projects, and internships during my PhD,
- Teaching assistant for Bachelor's (fluid mechanics) and Master's courses (i. hydrological risks and land use planning and ii. flood waves and dam failure) during my PhD,
- Peer reviewing for Water Resources Research (WRR).

INTERESTS

Photography, Hiking, Camping, Alps, Traveling, Cycling, Playing Chess, Ping Pong, and Tennis.